Stability of Quadrilateral Plates and Panels for Aerospace Design

Paul Huyton

Submitted for Degree of Doctor of Philosophy

The University of Edinburgh

2002

Declaration

The writing of this thesis and the research presented herein was carried out solely by the named author under the supervison of Dr C.B. York.

The inclusion of the work of others is acknowledged and referenced in full.

Paul Huyton

Acknowledgements

The author gratefully acknowledges the help and support, financial or otherwise, of: Dr C.B. York (supervisor); Engineering and Physical Sciences Research Council (grant number GR/L86661); School of Civil and Environmental Engineering, The University of Edinburgh; and The Department of Aerospace Engineering, The University of Glasgow.

Abstract

This thesis presents new knowledge in the area of plate buckling, which has use in practical applications in the design of aircraft structures, such as wing or fuselage panels and thin-walled civil engineering structures.

The focus of the research is on plates that are skew (parallelogram) in planform and the buckling strength gains that arise because of a stiffening effect caused by the acute angle of the plate and the fixity along the plate edges that continuity of adjacent skew plates imposes.

A finite element code, ABAQUS, is adopted to compare the buckling strength of plates that are continuous over an infinite number of bays with isolated (non-continuous) plates that have varying magnitudes of rotational restraint applied along the edges. The continuous results, obtained from VICONOPT, are available in the open literature. The results are presented as comprehensive buckling curves.

The continuous VICONOPT solutions are verified using a finite element model and the validity of the assumptions used to obtain the VICONOPT results is assessed.

The work on skew plates is extended to assemblies of plates that form skew panels of the type typically used in aerospace applications. Buckling calculations are presented for varying magnitudes of orthotropy and skew angles. Analysis of the panel is compared with a plate having the equivalent orthotropic properties and the results compared to closed-form solutions for equivalent rectangular plates.

Because modern aircraft wings are generally 'swept' and tapered along their length, the resulting plates that make up the panels are not only skew but also tapered in planform. The effect of this taper together with skew is considered and the buckling strength changes that arise because of the stiffening effect of the planform taper assessed.

Finally, panels taken from an optimised benchmark wing, are assessed for buckling to ascertain the effect of making simplifying assumptions about the planform geometry of the panels and the consequences of these assumptions on the panel buckling strength.

Contents

Chapter 1

Introduction

This chapter introduces the approach and background to the thesis and gives an overview of the relevant findings of each chapter. Specific conclusions drawn from each chapter are given in chapter 9.

1.1 Background and Approach

Over the last few decades, the buckling strength of rectangular plates and panels *i.e.* stiffened plates, has been extensively studied for a wide range of loading cases and boundary conditons [113]. In contrast, quadrilateral plates that have less regular geometry have been the subject of far fewer studies, even though they are widely used in many applications. This thesis considers the stability and buckling behaviour of skew plate structures that are of particular practical importance to aircraft wing and fuselage design.

Studies investigating the buckling strength of skew plate structures are generally very limited in scope and provide few buckling predictions, hence it is difficult to fully understand the buckling behaviour of plates and panels. Notable exceptions to this are the works of Wittrick [105, 106], York [112] and Anderson [5]. The latter two of these studies considered plates that are continuous in either the longitudinal or both in-plane directions and therefore do not provide solutions for isolated plates, *i.e.* those with simply supported or clamped edges (or combinations of these). The accuracy of the works by Wittrick are limited by the computational technology available at the time in which it was conducted (as was Anderson's) and by the fact that it does not account for skew plates that are also tapered in planform, as is the case in a modern-day aircraft wing.

The work of the thesis addresses the short-comings and lack of illustrative results describing the buckling behaviour of plates with non-rectangular geometry. It comprises of a number of carefully considered and comprehensive studies into the buckling behaviour of skew plates and panels with and without planform taper with the aim of providing useful results for plate and panel sizing relevant to aircraft wing design. This will enable the buckling strength increases associated with plates that are not rectangular to be exploited leading to a more economic design and/or more suitable starting designs for optimisation routines. Currently panel and plate sizing is generally, undertaken at the preliminary design stage using rectangular approximations for which there is a large amount of results, many of which have been incorporated into design charts; for example those by the Engineering Sciences Data Unit (E.S.D.U.) and the National Aeronautics and Space Administration (N.A.S.A.), previously the National Advisory Committee for Aeronautics (N.A.C.A.). The thesis also assimilates a collection of previous work on the buckling strength of skew plates which shows the current limitations of understanding in this area.

The work addresses a number of issues:

- it determines buckling strength increases as a result of continuity between the transverse skew edge of a panel and makes comparison with an equivalent rotational stiffness applied to the plate edges;
- it extends the range of buckling solutions for isotropic plates by considering the buckling strength of orthotropic skew panels, for which very limited and incomplete studies currently exist and;
- it considers the effect of tapered planform geometry on the buckling strength of skew plates and panels.

Only initial (elastic) buckling loads of plates are considered in this thesis because the elastic buckling load is generally of most importance in the design of aerospace panels. This is because it is desirable to have flat and wrinkle-free control surfaces and solutions of this type can be presented as buckling curves.

The elastic buckling strength of a plate is given by the solution of an eigenvalue problem and is solved using ABAQUS [3], a commercially avaliable finite element code. ABAQUS has very general capabilities and it could be argued that it is not so well suited for the studies undertaken as is a purpose written buckling code. However, it is considered that the time taken to write a specific purpose code will be more than offset by any additional time required to run ABAQUS analyses. In addition, ABAQUS is well-used, tested and validated and can therefore be regarded as being accurate. This may not be the case with a purpose written program, especially if it makes use of third-party subroutines.

Finite element analysis is well-suited to analysing problems that do not have regular boundaries and is therefore very suitable for analysis of the plates and panels under investigation. Other numerical methods to solve energy problems, for example the finite difference method and Raleigh Ritz solutions are not easily applied to problems with irregular geometrical boundaries *i.e.* non-rectangular and, because most of the previous work on plates uses these methods of analysis, this explains why plates with the geometries adopted in this thesis have not been well researched.

A uni-axial compression loading is adopted for all the presented results, which is considered to be the most important loading case in the design of a wing structure. A compression loading is introduced in a wing skin by a wing tip deflection. This results in the top surface of an aircraft wing structure resisting a compressive stress and the underside a tensile stress. Shear stresses are introduced by twisting about the wing root and reaction between the ribs and spars of the wing structure. In practice, any shear is taken to be so small as to be negligible. In addition, the buckling strength of plates in shear is higher than for plates in compression because of the stabilising diagonal tensile stresses formed.

The orthogonal compression loading is shown in Figure 1.1 for a typical 'swept' wing with skew and tapered panels.

1.2 Overview of the thesis

The thesis comprises of nine chapters. Chapter one introduces the theory used to obtain the results and comparisons. Chapter two presents a review of the previously published work dealing with buckling of skew plates under in-plane loadings and the remaining chapters each deal with a specific area of the work. The work comprises of carefully considered studies addressing the stability of skew plates, panels and tapered plates. Chapter eight aims to broadly extend the work and give it some application as well as drawing conclusions about the results presented in the earlier chapters by considering a practical problem.

Chapter 2 - Theory

Chapter two introduces the theoretical approaches used in the thesis. The results presented in the thesis are obtained using classical thin-plate theory and the chapter discusses the advantages, limitations and applicabity of the theory for the plate buckling predictions.

The second part of the chapter introduces the theory of the finite strip code, VICONOPT. The theory provides buckling solutions for skew plates panels that are continuous over otherwise simple supports. Published results available in the open literature obtained using this continuous analysis are used in subse-

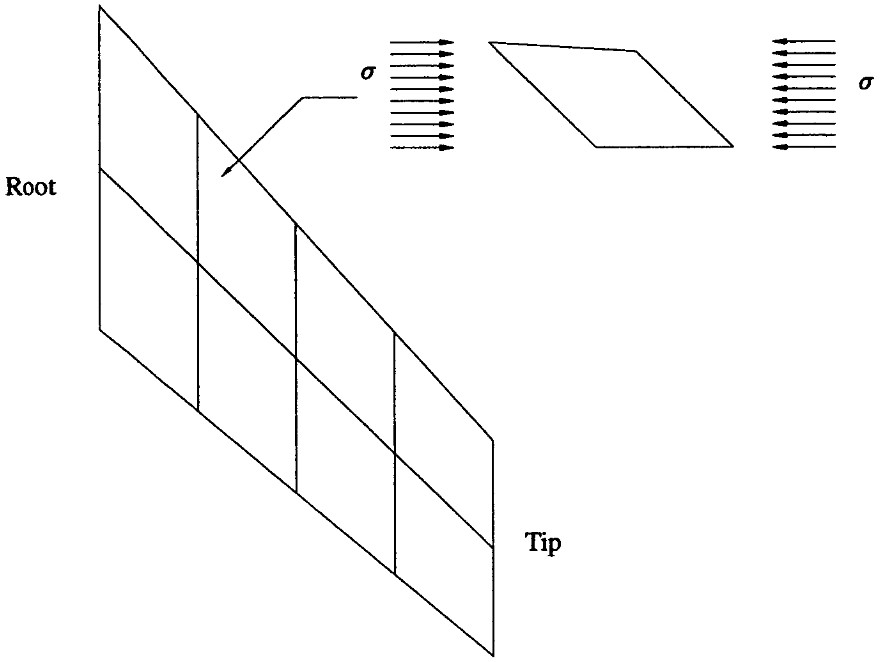

(a) Typical ‘swept’ aircraft wing and panel with compression loading as a result of a wing tip displacement.

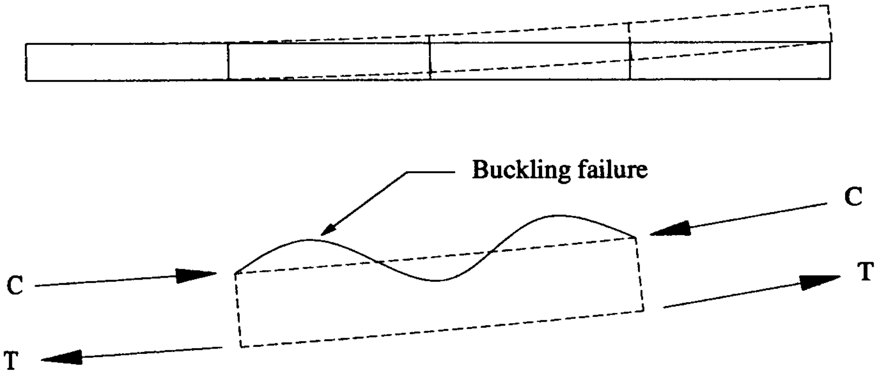

(b) Section through the central spar of the wing showing displacement (dashed) and a section through a wing bay with the resulting skin stresses: Compression (C) and tension (T) loading in the upper- and lower-skin.

Figure 1.1: Basis for plate and panel loading based on a ‘swept’ aircraft wing.

quent chapters for comparison with isolated plate buckling load predictions obtained by the finite element method.

Chapter 3 - Review of buckling solutions for skew plates with simply supported and clamped boundary conditons

This chapter assimilates and presents a comprehensive account of previous work on the stability of in-plane loaded skew plates.

Chapter 4 - Buckling strength of skew plates with rotational edges restraint

The work contained in this chapter has been published in the following articles:

P. Huyton and C.B. York, 'Buckling of Skew Plates with Continuity or Rotational Edge Restraint', Journal of Aerospace Engineering, 14(3); July 2001; and

P. Huyton and C.B. York, 'Buckling of compression loaded skew plates with rotational edge restraint', Proc. 22nd International Congress of Aeronautical Sciences, Harrogate, U.K., September 2000. (Paper No. ICA0745).

This chapter investigates the buckling behaviour of skew plates with a uniformly applied magnitude of rotational restraint applied along the plate edges using a finite element model. This rotational restraint aims to model the effect of a supporting spar or stiffener in an aircraft wing. Comparisons are made with the buckling predictions made using the discrete values of rotational restraint and analysis of plates continuous over otherwise simple supports taken from the open literature.

The results of the analysis are presented as a series of compact and comprehensive buckle curves that can be used for plate design and sizing purposes. The results are verified, where possible, with plates having simply supported or clamped edges that provide lower– and upper–bound buckling predictions available in the open literature.

Chapter 5 - Elastic Buckling of Continuous Skew Plates

This chapter describes a finite element model used to model plates that are continuous over an infinite number of bays in the longitudinal direction and both in-plane directions (uni-axial and bi-axial continuity respectively). The results from the finite element model are compared with buckling predictions for continuous skew plate analysis in the open literate that were also used for comparison in the previous chapter.

Very good correlation between the finite element model and the published continuous results are obtained and the chapter therefore verifies the continuous results and the validty of the comparisons made in the chapter 4.

Chapter 6 - Buckling of Orthotropic Skew Plates

This chapter expands on the the previous two chapters by considering assemblies of plates that make skew stiffened panels. A set of square benchmark panels is adopted for the analysis, for which a small number of buckling solutions are available in the open literature. The panels are individually modelled for varying magnitudes of shear and in-plane compression load using ABAQUS finite element code and the resulting shear/in-plane load interaction curves are drawn and compared with those in the open literature. Hence this chapter also accumulates a small body of research specifically dealing with these panels. The finite element analysis results are shown to generally compare well with the previously published analysis and with these results verify the model.

A selection of the panels are made skew and critical buckling loads presented in the form of curves showing the relationship between panel aspect ratio and buckling load. In addition, the orthotropy of the panels is changed and hence, buckling curves are produced that show the change in buckling load as a skew plate becomes increasingly orthotropic. Analysis of the panels is also compared with a plate having the same orthotropic properties as the modelled panels.

Chapter 7 - Buckling of Plates Tapered in Planform

The previous work considers only plate that are skew. In reality, 'swept' aircraft wings are also generally tapered towards the tip. This results in plates and panels in the wing also being tapered in planform geometry as well as skew. This chapter presents a study into the buckling strength of elastic plates that are tapered in planform.

Buckling design curves are presented for the tapered and skew plates and relate buckling strength with plate aspect ratio for varying magnitudes of taper and the skew angles used in the previous chapters. Hence the effect of planform on the plate buckling load is quantified.

Chapter 8 - Elastic Buckling of Swept-back Aircraft Wing Panels - A Practical Example

The work contained in this chapter has been published in the following articles:

Huyton, P. and York, C.B., 'Wing panel geometry and implications for design', Proceedings, 2nd International Conference on Advanced Engineering Design ,Glasgow, U.K. pages 69-74, June 2001.

The buckling predictions of the previous chapters showed that changing the planform geometry of a plate has the effect of stiffening plates and panels at acute corners or tapered ends. This resulted in a increase in buckling strength of the plate or panel.

The aim of the final analysis chapter addresses the effect of designing panels using rectangular simplifications, a skew simplification and finally a skew taper geometry representing the actual planform geometry of the panels. The panels, stiffened with blades, are taken from the open literature from an optimisation study of a 'swept' and tapered wing. Buckling predictions for the panels with simply supported edges are obtained for each of geometric configurations and the buckling strength changes calculated.

These simply supported panel buckling results are then used as reference results with which to compare the effect of applying varying magnitudes of rotational restraint to the panel edges in a manner similar to that used in the chapter 4. Buckling curves are presented that describe the buckling strength of the plates as they move from being simply supported to being fully clamped.

Chapter 9 - Conclusions

The final chapter presents the conclusions of the work presented and makes recommendations for further work.

Chapter 2

Theory

2.1 Introduction

This chapter presents the theory, together with the assumptions of thin-plate buckling theory which is used to produce the results in the thesis. It is split into five sections that address: (a) the assumptions of thin-plate theory and a derivation of the governing equation of equilibrium; (b) presentation of the classical solution of the equations for a simply supported rectangular plate and the buckling problem as an eigenvalue equation; (c) the sole solution of the governing equations for a skew plate; (d) the theory of the buckling routines, VIPASA and VICON in VICONOPT, the results of which are used to comparison results for some of the results in the thesis because they are for continuous arrays of plates; and (e) the limitations of thin-plate theory that arise because of the assumptions made in its derivation.

2.2 Thin Plate Theory

2.2.1 Nomenclature

The following nomenclature is used throughout the discussion. Forces and Moments (denoted N and M respectively) are given two subscripts denoting the directions in which they act. The first subscript gives the normal to the face on which the force acts and the second the direction in which it acts. Forces are positive if the normal to the face on which the force acts and the direction of the force (in the Cartesian coordinate system) are both positive or both negative. Forces are negative if the normal to the face on which it acts and its direction are of opposite signs in the Cartesian coordinate system.

Moments are defined using the 'right-hand-screw rule' and the subscripts and sign of the moments have the same meaning as for forces.

2.2.2 Elementary Bending Theory for Thin Plates

The text of this section relating to the derivation of classical thin-plate theory has been compiled using Timoshenko and Woinowsky-Krieger[89]; Timoshenko and Gere [88]; Bulson [20]; Morley [68]; Coates, Coutie and Kong [23]; Gerard and Becker [34], Jaeger [43] and Ugural [90].

Consider a section of plate with a large ratio of width to thickness and make the following assumptions:

1. Normals to the middle plane (neutral axis) before bending remain normal to the plane after bending.
2. The middle plane remains neutral during bending - it is not strained.
3. σ_z is negligible compared with the other stresses.

A discussion of erroneous buckling predictions that can arise from making these assumptions and their application is given in section 2.7.

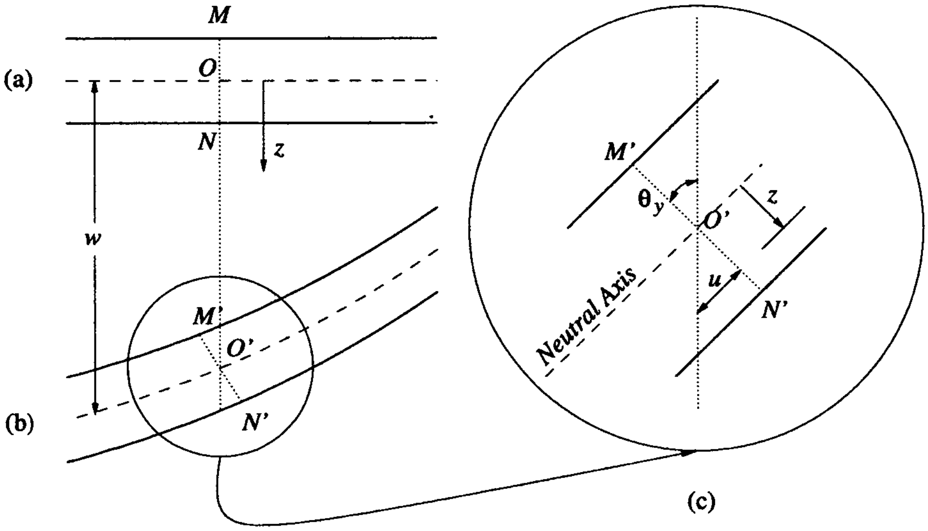

Figure 2.1: Thin-plate section before (a) and after (b & c) bending.

If a moment is applied along its edges, the neutral axis of the plate will deform a distance w, from O to O' as shown in Figure 2.1. From assumption 1, $M - O - N$ and $M' - O' - N'$ will both be normal to the plate surface and O' will lie directly below O (see Figure 2.1(a and b)).

Assuming small deflections, from Figure 2.1(c) $u = z\theta_y$ and by similar consideration a displacement in the $y-$direction will be given by $v = -z\theta_x$. It is also clear that,

$$\theta_y = -\frac{\partial w}{\partial x}; \qquad \theta_x = \frac{\partial w}{\partial y}$$

with the result that;

$$u = -z\frac{\partial w}{\partial x}; \qquad v = -z\frac{\partial w}{\partial y}$$

The strains, ε_x,ε_y and γ_{xy} are given by:

$$\varepsilon_x = \frac{\partial u}{\partial x} = -z\frac{\partial^2 w}{\partial x^2}$$

$$\varepsilon_y = \frac{\partial v}{\partial y} = -z\frac{\partial^2 w}{\partial y^2}$$

$$\gamma_{xy} = \frac{\partial v}{\partial x} + \frac{\partial u}{\partial y} = -2z\frac{\partial^2 w}{\partial x \partial y}$$

Assuming plane strain ($\sigma_z = 0$)

$$\sigma_{xx} = \frac{E}{(1-\nu^2)}[\varepsilon_x + \nu\varepsilon_y] = -\frac{Ez}{(1-\nu^2)}\left[\frac{\partial^2 w}{\partial x^2} + \nu\frac{\partial^2 w}{\partial y^2}\right]$$

$$\sigma_{yy} = \frac{E}{(1-\nu^2)}[\varepsilon_y + \nu\varepsilon_x] = \frac{Ez}{(1-\nu^2)}\left[\frac{\partial^2 w}{\partial y^2} + \nu\frac{\partial^2 w}{\partial x^2}\right]$$

$$\tau_{xy} = -2Gz\frac{\partial^2 w}{\partial x \partial y} = -\frac{Ez}{(1+\nu)}\frac{\partial^2 w}{\partial x \partial y}$$

From Figure 2.2 the moments on the plate given in terms of stress are:

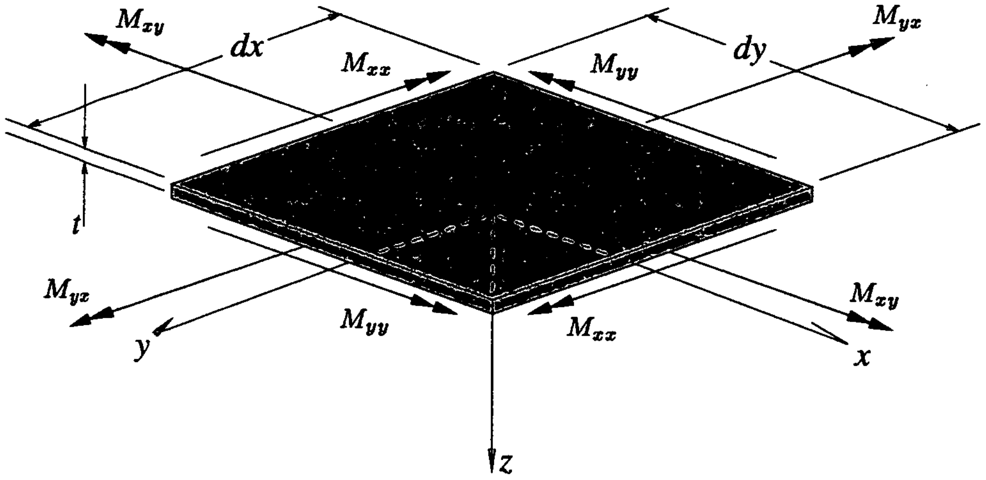

Figure 2.2: An infinitesimal plate element in pure bending

$$\begin{aligned} M_{yy} &= -\int_{-t/2}^{t/2} \sigma_{yy} z \, \mathrm{d}z \\ &= \int_{-t/2}^{t/2} \frac{Ez^2}{(1-\nu^2)} \left[\frac{\partial^2 w}{\partial y^2} + \nu \frac{\partial^2 w}{\partial x^2} \right] \mathrm{d}z \\ &= \frac{Et^3}{12(1-\nu^2)} \left[\frac{\partial^2 w}{\partial y^2} + \nu \frac{\partial^2 w}{\partial x^2} \right] \end{aligned} \tag{2.1}$$

$$M_{xx} = \int_{-t/2}^{t/2} \sigma_{xx} z \, \mathrm{d}z \quad = \quad -\frac{Et^3}{12(1-\nu^2)} \left[\nu \frac{\partial^2 w}{\partial y^2} + \frac{\partial^2 w}{\partial x^2} \right] \tag{2.2}$$

$$M_{xy} = -\int_{-t/2}^{t/2} \tau_{xy} z \, \mathrm{d}z \quad = \quad \frac{Et^3}{12(1-\nu^2)} (1-\nu) \frac{\partial^2 w}{\partial x \partial y} \tag{2.3}$$

$$M_{yx} = -\int_{-t/2}^{t/2} \tau_{yx} z \, \mathrm{d}z \quad = \quad -M_{xy} \tag{2.4}$$

Note that $Et^3/12(1-\nu) = D$ and is the flexural rigidity of the plate.

2.2.3 Plate Equilibrium

Considering equilibrium of an infinitesimal element of a plate as shown in Figure 2.3, for horizontal equilibrium in the x–direction,

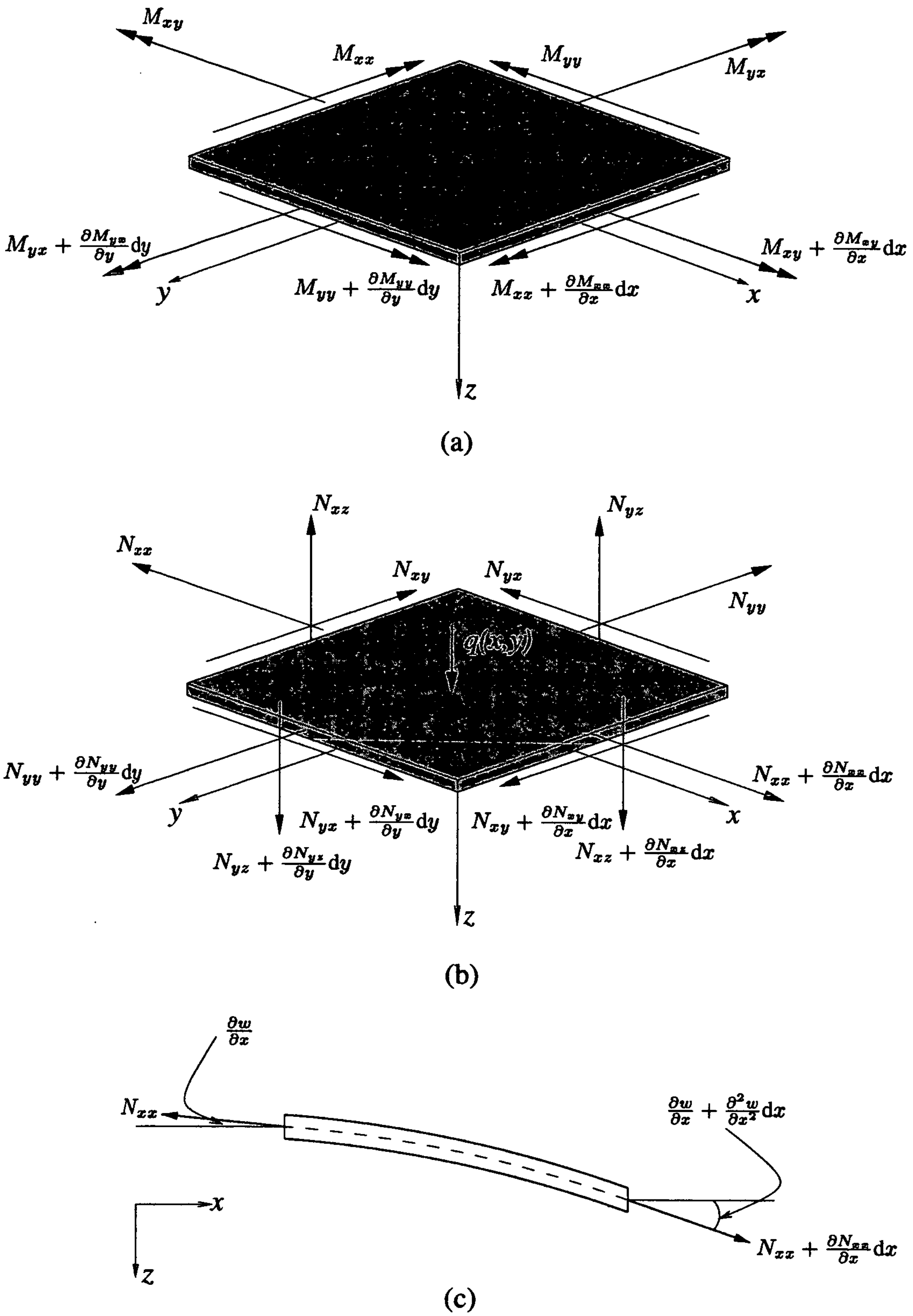

Figure 2.3: An infinitesimal plate element subject to moments (a) and in-plane and transverse loads (b). (c) shows a section through the plate and projections of N_{xx} forces on the z-axis

$$N_{xx}\mathrm{d}y + N_{yx}\mathrm{d}x = N_{xx}\mathrm{d}y + \frac{\partial N_{xx}}{\partial x}\mathrm{d}x\mathrm{d}y + N_{yx}\mathrm{d}x + \frac{\partial N_{yx}}{\partial y}\mathrm{d}x\mathrm{d}y$$

$$\Rightarrow \frac{\partial N_{xx}}{\partial x} + \frac{\partial N_{yx}}{\partial y} = 0 \tag{2.5}$$

and for the $y-$direction,

$$N_{yy}\mathrm{d}x + N_{xy}\mathrm{d}y = N_{yy}\mathrm{d}x + \frac{\partial N_{yy}}{\partial y}\mathrm{d}x\mathrm{d}y + N_{xy}\mathrm{d}y + \frac{\partial N_{xy}}{\partial x}\mathrm{d}y\mathrm{d}x$$

$$\Rightarrow \frac{\partial N_{yy}}{\partial y} + \frac{\partial N_{xy}}{\partial x} = 0 \tag{2.6}$$

For equilibrium in the vertical direction, consideration has to be given to the vertical components of N_{xx}, N_{yy}, N_{xy} & N_{yx} arising from a small deflection in addition to the vertical pressure $q(x.y)$. Figure 2.3 (c) shows the projections of N_{xx} on the $z-$axis. From the figure it can be seen that the vertical component of these forces is given by:

$$N_{xx}\mathrm{d}y\frac{\partial w}{\partial x} = \left[N_{xx} + \frac{\partial N_{xx}}{\partial x}\mathrm{d}x\right]\left[\frac{\partial w}{\partial x} + \frac{\partial^2 w}{\partial x}\mathrm{d}x\right]\mathrm{d}y$$

which, if higher order terms are neglected, gives the vertical component as

$$\frac{\partial}{\partial x}\left(N_{xx}\mathrm{d}y\frac{\partial w}{\partial x}\right)\mathrm{d}x = \left[N_{xx}\frac{\partial^2 w}{\partial x^2} + \frac{\partial N_{xx}}{\partial x}\frac{\partial w}{\partial x}\right]\mathrm{d}x\mathrm{d}y$$

and in a similar manner vertical components are given for N_{yy}, N_{xy} & N_{yx} by

$$\frac{\partial}{\partial y}\left(N_{yy}\mathrm{d}y\frac{\partial w}{\partial y}\right)\mathrm{d}x = \left[N_{yy}\frac{\partial^2 w}{\partial y^2} + \frac{\partial N_{yy}}{\partial y}\frac{\partial w}{\partial y}\right]\mathrm{d}x\mathrm{d}y$$

$$\frac{\partial}{\partial x}\left(N_{xy}\mathrm{d}x\frac{\partial w}{\partial y}\right)\mathrm{d}y = \left[N_{xy}\frac{\partial^2 w}{\partial x\partial y} + \frac{\partial N_{xy}}{\partial x}\frac{\partial w}{\partial y}\right]\mathrm{d}x\mathrm{d}y$$

$$\frac{\partial}{\partial x}\left(N_{yx}\mathrm{d}x\frac{\partial w}{\partial x}\right)\mathrm{d}y = \left[N_{yx}\frac{\partial^2 w}{\partial x\partial y} + \frac{\partial N_{yx}}{\partial y}\frac{\partial w}{\partial x}\right]\mathrm{d}x\mathrm{d}y$$

If there is a transverse load, $q(x, y)$ per unit area of plate,

$$q\mathrm{d}x\mathrm{d}y = -\frac{\partial N_{yz}}{\partial y}\mathrm{d}y\mathrm{d}x - \frac{\partial N_{xz}}{\partial x}\mathrm{d}x\mathrm{d}y$$

Vertical Equilibrium of the plate from consideration of all the above gives,

$$q+N_{xx}\frac{\partial^2 w}{\partial x^2}+2N_{xy}\frac{\partial^2 w}{\partial x\partial y}+N_{yy}\frac{\partial^2 w}{\partial y^2}+\left(\frac{\partial N_{xx}}{\partial x}+\frac{\partial N_{xy}}{\partial x}\right)\frac{\partial w}{\partial x}+\left(\frac{\partial N_{yy}}{\partial y}+\frac{\partial N_{xy}}{\partial y}\right)\frac{\partial w}{\partial y}=-\frac{\partial N_{yz}}{\partial y}+-\frac{\partial N_{xz}}{\partial x}$$

From equations (2.5) & (2.6) regarding equilibrium in the $x-$ & $y-$directions this reduces further to

$$q + N_{xx}\frac{\partial^2 w}{\partial x^2} + 2N_{xy}\frac{\partial^2 w}{\partial x\partial y} + N_{yy}\frac{\partial^2 w}{\partial y^2} = -\frac{\partial N_{yz}}{\partial y} - \frac{\partial N_{xz}}{\partial x} \tag{2.7}$$

The left-hand side of this equation can be written in terms of moments using moment equilibrium.

Equilibrium about $x = 0$ gives,

$$\frac{\partial M_{xy}}{\partial x}\mathrm{d}x\mathrm{d}y + \frac{\partial M_{yy}}{\partial y}\mathrm{d}y\mathrm{d}x + N_{yz}\mathrm{d}x\mathrm{d}y = 0$$

$$\Rightarrow N_{yz} = -\frac{\partial M_{xy}}{\partial x}\mathrm{d}x\mathrm{d}y - \frac{\partial M_{yy}}{\partial y}\mathrm{d}y\mathrm{d}x$$

and for equilibrium about $y = 0$,

$$\frac{\partial M_{yx}}{\partial y}\mathrm{d}y\mathrm{d}x + \frac{\partial M_{xx}}{\partial x}\mathrm{d}y\mathrm{d}x - N_{xz}\mathrm{d}y\mathrm{d}x = 0$$

$$\Rightarrow N_{xz} = \frac{\partial M_{yx}}{\partial y}\mathrm{d}y\mathrm{d}x + \frac{\partial M_{xx}}{\partial x}\mathrm{d}y\mathrm{d}x$$

Differentiating the 2 equations above, noting that $M_{xy} = -M_{yx}$ and substitution into equation (2.7) gives,

$$q + N_{xx}\frac{\partial^2 w}{\partial x^2} + 2N_{xy}\frac{\partial^2 w}{\partial x\partial y} + N_{yy}\frac{\partial^2 w}{\partial y^2} = \frac{\partial^2 M_{xy}}{\partial x\partial y} + \frac{\partial M_{yy}}{\partial y^2} - \frac{\partial^2 M_{yx}}{\partial y\partial x} - \frac{\partial^2 M_{xx}}{\partial x^2} \tag{2.8}$$

Differentiating equations (2.1) - (2.4) permits the right-hand side of equation (2.7) to be written in terms of w to get:

$$\frac{1}{D}\left\{q+N_{xx}\frac{\partial^2 w}{\partial x^2}+2N_{xy}\frac{\partial^2 w}{\partial x\partial y}+N_{yy}\frac{\partial^2 w}{\partial y^2}\right\}=\frac{\partial^4 w}{\partial x^4}+2\frac{\partial^4 w}{\partial x^2\partial y^2}+\frac{\partial^4 w}{\partial y^4} \tag{2.9}$$

This is the governing equation of equilibrium for a thin plate, given the initial assumptions and the solution of it forms the basis of the entire thesis. It was partially derived by Bernoulli[1] in 1789 for out-of-plane loading, q, however he neglected the twisting term (the second term on the right-hand-side of the equation). Lagrange in 1811 and Navier[2] in 1820 included this twisting term and Saint Venant[3] incorporated in-plane loads in 1883 (historical information from reference [100]).

2.2.4 Energy Equation

Strain Energy Due to Bending

Equation (2.9) can be used to determine the strain energy in the plate caused by loading. Neglecting shearing and stretching of the mid-plane of the plate (as was assumed in the formation of the governing equation) the strain energy stored in the plate is equal to the total work done by the bending moments. For an infinitesimal portion of the plate this is by[4]:

$$\text{in the } x-z \text{ plane,}\quad -\frac{1}{2}M_{xx}\frac{\partial^2 w}{\partial x^2}dxdy$$

$$\text{in the } y-z \text{ plane,}\quad -\frac{1}{2}M_{yy}\frac{\partial^2 w}{\partial y^2}dy$$

$$\text{for twisting moments,}\quad M_{xy}\frac{\partial^2 w}{\partial x\partial y}$$

Hence the strain energy due to bending in an infinitesimal element of plate dU is governed by,

$$dU_b=-\frac{1}{2}\left\{M_{xx}\frac{\partial^2 w}{\partial x^2}+M_{yy}\frac{\partial^2 w}{\partial y^2}+2M_{xy}\frac{\partial^2 w}{\partial x\partial y}\right\}dxdy$$

---

[1] *Nova Acta*, 5, St.Petersburg.

[2] Paper presented to the French Academy. Abstract printed in *Bull. Soc. Phil-math, Paris.*

[3] Discussion in *Theorie de l'élasticité des corps soldies*, Celbsh, 704

[4] In the case of the twisting moments, $M_{xy}=M_{yx}$ and their respective rotations are therefore both $\frac{\partial^2 w}{\partial x\partial y}$.

Using the expressions in equations (2.4)-(2.1), and after some algebraic manipulation, the strain energy of the infinitesimal section of the plate, dU_b is given by,

$$dU_b = \frac{1}{2}D\left[\left(\frac{\partial^2 w}{\partial x^2}+\frac{\partial^2 w}{\partial y^2}\right)^2 - 2(1-\nu)\left[\frac{\partial^2 w}{\partial x^2}\frac{\partial^2 w}{\partial y^2}-\left(\frac{\partial^2 w}{\partial x \partial y}\right)^2\right]\right]dxdy \tag{2.10}$$

This expression neglects the energy in the plate as a result of the external in-plane forces N_{xx}, N_{yy}, N_{xy} & N_{yx}. For the case when the plate is subject to in-plane loading as well as bending, it is assumed that the in-plane loading is applied before there is any bending, resulting in a 2-D elasticity problem, such that,

$$\varepsilon_{xx} = \frac{1}{tE}(N_{xx} - \nu N_{yy}) \tag{2.11}$$

$$\varepsilon_{yy} = \frac{1}{tE}(-\nu N_{xx} + N_{yy}) \tag{2.12}$$

$$\gamma_{xy} = \frac{N_{xy}}{tG} = \frac{2(1+\nu)N_{xy}}{tE} \tag{2.13}$$

where $\varepsilon_{xx}, \varepsilon_{yy}$ & γ_{xy} are strain components in the middle plane of the plate, t is the plate thickness and ν is Poisson's ratio of the plate. The energy due to the deformation of the middle plane of the plate is therefore given by

$$U_0 = \frac{1}{2}\int_0^b\int_0^a (N_{xx}\varepsilon_{xx} + N_{yy}\varepsilon_{yy} + N_{xy}\gamma_{xy})dxdy$$

which on substitution of equations (2.11)-(2.13) becomes,

$$U_0 = \frac{1}{2Et}\int_0^b\int_0^a \left\{N_{xx}^2 + N_{yy}^2 - 2\nu N_{xx}N_{yy} + 2(1+\nu)N_{xy}^2\right\} dxdy \tag{2.14}$$

This energy is assumed to be constant during bending (the forces N_{xx}, N_{yy} & N_{xy} are assumed to be constant during bending). Energy changes as a result of bending caused by the lateral load however do need to be considered. Figure 2.4(a) shows the displacement due to an increase in lateral loading that results in bending acting on an infinitesimal element $dxdy$ resulting in displacements, u, v, w in the x, y, z directions respectively. From the figure the displacement due to elongation in the $x-$direction is $(\partial u/\partial x)du$. Elon-

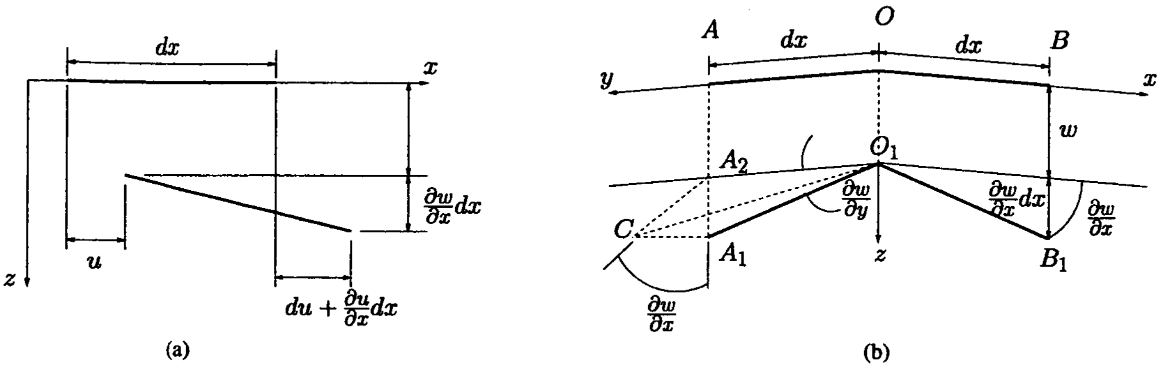

(a) (b)

Figure 2.4: Displacements due to bending caused by the application of an in-plane load.

gation due to the displacement w is $1/2(\partial w/\partial x)^2$ (from consideration of the projection of the deformed element on the x-axis). Hence the strain in the x-direction, ε' is given by,

$$\varepsilon' = \frac{\partial u}{\partial x} + \frac{1}{2}\left(\frac{\partial w}{\partial x}\right)^2 \tag{2.15}$$

and in the y-direction by a similar argument

$$\varepsilon' = \frac{\partial v}{\partial y} + \frac{1}{2}\left(\frac{\partial w}{\partial y}\right)^2 \tag{2.16}$$

For the shear strain on the element, consider Figure 2.4(b) which shows an element of plate $dydx$ which has undergone a displacement w. That is O has moved a distance w to O_1 with the result that the shearing strains have caused the right angle AOB to become the acute angle $A_1O_1B_1$. The change in shear strain caused by the displacement w is obviously the difference between AOB and $A_1O_1B_1$ which is given by the angle CO_1A_1. The angle CO_1B_1 is a right angle.

$$CO_1A_1 \approx \frac{CA_1}{A_1O_1} = \frac{\frac{\partial w}{\partial x}\frac{\partial w}{\partial y}dy}{dy} = \frac{\partial w}{\partial x}\frac{\partial w}{\partial y}$$

The strain due to displacements u, v is $\partial u/\partial y + \partial v/\partial x$, hence the change in shear strain, γ'_{xy}, for a displacement u, v, w is

$$\gamma'_{xy} = \frac{\partial u}{\partial y} + \frac{\partial v}{\partial x} + \frac{\partial w}{\partial x}\frac{\partial w}{\partial y} \tag{2.17}$$

The strain energy as a result of this additional stretching to the middle plane of the plate, $dU_{o'}$ is given by,

$$dU_{\sigma'} = \left(N_{xx}\varepsilon'_{xx} + N_{yy}\varepsilon'_{yy} + N_{xy}\gamma'_{xy}\right) dxdy \tag{2.18}$$

Substituting the relevant expressions for the change in strain in the equation above, adding the change in strain energies as a result of bending (U_b) and integrating over the surface of the plate, the total change in energy of the plate due to bending is given by

$$U = \int\int \left\{N_{xx}\frac{\partial u}{\partial x} + N_{yy}\frac{\partial v}{\partial y} + N_{xy}\left(\frac{\partial u}{\partial y} + \frac{\partial v}{\partial x}\right)\right\} dxdy+ \tag{2.19}$$

$$\frac{1}{2}\int\int \left\{N_{xx}\left(\frac{\partial w}{\partial x}\right)^2 + N_{yy}\left(\frac{\partial w}{\partial y}\right)^2 + 2N_{xy}\frac{\partial w}{\partial x}\frac{\partial w}{\partial y}\right\} dxdy+ \tag{2.20}$$

$$\frac{1}{2}D\int\int \left\{\left(\frac{\partial^2 w}{\partial x^2} + \frac{\partial^2 w}{\partial y^2}\right)^2 - 2(1-\nu)\left[\frac{\partial^2 w}{\partial x^2}\frac{\partial^2 w}{\partial y^2} - \left(\frac{\partial^2 w}{\partial x\partial y}\right)^2\right]\right\} dxdy \tag{2.21}$$

The first integral in the above expression represents the strain energy resulting from the application of in-plane loads (and any body forces) acting in the middle of the plate and the last two integrals represent work done by bending the plate as a result of loads normal to the plate. If (see section 2.2.2) membrane stresses acting in the middle plane of the plate are ignored (*i.e.* the deformed surface is developable) then the expression given in equations (2.15)-(2.17) must each be equal to 0. Setting these equations to 0, it is concluded that,

$$\frac{1}{2}\left(\frac{\partial w}{\partial x}\right)^2 = -\frac{\partial u}{\partial x}$$

$$\frac{1}{2}\left(\frac{\partial w}{\partial y}\right)^2 = -\frac{\partial v}{\partial y}$$

$$\frac{\partial w}{\partial x}\frac{\partial w}{\partial y} = -\frac{\partial u}{\partial y} - \frac{\partial v}{\partial x}$$

From which the the work done by the forces in the middle of the plane can be represented by substitution of the above three equations giving,

$$\text{work done by in} - \text{plane forces} = -\frac{1}{2}\int\int\left[N_{xx}\left(\frac{\partial w}{\partial x}\right)^2 + N_{yy}\left(\frac{\partial w}{\partial y}\right)^2 + 2N_{xy}\frac{\partial w}{\partial x}\frac{\partial w}{\partial y}\right]dxdy \tag{2.22}$$

Therefore, by taking the work done by in-plane forces as T_1 and the remaining work (*i.e.* that done by forces normal to the plate) as T_2,

$$U = T_1 + T_2 = \frac{1}{2}D\int\int\left\{\left(\frac{\partial^2 w}{\partial x^2} + \frac{\partial^2 w}{\partial y^2}\right)^2 - 2(1-\nu)\left[\frac{\partial^2 w}{\partial x^2}\frac{\partial^2 w}{\partial y^2} - \left(\frac{\partial^2 w}{\partial x \partial y}\right)^2\right]\right\}dxdy \tag{2.23}$$

2.3 Closed-Form Solutions

Given the general governing partial differential equation for plate equilibrium, solving the equation using the energy method provides the closed-form solutions and an eigenvalue equation which is useful for other approximate methods.

Using the assumption that the plate, which is stressed by forces acting in the middle of the plane, undergoes some small lateral bending consistent with the plate boundary conditions such that there are no membrane actions (i.e. stretching of the middle plane), the plate equilibrium equation will hold. If the work done by these forces in the plate is T and the internal strain energy in the plate resulting from the action of these forces is U, then for equilibrium,

$$T = U \tag{2.24}$$

From the equilibrium equation therefore,

$$-\frac{1}{2}\int\int\left[N_{xx}\left(\frac{\partial w}{\partial x}\right)^2 + N_{yy}\left(\frac{\partial w}{\partial y}\right)^2 + 2N_{xy}\frac{\partial w}{\partial x}\frac{\partial w}{\partial y}\right]dxdy =$$
$$\frac{D}{2}\int\int\left\{\left(\frac{\partial^2 w}{\partial x^2} + \frac{\partial^2 w}{\partial y^2}\right)^2 - 2(1-v)\left[\frac{\partial^2 w}{\partial x^2}\frac{\partial^2 w}{\partial y^2} - \left(\frac{\partial^2 w}{\partial x \partial y}\right)^2\right]\right\}dxdy$$

Assuming that N_x, N_y & N_{xy} are constant and represented by a common factor, so that the buckling loads are represented by,

$$N_{xx} = \lambda N'_{xx} \quad N_{yy} = \lambda N'_{yy} \quad N_{xy} = \lambda N'_{xy}$$

buckling will occur when λ reaches a critical value given by

$$\lambda = \frac{D\int\int\left\{\left(\frac{\partial^2 w}{\partial x^2} + \frac{\partial^2 w}{\partial y^2}\right)^2 - 2(1-v)\left[\frac{\partial^2 w}{\partial x^2}\frac{\partial^2 w}{\partial y^2} - \left(\frac{\partial^2 w}{\partial x \partial y}\right)^2\right]\right\} dxdy}{-\int\int\left[N'_{xx}\left(\frac{\partial w}{\partial x}\right)^2 + N'_{yy}\left(\frac{\partial w}{\partial y}\right)^2 + 2N'_{xy}\frac{\partial w}{\partial x}\frac{\partial w}{\partial y}\right] dxdy} = \frac{I_1}{I_2}$$

The critical buckling load will correspond to the state when the above equation is a minimum, that is when $\delta\lambda = 0$. Thus

$$\delta\lambda = \frac{I_2 \delta I_1 - I_1 \delta I_2}{I_2^2} = 0$$
$$\Rightarrow \frac{1}{I_2}\left(\delta I_1 - \lambda \delta I_2\right) = 0$$

which is an eigenvalue equation. The eigenvalue being $\lambda = I_1/I_2$.

The solution above shows how the buckling problem can be presented as an eigenvalue problem, exact solutions can be found using the energy equations in a more direct manner. Note that a solution of all these problems requires a function for the displacement of the plate to be determined first, it is this pre-requisite of a solution that leads to uncertainties in the validity of the solution for plates that are more complex in geometry than a simple rectangular plate. In these cases, the buckled form of the plate is not easily modelled using simple functions.

2.3.1 Buckling of an in-plane, uni-axially loaded plate with simple supports.

Assume a rectangular plate of longitudinal length, a , transverse length, b subject to a uniform, in-plane loading N_{xx} along the transverse plate edge. The critical value of N_{xx} can be found using the energy equation thus far derived or directly from the governing equation of plate equilibrium; the same result is obtained using either method.

In both cases, the boundary conditions of the simply support are satisfied by the assumed buckled form below. The boundary conditions being: $w = 0$ at $x = 0, a; y = 0, b$ and $\partial^2 w/\partial x^2 = 0$ at $y = 0.b$ and $\partial^2 w/\partial y^2 = 0$ at $x = 0, a$.

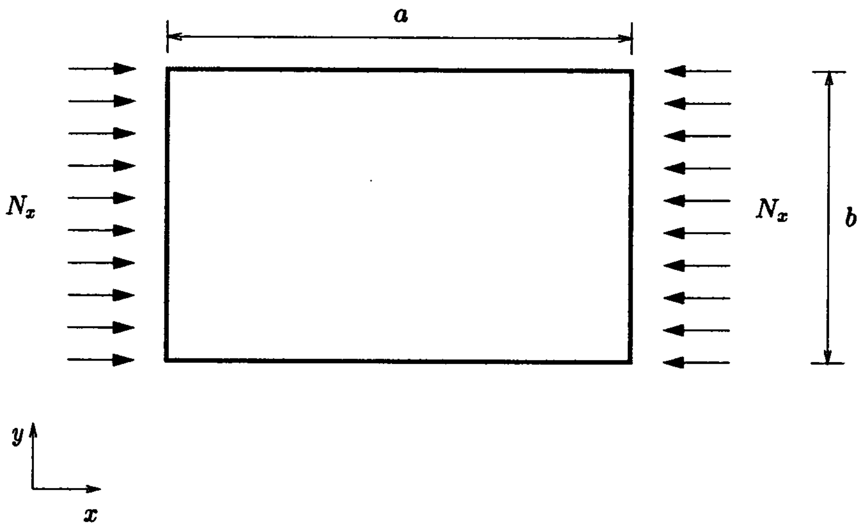

Figure 2.5: Simply supported plate subject to a uni-axial, in-plane load having length a and width b

$$w = \sum_{m=0}^{m=\infty} \sum_{n=0}^{n=\infty} a_{mn} \sin \frac{mx\pi}{a} \sin \frac{ny\pi}{b} \tag{2.25}$$

Using the solution of strain energy due to bending given in equation (2.23) and performing the differentiation for substitution into the equation and then the integrals to obtain expressions for the energy stored in the plate, the strain energy of bending is given by

$$U = \frac{\pi^4 abD}{8} \sum_{m=0}^{m=\infty} \sum_{n=0}^{n=\infty} a_{mn}^2 \left(\frac{m^2}{a^2} + \frac{n^2}{b^2} \right)^2$$

and the energy done by the external in-plane force N_{xx} is given by equation (2.22) where $N_{yy} = N_{xy} = 0$. Thus

$$T_1 = \frac{1}{2} N_{xx} \int_0^a \int_0^b \left(\frac{\partial w}{\partial x} \right)^2 dxdy = \frac{\pi^2 b}{8a} N_{xx} \sum_{m=0}^{m=\infty} \sum_{n=0}^{n=\infty} m^2 a_{mn}^2 \tag{2.26}$$

and at buckling the critical compressive loading can be deduced from

$$\frac{\pi^4 abD}{8} \sum_{m=0}^{m=\infty} \sum_{n=0}^{n=\infty} a_{mn}^2 \left(\frac{m^2}{a^2} + \frac{n^2}{b^2} \right)^2 = \frac{\pi^2 b}{8a} N_{xx} \sum_{m=0}^{m=\infty} \sum_{n=0}^{n=\infty} m^2 a_{mn}^2$$

$$\Rightarrow N_{xx} = \frac{\pi^2 a^2 D \sum_{m=0}^{m=\infty} \sum_{n=0}^{n=\infty} a_{mn}^2 \left(\frac{m^2}{a^2} + \frac{n^2}{b^2} \right)^2}{\sum_{m=0}^{m=\infty} \sum_{n=0}^{n=\infty} m^2 a_{mn}^2}$$

from which the lowest value of N_{xx} will be obtained when all the coefficients of a_{mn} are 0 except for one resulting in the critical value of N_{xx} being given as

$$N_{xx_{\text{crit}}} = \frac{\pi^2 a^2 D}{m^2}\left(\frac{m^2}{a^2} + \frac{n^2}{b^2}\right)^2$$

from which it is obvious that the critical buckling value of N_{xx} will be given by $n = 1$. Here n is the number of half wavelengths in the transverse direction with the result that after simplifying

$$N_{xx_{\text{crit}}} = \frac{\pi^2 D}{a^2}\left(m + \frac{1}{m}\frac{a^2}{b^2}\right)^2$$

The minimum value of $N_{xx_{\text{crit}}}$ is given for $m = 1$ (n.b. m cannot be less than 1 if the boundary conditions are to be satisfied) implying that

$$N_{xx_{\text{crit}}} = \frac{\pi^2 D}{b^2}\left(\frac{b}{a} + \frac{a}{b}\right)^2$$

which by inspection must be a minimum for $a = b$ with the result that the critical buckling load of a square plate under uniform, uniaxial compression is

$$N_{xx_{\text{crit}}} = k\frac{\pi^2 D}{b^2} = 4\frac{\pi^2 D}{b^2}$$

where k is a buckling factor which, for a rectangular plate having simply supported boundary conditions must always be greater than 4. The above expression can be derived by consideration of the plate equilibrium equation (previously derived as equation (2.9)) and using a deflected form of the plate $w = a_{11}\sin\frac{m\pi x}{a}\sin\frac{n\pi y}{b}$. This expression for the deflected surface of the plate can be shown to be an exact solution to the partial differential equation, be substituted into it and solved directly.

From the plot in Figure 2.6 showing the relationship between aspect ration (a/b) and critical buckling factor for different values of m, the curves are seen to form cusps where the buckling curves have coincident values corresponding to different values of m. Using the equation for the value k these critical coincident values occur when $a/b = \sqrt{m(m+1)}$. The critical buckling value of the plate is found at a minimum solution of k for a given aspect ratio which occurs when $a/b = m$. For a very long plate, therefore the buckled form of the plate will consist of a number of half wavelengths approximately equal to the width of the plate.

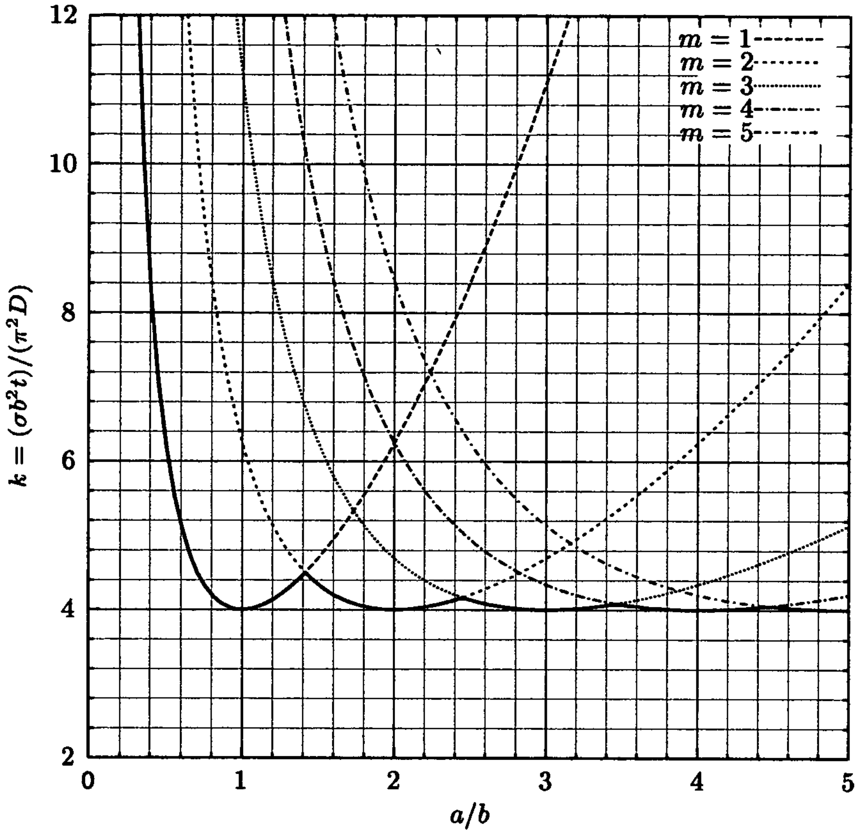

Figure 2.6: Plot of critical buckling load equation $k = (\frac{mb}{a} + \frac{a}{mb})^2$ for a simply supported rectangular plate with variation in plate aspect ratio. k is the buckling factor given by $N_{xx}b/\pi^2 D$. a/b is plate aspect ratio, where a is the length of a plate and b is the transverse width of the plate. The thick solid line shows the portions of the curves for each m that represent the critical buckle mode.

2.4 Solution of the governing partial differential equations for skew plates

There is one closed-form solution for the critical buckling load of skew plates and it was presented by Anderson in reference [5]. The solution appears not to be well known and doesn't feature in the many texts on thin-plate buckling solutions, for example Bulson [20], Column Research Committee of Japan [70], Morley's monograph on skew plate structures [68] and Ugural [90]. The solution is, in general, not especially useful for design purposes, because it only applies to one aspect ratio and a loading conditon that is not often met. However, it is included in this theory section for completeness.

The absence of closed-form solutions for skew plates arises because there is only one known deflection function that satisfies the governing partial differential equation of plate equilibrium. Anderson presents

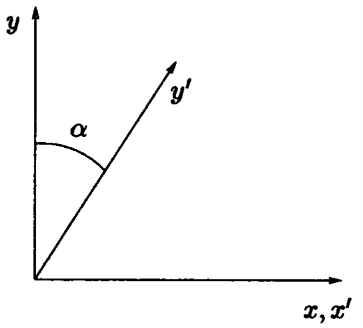

Figure 2.7: Transformation of rectangular Cartesian coordinates to skew Cartesian coordinate system. Transformation is obtained using the equations $x' = x - y\tan\alpha$ and $y' = y\sec\alpha$.

his solution using the governing equation for thin-plate equilibrium transformed into skew coordinates using the transformations:

$$x' = x - y\tan\alpha \qquad\qquad y' = y\sec\alpha \tag{2.27}$$

These transformations are shown graphically in Figure 2.7.

Hence the equation of equilibrium for the skew plate is given by,

$$\begin{aligned}\frac{\partial^4 w}{\partial x'^4} + 2\left(1 + 2\sin^2\alpha\right)\frac{\partial^4 w}{\partial x'^2\partial y'^2} + \frac{\partial^4 w}{\partial y'^4} - 4\sin\alpha\left(\frac{\partial^4 w}{\partial x'^3\partial y'} + \frac{\partial^4 w}{\partial x'\partial y'^3}\right) = \\ -\frac{\sigma_x t}{D}\frac{\partial^2 w}{\partial x'^2}\cos^4\alpha - \frac{\sigma_y t}{D}\cos^2\alpha\left(\frac{\partial^2 w}{\partial x'^2}\sin^2\alpha - 2\frac{\partial^2 w}{\partial x'\partial y'}\sin\alpha + \frac{\partial^2 w}{\partial y'^2}\right)\end{aligned} \tag{2.28}$$

where: w is the out-of-plane displacement; x' and y' are the skewed coordinates; D is the flexural rigidity of the plate; and σ is a uniform in-plane stress applied in the $x-$ and $y-$ direction.

For the case when the skew plate is simply supported, has sides of equal length and the loading applied to the plate is a uniform, uni-axial compression acting perpendicular to one set of the plate sides (shown in Figure 2.8), the equation of equilibrium is satisfied exactly by the deflection function,

$$w = \sin\frac{\pi x'}{a}\sin\frac{\pi y'}{a} \tag{2.29}$$

The resulting buckling loads for the plate are given by the buckling coefficient,

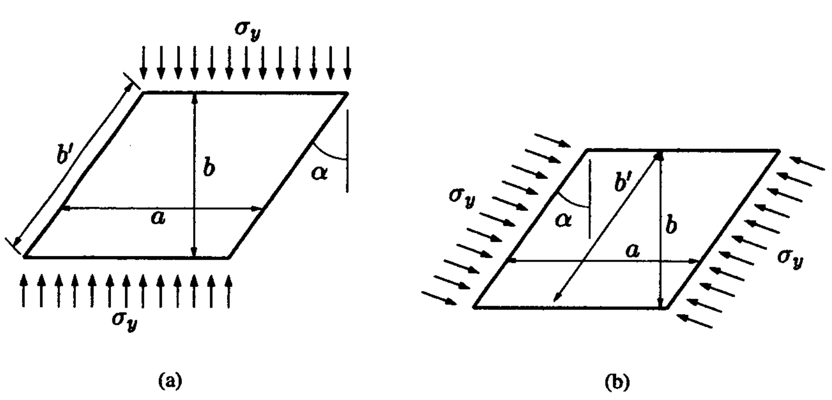

Figure 2.8: Loading regimes under which the solution to equation 2.28 is valid for the deflection function given in equation (2.29). Note that the loading in (b) is simply a transformation of that in (a)

$$4 = \frac{\sigma_y t b^2}{\pi^2 D} \tag{2.30}$$

This solution is for an isolated plate with simply supported edges and is the same as for a simply supported square plate. The buckling solution is independent of skew angle and the solution therefore gives a reliable way of checking convergence of numerical techniques. Numerical techniques used to solve skew plate problems become more onerous and require numerical models with larger numbers of degrees of freedom as the angle of skew of the plate increases [64, 68].

The ABAQUS plate models that are used in subsequent chapters presenting studies of skew plates are verified against this solution of the equation of equilibrium. Critical buckling modes given by the exact solution for a simply supported, isolated skew plate described in the previous paragraphs are shown in Figure 2.9 (a–d) and all have the solution $k = 4 = (\sigma_y t b^2)/(\pi^2 D)$. Only the central portion of the figures, showing the entire plate, is of relevance, the edges of which are simply supported. These exact buckling modes are compared against a finite element solution using a 30 × 30 mesh of ABAQUS type S8R5 elements in Figure 2.9 (e–h). The finite element solution predicts that the buckling strength of all the plates is given by $k = (\sigma_y b^2 t)/(\pi^2 D) = 4.000 \pm 0.1\%$. This finite element model is used throughout the thesis for skew plate buckling predictions and the comparisons presented therefore verify the use of the model.

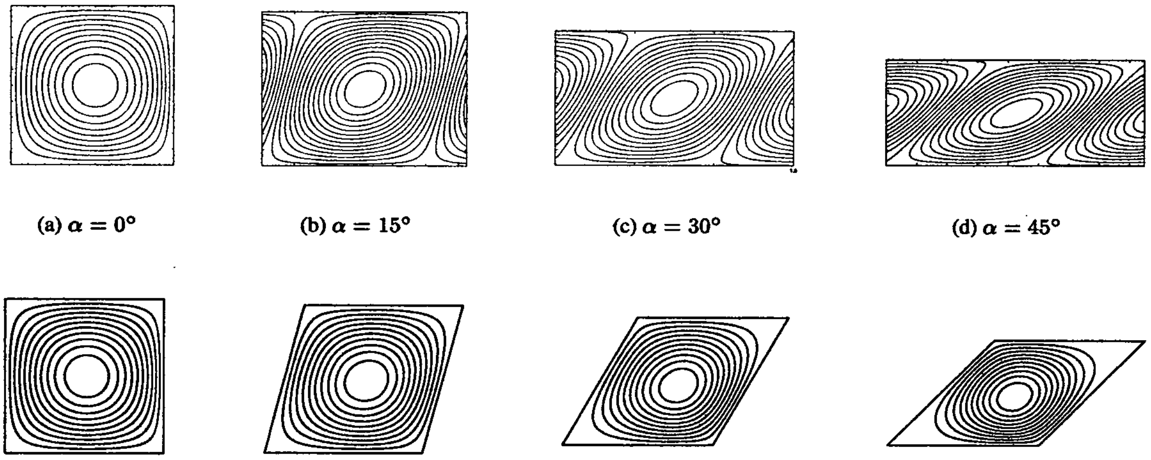

(a) $\alpha = 0°$ (b) $\alpha = 15°$ (c) $\alpha = 30°$ (d) $\alpha = 45°$

(e) $\alpha = 0°$ (f) $\alpha = 15°$ (g) $\alpha = 30°$ (h) $\alpha = 45°$

Figure 2.9: Exact solutions to the governing equation of thin-plate equilibrium for $a/b' = 1.0$ and a uniform in-plane compressive stress applied normal to the longitudinal plate edges (top line, (a)-(d)). The solution provides a benchmark result with which to confirm numerical methods for skew plate analysis, although it is rarely used. Example buckle modes obtained from ABAQUS finite element code are provided as comparison (bottom line (e)-(h)). The ABAQUS finite element model which is validated by the closed-form solution is used throughout the remainder of the thesis where applicable. In all cases, the critical buckle stress is independent of the skew angle, α, and is given by, $k = (\sigma_y b^2 t)/(\pi^2 D) = 4$. The finite element buckling predictions are accurate to within 0.1% of the exact solution.

Erroneous results and error arising from numerical approximations to the deflected form of the plate

Because there are in general, no deflection functions that are the solution to equation (2.28), a numerical approximation of the deflection function has to be made which is often an expansion of an infinite set of functions, which generally satisfy the boundary conditions to be imposed. Because this expansion is truncated, it only approximates the buckled shape of the plate and as a consequence, the potential energy of the plate is greater than 0. That is (from equation (2.24)),

$$T - U > 0 \tag{2.31}$$

which results in the buckling predictions of the plate always being higher than would an exact solution to the equilibrium equation [34].

Usefully, if deflection functions are chosen such that geometrical boundary conditions are not satisfied exactly, a lower bound solution to the buckling problem is obtained (*i.e.* $T - U < 0$). Budiansky and Hu [18] showed that upper- and lower- bound solutions to the critical buckling of rectangular plates can be found using the method of Lagrangian multipliers.

2.5 VICONOPT Buckling Routine Theory

This section presents the theory relevant to VICON [101, 4, 114], a buckling routine in VICONOPT, previously published results of which are used to provide the continuity comparison results in chapters 4–6 and 8 as comparison data for the finite element solutions presented.

The section presents a background to VICON with a brief history of development and later a concise theory. VIPASA theory, which describes the fundamental theory of VICON is given first and then the addition theory relating to VICON.

2.5.1 Background

VICON (VIpasa with (Lagrangian) CONstraints) is a buckling routine in a sophisticated and comprehensive panel optimisation program VICONOPT (VICON with OPTimisation) [102, 103]. The buckling routine VICON stems from VIPASA (Vibration and Instability of Plate Assemblies with Shear and Anisotropy), another buckling routine in VICONOPT, but improves on the VIPASA analysis by increasing (often considerably) the accuracy of the buckling predictions when a shear load is applied the plate assemblies and/or the plates assemblies are anisotropic, at the expense of an increased solution time.

VICONOPT can analyse single plates or assemblies of plates and advantage can be taken of the ability to use recurrence equations to analyse prismatic structures that have repetitive cross sections [104, 33].

2.5.2 VIPASA Analysis

VIPASA is based on the exact solution of general plate equilibrium equation that satisfies the Kirchoff-Love hypothesis, namely [54],

$$D_{11}\frac{\partial^4 w}{\partial x^4} + 4D_{16}\frac{\partial^4 w}{\partial x^3 \partial y} + 2(D_{12} + 2D_{66})\frac{\partial^4 w}{\partial x^2 \partial y^2} + 4D_{26}\frac{\partial^4 w}{\partial x \partial y^3} + D_{22}\frac{\partial^4 w}{\partial y^4} = - N_x\frac{\partial^2 w}{\partial x^2} - 2N_{xy}\frac{\partial^2 w}{\partial x \partial y} - N_y\frac{\partial^2 w}{\partial y^2} \quad (2.32)$$

Where the forces N_x, N_y and N_{xy} are defined in Figure 2.10(a).

This is an extension of the equation developed in the preceeding sections to include all nine independent material constants for in-plane stress-strain assumptions.

Plane stress-strain relationships are assumed, as is classical lamination theory (CLT) [92] if laminated composites are modelled.

Figure 2.10 (a) shows typical loading configurations avaliable in VICONOPT applied to an infinitely long panel having a finite width, b. These forces are N_x, N_y and N_{xy} per unit length of plate corresponding to uniform longitudinal, transverse and shear flow respectively (note that $N_{xy} = N_{yx}$ using the common nomenclature, hence all shear flow will be referred to using N_{xy}).

The deflections of the plate assembly are assumed to vary sinusoidally in the longitudinal (x) direction with half-wavelength, λ, where w (equation. 2.32) is given by the real part of,

$$w = Re[F(y)\exp(i\pi x/\lambda)] \quad (2.33)$$

Where: $i = \sqrt{-1}$; x is longitudinal coordinate in figure 2.10; and λ is the half-wavelength of the buckled form of the plate assembly.

Similar deflection expressions are used for displacements in the $x-$ and $y-$ directions, termed 'u' and 'v' respectively. Writing $F(y) = f_1(y) + i.f_2(y)$, the buckling displacement can be written as,

$$w = f_1(y)\cos\frac{\pi x}{L} - f_2(y)\sin\frac{\pi x}{L} \tag{2.34}$$

The functions $f_1(y)$ and $f_2(y)$ allow the setting of boundary conditions along the longitudinal edges (Edges 1 and 2 in Figure 2.10(b)).

If panels are isotropic or orthotropic and the applied loading is uniform uni– or bi–axial compression (*i.e.* there is no shear loading), $f_2 = 0$ and the displacement of the plate assembly is $w = f_1(y)\cos(\pi x/L)$. The solution of this deflection function produces a series of nodal lines spaced at regular intervals running normal to the longitudinal edges, λ (half wavelength of the buckle mode) apart. For the buckled form of the plate assembly, $\lambda = \lambda_j = a/j$ where j is a positive integer and a is the length of the plate assembly. These nodal lines satisfy the boundary conditions $v = w = 0$ with the quantities, u and $\partial w/\partial x$ being free which are synonymous with a classical simple support.

When plate assemblies are subject to shear loading and/or are anisotropic, then $f_2(y)$ of equation (2.34) is not equal to zero and the nodal lines produced in the solution are skewed. Hence the simply supported boundary condition is no longer satisfied and the buckling predictions can become very conservative if the critical buckle mode is 'overall' *i.e.* $\lambda \approx a$ (see reference [85] and chapter 6).

Displacements at nodes or junctions between plates are given by the real part of $\mathbf{D}'_j \exp(i\pi x/\lambda_j)$ for buckling analyses. $\mathbf{D}'_j$ contains the four complex displacement amplitudes for each nodal line corresponding to ψ, w, v and u shown in Figure 2.10.

A linear elastic buckling analysis is simply the solution of the eigenvalue equation, where the eigenvalue is a factor of the applied preloading to the structure that causes buckling. Hence a solution to $\mathbf{K}_j\mathbf{D}_j = \mathbf{0}$ is sought (or rather $|\mathbf{K}_j| = \mathbf{0}$ because non-trivial solutions to the problem are required). $\mathbf{D}'_j$ is obtained by multiplying every fourth element of $\mathbf{D}_j$ by i to account for a spatial phase difference between displacements if the plate assemblies are orthotropic and subject to in-plane compression loading only. Because sinusoidal functions are used to describe the deflected shape of the plate in the transverse direction, $\mathbf{K}_j$ is transcendental and changes from being Hermitian and complex to being real symmetric when plate assemblies are isotropic or orthotropic and there is no shear loading. This transcendental property of the stiffness matrix results in eigenvalue equations that cannot be solved directly by linear eigen-solvers and the Wittrick-Williams algorithm [108, 109] is used to ensure that there is no possibility of eigenvalues ever being missed.

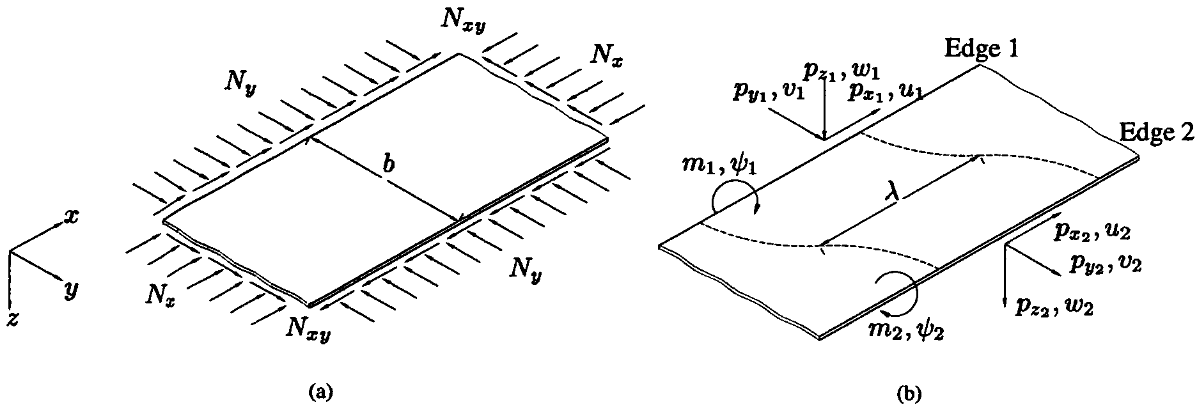

(a) (b)

Figure 2.10: Figure showing: (a) a component plate of width, b subject to forces N_x, N_y and N_{xy}, together with a reference axis system;.and (b) the skew model lines resulting from shear and/or material anisotropy predicted by a VIPASA analysis. Perturbation forces are given by p and m and displacements u, v, u corresponding to deflections in x, y, z directions shown in (a) along the longitudinal plate edges. In the case of buckling problems, these edge forces need to be multiplied by $\exp(i\pi x/\lambda)$

2.6 VICON Theory

The previous section briefly described the theory of VIPASA and highlighted the fundamental problem with the VIPASA analysis, namely that boundary conditions cannot be specified along the transverse plate assembly edges. VIPASA results become very conservative as $\lambda \to a$ if the plate assembly has anisotropic material properties and/or there is shear loading. In addition, the geometry of the plates is confined to have tranverse edges that run normal to the longitudinal edge, *i.e.* square or rectangular geometry. VICON overcomes these inherent shortcomings in VIPASA by using Lagrangian multipliers to provide point supports at which boundary conditions can be imposed. A sufficient number of these point supports running along the transverse edge of the panel accurately models a plate edge. The point supports in VICON can constrain any of the four displacement amplitudes ψ, u, v and w as well as rotation about the $y-$ and $z-$ axis in order that clamped boundary conditions can be modelled (see Figure 2.10(b)).

The inclusion of point supports into VIPASA results in the following eigenvalue equation [4],

$$a\mathbf{K}_m\mathbf{D}_m + \mathbf{e}_m^H\gamma_n = \mathbf{0} \qquad (m = n + qM \quad q = 0, \pm1, \pm2, \ldots)$$

$$\sum \mathbf{e}_m\mathbf{D}_m = \mathbf{0} \tag{2.35}$$

where: 'H' denotes a Hermitian transpose; γ_n and $\mathbf{e}_m$ are the Lagrangian multiplier vectors and constraint matrices; and $\mathbf{K}_m$ and $\mathbf{D}_m$ are the $\mathbf{D}_j$ and $\mathbf{K}_j$ defined in the VIPASA analysis.

The analysis assumes that the nodal displacements and forces can be represented by the Fourier series

$$\mathbf{D}_A = \sum_{m=-\infty}^{\infty} \mathbf{D}_m \exp(2i\pi mx/L) \tag{2.36}$$

$$\mathbf{P}_A = \sum_{m=-\infty}^{\infty} \mathbf{K}_m\mathbf{D}_m \exp(2i\pi mx/L) \tag{2.37}$$

These Fourier series are repetitive over a length, L, which is not necessarily equal to the length of the panel assembly, a. Hence, because integration of the displacement and force matrices are over a length L, the buckling solution obtained is for a number of equal and adjacent plate assemblies over which the function repeats. The buckling mode of the assembly therefore repeats over M equal bays and $L = aM$. The half-wavelength of this buckling mode, $\lambda = \lambda_m$, is $\lambda_m = L/2m$, where m is a positive integer determined by the n, q and M. All the modes which repeat over this length can be obtained by simultaneously satisfying equation (2.35) for each value of n given by,

$$-M'' \leq n \leq M' \tag{2.38}$$

where M'' and M' are the integer parts of $(M-1)/2$ and $M/2$ respectively.

The total energy of the plate assembly is given by,

$$V = \frac{1}{2}\int_0^L \mathbf{D}_A^T\mathbf{P}_A dx \tag{2.39}$$

which is minimised subject to the constraints on the point supports. VICON solves equation 2.35 in the form given below,

$$\begin{bmatrix} L\mathbf{K}_0 & & & & & & \mathbf{E}_0^T \\ & L\mathbf{K}_1 & & & & & \mathbf{E}_1^H \\ & & L\mathbf{K}_{-1} & & & & \mathbf{E}_{-1}^H \\ & & & L\mathbf{K}_2 & & & \mathbf{E}_2^H \\ & & & & L\mathbf{K}_{-2} & & \mathbf{E}_{-2}^H \\ & & & & & \ddots & \vdots \\ \mathbf{E}_0 & \mathbf{E}_1 & \mathbf{E}_{-1} & \mathbf{E}_2 & \mathbf{E}_{-2} & \cdots & 0 \end{bmatrix} \begin{Bmatrix} \mathbf{D}_0 \\ \mathbf{D}_1 \\ \mathbf{D}_{-1} \\ \mathbf{D}_2 \\ \mathbf{D}_{-2} \\ \vdots \\ \mathbf{P}_L \end{Bmatrix} = \mathbf{0} \tag{2.40}$$

The above equation is valid for a plate assembly which buckles in a mode that repeats over length LM. The Lagrangian multipliers repeat over this length, such that

$$\mathbf{P}_{LK} = [\mathbf{P}_{L0}^T, \mathbf{P}_{L1}^T, \mathbf{P}_{L2}^T, \ldots] \tag{2.41}$$

where $\mathbf{P}_{LK} = \mathbf{P}_{L,k+M}$ represent the Lagrangian multipliers in the interval $kL \leq x \leq (k+1)L$. The above equation is satisfied by the complex Fourier series,

$$\mathbf{P}_{LK} = \sum_{j=-M''}^{M'} \gamma_j \exp(2i\pi jk/M) \tag{2.42}$$

and the corresponding constraint matrix is given by

$$\mathbf{e}_m^T = [\mathbf{e}_m^T, \mathbf{e}_{m1}^T, \mathbf{e}_{m2}^T, \ldots] \tag{2.43}$$

where $\mathbf{e}_{mk}$ is the constraint matrix for the bay $kL \leq x \leq (k+1)L$.

The solutions given above will give buckling loads for all the modes with wavelength, L, $L/2$, $L/3$ *etc.* However by decoupling the equations, greater economy in solution can be achieved by only performing eigenvalue extraction for unique wavelengths that repeat over a whole number of bays. Thus buckling predictions are not made for values of m that do not contribute to the solution.

Given that the half-wavelength of the buckled assembly, λ_m is,

$$\begin{aligned} &\lambda_m = L/2m \\ \Rightarrow &\lambda_m = Ma/2m \qquad \text{from } L = Ma \\ \Rightarrow &\lambda_m = Ma/((2n/m) + 2q) \qquad \text{from } m = n + qM \text{ (Equation (2.35))} \end{aligned} \tag{2.44}$$

where $q = \pm1, \pm2, \pm3, \ldots, q_{\max}$.

λ_m is a function of M/n and not independently of M and n. It is therefore unnecessary to consider buckling solutions to values of m that share the same value of M/n and buckling predictions are considered only for these unique values of m. Writing $\xi = 2n/M$, λ_m becomes,

$$\lambda_m = \frac{a}{\xi + 2q} \qquad q = 0, \pm1, \pm2, \pm3, \ldots, q_{\max} \tag{2.45}$$

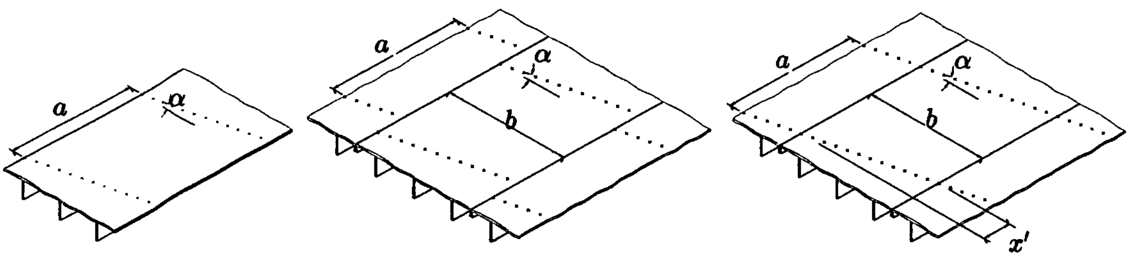

(a) (b) (c)

Figure 2.11: Figure showing: (a) a panel with a skew traverse support of $\alpha°$ with an infinite length and finite width, b. The skew geometry is enforced with Lagrangian constraints which provide point supports (shown as crosses); (b) a panel of infinite length and width with point supports discontinuous in the transverse direction; and (c) the 'corrected' model of (b) in which a shift of x' is applied to the transverse point supports, hence the support is now continuous in the transverse direction.

The buckling predictions become more exact as the values of $q_{\max}$ increases at the expense of increased execution time.

2.6.1 Transverse Repetition

The theory for VICON has been presented for an infinite longitudinal array of equal panels with length a. However by making use of suitable recurrence functions, plate assemblies that are infinite in the transverse as well as the longitudinal direction can also be analysed [33]. Transverse repetition is also used to speed modelling of assemblies that have some repetitive cross section.

In the case of VICON transverse repetition must also include the Lagrangian restraints which must be continuous in adjacent transverse bays. In order to prevent the saw-tooth type constraints shown in Figure 2.11(b), a constant longitudinal shift of x' must be incorporated, where $x' = b.tan\alpha$.

As a result of repetitive transverse modelling, the fundamental equations (equations 2.35) become,

$$a\mathbf{K}_{m0}\mathbf{D}_{m0} + \mathbf{e}_{m0}^{H}\gamma_{n0} = \mathbf{0} \qquad (m = n + qM \quad q = 0, \pm 1, \pm 2, \ldots) \tag{2.46}$$

$$\sum \mathbf{e}_{m0}\mathbf{D}_{m0} = \mathbf{0} \tag{2.47}$$

where

$$\mathbf{K}_{m0} = \mathbf{K}_{m11} + \mathbf{K}_{m12} \exp -i(\phi - 2\pi m x'/Ml) + \mathbf{K}_{m12} \exp i(\phi - 2\pi m x'/Ma) \tag{2.48}$$

These equations are solved in the same manner as for the longitudinally infinite panels, except that suitable values of ϕ must now be found. In general (when $M \geq 2$ [33]), $-\pi \leq \phi \leq +\pi$ and buckling solutions are obtained for,

$$\phi = \pi g/P \qquad g = -(P-1), \ldots, P \tag{2.49}$$

where P is the number of transversely repeating portions of width b and ϕ is restricted to those modes which repeat over no more than two tranverse bays [33]. Hence the transverse wavelength, λ_T is given by,

$$\lambda_T = Pb/g = \pi b/\phi \tag{2.50}$$

Note that in the case of skew panels, this λ_T is the half-wavelength measured normal to the longitudinal plate array edge and is therefore not the true half-wavelength of the transverse buckle.

2.7 Limitations of Thin Plate Theory

The previous sections deal with background and theory for buckling analysis of plates that are classically thin and satisfy the Kirchoff-Love hypothesis. This section discusses the limitations of thin-plate theory which can lead to poor plate buckling predictions if the assumptions are not valid. Each of the assumptions presented in section 2.2.2 is considered independently.

2.7.1 Assumption 1

The first assumption states that *normals to the middle plane (neutral axis) remain plane and normal after bending* as in 2.1.

In reality these normals become skew after bending or buckling and there is a transverse shear deformation (through thickness deformation) which is parabolic [95]. This through thickness deformation is accounted for in *shear deformation theory* or *thick plate theory*, originally presented for bending of plates by Reissner [75] and for plate vibration by Mindlin [63] and is described comprehensively in the monograph of Wang *et al.* [95]. These first shear deformation theories assumed that the normal rotates about the neutral axis of the plate, but that the through thickness plate deformation is linear, hence they are known as first order shear deformation theories. The error arising out of the assumed linear deformation and actual parabolic though thickness deformation is corrected by means of a shear factor and is a function of the Poisson's ratio of the plate [63]. Second and third order shear deformation theories build on the first order theory by approximating through thickness deformation using second and third order functions respectively, often with little increase in accuracy [95].

The effect on the buckling load of plates due to shear deformation is slight if the ratio of breadth of buckle mode half–wavelength to thickness of the plate is large. Typical values of ratio of plate breadth to thickness at which thin-plate assumptions lead to unacceptably large errors range from $b/t = 20 - 13$, ABAQUS user manual [3] and reference [43] respectively (Roark [78] suggests $b/t \leq 4$). For plates with b/t less than these values, the critical buckling load of plates is over predicted using thin-plate theory. An example of the magnitude by which the buckling loads for simply supported plates are over-estimated are shown in Table 2.1. The table shows elastic buckling predictions for square and skew plates of increasing thickness, including comparison analyses made using the finite element code ABAQUS by the author. The classical thin plate theory buckling predictions become increasingly more conservative as the thickness of the plate increases. The results presented for comparison suggest that a $5 - 10\%$ decrease in plate buckling strength is observed for $t/b = 0.05$.

Shear deformation plate theory becomes more onerous as the ratio of b/t decreases further and reliable results are only given by the use of fully 3-D models [10].

In aerospace applications, panels and/or plates generally have ratios of b/t a number of factors greater than 20 and the effect of shear deformation on the elastic buckling strength of the panels is therefore relatively unimportant. Hence the results presented in this thesis are presented ignoring shear deformation.

2.7.2 Assumption 2

The second assumption states that that *the middle plane remains neutral during bending - it is not strained.* This assumption is valid if the deflected shape of the plate is developable and if the deflections of the plate are small in comparison to its overall dimensions so that the curvature expressions for the plate are valid. Clearly, the deformed surface of a simply supported plate is not developable and the assumption that the mid-plane of the plate remains unstressed is valid only if the out-of-plane deflection of the plate is small compared to the plate thickness.

Large deflection theory addresses the short-comings of the small displacement assumption by deriving an equation of equilibrium for membrane stresses which is simultaneously solved with the derived equation for thin plate stability. These two equations are generally solved using Airy's stress functions where

Table 2.1: Buckling predictions for skew plates with increasing thickness, subject to an in-plane, uni-axial stress acting on the skew transverse plate edges parallel to the longitudinal edge. The skew angle, α, is defined in Figure 2.8. Results are obtained from current literature for first-order shear deformation theory for simply supported and fully clamped boundary conditions. Comparison is made with ABAQUS finite element buckling predictions by the author. The plates have sides of equal length and results are presented as the ratio of t/b (plate thickness to transverse plate width) increases. The critical buckling load of the plates is given using the general buckling coefficient, $k = (\sigma b^2 t)/(\pi^2 D)$, where b is measured parallel to the skew edge. $t/b = 0.001$ is the classical thin-plate theory result.

	Simply Supported				Fully Clamped			
Author t/b	0.001	0.05	0.1	0.15	0.001	0.05	0.1	0.15
Kitipornchai [48]	4.0000	3.7835	3.4950	3.1859	10.0738	9.5588	8.2917	6.7595
ABAQUS†	4.0000	3.7781	3.4946	3.1858	10.1426	9.5587	8.2917	6.7595
Venkateswara Rao *et al.* [91]	–	–	–	–	10.0850	9.6025	8.3974	6.9029
Wang [96]	–	–	–	–	10.0737	–	8.0232	–
Sarath Babu & Kant‡ [79]	–	–	–	–	10.07	–	8.03	–

(a) $\alpha = 0°$

	Simply Supported				Fully Clamped			
Author t/b	0.001	0.05	0.1	0.15	0.001	0.05	0.1	0.15
Kitipornchai [48]	4.3940	4.1314	3.8027	3.4564	10.8345	10.2312	8.7741	7.0589
ABAQUS†	4.3915	4.1241	3.8022	3.4564	10.8320	10.2312	8.7742	7.0589
Wang [96]	–	–	–	–	–	–	8.4732	–
Sarath Babu & Kant‡ [79]	–	–	–	–	–	–	8.48	–

(b) $\alpha = 15°$

	Simply Supported				Fully Clamped			
Author t/b	0.001	0.05	0.1	0.15	0.001	0.05	0.1	0.15
Kitipornchai [48]	5.9026	5.4182	4.9324	4.4275	13.5377	12.5711	10.3760	8.0098
ABAQUS†	5.8940	5.4068	4.9314	4.4273	13.5310	12.5712	10.3761	8.0100
Wang [96]	–	–	–	–	13.5378	–	9.9593	–
Sarath Babu & Kant‡ [79]	–	–	–	–	–	–	9.97	–

(c) $\alpha = 30°$

	Simply Supported				Fully Clamped			
Author t/b	0.001	0.05	0.1	0.15	0.001	0.05	0.1	0.15
Kitipornchai [48]	10.1428	8.7328	7.7236	6.6376	20.1115	17.9652	13.6909	9.7994
ABAQUS†	9.6720	8.7164	7.7212	6.6369	20.0650	17.9685	13.6915	7.0481
Wang [96]	–	–	–	–	20.1213	–	13.0197	–
Sarath Babu & Kant‡ [79]	–	–	–	–	20.12	–	13.05	–

(d) $\alpha = 45°$

† ABAQUS results by the author using a 30 × 30 mesh of type S8R5 elements for $b/t = 0.001$ and type S8R elements for all other results.

‡ Sarath Babu and Kant produced both first– and second–order shear deformation results. These are the first–order ones.

Bulson[20] gives,

$$\sigma_x = \frac{\partial^2 F}{\partial y^2} \qquad \sigma_y = \frac{\partial^2 F}{\partial x^2} \qquad \tau_{xy} = -\frac{\partial^2 F}{\partial x \partial y} \tag{2.51}$$

and the governing equation for plate equilibrium (2.9) is now given by

$$\frac{\partial^4 w}{\partial x^4} + 2\frac{\partial^4 w}{\partial x^2 \partial y^2} + \frac{\partial^4 w}{\partial y^4} = \frac{t}{D}\left\{\frac{q}{t} + \frac{\partial^2 F}{\partial y^2}\frac{\partial^2 w}{\partial x^2} + \frac{\partial^2 F}{\partial x^2}\frac{\partial^2 w}{\partial y^2} - 2\frac{\partial^2 F}{\partial x \partial y}\frac{\partial^2 w}{\partial x \partial y}\right\} \tag{2.52}$$

which is to be solved simultaneously with the equation describing mid-plane stress

$$\frac{\partial^4 F}{\partial x^4} + 2\frac{\partial^4 F}{\partial x^2 \partial y^2} + \frac{\partial^4 F}{\partial y^4} = E\left[\left(\frac{\partial^2 w}{\partial x \partial y}\right)^2 - \frac{\partial^2 w}{\partial x^2}\frac{\partial^2 w}{\partial y^2}\right] \tag{2.53}$$

The above equations are coupled and non-linear and there are no closed-form solutions that solve them. They apply to the early stages of post-buckling, *i.e.* initially after the bifurcation point found by solution of the linear elastic solution and assume that the material behaves in a linear elastic fashion. The equations predict a reduced plate stiffness beyond the initial elastic buckling load.

Solutions of the equations for basic loading and boundary conditions are given a through account in Bulson [20] and a more general set of solutions for more complex loading and boundary conditions for square plates is covered in Williams and Aalami [100] using an explicit finite difference method.

Past the initial stages of post buckling, plate behaviour is highly geometrically non-linear and subject to 'snap-though' (especially if the plates are long). These stability problems are generally solved by tracing the equilibrium path of the structure for applied increments of loading or displacement for which Rik's method is suitable when the solution is unstable [3, 24, 77] or a Newton-Raphson [3] for the initial stages of post-buckling when the solution is known to be stable. Further into the post-buckling regime, the non-linear behaviour of the material also has to be accounted for. A comprehensive account of post-buckling analysis and behaviour of plates is given in Chia [22].

An example of the initial post-buckling behaviour of a linear-elastic square plate under a uniform end-shortening is given in Figure 2.12 that show its load versus end-shortening and load versus central deflection relationship. The results are obtained using ABAQUS by the author and are compared with Yamaki [111].

The curves of Figure 2.12 show that strength increases are associated with post-buckling. However, in aerospace applications, it is generally undesirable for wings and fuselage panels to wrinkle and deform

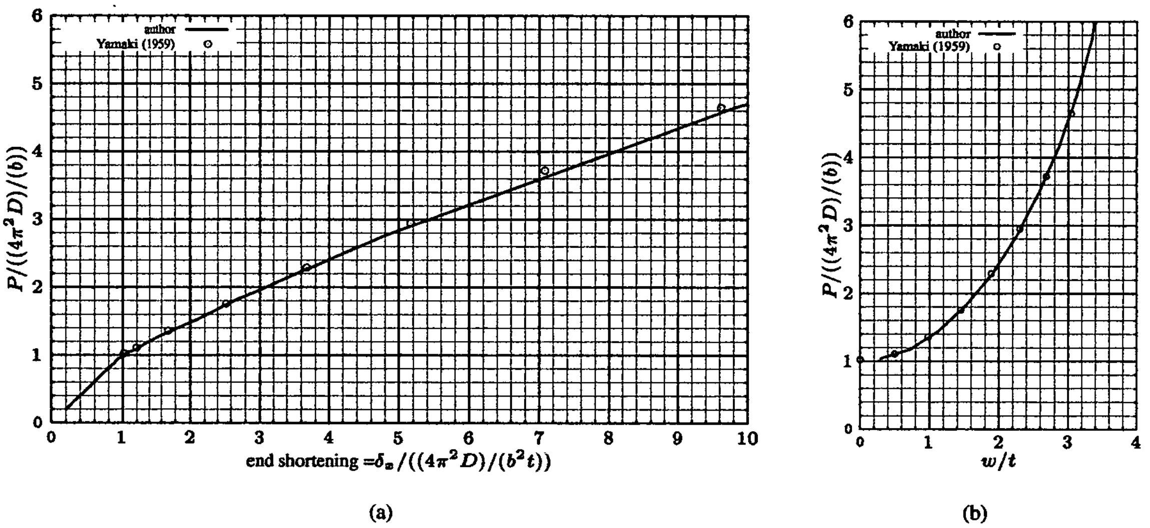

Figure 2.12: Example curves for non-linear geometric buckling of a square plate subject to a uni-axial in-plane end-shortening along the transverse edges with the longitudinal edges restrained to remain straight. (a) shows the load Vs end-shortening curve and (b) Load Vs central deflection curves. In both cases, the loading (abscissa) is shown as a factor of the elastic buckling load. In the case of (a) the end-shortening is shown as a factor of the end-shortening at the elastic buckling load and in (b) the deflection at the mid-point of the beam, w, is given as a factor of the plate thickness, w.

visibly, hence bifurcation predications are required. In addition, the elastic buckling predictions can be used to create useful design curves relating panel geometry and buckling strength. These curves are especially useful in preliminary design by hand calculation and sizing for more complex optimisation calculations where they can be used to provide realistic start designs. ESDU (Engineering and Sciences Data Unit) provide a limited number of curves of elastic buckling predictions for this purpose.

2.8 Concluding Remarks

This chapter presents a summary of classical thin-plate theory from the literature, identifies the assumptions made and their validity.

Energy expressions are presented and it is shown how these are used to present the critical buckling load of a plate as an eigenvalue problem.

The classical solution for a rectangular simply supported plate is presented. This solution is used extensively to test the validity of the finite element models used in the studies and results sections in the remaining chapters of the thesis.

The governing equation of equilibrium is presented, written in terms of skew coordinates, from which it is clear that finding deflection functions that satisfy the equation and thus give closed-form solutions that predict the elastic buckling load for skew plates is unlikely. However, it is noted that Anderson[5] observed that a simple deflection function can be used to solve the governing equation for skew plates with equal sides and a uniform compression loading applied normal to one set of parallel edges. This solution is presented together with the buckle modes arising from the solution. This exact solution is modelled using ABAQUS finite element analysis code which gives very accurate buckling predictions for this one case.

The theory of the buckling routines in VICONOPT [103, 102], VIPASA and the extension of VIPASA, VICON is also briefly presented. The results from this analysis are for an infinite array of plates and the boundary conditons gives buckling predictions for plates that are continuous over an infinite number of equal bays. The effect of this continuity is considered in chapters 4 and 5 in this thesis.

Chapter 3

Review of Buckling solutions for skew plates with simply supported and clamped boundary conditons

This chapter reviews the elastic buckling methods and solutions for skew plates available in the open literature. A review of the published material relevant to other parts of the work considered in the thesis, for example tapered and stiffened panels, is given at the beginning of the appropriate chapter.

The review considers loading to the skew plates separately where possible, hence the first section considers compression loading and the second shear loading. Shear loading is not considered in the thesis, because the critical design case for plates and panels in aerospace applications is assumed to be an in-plane compression load, but is included in this review for completeness. The buckling methods and solutions are presented in chronological order and show the logical progression of the solution of the buckling problem for the most readily obtainable cases (those with fully clamped boundary conditons) to modern-day solutions based on finite element and finite strip methods for laminated plates.

3.1 Skew plates in Compression

The nomenclature relating to skew plates is consistent with that used throughout the remainder of the thesis. For clarity a schematic of a plate is given in Figure 3.1 showing the nomenclature. The figure shows a plate

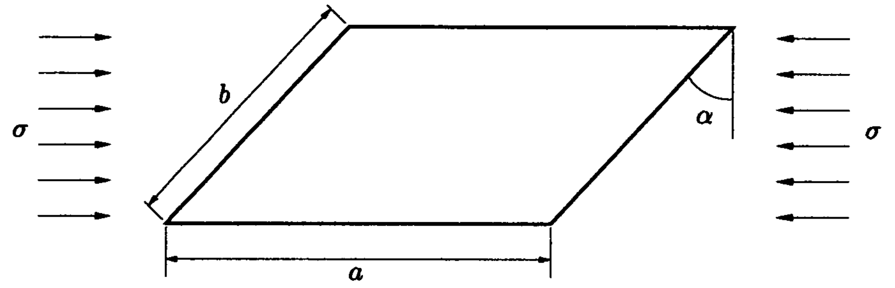

Figure 3.1: Schematic of a skew plate showing nomenclature used throughout the chapter. The figure shows a plate of longitudinal length a, transverse width measured parallel to the skew transverse edge, b and skew angle, measured between the transverse plate edge and the global vertical. The plate is subject to a uniform in-plane compressive stress, σ.

under a uniform, uni-axial compressive stress, σ, consistent with the loading conditons considered in the thesis.

The first published work dealing with the buckling of skew plates appeared in the early 1950s as the aerodynamic advantages of a 'swept' planform wing shape were realised.

The first buckling calculations for skew plates were produced by Guest [37] and were an extension of the work on clamped rectangular panels by Budiansky and Hu [19]. The buckling predictions were obtained for clamped skew plates under a uniform in-plane compressive stress acting as in Figure 3.1. Guest used a double Fourier series to represent the deflection of the plate and solved the energy equations using the method of Lagrangian multipliers. By minimising all of the coefficients in the expression for the internal energy of the plate and using a truncated series to describe the boundary conditions, a lower bound solution for the buckling load was found (*i.e.* $V - T < 0$). Reversing the process and satisfying the boundary conditons exactly and truncating the series for internal energy provided an upper bound solution. Critical buckling loads were predicted to be $13.53 \leq (\sigma b^2 t)/(\pi^2 D) \leq 13.89$ and $20.7 \leq (\sigma b^2 t)/(\pi^2 D) \leq 21.6$ for plates with skew angles of 30° and 45° respectively. Guest draws a comparison with an unpublished (at the time) solution for the 30° case by Wittrick using a Galerkin method (and hence upper-bound), predicting that $(\sigma b^2 t)/(\pi^2 D) = 13.6$. This work on skew plates with clamped boundary conditons was subsequently published in reference [38]. Guest extended his Lagrangian multiplier analysis to present a buckling prediction for a simply supported skew plate having sides of equal length and a skew angle of 30 degrees. The deflection functions used by Guest only permitted an upper-bound solution to the problem to be found, because the lower bound series did not converge. Accordingly the upper bound limit for the skew plate is recorded as $13.7 < (\sigma b^2 t)/(\pi^2 D)$ which is almost equivalent to that of the clamped skew plate and is much too high.

Anderson [5] presented buckling predictions for an infinite plate split into equal skew bays under a uniform, uni-axial compressive stress and was the first author to consider the buckling strength increases arising from continuity between adjacent skew plates. He also recognised the existence of the only published closed-form solution for a skew plate described in the previous chapter – a solution which appears not to have been recognised by many authors investigating the stability of skew plate structures today. Anderson's work is compared with the current analysis and described in detail in chapter 5. Anderson's buckling solutions were later adopted by the Engineering Sciences Data Unit (ESDU) and published as a design guide for use in plate sizing, see reference [30].

Mansfield [60] recognised the difficulties of finding suitable deflection functions to adequately approximate the buckling mode of the failed plate and suggested guidelines for predicting the critical buckling load for clamped skew plates using rectangular plate approximations to the skew plate. He proposed that for skew plates with an aspect ratio greater than 2, the buckling load of the plate would be bounded by the critical buckling load for a rectangular plate with an aspect ratio of $(a + b\sin\alpha)/b\cos\alpha$ and $(a - b\sin\alpha)/b\cos\alpha$. For plates with $a < 0.5b$, Mansfield suggested that upper and lower bounds to the buckling problem may be obtained by considering the buckling loads of the rectangular plates formed by dropping perpendiculars on the two, diametrically opposed skew edges. The buckling load of the skew plate will therefore be bounded by the buckling load for a rectangular panel having aspect ratios $(a\cos\alpha)/(b + a\sin\alpha)$ and $(a\cos\alpha)/(b - a\sin\alpha)$. The rectangular approximations are shown in Figure 3.2. The approximations will clearly become more in error as the skew angle of the plate increases, to such a degree, that they will become rather useless. The approximation for the short aspect ratio panels doesn't consider the effect of changing the direction in which the compressive stress acts. In between the ratios for which rectangular approximations are given, Mansfield presents a simplistic energy method solution for the problem. There were no skew plate buckling solutions with which to validate the effectiveness of the approximations.

Wittrick [105] considered the buckling load of clamped skew plates in compression using a Galerkin form of the Raleigh Ritz procedure and Iguchi functions to approximate the buckled form of the plate. He extends the work by Guest by producing buckling curves for plates with skew angles of $15°, 30°$ and $45°$ and aspect ratios in the range $0.5 \leq a/b \leq 3.0$. Along with the work of Anderson [5], it represents some of the most complete work dealing with the behaviour of skew plates at the time. The results for Wittrick's $30°$ plate with all sides having the same length falls within the upper- and lower- bound approximation by Guest [37].

Some of this early work, previously discussed, on the stability of skew plates is reported in the monograph of Morley [68].

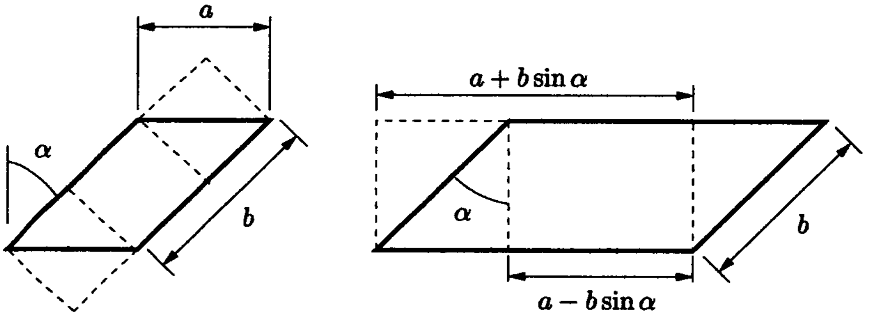

Figure 3.2: Rectangular approximations suggested by Mansfield [60] to provide upper and lower bound buckling load predictions for skew plates. The left approximation is suggested for $a < 0.5b$ and the right one for $a > 2b$. The dashed lines show the rectangular approximation.

Hamanda [39] produced buckling predictions for clamped skew plates with sides of equal length under a uniform bi-axial compressive stress using the energy method for a plate with skew angle $0°, 15°, 30°$ and $45°$. The compressive stress in this case acts normal to the skew transverse edge. Results are also given for the fundamental frequency of the plates as well as buckling solutions for plates under a pure shear load.

Argyris [7] used the finite element to produce a limited number of buckling predictions for skew plates under a uniform uni-axial compressive stress. These represent the first solutions to the skew plate buckling problem by the finite element method.

Ashton [8] used a Raleigh Ritz formulation with Iguchi functions to describe the buckled form of a plate to determine the critical buckling loads of clamped skew plates with sides of equal length loaded in pure in-plane uniaxial compression, pure bi-axial compression and pure uniform shear as well as varying ratios of bi-axial compression and uni-axial compression and shear.

Yoshimura and Iwata [118] produced buckling results for simply supported skew plates under a pure in-plane compression load and pure in-plane shear loading. They were some of the first researchers to consider simply supported skew plates. Plates with skew angles of $15°, 30°$ and $45°$ were considered with aspect ratios of $a/b = 1.0$ and 2.0. Durvasula [28] considers their results to be fictitiously low due to an error in a presented equation, however comparisons for the compression loaded case in Table 4.2 on page 63 appear to be fairly consistent with the other published work in this area.

Durvasula produced a considerable number of results for skew plates using the Galerkin method using a double series of beam characteristic functions to approximate the buckled shape of the plate. Clamped plates [27] were initially considered with results presented for pure in-plane shear and pure in-plane compression loading as well as combinations of both. This was later followed by a study of simply supported skew plates [28]. Using the Galerkin method, Durvasula *et al.* [29] extended the work on simply supported and clamped isotropic plates to generally orthotropic skew plates, having orthotropy comparable to either: a steel, grooved plate; or a fibre-glass epoxy composite. Fundamental frequencies of vibration are also included in this reference. Finally, Mahabaliraja and Durvasula [59] produce buckling interaction cures for bi-axial in-plane stress and shear loading.

Buckling predictions for clamped and simply supported skew plates under a pure in-plane compression load and pure in-plane shear load were presented by Fried and Schmitt [32]. The results were obtained using a finite element analysis. Results are presented for $\alpha = 15°, 30°$ and $45°$ and three aspect ratios. The results are complemented by a set of results for the fundamental frequency of vibration of skew plates.

Chan and Kabila [21] present a finite element formulation for analysing skew plates, but do not verify the element by presenting any comparable bucking results.

Srinivasan and Ramachandran [80] extend the work by Durvasula *et al.* [29] and present buckling solutions for generally orthotropic skew plates using a finite difference formulation for clamped boundary conditons and in-plane, uni-axial compression loading and in-plane shear loading.

Thangam Babu and Reddy [87] use the finite strip method to produce a comprehensive analysis of skew plates that are orthotropic to varying degrees and include isotropic solutions for verification with the open literature. The finite strip used a third order displacement function to describe deflection longitudinally along the plate and assumed sinusoidal transverse displacements. The finite strip formulation can therefore be used to analyse plates that are simply supported along the longitudinal edges, with the third order polynomial allowing simply supported, clamped or free boundary conditons along the transverse edges. The study presents buckling curves for skew plates with $\alpha = 15°, \alpha = 30°$ and $\alpha = 45°$ that have various combinations of the simply supported, clamped and free boundary conditons. The plates are loaded with pure, uni-axial and bi-axial in-plane compressive stress. The authors' buckling solutions for plates with skew angles greater than 15° are, by the authors' own admission, unreliable. Thangam Babu and Reddy postulated that, "the accuracy of the results can be improved to a great extent by using a higher order finite strip method".

Kennedy and Prabhakara [46, 45] also consider generally orthotropic skew plates using a exact solution method based on Fourier series. Plates with simply supported boundary conditons and loaded with in-plane uni-axial and bi-axial compression and shear are considered. Buckling predictions are presented in the form of design curves. Tabulated data [46] are presented for isotropic plates to allow comparison with previously published analysis. Comparison is made with Durvasula's [28] results. Kennedy and Prabhakara note that their solutions are often significantly (up to 50%) lower. They attribute this to the

Galerkin solution used by Durvasula not accurately satisfying the boundary conditions.

Mizusawa *et al.* [66] used the Raleigh Ritz method with B-spline deflection functions to analyse skew stiffened plates and skew plates with clamped and simply supported boundary conditons under uniform uni-axial compression or uniform in-plane shear stresses. The method was extended by incorporating Lagrangian multipliers to permit analysis of skew plates with varying boundary conditons [65]. Accordingly, buckling results are presented for: skew plates with simple supports; orthotropic skew plates with simple supports; and fundamental frequency vibration analysis for plates with combinations of simple supports and free edges for validation. Further work by Mizusawa and Kajita considered skew plates with varying degrees of rotational restraint applied along the skew transverse edges for plates under uni-axial in-plane compression [64]. Buckling and vibration analysis by Mizusawa and Leonard [67] of skew plates using the B-Spline Raleigh Ritz method considered combinations of clamped and simple supports along the same edge.

Tham and Szeto [86] present buckling predictions for skew plates with equal sides and simply supported and clamped boundary conditions using a spline finite strip method. The results are presented to validate the methods and consider uni-axial and bi-axial in-plane compressive stresses.

Wang *et al.* [94] used the Raleigh Ritz method with two-dimensional polynomial, basic functions (pb2-functions) to solve the plate buckling problem. Uni-axial compression loaded plates are considered and the effect of two corner conditons considered: one in which the corner is imposed by not permitting a rotation (*i.e.* there is zero slope at the plate corners); and one in which there is zero moment at the corner. The latter case will have a slight stiffening effect on the plate and increase its buckling load. The former buckling case leads to a singularity in which zero moment is accompanied by zero slope. The stiffening effect of the first corner conditon was shown to lead to buckling strength increases up to 8% higher than the second corner conditon for plates with sides of equal length. Finite element models will generally adopt the zero rotation type corner.

Wang *et al.* [93] considered the effect of shear deformation on the buckling stability of skew plates and produced, for verification and comparison purposes, thin-plate buckling solutions for skew plates with aspect ratios of $1.0, 1.5$ and 2.0 and skew angles of $\alpha = 15°$ and $\alpha = 30°$. The plates have simply supported, fully clamped and varying combinations of simply supported and clamped boundary conditons. Analysis of the plates is by the pb-2 Raleigh-Ritz method and factors are introduced that permit an accurate estimate of the buckling strength of a 'thick' plate from a thin-plate buckling solution.

Jaunky *et al.* [44] consider the buckling strength of anisotropic plates using a Raleigh-Ritz procedure.

Buckling predictions are presented for skew plates under uni-axial, bi-axial compression and in-plane shear. Predictions are also presented for varying degrees of orthotropy. The results are compared against VICONOPT [103] and STAGS [16].

Wang, Striz and Bert [98] use the differential quadrature method to predict the critical buckling loads for skew plates with equal sides and simply supported and fully clamped edge boundary conditons. They also determine fundamental frequencies for the vibration of these plates.

Krishna Reddy and Palaninathan [53] consider the buckling strength of skew, laminated plates using a finite element formulation. The study considers the changes in buckling strength for plates having sides of equal length and skew angle of $15^\circ, 30^\circ$ and 45° as the orientation of the laminate is rotated through 90°. Two stacking sequences of the laminate are considered: antisymmetric of 2,4,6,8 or 10 layers; and antisymmetric cross-ply. Verification of the model is by comparison with the buckling solutions of Kennedy and Prabhakara [46, 45] for orthotropic skew plates. The results are presented as buckling curves showing the change in buckling coefficient as the ply angle changes.

York [112] produced buckling results for skew plates using VICON, the buckling routine in VICONOPT (see chapter 2 on page 8). Buckling predictions are presented for: an infinitely long plate split into equal skew bays; and an infinite sheet of equal skew bays (comparable with the analysis by Anderson [5]). The skew angle of the bays considered are $\alpha = 15^\circ, 30^\circ$ and 45°. Aspect ratios of the bays range from 0.5 to 2.5 with the aspect ratio being defined with the breadth measured parallel to the skew, transverse edge. Hence the analysis considered plates that have continuity over otherwise simple supports. Buckling curves were presented for isotropic plates with uni-axial compression loading and a pure in-plane shear loading.

Wang [97] also considers skew plates made from composite laminates. Plates with skew angles of 30° or 45° and sides of equal length are considered. Analysis is by the Raleigh-Ritz method with B-spline deflection functions and after verification of the buckling results with isotropic skew plates, critical buckling loads for skew plates are obtained for uni-axial, bi-axial compression and in-plane shear for: one layer laminates (*i.e.* generally orthotropic plates); anti-symmetric laminates with 2 cross-ply lay-ups $[0^\circ/90^\circ]$; antisymmetric laminates with four cross-ply lay-ups $[0^\circ/90^\circ/0^\circ/90^\circ]$; anti-symmetric laminates with two layers $[45^\circ/-45^\circ]$; and anti-symmetric laminates with four layers $[45^\circ/-45^\circ/45^\circ/-45^\circ]$.

Wang extends the work described in the previous paragraph on skew plates made from composite laminates to include shear deformation in the analysis [96]. The analysis described in the previous paragraph is repeated using a first-order shear deformation implementation of the B-spline Raleigh Ritz procedure for a plate with breadth to thickness ratio of 10. The results of the analysis show that there is a very significant loss in buckling strength of the plates as the skew angle of the plates, fibres and number of antisymmetric layers increases over a comparable thin-plate buckling solution. For example, a single layer composite laminate plate loaded under a uniform, uni-axial, in-plane compressive stress and having sides of equal length, a skew angle of 45°, a thickness to breadth ratio of 0.1 and the ply orientated at 15° has a bucking factor of $k = 1.4887$. The same plate, but with a thickness to breadth ratio of 0.001 (classically thin) has a critical buckling factor of 4.1062. The results suggest that this is a very significant area for further research.

Sarath Babu and Kant [79] essentially extend the results by Krishna Reddy and Palaninathan [53] by re-running the analysis using a finite element model that includes the effect of shear deformation theory. A first order and higher order shear deformation theory are considered and their findings also suggest, in agreement with Wang [96] that the effect of shear deformation is very significant.

The account given has presented buckling solutions for, primarily, skew plates with in-plane uni-axial or bi-axial compression loading. It shows that although a considerable number of solutions have been presented for skew plates, few actually describe the behaviour of skew plates as the aspect ratio of the plate increases. Most of the buckling solutions are presented for a plate with equal sides – with the notable exception of Wittrick, York and Anderson (York and Anderson only consider infinite arrays of plates). For example these limited published results mean that the aspect ratio at which a skew plate can accurately be treated as being rectangular has not, with any certainty be ascertained.

A comparison of the buckling predictions for skew plates made by previous researchers for plates that are simply supported and clamped and loaded with a uniform, uni-axial, in-plane compression stress is presented in Tables 4.3 on page 64 and 4.2 on page 63 in chapter 4 together with a discussion. Unless otherwise stated, the following work considers elastic buckling of isotropic plates subject to in-plane loadings.

The next section, for completeness considers skew plates with shear loading. Much of the later literature considers in-plane compression and shear loading in unison and has been considered in the current section, but early papers treat the loadings separately.

3.2 Skew plates with shear loading

A review of the literature dealing with the buckling strength of shear loaded skew plates identifies two cases of loading: that of a plate with a shear applied parallel to all the plate edges, and that when an infinitesimal element of the plate is under a pure shear. The two loading cases are shown in Figure 3.3 on the following page. For ease of reference, the shear loadings will be termed '*P*' (parallel) loading and '*O*' (orthogonal)

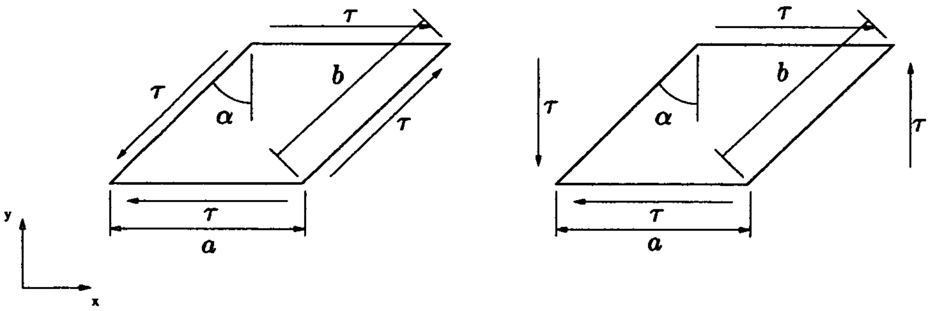

Figure 3.3: Alternative shear loading: right 'P' type loading; and left 'O' type loading

loading respectively. The shear loading of type 'P' will change as the skew angle of the plate changes.

Because skew plates do not exhibit symmetry, unlike a rectangular plate, the direction in which the shear forces act affects the buckling load of the plates. A positive shear is defined in this discussion using the standard nomenclature used in chapter 2 on page 8 and hence those plates drawn in Figure 3.3 show a positive shear. A negative shear acts in the opposite direction.

For the 'P' type shear, the plate buckles at a higher load if the shear acts in the positive direction rather than the negative one. This is because when the shear is positive, the in–plane forces acting on an infinitesmal rectangular element of the plate are a shear and a uniaxial tension on its transverse edges. When the direction of the shear is reversed, the in-plane forces acting on an infinitesimal rectangular element are a shear and a uniaxial compression. In the former case the uniaxial, in–plane tension has a stabilising effect on the plate and in the latter case; the in–plane compression has a destabilising effect.

For the 'O' type loading, plates buckle at a higher load if the shear acts in the negatively defined direction rather than the positive one. This is because in the positive shear case, a compressive stress develops across the plate's obtuse corners and a tension across the acute ones. The obtuse corners are less stiff than the acute corners and the plate buckles at a lower load if a compressive stress develops at them. When the shear load acts in the opposite (negative) direction, a tension acts across the obtuse plate corners and a compression across the acute ones with the result that the plate buckles at a higher load.

The first published skew plate results for shear were by Wittrick [106] using the Raleigh Ritz method with Iguchi functions in a similar manner to his solution for skew plates under a uniform in-plane compression [105] with clamped edges. He produced results only for the positive, critical, shear case; presenting them as buckling curves showing the relationship between critical buckling load and plate aspect ratio for plates with skew angles of $\alpha = 15°, 30°$ and $45°$. The results reveal that shear buckling loads for skew plates can be lower than for an equivalent rectangular plate. Buckling results for shear loading are considerably higher than for uni-axial compression loading.

Hasegawa [40] used a Raleigh–Ritz method to determine the buckling load for skew plates with a 'P' type shear loading. Results are presented for skew plates with sides of equal length and skew angles of $\alpha = 15°, 20°, 30°, 35°$. A square case was included for verification. Hasegawa doesn't seem to have appreciated that the shear loading corresponds to that which will predict the highest buckling loads. Naturally, his results show increases in buckling strength of the plates as the skew angle increases.

Klein [51] uses the collocation method to obtain buckling solutions for a skew plate with equal sides and fully clamped edges. Unusually, the skew angle of the plate is presented as the ratio of the two diagonals of the plate, for which it is considered up to ratios of 3 and a negative shear stress *i.e.* the critical direction of shear stress.

Work in the years proceeding Klein's collocation solution, also treats uni-axial in-plane compression as well shear loading and has been described in the preceeding section. However, more recently, Xiang, Wang and Kitipornchai [110] considered shear loading to plates in isolation. In addition to presenting solutions for classically thin plates, they also considered plates that are thick enough to be affected by shear deformation. The analysis shows that there is a significant decrease in buckling strength of the plate when shear deformation is accounted for.

To complete the discussion on shear loading, Tables 3.1 on page 52 and 3.2 on page 53 assimilate the buckling strength predictions for shear loaded skew plates in a similar manner to that for uni-axial compression given in Tables 4.3 on page 64 and 4.2 on page 63. Tables 3.1 and 3.2 give buckling predictions for plates with simply supported and clamped boundary conditons respectively for both positive and negative shear and the 'O' and 'P' cases previously described.

For a comparison with the skew plate cases, Timoshenko [88] gives the critical buckling coefficient of a square, simply supported, shear loaded plate as $k = 9.34 = (\tau b^2 t)/(\pi^2 D)$.

3.2.1 Discussion of shear buckling results

The shear buckling results assimilated from the literature showing critical elastic buckling loads of skew plates under shear loading in Tables 3.1 (simply supported boundary conditions) and 3.2 (clamped boundary conditions) show that negative 'O' type shear is stronger in buckling than positive 'O' type shear and that positive 'P' type shear is stronger in buckling than negative 'P' type shear.

The results in the tables show that, especially for the highest skew angle, there is often little agreement on the buckling load. The reasons for this are lack of convergence in the solution and satisfying boundary conditions. Convergence to a solution decreases with an increase in skew angle and explains the larger discrepancies for the higher skew angles. In addition, authors (*e.g.* Wittrick [106]) have found that convergence is obtained more readily for positive shear than negative shear for 'O' type loading.

Considering the simply supported buckling results (Table 3.1): type 'O' was considered by Xiang *et al.* [110], Durvasula [27], Kennedy and Prabhakara [46], Argyris [7] (positive shear only) and Wang [97] (negative shear only). The results by Durvasula [28], produced using a Raleigh–Ritz formulation with eighteen terms give the highest buckling predictions of the set, this upper–bound is improved on by Kennedy and Prabhakara for negative shear using the first nine harmonics of a double Fourier series. For Kennedy and Prabhakara's positive shear buckling case, the boundary conditions have not been correctly satisfied and the resulting buckling predictions are very low. Xiang *et al.* used a $pb-2$ Raleigh-Ritz method for all the simply supported loading cases and the results for $a/b = 1$ compare favourably (within +0.2% for $\alpha = 15° - 45°$) with Wang's [97] buckling predictions obtained using Raleigh-Ritz B-spline analysis with 8 B-spline sections. Wang's solution for this simply supported case was well converged (better than 1%). Argyris' [7] lower–bound coarse finite element solution agrees with the positive shear results of Xiang *et al.* to within 3%.

The simply supported 'P' type shear loading shows good agreement (better than 1% difference) between Xiang *et al.* and Fried and Schmitt's [32] finite element solution (using a 14×14 mesh of 16 degree–of–freedom elements). For the negative shear, further confirmation of the Xiang *et al.* and Fried and Schmitt solutions are provided by Mizusawa *et al.* . The Yoshimura and Iwata solution was obtained using a five term Raleigh–Ritz method and clearly is not converged, with better results given for the positive shear case. Comparison with the other authors suggests that the negative shear case results are too high. The results of Yoshimura and Iwata represent the first set of simply supported for 'P' type loading and could therefore not have been verified against other work.

Considering the clamped results (Table 3.2): type 'O' buckling results by Wittrick [106] (positive only), Ashton [8] (positive only), Durvasula [27], Wang [97] (negative only) and York [112] are compared. The positive shear results are in close agreement with the exception of Ashton's predictions which are given to two significant factors obtained using a Raleigh–Ritz formulation with three terms and therefore provide an upper–bound solution. Wittrick's [106] prediction was obtained using the Galerkin method with eight terms, he was unable to obtain a converged solution using twelve terms for the opposite, negative shear case. The buckling predictions produced by Durvasula were produced using the Galerkin method with eighteen terms and compare very well (within 0.2%) with those produced using VICONOPT (see section 2.5) by York [112] for the positive shear case. For negative loading, as predicted by Wittrick's findings when attempting to produce buckling solutions for this case, the buckling stresses given by Durvasula are higher than those of both York [112] and Wang [97] (using Raleigh–Ritz B–spline method as described previously). The difference is due to a lack of convergence which the author noted and is especially apparent when $a/b = 0.5$ where there is a difference of 38.3% between York's and Durvasula's predictions.

Type 'P' shear loading buckling predictions for clamped plates were produced by Fried and Schmitt [32], Hamada [39], Mizusawa [66] (negative shear only) and Hasegawa [40] (positive shear only). The results of Fried and Schmitt have been shown to be accurate for the other cases considered and they compare well with Hamada's eight term Raleigh–Ritz solution for the positive shear case. Hamada's results are 0.7% higher than Fried and Schmitt's for both skew angles. For the negative case Hamada's results differ from Fried and Schmitt's by 0.6% for $\alpha = 15°$ and 15% for $\alpha = 30°$. Fried and Schmitt's buckling prediction for plates with $\alpha = 45°$ and negative shear compare well with Mizusawa's. The positive shear predictions by Hasegawa were obtained with a five term Raleigh-Ritz method and comparison with Hamada and Fried and Schmitt shows that they are not converged, with the discrepancy between the published results increasing with an increase in skew angle.

Table 3.1: Buckling strength of simply supported skew plates. The buckling load is given as the buckling strength coefficient, $k = (\tau b^2 t)/(\pi^2 D)$. Results for both the 'O' (orthogonal shear loading) and 'P' (parallel loading) cases are presented (see Figure 3.3 on page 48).

	$\alpha = 15°$				$\alpha = 30°$				$\alpha = 45°$				
	+ shear		− shear		+ shear		− shear		+ shear		− shear		
a/b	O	P	O	P	O	P	O	P	O	P	O	P	Author
0.5	6.94	—	—	—	—	—	—	—	—	—	—	—	Kennedy and Prabhakara [46]
	—	—	—	—	—	—	—	—	—	—	—	14.16	Mizusawa *et al.* [66]
	13.21	—	—	—	9.74	—	—	—	11.17	—	—	—	Kennedy and Prabhakara [45]
1.0	7.539	14.62	12.12	6.835	7.150	26.87	16.08	5.778	9.35	61.541	22.87	5.794	Xiang *et al.* [110]
	7.61	—	12.4	—	7.54	—	17.1	—	10.7	—	27.7	—	Durvasula [28]
	—	—	—	—	7.07	—	—	—	9.04	—	—	—	Argyris [7]
	—	—	—	—	—	—	—	—	—	—	—	5.804	Mizusawa *et al.* [66]
	6.94	—	14.38	—	—	—	17.24	—	—	—	25.27	—	Kennedy and Prabhakara [46]
	7.39	—	—	—	6.63	—	—	—	7.85	—	—	—	Kennedy and Prabhakara [45]
	—	—	12.1156	—	—	—	15.0714	—	—	—	22.8174	—	Wang [97]
	—	14.637	—	6.841	—	26.927	—	5.791	—	61.648	—	5.845	Fried and Schmitt [32]
	—	14.800	—	7.050	—	30.700	—	6.700	—	63.610	—	9.380	Yoshimura and Iwata [118]
1.5	—	—	—	—	—	—	—	—	—	—	—	4.554	Mizusawa *et al.* [66]
	6.95	—	—	—	7.19	—	—	—	8.58	—	—	—	Kennedy and Prabhakara [45]
	—	10.905	—	5.287	—	19.782	—	4.553	—	44.790	—	4.568	Fried and Schmitt [32]
2.0	—	—	—	—	—	—	—	—	10.01	39.353	12.59	4.043	Xiang *et al.* [110]
	—	—	—	—	—	—	—	—	11.2	—	13.8	—	Durvasula [28]
	6.34	—	—	—	6.68	—	—	—	8.47	—	—	—	Kennedy and Prabhakara [45]
	—	9.910	—	4.831	—	17.656	—	4.074	—	39.388	—	4.052	Fried and Schmitt [32]

Table 3.2: Buckling strength of clamped skew plates. The buckling load is given as the buckling strength coefficient, $k = (\tau b^2 t)/(\pi^2 D)$. Results for both the 'O' (orthogonal shear loading) and 'P' (parallel loading) cases are presented.(see Figure 3.3 on page 48)

	$\alpha = 15°$				$\alpha = 30°$				$\alpha = 45°$				
	+ shear		− shear		+ shear		− shear		+ shear		− shear		
a/b	O	P	O	P	O	P	O	P	O	P	O	P	Author
0.5	—	—	—	—	—	—	—	—	—	—	—	27.87	Mizusawa *et al.* [66]
	34.58	—	55.36	—	31.58	—	76.90	—	40.54	—	128.3	—	Duravasula [27]
	34.831	—	48.634	—	31.478	—	62.993	—	40.442	—	92.76	—	York [112]
1.0	—	—	—	—	—	—	—	—	24.32	—	—	—	Wittrick [106]
	—	—	—	—	—	—	—	—	—	—	—	9.24	Mizusawa *et al.* [66]
	—	—	16.9644	—	—	—	21.9026	—	—	—	31.5207	—	Wang [97]
	15	—	—	—	17	—	—	—	25	—	—	—	Ashton [8]
	—	22.28	—	11.0	—	39.92	—	10.760	—	—	—	—	Hamada [39]
	—	22.13	—	10.933	—	39.640	—	9.360	—	88.725	—	9.250	Fried and Schmitt [32]
	—	23.1748	—	—	—	46.3245	—	—	—	—	—	—	Hasegawa [40]
	14.39	—	17.24	—	16.66	—	23.64	—	24.08	—	32.56	—	Durvasula [27]
	14.406	—	17.175	—	16.629	—	22.173	—	24.042	—	31.650	—	York [112]
1.5	—	—	—	—	—	—	—	—	—	—	—	7.26	Mizusawa *et al.* [66]
	12.01	—	12.73	—	14.05	—	15.19	—	20.21	—	22.37	—	Duravasula [27]
	—	17.126	—	8.736	—	30.259	—	7.419	—	66.980	—	7.290	Fried and Schmitt [32]
	12.047	—	12.291	—	14.032	—	15.104	—	20.177	—	21.911	—	York [112]
2.0	10.84	—	11.10	—	13.34	—	13.73	—	19.24	—	20.35	—	Duravasula [27]
	—	15.478	—	7.753	—	27.577	—	6.764	—	61.308	—	6.754	Fried and Schmitt [32]
	10.836	—	11.088	—	13.307	—	13.624	—	19.185	—	19.860	—	York [112]

Chapter 4

The Buckling Strength of Uni-axial Compression Loaded Skew Plates with Elastic Rotational Edge Restraint

4.1 Introduction

In most buckling studies of both rectangular and skew plates, the adopted boundary conditons are generally assumed to be either simply supported, clamped, free or combinations of these. Although these boundary conditons are useful because they provide upper- and lower- bound buckling predictions to a more general problem, they lead to loss of economy in design, because they do not permit the benefits of restraint and continuity to be included safely in the design process. In real structures there is continuity between adjacent panels and other structural elements which offer bending and torsional stiffness to the plate edges.

This chapter presents a parametric study showing the buckling strength increases resulting from rotational restraint along the edges of a skew plate. The buckling strength of the plates is presented as a series of compact and comprehensive buckling curves that can be used for plate sizing.

Comparison is made with the limited results that address the effect of a rotational restraint applied along the transverse edges of skew plates by Mizusawa [64] and with continuous plate buckling predictions from the open literature.

4.2 Background

The background to the buckling analysis of skew plates with simply supported and fully clamped boundary conditons is considered in chapter 3. This section considers the background relating the addition of rotational restraint and continuity in plate analysis.

Rotational restraint arises along the edges of a plate from two causes: the torsional stiffness of a supporting spar, rib or stiffener and by continuity over a simple support which is assumed to possess no rotational stiffness. In the case of an elastic plate, superposition can be used to determine the correct rotational stiffness to be used in analysis.

Rotational restraint due to continuity of a structure over otherwise simple supports is observed in the analysis of infinite arrays of classically thin skew plates. It arises because rotations occur normal to the skew transverse edge. Consequently, there is rotation in both global axes along the skew edge and adjacent plates provide some fixity along it. In the case of square or rectangular plate, edge rotations (which occur only in the global axis normal to the plate edge) are the same regardless of whether the plate is isolated or a bay in an infinite array of plates continuous over otherwise simple supports and no buckling strength increases are observed.

The earliest studies of plate buckling with rotational edge restraint considered infinitely long, rectangular plates in compression and were carried out by Lundquist and Stowell [56, 57] and Batdorf *et al.* [11]. The rotational stiffness was assumed to be due to an infinitely stiff supporting spar, rib or plate stiffener and the analysis was based on an exact solution of the governing plate differential equations. Related work by Anderson and Semonian [6] used an energy method, Budinasky and Hu [18] used an energy method incorporating Lagrangian multipliers and Lundquist *et al.* [58], the energy method and an application of the moment distribution method. These analyses provided a series of design curves for compression loaded plates continuous over two, three and an infinite number of transverse bays with supporting stiffeners that provide for either flexural of torsional stiffness. Stowell and Schwartz [83] added to the pure in-plane compression results by producing buckling curves for infinite strips under combined loadings of uni-axial in-plane compressive stress and shear using an energy method.

More recent studies, presented by Bank and Jiansheng Jin *et al.* [9] have produced buckling solutions using a solution of the governing equations to determine the critical buckling loads of plates having one rotationally restrained longitudinal edge, the other free and both transverse edges simply supported. Square, orthotropic plates are considered and buckling curves presented which show the relationship between buckling strength and rotational stiffness and different orthotropy.

Paik and Thayamballi [71] used an approximate method to solve the governing equations of equilibrium for rectangular plates having stiffeners running along the longitudinal or transverse edges. The stiffeners were used to provide the rotational restraint. Buckling design curves are presented that show the buckling load of the plates as the plate aspect ratio and the polar second moment of area of the stiffener increases. The plate assemblies are loaded under a uniform in-plane compressive stress.

Initial post-buckling response of rectangular thin-plates with rotational restraint applied along the edges has been studied by Rhodes and Harvey [76] and more recently by Khong and Ong [47]. Both sets of authors present curves of end–shortening against applied load.

4.3 Modeling

The following section describes the parameters of a parametric study carried out to establish the buckling strength of isolated skew plates with varying magnitudes of rotational restraint applied along the plate edges. The results are compared with buckling solutions for plates that are continuous in either the longitudinal or both longitudinal and tranverse direction. The parameters of the study are: skew angle; plate aspect ratio; and degree of rotational stiffness.

Eigenvalue extraction is performed using ABAQUS finite element code to determine the elastic buckling strength of the plates. In the case of the continuity, comparison is made with results that are available in the open literature by York [112] using VICONOPT and Anderson [5].

Because a classical thin-plate buckling solution (through-thickness shear deformation is ignored) is desired, a type S8R5 element [3] (see Appendix A) is used in all the subsequent finite element analysis. A high mesh density is used to account for the high stresses [66] that develop at the obtuse corners of the skew plate as opposed to biasing the mesh towards these corners to simplify loading input. Following a careful mesh convergence study, a mesh of 30 × 30 elements gives buckling predictions within 1% of the converged value. The same mesh density is used for the remainder of the analysis, hence the number of elements in each plate increases proportionally with aspect ratio (*i.e.* a 30 × 45 mesh is used for $a/b = 1.5$).

Results of a mesh convergence study for the S8R5 element are reproduced in Table 4.1.

4.3.1 Plate geometry

The plates are loaded under a uniform, in-plane compressive stress applied to the skew, transverse edges of the plate.

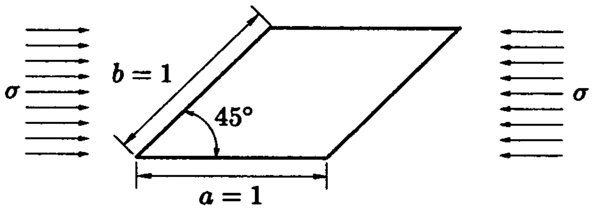

Mesh	10 x 10	20 x 20	30 x 30	40 x 40	60 x 60
D.O.F.	4205	17405	39605	79805	160205
$k = (\sigma b^2 t)/(\pi^2 D)$	9.986	9.686	9.672	9.669	9.669
Difference (%)	—	3.097	1.447	0.03	0.000

Table 4.1: Results of convergence for a skew plates with $a/b = 1$ and $\alpha = 45°$. The meshes used are all uniform. The 'Difference (%)' row shows the percentage difference between each successive mesh refinement.

The plate geometry is modified in two ways:

1. the skew angle of the plate is either 15°, 30° of 45°. The definition of skew angle is given graphically in Figure 4.1.
2. the aspect ratio of the plate a/b is varied in the range $0.5 \leq a/b \leq 2.5$. The definition of a and b is graphically shown in Figure 4.1.

Material properties for the plate are consistent with aluminium plate [15] and taken as: Young's modulus, $E = 72.4 \times 10^3 Nmm^{-2}$ and Poisson's ratio, $v = 0.3$. These choices, particularly pertaining to aspect ratios and skew angles, allow direct comparisons to be made with existing literature on the stability of skew plates and the published solutions for continuous skew plates [5, 112].

A note on the definition of aspect ratio

The choice of definition for aspect ratio is chosen so that comparisons can be made with existing results, which are generally presented with plate aspect ratio defined in the manner of Figure 4.1 *i.e.* one in which the breadth of the plate is measured parallel to the skew, transverse edge. The definition of plate aspect ratio as is, leads to a decrease in the planform area of plates, with the same aspect ratios, as the skew angle of the plate increases because its transverse width decreases. The planform area of the plate, $A = a \times b \cos\theta$. A comparison of the results obtained using this definition and one of constant planform area is considered in Section 4.6.

4.3.2 Boundary Conditions

Figure 4.1 shows schematically all the boundary condition cases considered in the study as well as the nomenclature used to define the plates. Gaps in the figure correspond to boundary condition cases which are either not considered or continuity cases that have not been published in the open literature.

Boundary conditions are taken to be the same on opposing edges of the plate and all the possible combinations of simply supported, clamped and elastic rotational restraint are considered. Therefore, a total of 9 cases are considered including those cases that have the same boundary conditions on all four edges. Continuity results are available for two cases: skew transverse edges continuous and longitudinal edges simply supported [112]; and both skew transverse and longitudinal edges continuous [5, 112]. Hereinafter these two cases will be termed '*uni-axially continuous*' and '*bi-axially continuous*' respectively. These two boundary condition cases take the total number of cases in the study to be 11. Each combination is given a notation Case $x - y'$ in which the x refers to the boundary condition along the longitudinal edge of the plate and y' the boundary condition along the skew, transverse edge of the plate. Rotations are considered normal to this edge. x and y' take a number 1-4 corresponding to:

1. simply supported edge (free rotation);
2. elastic rotationally restrained edge;
3. continuous edge (published continuous results);
4. clamped edge (no rotation).

Thus Case 1-1 refers to a plate having all edges simply supported; Case 1-2 to a plate having simply supported longitudinal edges and elastic rotationally restrained skew, transverse edges; Case 1-3 to a plate having uni-axial continuity and Case 1-4 to a plate with simply supported longitudinal edges and clamped skew, transverse edges.

4.3.3 Elastic rotational restraint

The elastic rotational restraint applied to the plate edges in the applicable boundary condition cases is modelled in ABAQUS using linear elastic, type SPRING1 [3], elements (1 per element along the edge being studied). The springs have rotational degrees of freedom aligned along the plate edge. The use of a constant magnitude of rotational stiffness along the plate edge is an over simplification regarding the actual

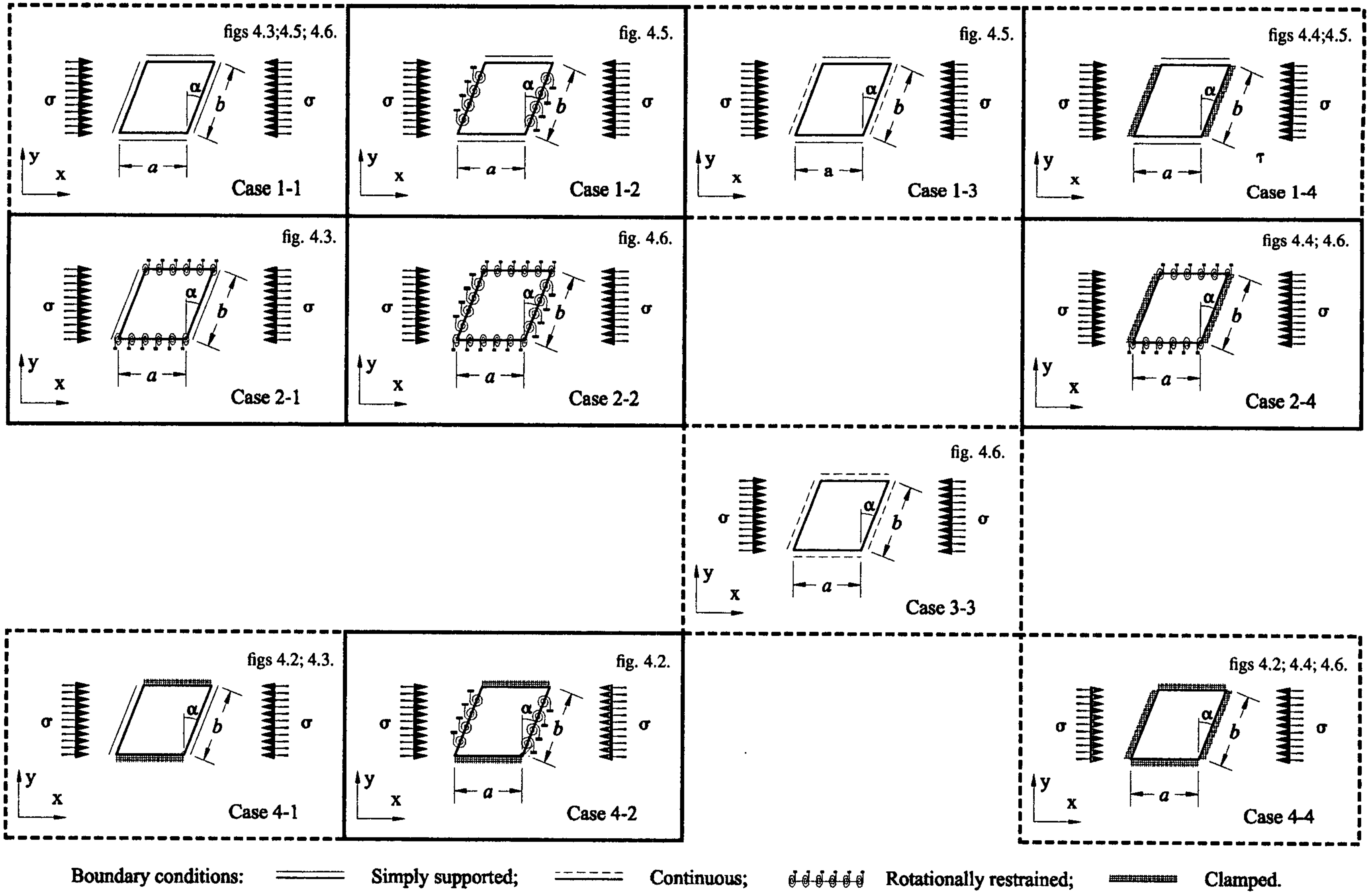

Figure 4.1: Plate geometry showing skew angle, α, side lengths a, b, principal axis system and applied uniform, uniaxial compression loading. The figure also provides a key for boundary condition cases and associated identifying nomenclature. The figure number in the top right-hand corner of each schematic correspond to the figure containing the buckling curves associated with the boundary condition shown.

rotational restraint that might be applied to a plate edge by the torsional stiffness of a beam (or likewise a supporting spar, rib or stiffener). A supporting spar or rib unless it is very stiff and has firm supports, will impose a varying rotational stiffness along the plate edge [56].

Rotational restraint is applied in discrete magnitudes described using a non-dimensional 'rotational stiffness coefficient, κ.

$$\kappa = \frac{\beta b}{D} \tag{4.1}$$

where:

β $= M/\theta =$ moment per unit rotation per unit length or spring stiffness per unit length along the plate edge. M and θ are moments and rotation occurring normal to the plate edge respectively;

b is the skew, transverse plate width;

D is the flexural rigidity of the plate given by $(Et^3)/12(1-\nu^2)$.

Buckling strength predictions are calculated for seven discrete values of $\kappa = 0.2, 0.4, 1.0, 2.0, 4.0, 10, 20$. Simply supported and clamped edges which are also modelled correspond to $\kappa = 0.0$, $\kappa = \infty$ respectively.

4.3.4 Definition of Buckling Coefficient

The elastic buckling load is defined using a dimensionless coefficient, k

$$k = \frac{\sigma b^2 t}{\pi^2 D} \tag{4.2}$$

where:

σ is the critical buckling stress;

b is the plate width;

t is the plate thickness;

D is the flexural rigidity of the plate.

4.3.5 Model Verification

An extensive collection of previously published buckling predictions for the elastic buckling strength of simply supported and clamped plates is presented together with the current ABAQUS results in Tables 4.1 and 4.2 as an exercise in model verification. The comparison results are, in general, exhaustive of the buckling predictions to be found in the open literature. Current results compare well, but it is obvious that as the skew angle of the plates increases, the range of the results reported also increases and the buckling predictions become increasingly uncertain, especially for the simply supported boundary condition case

The wide range of results can be attributed to not satisfying boundary conditions (by choice of deflection function for example) and lack of convergence to a solution. Convergence to a solution is more difficult, requiring larger meshes or terms in deflection series as the skew angle of a plate increases because of the large stress concentrations that occur in the obtuse corners of the plate.

Simply supported results

The results of Thangam Babu and Reddy [87] are, by the authors' own admission in large error and could be improved by increasing the order of the finite strip used to calculate them. The results of Durvasula [28] and Yoshimura and Iwata, both calculated using the Raleigh-Ritz method, are also in error and suffered from convergence problems using 11 and 5 terms in the deflection series respectively.

The remaining results fall into two categories those by Kennedy and Prabhakara [46], Krishna Reddy and Palaninathian [53] and Mizusawa *et al.* [66] who report buckling values for plates with $a/b = 1.0$ and $\alpha = 45°$ in the range $k = 8.47 - 8.643$ and the other authors who report buckling factors between $k = 10.2 - 10.60$. Variation within the two sets can be explained by a lack of convergence. The reasons for the apparent discrepancies may be attributable to the latter authors not satisfying the boundary condition of zero moment normal to the plate edges in the obtuse corners of the plate. Mizusawa [66] and Wang *et al.* [94] considered the effect of the obtuse corner conditions that satisfy the singularity of zero moment and zero slope at the obtuse corners of the plate by providing two buckling solutions for a skew plate. In the Mizusawa *et al.* case, a solution was obtained using the B-Spline Raleigh-Ritz method with boundary conditions satisfied Lagrangian multipliers resulting in there being zero moment in the obtuse plate corners [65]. They reported a buckling factor of 8.643 for $a/b = 1.0$ with$\alpha = 45°$. The alternative solution used the B-Spline method and a series of springs to impose the boundary conditions giving $k = 10.22$ which agrees well with second set of authors (a buckling prediction obtained using more knots and B-Splines of six degrees gave $k = 9.886$ for the same plate [66]). In this latter analysis, the condition of zero slope at the obtuse corners of the plate was maintained by fixing them against rotation and a moment was imposed at the obtuse plate corners. Wang *et al.* [94] used the Raleigh-Ritz method with pb-2 Ritz functions to determine buckling loads for skew plates with two corner conditions: type I in which the obtuse corners were free to rotate and type II in which the conditon of zero moment and zero slope was satisfied. The results are different from Mizusawa *et al.* [66, 65] however with the type I buckling load for a plate with $a/b = 1.0$ and $\alpha = 45°$ of $k = 9.87$ and a type II buckling load for the same plate of $k = 10.6$. The results by Mizusawa appear more consistent with those published by the other authors.

The ABAQUS results buckling results compare well with other authors for the two lower values of skew angle especially with Wang [97], Wang *et al.* [93] and Fried and Schmitt [32]. For the 45° case, the ABAQUS results are lower than the Fried and Schmitt and Wang results which is attributed to the boundary condition that imposed no rotational restraint at any of the four plate corners.

The ABAQUS results are also verified against the closed-form solution derived by Anderson [5] for a simply supported skew plate with $a/b = 1.0$ and a uni–axial in-plane loading acting normal to the skew edge in section 2.4 . There is an error of less the 0.1% between the closed-form solution and the ABAQUS buckling prediction. None of the authors said that they had tested their models against Anderson's solution.

Clamped boundary conditions

The observation that boundary conditions are the most likely cause of the wide variation in buckling solutions for simply supported plates is supported by the buckling predictions for clamped plates. For this boundary condition case, there is no ambiguity regarding the boundary conditions to be satisfied. High buckling predictions can be explained by a lack of convergence e.g. those results by Ashton [8] and Wittrick [105]. The ABAQUS results in this case lie at the low end of the buckling predictions for all the skew angles, which is consistent with the highly converged solution presented. The ABAQUS results lie within 1% of those by York [112], Wang [97], Wang *et al.* [93], Sarath Babu and Kant [79], Mizusawa *et al.* [66], Jaunky *et al.* [44] and Fried and Schmitt [32] for all the skew angles at $a/b \geq 1$. Convergence issues may explain the higher differences observed for $\alpha = 45$ at $a/b = 0.5$.

4.4 Results

The critical buckling load of plates having aspect ratios increasing in increments of $0.1a/b$ over the range $0.5 \leq a/b \leq 2.5$ are calculated.

Table 4.2: Comparison of critical buckling coefficients for Case 1-1 (all edges simply supported) skew plates under a uniform uni-axial compression load. Note that the results in the table for Wang [97] also appear in reference [96].

	$\alpha = 15°$				$\alpha = 30°$				$\alpha = 45°$				
Aspect Ratio	0.5	1.0	1.5	2.0	0.5	1.0	1.5	2.0	0.5	1.0	1.5	2.0	Method
Argyris [7]	-	-	-	-	-	6.410	-	-	-	9.7	-	-	2
Durvasula [28]	7.070	4.480	4.770	4.430	10.400	6.410	6.370	6.030	21.400	12.300	10.900	10.300	1
Fried & Schmitt [32]	6.982	4.395	4.678	-	9.943	5.912	4.796	-	18.908	10.216	12.275	-	2
Jaunky *et al.* [44]	-	4.402	-	-	-	6.009	-	-	-	10.836	-	-	1
Kennedy & Prabhakara [46]	6.940	4.330	4.620	4.270	9.600	5.530	5.580	5.200	17.170	8.470	7.890	7.680	5
Krishna Reddy & Palaninathan [53]	-	4.32	-	-	-	5.55	-	-	-	8.64	-	-	2
Mizusawa *et al.* [66]	-	4.336	-	-	-	5.612	-	-	-	8.643	-	-	3
Mizusawa *et al.* [65]	-	-	-	-	-	-	-	-	19.300	10.220†	12.280	-	3
Mizusawa *et al.* [64]	7.000	4.410	4.700	4.360	10.020	6.030	6.030	5.730	19.550	10.750	9.640	9.340	3
Mukhopadhyay & Mukherjee [69]	-	4.77	-	-	-	6.169	-	-	-	10.22	-	-	2
Sarath Babu & Kant [79]	-	4.400	-	-	-	5.920	-	-	-	10.230	-	-	2
Tham & Szeto [86]	-	4.40	-	-	-	5.93	-	-	-	10.36	-	-	4
Thangam Babu & Reddy [87]	-	4.906	-	-	-	8.896	-	-	-	24.018	-	-	4
Wang *et al.* [94] (type I corner)	-	4.39	-	-	-	5.98	-	-	-	10.60	-	-	5
Wang *et al.* [94] (type II corner)	-	4.44	-	-	-	6.190	-	-	-	10.60	-	-	5
Wang *et al.* [98]	-	4.39	-	-	-	5.87	-	-	-	9.79	-	-	6
Wang [97]	-	4.3938	-	-	-	5.8964	-	-	-	10.1029	-	-	3
Yoshimura & Iwata [118]	-	4.538	-	-	-	6.489	-	-	-	12.840	-	-	1
CURRENT	6.972	4.390	4.676	4.339	9.869	5.854	5.894	5.591	18.905	9.672	8.946	8.796	2

Key to method:

1, Raleigh–Ritz; 2, Finite element method; 3, B-Spline Raleigh–Ritz; 4, Spline finite strip; 5,Raleigh–Ritz pb-2; 6, Differential Quadrature.

† $k = 9.886$ using higher order B-splines in reference [66].

Table 4.3: Comparison of critical buckling coefficients for Case 4-4 (all edges clamped) skew plates under a uniform uni-axial compression load. Results for Wang [97] are reproduced in reference [96]. The lower-bound solution given by Guest [38] is reproduced in reference [37].

	$\alpha = 15°$				$\alpha = 30°$				$\alpha = 45°$				
Aspect Ratio	0.5	1.0	1.5	2.0	0.5	1.0	1.5	2.0	0.5	1.0	1.5	2.0	Method
Argyris [7]	-	-	-	-	-	13.8	12.3	-	-	20.4	18.0	-	2
Ashton [8]	-	11.010	-	-	-	13.790	-	-	-	20.616	-	-	1
Durvasula [27]	21.630	10.870	8.971	8.700	-	13.580	-	-	55.26	20.440	17.100	15.740	1
Fried & Schmitt [32]	21.546	10.813	8.913	-	31.034	13.507	11.004	-	55.946	20.075	16.247	-	1
Guest (Upper-bound) [37]	-	-	-	-	-	13.89	-	-	-	21.6	-	-	1
Guest (Lower-bound) [38]	-	-	-	-	-	13.53	-	-	-	20.7	-	-	1
Jaunky *et al.* [44]	-	10.838	-	-	-	13.548	-	-	-	20.616	-	-	2
Krishna Reddy & Palaninathan [53]	-	10.76	-	-	-	13.64	-	-	-	20.62	-	-	2
Mizusawa *et al.* [66]	-	-	-	-	-	13.51	-	-	-	20.08	-	-	3
Mukhopadhyay & Mukherjee [69]	-	10.93	-	-	-	14.00	-	-	-	21.70			2
Sarath Babu & Kant [79]	-	10.84	-	-	-	13.54	-	-	-	20.12	-	-	2
Tham & Szeto [86]	-	10.84	-	-	-	13.60	-	-	-	20.76	-	-	4
Wang *et al.* [94]	-	10.89	-	-	-	13.75	-	-	-	20.69	-	-	5
Wang *et al.* [98]	-	10.84	-	-	-	13.54	-	-	-	20.23	-	-	6
Wang [97]	-	10.8347	-	-	-	13.5383	-	-	-	20.1225	-	-	3
Wittrick [105]	-	-	-	-	-	13.64	11.34	-	-	21.64	19.40	-	1
York [112]	21.634	10.853	8.959	8.407	29.950	13.581	11.061	10.311	54.674	20.207	16.303	15.181	7
CURRENT	21.541	10.832	8.931	8.385	30.214	13.531	11.025	10.279	54.050	20.065	16.239	15.142	2

Key to method:
1, Raleigh–Ritz; 2, Finite element method; 3, B–Spline Raleigh–Ritz; 4, Spline finite strip; 5,Raleigh–Ritz pb-2; 6, Differential Quadrature; 7, VICONOPT.

The results of the analysis are presented as a series of design curves in Figures 4.2 to 4.6. Each of the figures showing the buckling curves contains three graphs corresponding to one of the three skew angles used for the study. A schematic of the boundary condition relevant to the buckling curves is included in the figure. The curves show the buckling coefficient of the plate as a function of aspect ratio. Each figure has nine curves corresponding to the 9 magnitudes of elastic rotational stiffness applied to the plate edge. In all the curves, the range of the ordinate in each case is constant, however because it appears that there is a buckling strength increase with increasing skew angle, the minimum buckling coefficient shown is changed to preserve clarity. The curves are in the classic 'garland' [20, page 29] form. The cusps correspond to critical buckling modes with 'n' half-wavelengths and '$(n + 1)$' half-wavelengths that have coincident buckling loads and aspect ratio. Hence this cusp marks the aspect ratio at which there is a change in critical buckling mode.

The figures are ordered according to the critical upper– and lower– boundary conditon case. Figures 4.2 (Case 4-2: clamped skew, transverse edges and rotationally restrained longitudinal edges) and 4.4 (Case 2-4: rotationally restrained longitudinal edges and clamped skew, transverse edges) both contain curves for the upper-bound (all four edges clamped) solution. The lower–bound solutions for these boundary conditon cases are Case 4-1 and Case 1-4 and give the upper-bound curves for Case 2-1 and Case 1-2 respectively. These nesting qualities give the order of the figures, which when combined enable the study of plate stability when a fully clamped plate has rotational restraint removed in discrete magnitudes from one pair of opposite edges until it is simply supported and then the other pair. The lower curve on each of Figures 4.5 and 4.3 is equivalent to Case 1-1 (all four edges simply supported) in both cases.

The cusp location on the buckling curves is found by drawing a spline curve through the buckling loads determined from the analysis that correspond to the same buckling mode. The derived curves are then 'cropped' above the buckling coefficients at which these curves intersect. Further buckling analyses were made around the location of these cusps to verify their location to be correct.

Figure 4.7 shows typical buckling modes for a skew plate given by the lower– and upper– bound solution to boundary condition Case 2-1 and an intermediate magnitude of rotational stiffness ($\kappa = 20$) for $a/b = 1.9$, $\alpha = 30°$. The critical buckling modes in this case comprise two half-wavelengths, three half-wavelengths and four half-wavelengths as two, three and four cusps on the buckling curves are passed on to reach $a/b = 1.9$ respectively.

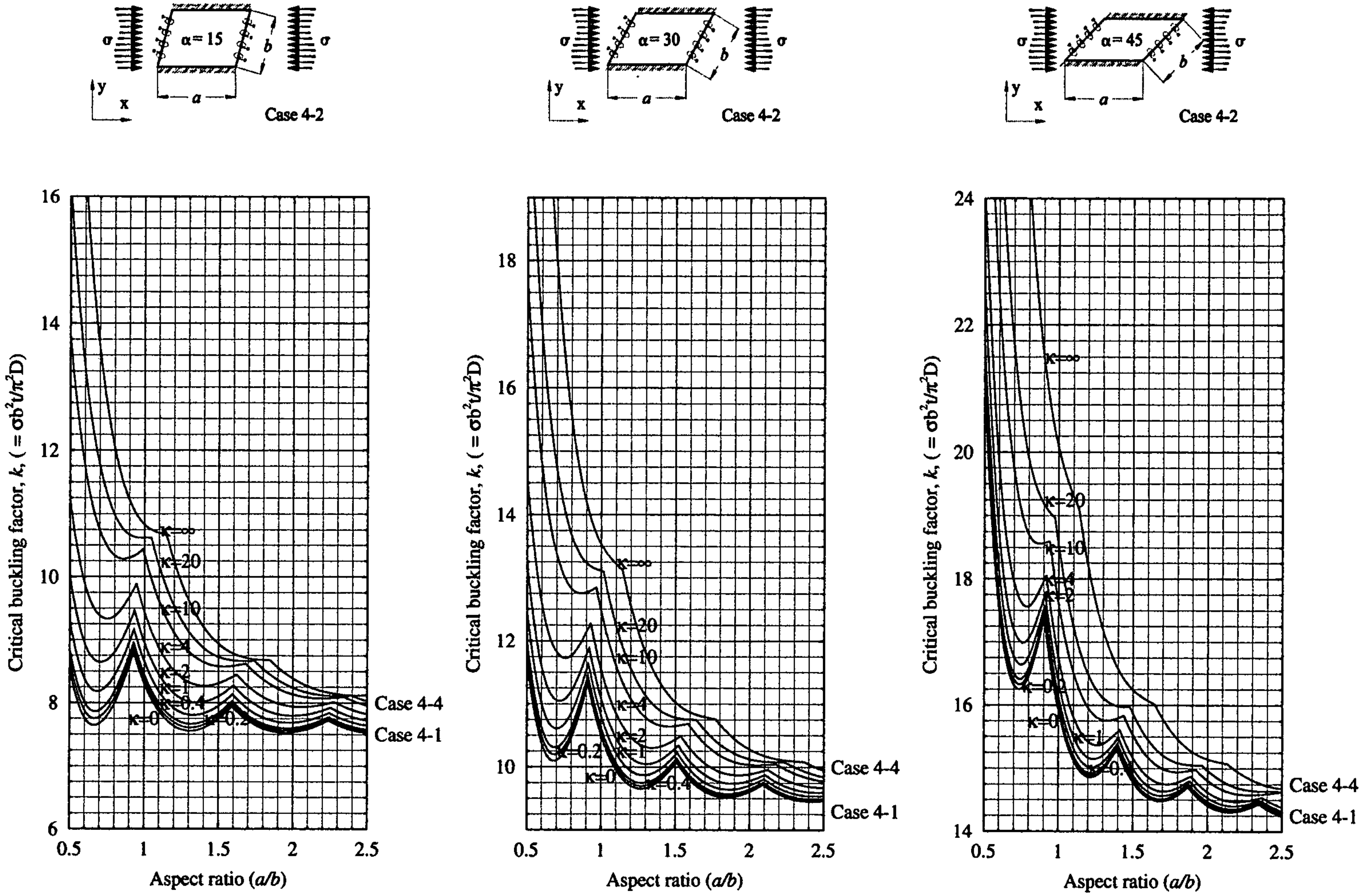

(a) $\alpha = 15°$

(b) $\alpha = 30°$

(c) $\alpha = 45°$

Figure 4.2: Case 4-2, design curves for plates with skew angle $\alpha = 15° (a), 30° (b) \& 45° (c)$, having loaded, skew transverse edges elastically restrained against rotation and longitudinal edges clamped.

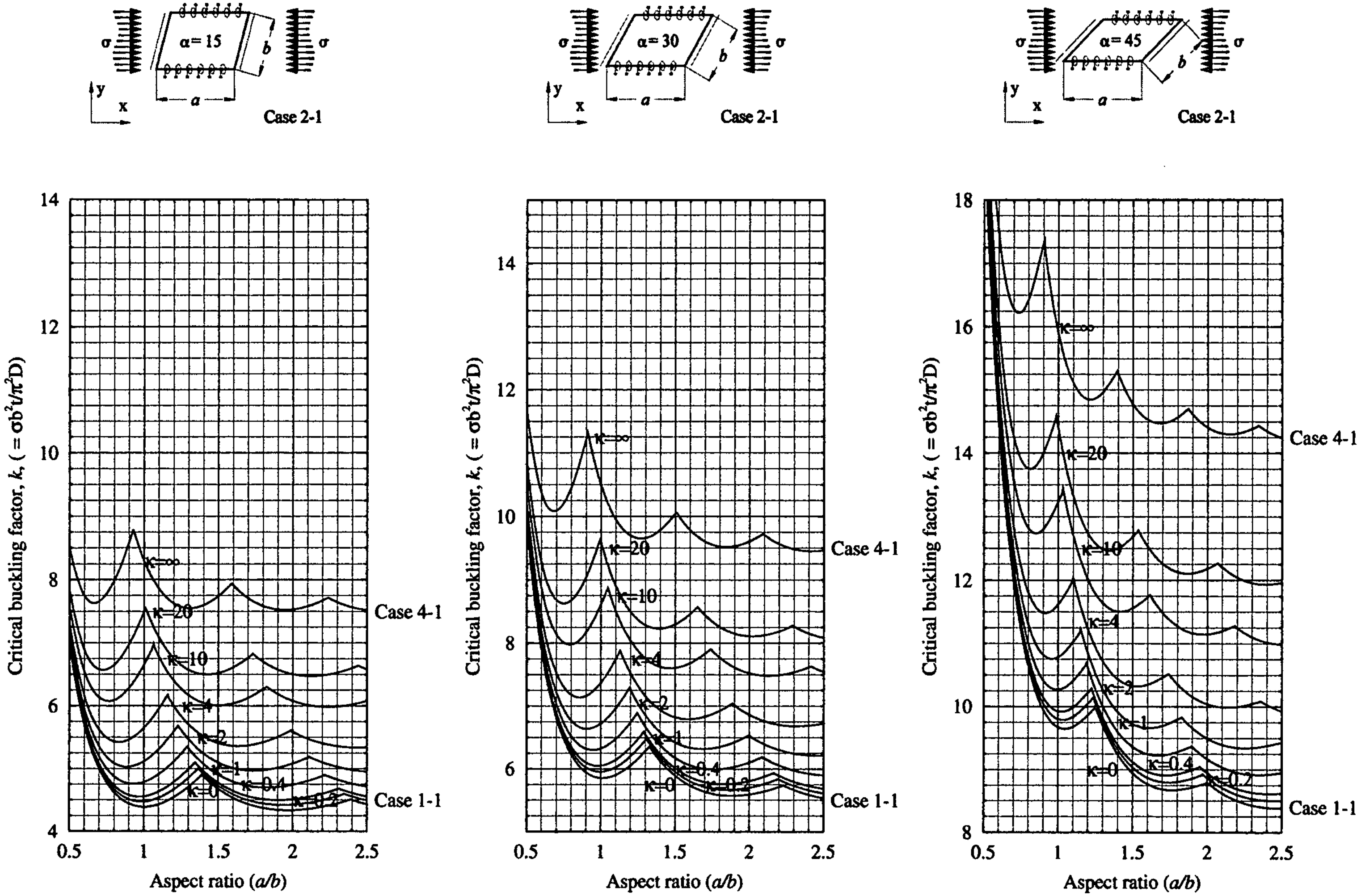

(a) $\alpha = 15°$ (b) $\alpha = 30°$ (c) $\alpha = 45°$

Figure 4.3: Case 2-1, design curves plates with skew angle $\alpha = 15°$ (a), $30°$ (b) & $45°$ (c), having loaded, skew transverse edges elastically restrained against rotation and longitudinal edges simply supported.

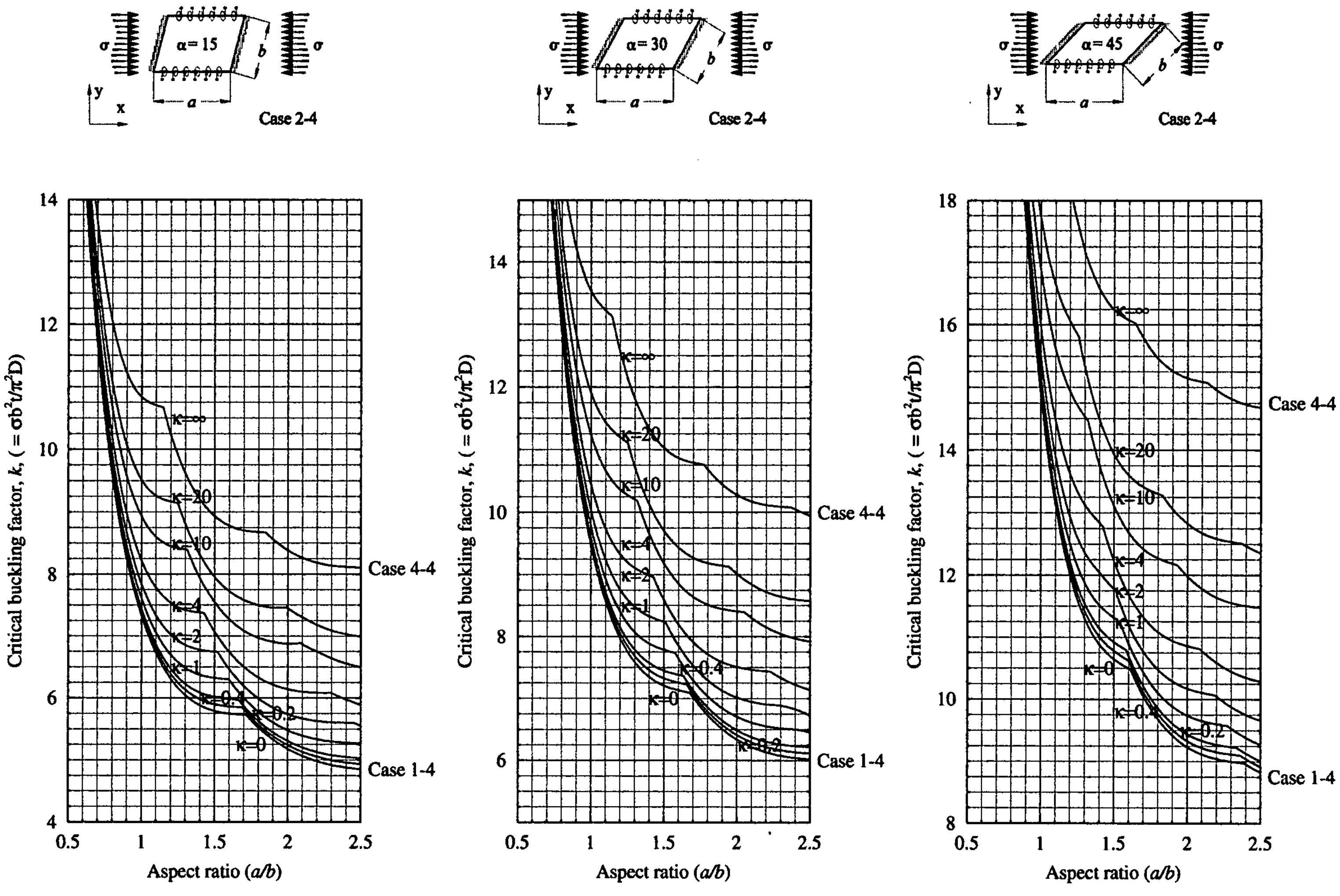

(a) α = 15°

(b) α = 30°

(c) α = 45°

Figure 4.4: Case 2-4, design curves plates with skew angle $\alpha = 15° (a), 30° (b) \& 45° (c)$, having loaded, skew transverse edges clamped and longitudinal edges elastically restrained against rotation.

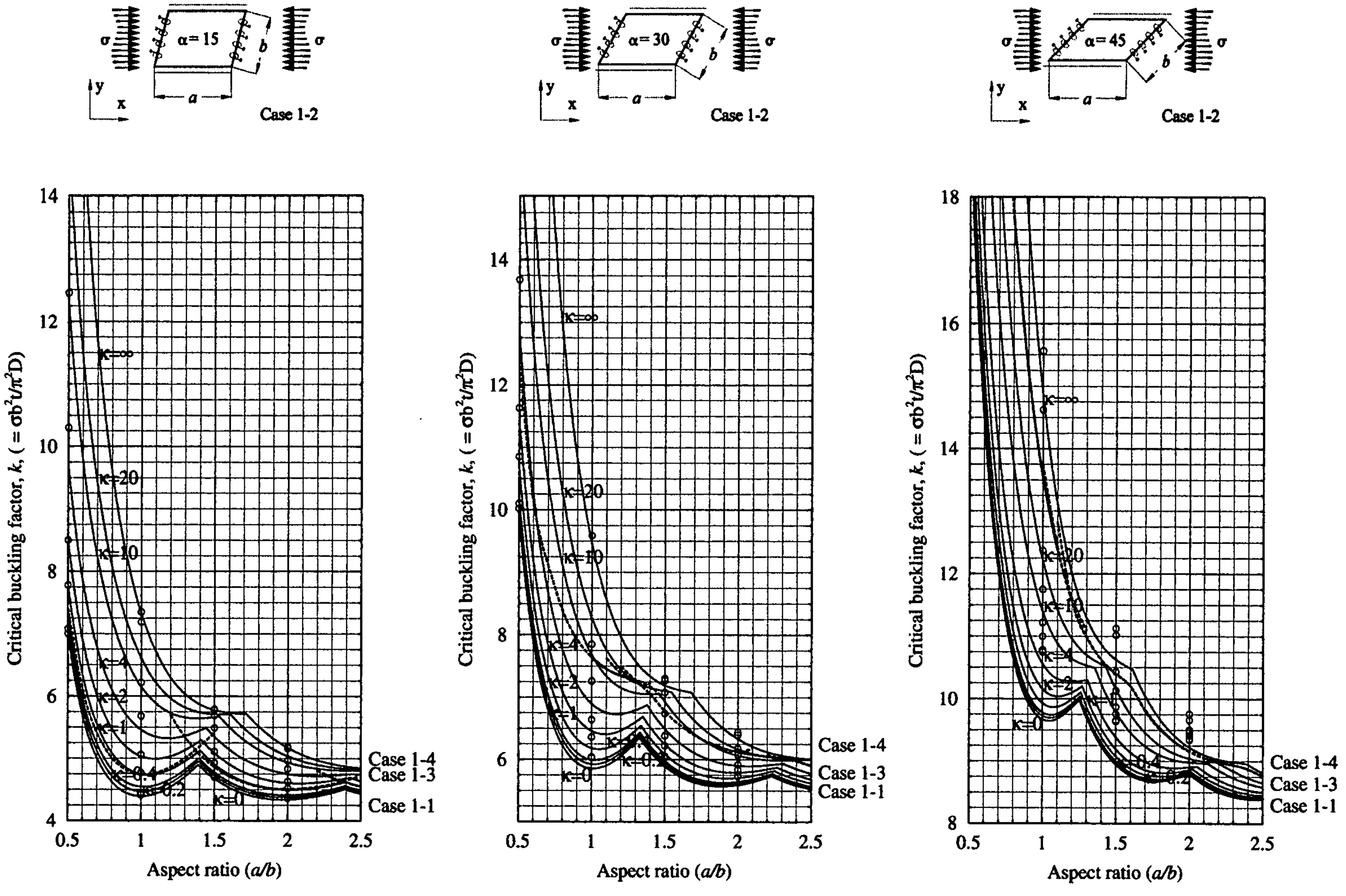

(a) $\alpha = 15°$ (b) $\alpha = 30°$ (c) $\alpha = 45°$

Figure 4.5: Case 1-2, design curves plates with skew angle $\alpha = 15°\,(a), 30°\,(b)\,\&\,45°\,(c)$, having loaded, skew transverse edges elastically restrained against rotation and longitudinal edges simply supported. Comparisons are made between those of Mizusawa *et al.* for magnitudes of discrete rotational stiffness applied along the skew, transverse edge, $\kappa = 0.0, 0.1, 1, 2, 5, 10, 100\,\&\,\infty$ (shown as ∘) and VICON results for uni-axial continuity (Case 1-3, dashed lines).

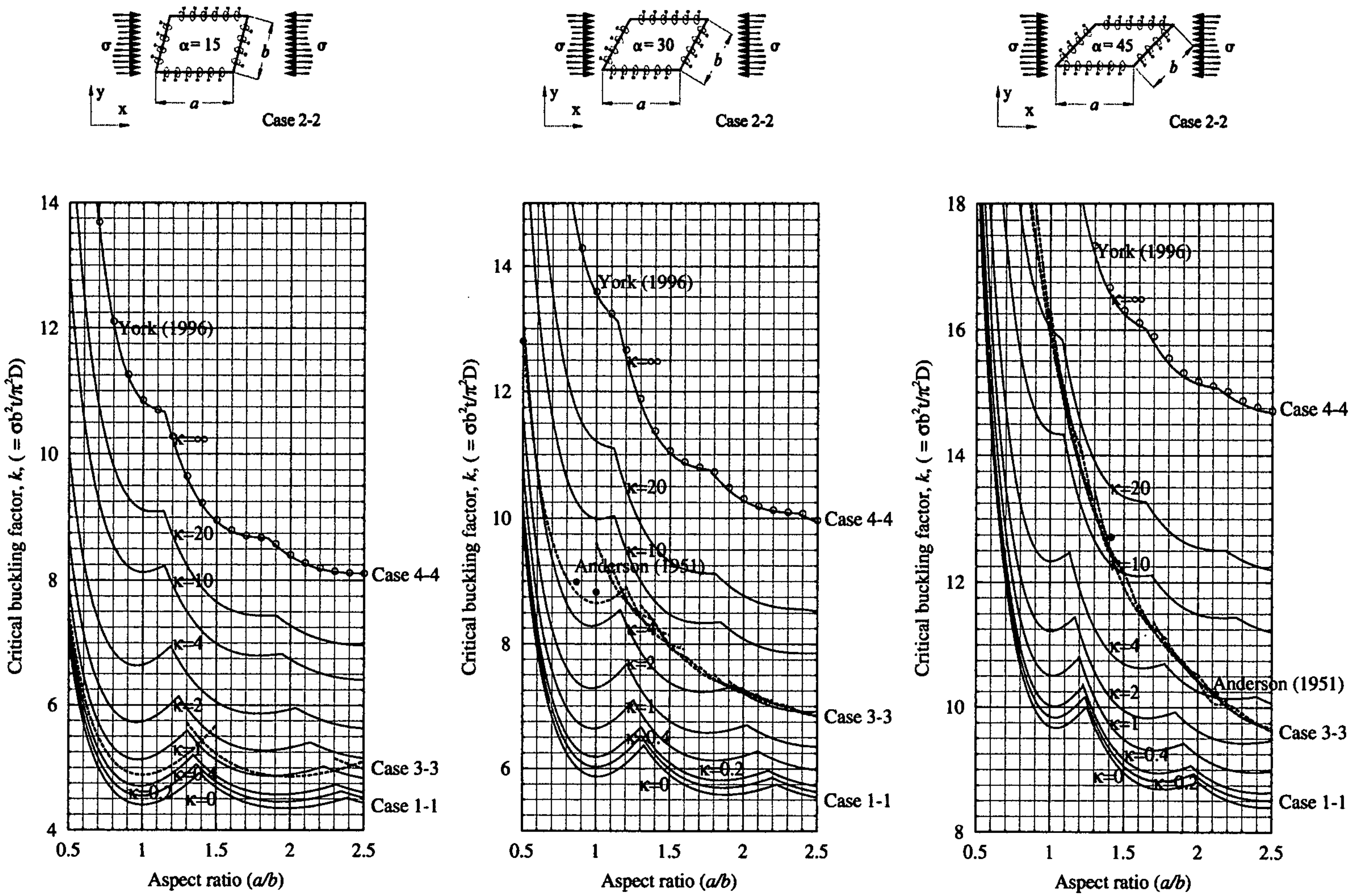

(a) $\alpha = 15°$

(b) $\alpha = 30°$

(c) $\alpha = 45°$

Figure 4.6: Case 2-2, design curves plates with skew angle $\alpha = 15° \ (a), 30° \ (b) \ \& \ 45° \ (c)$, having both loaded, skew transverse edges and longitudinal edges elastically restrained against rotation. Comparison results are provided by York (1996) [112] (shown as ∘) for the fully clamped case, VICON results shown as dashed lines for bi-axial continuity and limited results by Anderson (1951) [5] (shown as •) for bi-axial axial continuity.

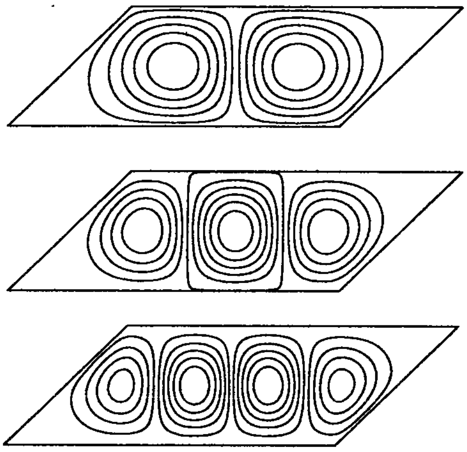

Figure 4.7: Typical buckling modes for Case 2-1 (Figure 4.3(*b*)). The plates all have the same aspect ratio ($a/b = 1.9$) and skew angle, $\alpha = 30°$. The rotational stiffness applied along the longitudinal edges causes the critical buckling modes to be different. The top plate is simply supported on all four edges (Case 1-1), the middle has an elastic rotational stiffness, $\kappa = 20$ applied along the longitudinal edge, the lower plate has clamped longitudinal edges (Case 4-1).

4.4.1 Verification of maximum aspect ratio used in the study

This subsection shows that range of aspect ratios used is sufficient to give convergence on an infinite plate result.

Figures 4.8(a) and 4.8(b) show the buckling strength of the lower–bound buckling solution as a percentage of the upper–bound one for each of the buckling curves. Figure 4.8(a) gives these relative buckling strength curves for plates with Case 4–2 and Case 2–1 type boundary conditions and shows relative buckling strengths for Case 4–1/Case 4–4 and Case 1–1/Case 4–1. Figure 4.8(b) shows the same relative buckling values for Case 2–4 and Case 1–2 buckling curves and gives curves for Case 1–1/Case 1–4 and Case 1–4/Case 4–4. The relative buckling strength for Case 2–2 boundary conditions is included on both of the figures as a reference result (*i.e.* Case 1–1/Case 4-4). Both sets of results converge on a relative buckling strength as plate aspect ratio increases. These converged values can be calculated using minimum buckling solutions for infinitely long rectangular plates because at high aspect ratios, the skew edge of the plate has a negligible effect on the buckling strength of the plate. The critical buckling load for an infinitely long rectangular plate with simply supported longitudinal edges is given by $k = (\sigma b^2 t)/(\pi^2 D) = 4.0$ and for one with fully clamped longitudinal edges by $k = 6.97$ [20]. Hence the relative buckling strength for a plate with simply supported longitudinal edges compared to one with fully clamped edges is 57.39%. This relative buckling strength is marked on the figures, and the curves are well converged on it for $a/b = 2.5$. For comparisons where the boundary conditon along the longitudinal edges is the same, relative buckling strengths will converge on 100%. This convergence is given by the curves describing Case 4–1/Case 4–4 and Case 1-1/Case 1-4. These curves are well converged on these relative buckling strengths, which shows that the aspect ratio range used in the study is large enough to give an accurate account of the buckling behaviour of the skew plates.

4.5 Discussion of Results

The buckling curves in Figures 4.2 to 4.5 show the relationships between plate buckling strength, skew angle, boundary conditions and aspect ratio.

4.5.1 Critical boundary conditons governing plate buckling

Figures 4.3 and 4.5 and Figures 4.2 and 4.4 compare the effect of increasing the rotational stiffness along the longitudinal and skew, transverse edges with the remaining edges being simply supported or clamped

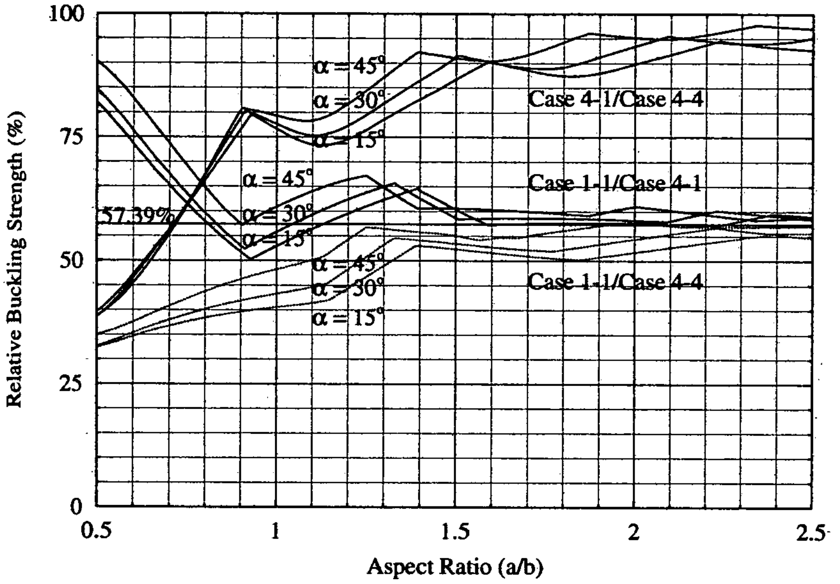

(a) Relative buckling strength for Cases 4-2 and 2-1

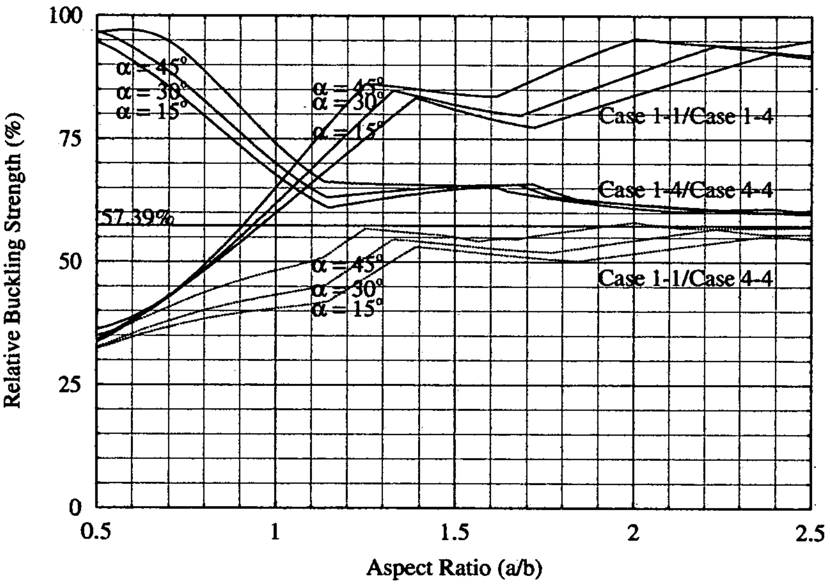

(b) Relative buckling strength of plates for Cases 2-4 and 1-2

Figure 4.8: Relative buckling strength of plates (lower-bound solution as a percentage of upper-bound solution) for (a) Case 4-2 and Case 2-1 (buckling curves in Figures 4.2 and 4.3 respectively) and (b) Case 2-4 and Case 1-2 (buckling curves in Figures 4.4 and 4.5 respectively). The results are compared with the lower bound solution, that of Case 1-1/Case 4-4 (buckling curves in Figure 4.6). The line at 57.39% represents the converged theoretical relative buckling strength at high aspect ratio.

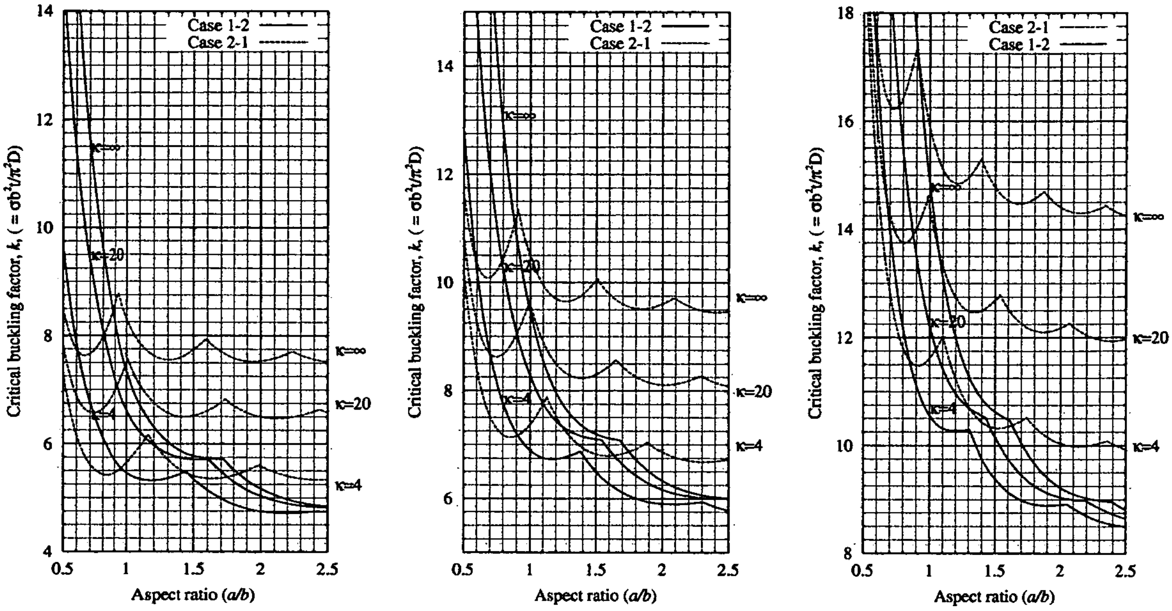

(a) $\alpha = 15°$ (b) $\alpha = 30°$ (c) $\alpha = 45°$

Figure 4.9: Location of critical boundary condition. Comparison of Case 1-2 and Case 2-1.

respectively. The widespread buckling coefficients for the cases with rotationally restrained longitudinal edges (Figures 4.3 and 4.4) demonstrate that at higher aspect ratios, the boundary conditions along these edges are critical factors governing the plate buckling load. Conversely, the steep drop in buckling load observed with increasing aspect ratio in Figures 4.5 and 4.2 demonstrates that the buckling load of a plate is governed by the boundary condition along the skew, transverse edge at smaller aspect ratios. The effect of this restraint is quickly lost as the plate aspect ratio increases and the effect of the restraint provided along the longitudinal edges becomes more critical in governing the buckling strength of the plate. There is therefore a critical aspect ratio at which a plate buckles with the same buckling coefficient regardless of whether some magnitude of rotational restraint is applied along its transverse of longitudinal edge.

The critical aspect ratio at which a fixed magnitude of rotational stiffness applied along the transverse edge of a skew plate gives the same critical buckling load for a plate rotationally restrained along the longitudinal edge can be determined from Figures 4.9 and 4.10. The figures compare the buckling curves for Case 1-2 and Case 2-1 and Case 2-4 and Case 4-2 respectively for a sample of three rotational stiffnesses. In the figures, moving from low to high aspect ratio, a higher buckling load is obtained if rotational stiffness is applied along the skew, transverse edge of the plate before the point of intersection of the two buckling curves representing the same rotational stiffness. After the point of intersection, a higher plate buckling

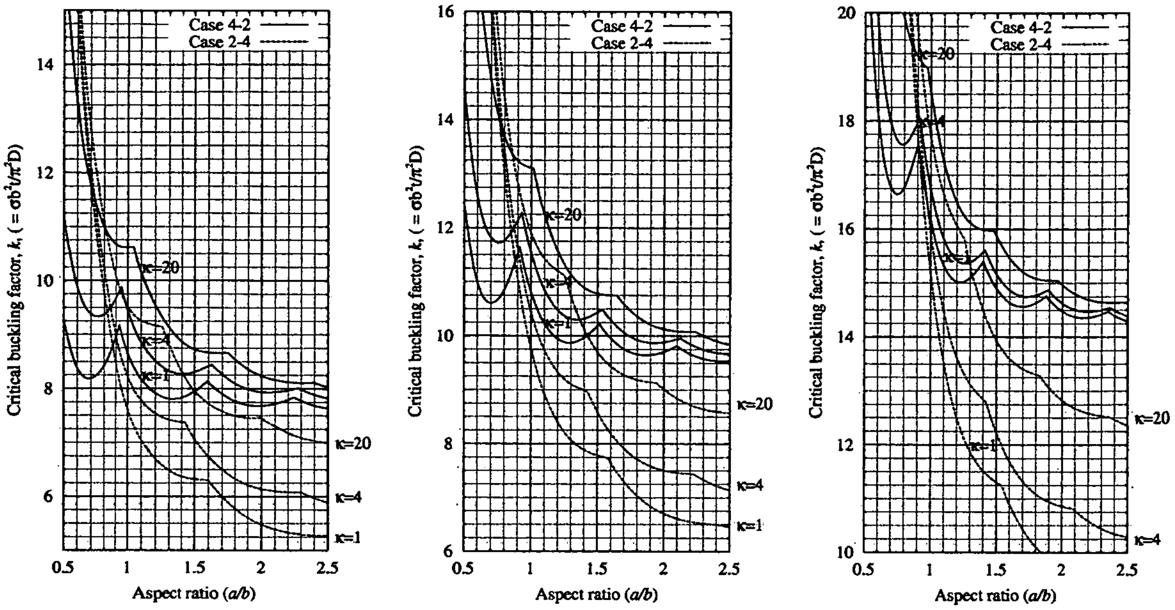

(a) $\alpha = 15°$ (b) $\alpha = 30°$ (c) $\alpha = 45°$

Figure 4.10: Location of critical boundary condition. Comparison of Case 2-4 and Case 4-2.

load is obtained if the rotational stiffness is transfered from the skew, transverse edge to the longitudinal edges of the plate. For Case 1-2 and Case 2-1 (Figure 4.9) this critical aspect ratio is approximately 0.9 for all three skew angles. For Case 4-2 and 2-4 the critical aspect ratios are seen to be slightly lower occurring at $0.8 \leq a/b \leq 0.9$. Note that the sample rotational stiffness used for the comparison, $\kappa = 4, 20$ are common to both figures, however, the upper bound solution ($\kappa = \infty$) is not valid for the comparison made in Figure 4.10 because it represents a fully clamped plate, the upper-bound solution for the buckling problem which cannot be exceeded. The graphs show that for plates with $a/b > 1$, the critical boundary condition is the one applied to the longitudinal plate edges.

4.5.2 Curve formation

In the buckling strength curves, the cusp location can be seen to sweep across the figures. In Cases 2-1, 2-4 and 2-2 these patterns sweep from high to low aspect ratio moving from simply supported to clamped boundary conditions. In the remaining two cases, Case 1-2 and Case 4-2 the patterns sweep from low to high aspect ratio moving from simply supported to clamped boundary conditons. These patterns arise because the plate is effectively being foreshortened in the dimension normal to the application of rotational

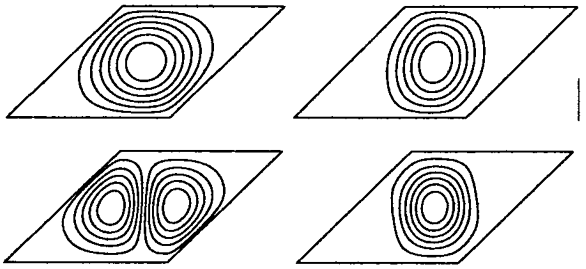

Figure 4.11: Buckling modes for lower- and upper-bound boundary condition solutions, Case 1-1, Case 1-4, Case 4-1 and Case 4-4, moving clockwise around the figure starting with the top left-hand graphic. $\alpha = 45°$, $a/b = 1.0$.

restraint and is explained in the following paragraph.

If the skew, transverse edge of the plate is rotationally restrained, the restraint shifts the area of the plate in which a buckle forms away from the transverse edges. This has the effect of making the plate buckle in manner consistent with a simply supported plate having a higher aspect ratio. The plate is therefore effectively foreshortened longitudinally. As a result, the cusp location sweeps from left to right as the magnitude of rotational restraint increases.

Applying rotational restraint to the longitudinal edges has the opposite effect. In this case, the buckle is now forced away from the longitudinal edges and the plate is foreshortened transversely. This causes the cusp location to sweep from right to left as the magnitude of rotational restraint increases.

Buckling modes which occur for the Cases 1-1, 1-4, 4-1 and 4-4 (clockwise from the top left-hand corner) are shown in Figure 4.11 for $\alpha = 45°$ and $a/b = 1.0$. At this aspect ratio, the critical buckling load for the Case 4-1 plate has already undergone a critical buckling mode change and buckles with two half-wavelengths whilst the plates with other combinations of rotational restraint along the edges buckle in one half-wavelength. The figure serves to demonstrate the argument above.

4.5.3 Comparison of results with other, related work

In Figure 4.5 (buckling curves for Case 1-2) the current results are compared with an analysis of skew plates with the same boundary conditions by Mizusawa *et al.* [64] using Raleigh–Ritz method with B-Spline functions (see Table 4.2). For this case, in which there is discrete rotational restraint along the skew, transverse edge and the longitudinal edges are simply supported, Mizusawa *et al.* produced results for discrete values of elastic rotational stiffness, $\kappa = 0.0, 0.1, 1, 2, 5, 10, 100\,\&\,\infty$. It is seen that there is generally good agreement between the two sets of buckling predictions for the small skew angles, but there is an increased divergence of the results as the skew angle increases. When $\alpha = 45°$, at the higher aspect ratios considered, the simply supported (Case 1-1) buckling predictions by Mizusawa *et al.* are higher than the current clamped results (Case 1-4). Comparison of buckling predictions for simply supported plates by Mizusawa *et al.* and those given in Table 4.2, show that buckling predictions by Mizusawa *at al.* are towards the high end of those reported. It is also of interest to note the large range over which the buckling stress of skew plates is reported by Mizusawa *et al.* [66, 65] (Table 4.2) in other articles using the same numerical method of analysis.

4.5.4 Comparison of discrete rotational restraint model and continuity results

Critical buckling loads for discrete magnitudes of rotational stiffness and continuity along the transverse plate edges are compared in Figure 4.5. The buckling predictions for the transverse continuous boundary condition (Case 1-3) are shown as bold, dashed lines. These continuity results have not, as is the case with the isolated plate buckling curves, had splines fitted through them. Instead, buckling predictions for all the eigenvalues around the critical buckling load are presented. It is seen that in this uni–axial continuity case, for the $\alpha = 15°$ case, there is good agreement between the buckle predictions for a plate having a rotational stiffness $\kappa = 0.4$ over the range of aspect ratios considered. At higher skew angles, there is no strong correlation between the critical buckling load and one magnitude of rotational restraint, however the minimum buckling load over the range of aspect ratios corresponds to a magnitude of increasing rotational stiffness. For example in the case, $\alpha = 30°$, the uni-axial continuity case does not predict buckling loads less than for an isolated plate with $\kappa = 2$ and in the case $\alpha = 45°$ not less that $\kappa = 10$. Increasing the skew angle therefore leads to an increase in the buckling strength of a skew plate. This increase is not synonymous with a discrete magnitude of rotational restraint, but the skew angle of the plate.

In Figure 4.6, the buckling loads of plates having all four edges elastically rotationally restrained are compared with the bi-axial continuity case and, for further model verification, the clamped VICONOPT buckling predictions by York[112] (see the penultimate row of Table 4.3). Excellent correlation is seen between the clamped ABAQUS and VICONOPT results which is expected because in the case in which all the plate edges are clamped, the continuity solution in VICONOPT degenerates into a clamped, isolated plate result. The Case 2-2 results can also be compared with those of Anderson [5] who reports critical buckling factors for a bi-axially continuous plate, with skew angles $\alpha = 30°$ and $\alpha = 45°$ and a limited number of aspect ratios. These results are given in Table 4.4. They compare well with the bi-axially continuous solution by York [112], but are a little higher. This is attributed to the simplifying assumptions made by

Table 4.4: Buckling coefficients given by Anderson [5] for bi-axial continuity, $\alpha = 30°$ and $\alpha = 45°$.

$\alpha = 30°$		$\alpha = 45°$	
a/b	$k = \frac{\sigma b^2 t}{\pi^2 D}$	a/b	$k = \frac{\sigma b^2 t}{\pi^2 D}$
0.500	12.80	0.354	48.24
0.866	8.99	0.707	22.92
1.000	8.23	1.414	12.72
–	–	2.121	10.22

Anderson regarding the buckling mode of the plate array, namely it will only repeat over a maximum of two transverse and longitudinal bays. The solutions by Anderson are incorporated into the current ESDU [30] design curves and due to their conservative nature provide 'safe' buckling stresses for design. York's [112] solutions show that more than two longitudinal bays are required to accurately model the the buckling modes and the associated critical buckling load.

Bi-axial continuity results predict higher buckling stresses than the the uni-axial continuity results which are higher than a simply supported plate.

For the $\alpha = 15°$ case, biaxial continuity leads to a critical plate buckling stress equivalent to that of an isolated plate with all edges that have an elastic rotational stiffness, $0.4 < \kappa < 2$ over the range of aspect ratios. A shift in the aspect ratio at which the first buckling mode transition occurs, to a higher aspect ratio in the bi-axial continuity solution than for the equivalent isolated skew plate means that there is not good correlation with an isolated plate solution as is the case with uni–axial continuity.

For $\alpha = 30°$, the bi-axially continuous plate buckling load, is given by an isolated plate with all four edges rotationally restrained, if $4 < \kappa < 10$ (between $1.9 < a/b < 2.0$ the bi-axial results lies slightly below $\kappa = 4$). For $\alpha = 45°$ the equivalent rotational stiffness is $2 < \kappa < \infty$. In this $\alpha = 45°$ case, the upper and lower values of rotational stiffness describing the bi-axial continuity results are observed at the smallest and highest aspect ratios considered. The ranges of rotational stiffness in which the continuity results lie are summarised in Table 4.5.

The fall in rotational stiffness bounded by the bi-axial continuous case is due to the very complex buckling modes that develop as a result of mode interaction between adjacent plates. At high skew angles, these interactions are complex and the buckling mode may repeat over many bays. Conversely, the buckling mode interactions at low angles are generally simpler tending towards those of a rectangle (in which case there is no strength advantage in considering continuity over simple supports). In these small skew angle cases, the buckling modes tend to repeat over a small number of bays (typically one or two). The inclusion

Table 4.5: Ranges of magnitude of elastic rotational stiffness to give buckling loads predicted by the continuity plate results. The value κ is the elastic rotational stiffness in Cases 1-2 and 2-2 which bound the continuous cases Cases 1-3 and 3-3 respectively.

Case 1-3 (uni-axial continuity)			Case 3-3 (bi-axial continuity)		
$a = 15°$	$\alpha = 30°$	$\alpha = 45°$	$\alpha = 15°$	$\alpha = 30°$	$\alpha = 45°$
$\kappa \approx 0.4$	$2 < \kappa < 20$	$20 < \kappa < \infty$	$0.4 < \kappa < 2$	$4 < \kappa < 10$	$2 < \kappa < \infty$

of continuity along more than one edge, as in the case of the bi-axially continuous plate complicates the buckling modes further. The complex buckling mode patterns observed in the bi-axially continuous case result in the buckling curves in Figure 4.6 for $\alpha = 45°$ and the higher aspect ratios of the $\alpha = 30°$ case. In these cases, many lines describe the plate bucking characteristics, each corresponding to an unique buckling mode, the lower of which is the critical one. From the figure it can be seen that there are many mode changes over the range of aspect ratios.

4.5.5 Increase in buckle strength due to continuity

Figures 4.12(a) and (b) show the relative increase in buckling load that uni-axial continuity and bi-axial continuity can provide to the plate respectively.

The figures show the buckling load of the continuous plate over that of the simply supported case as a proportion of the difference between the simply supported and fully clamped plate solution. All three skew angles are considered. Figure 4.12(a) shows the relative buckle strength increase associated with uni-axial continuity. For this uni-axially continuous case, there is an overall trend for the relative buckling strength of the plate to increase over the range of aspect ratios treated. For $\alpha = 15°$, at low aspect ratios, the relative buckling strength increase is small, but becomes larger as the skew angle of the plate increases. The troughs in the curves relate to asynchronous buckling mode changes that are observed between the simply supported, continuous and clamped boundary condition cases. There is also a trend for the uni-axial boundary condition to converge towards that of the clamped skew, transverse edge boundary condition for values of $\alpha = 30°$ and $\alpha = 45°$. This is because the upper- and lower- boundary condition case at high aspect ratios in the case of the Case 1-2 boundary condition both converge to that of simply supported plate (see Figure 4.8) and are well converged value at an aspect ratio of $a/b = 2.5$. The results presented in Figure 4.12 will consequently be sensitive to small changes in buckling load.

In the case of bi-axial continuity (Figure 4.12(b)) the opposite effect on the relative increase in buckling

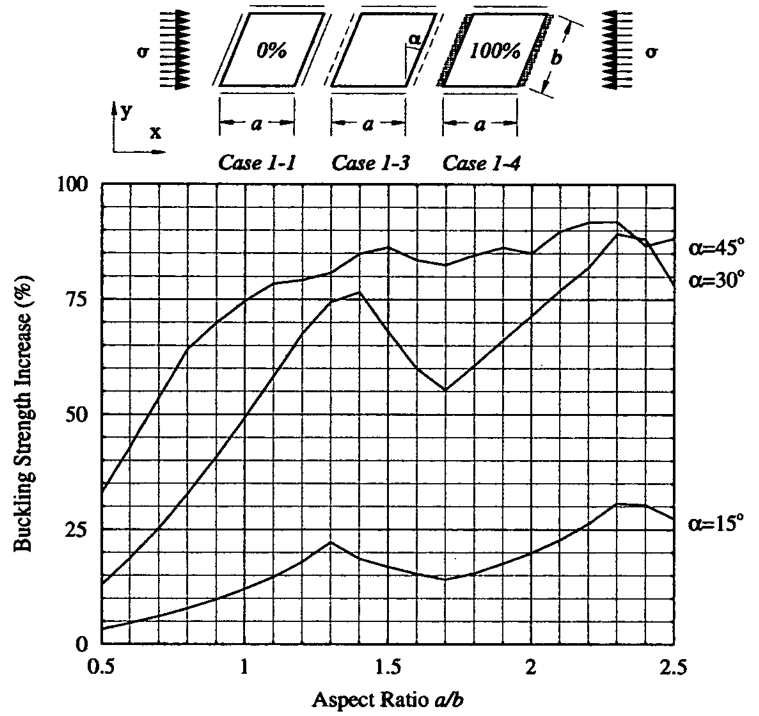

(a) Uni-axial continuity

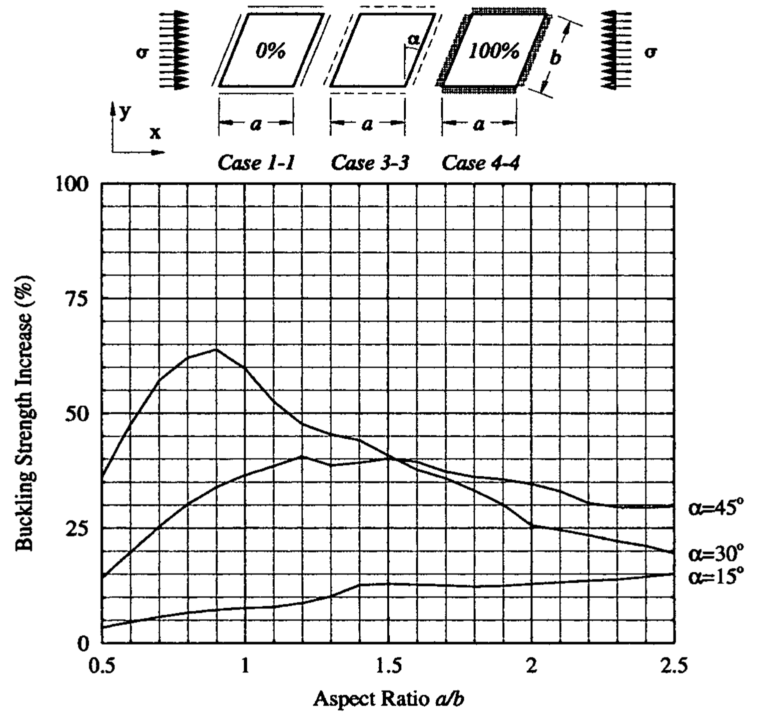

(b) Bi-axial continuity

Figure 4.12: Relative increase in buckling load due to (*a*) uni-axial continuity and (*b*) bi-axial continuity. This relative increase in buckling load is defined as the proportion of buckling load that the continuous plates carry over that of an equivalent simply supported plate compared with that of the appropriate upper-bound case (Case 1-4 for uni-axial continuity and Case 4-4 for bi-axial continuity). The illustrations along the top of the graph show the cases used in the comparison.

Table 4.6: Plate buckling coefficients, $k = \sigma b^2 t/\pi^2 D$, for ABAQUS analysis of a one-dimensional plate array on 'n' plates compared with the infinite exact uni-axial continuity VICON solution.

VICON	ABAQUS					
	$n = 1$	$n = 2$	$n = 3$	$n = 4$	$n = 5$	$n = 6$
7.63	9.47	8.18	7.83	7.74	7.67	7.66

load is seen when compared with the uni–axial continuity case. At low aspect ratios, the buckling strength increases are similar to those for uniaxial continuity, however plates with skew angles, $\alpha = 30°$ & $45°$ peak and the relative buckling load declines. For these skew cases, there is an obvious trend for the continuous buckling load due to fall as the aspect ratio increases beyond this peak, although the $\alpha = 15°$ case steadily rises beyond $a/b = 2.5$. This results in there being a wide spread in the buckling results at the highest aspect ratios considered (see Figure 4.8). This will make the graphical representation given in the figures less sensitive to small changes in buckling and asynchronous buckling mode changes.

An example analysis which aims to obtain a good approximation to a uni-axial continuous buckling load is carried out using ABAQUS for a plate with $\alpha = 30°$, $a/b = 1.0$. The critical buckling coefficient for varying numbers of plates that are continuous over otherwise simple supports is calculated. A clamped, skew, transverse edge boundary condition is chosen to prevent local buckling in the outer bays which occurs when the rotational stiffness applied to the outer skew, transverse edges is lower than that provided by continuity over the internal supports. The number of plates in the array is increased by one in each analysis until there are a total of six plates and compared with the equivalent VICONOPT solution of York [112] for an infinite array of identical plates. The buckling modes of the resulting analysis are given in Figure 4.6. The figures show that continuity over otherwise simple supports gives rise to modes that are more complex than the isolated plate buckling modes shown in Figure 4.13. Table 4.6 gives the buckle coefficients for each plate array, from which good convergence can be seen when an array of six adjacent plates is analysed.

4.6 Elastic Buckling Predictions of Skew Plates with a Constant Planform Area

Using the definition for aspect ratio, a/b, where b is measured parallel to the skew edge, the planform area of the plate decreases as the skew angle of the plate increases if the aspect ratio is fixed. This is because

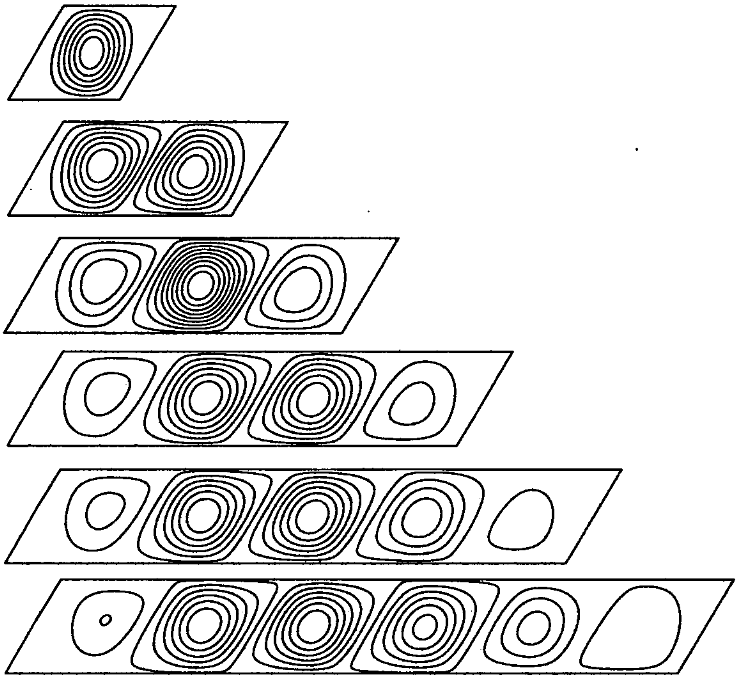

Figure 4.13: Buckling modes resulting from analysis of a one dimensional plate array of up to six adjacent plates, continuous over otherwise simple supports. Buckling loads corresponding to the buckling modes are given in Table 4.6. For a plate geometry, $a/b = 1.0$, $\alpha = 30°$ and longitudinal edges simply supported and skew transverse edges clamped.

the width of the plate measured normal to its longitudinal edge decreases. Therefore if a constant stress is applied to the plates, the total load applied decreases with an increase in skew angle.

Comparisons made previously are perfectly valid using the definition of aspect ratio a/b because no direct, quantitative comparisons are made between the buckling characteristics of plates having different angles of skew. It is necessary, when making quantitative comparisons about buckling load as a result of changes in skew angle that a definition of aspect ratio that preserves constant planform area between the plates is used. This is because the critical solution to the eigen equation, λ, gives the critical buckling load of the plate as λP, where λ is the critical eigenvalue and P the preload applied to the plate. If P is not constant over the range of skew angles, then quantitative comparisons of buckle strength for varying skew angles are not valid. Using the definition of aspect ratio measured parallel to the skew edge, P decreases with increasing skew angle to maintain a constant stress. If the plate width is measured normal to the longitudinal plate edge, b', as an alternative to b, then a constant stress can be maintained as well as a constant preload regardless of skew angle. An additional comparison can be also made of the relative strength advantage for varying angles of skew verses mass, if the plates are assumed to be made from the same material with a uniform density and are the same uniform thickness.

It is very uncommon for buckling analysis results for skew plates to be presented using a definition of aspect ratio that ensures that the plates have a constant planform area. Of the many references given in Tables 4.2 and 4.3, none of the authors quoted produced results in this way. Only Anderson [5] (results in Figure 4.6 and Table 4.4) and Wittrick [105] presented results using this definition for aspect ratio.

The analysis of the skew plates presented previously is valid for either definition of aspect ratio but it is required that the aspect ratio and the critical buckling load coefficient, k , which are all functions of b, are converted to the new constant planform area definition. Taking, b' as the new plate width, normal to the longitudinal plate edge,

$$b' = b\cos\alpha$$

Consequently, the new aspect ratio is,

$$\frac{a}{b'} = \frac{a}{b}.\frac{1}{\cos\alpha}$$

and the revised, critical buckle coefficient, k' is given by,

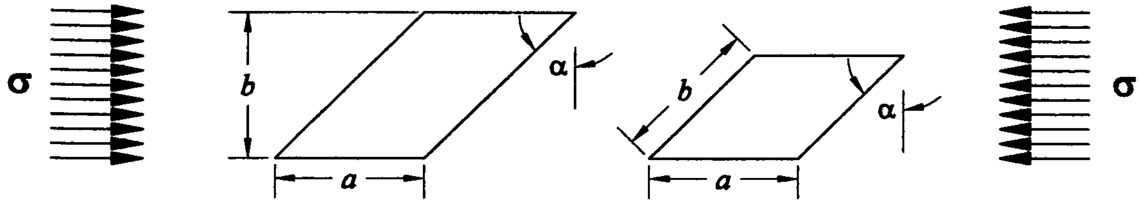

	b normal to longitudinal edge	b parallel to transverse edge	factor difference
Area	$a \times b$	$a \times b \cos\alpha$	$-\cos\alpha$
Perimeter	$2((b/\cos\alpha) + a)$	$2(a + b)$	$+([b/\cos\alpha] + a)/(a + b)$
In-plane load	σbt	$\sigma t.b\cos\alpha$	$-\cos\alpha$

Figure 4.14: Comparison of the two definitions used for aspect ratio showing: increase in planform area; increase in perimeter and increase in total applied force. The difference is given moving from definition of b measured normal to the longitudinal edge of the plate. A minus sign indicates an decrease and plus sign an increase

$$k' = \frac{\sigma b'^2 t}{\pi^2 D} = \frac{\sigma b^2 \cos^2 \alpha t}{\pi^2 D} = k \cos^2 \alpha$$

Figure 4.14 shows plates, with $\alpha = 45°$ defined using both definitions for aspect ratio. The plates are drawn to scale and have an aspect ratio of 1. The tabulated data in the figure shows the relative changes in planform area, perimeter and in-plane load if the parameter b is defined parallel to the skew edge of the plate rather than normal to the longitudinal plate edge. From the figure, and the equations above, the planform area decreases as α increases, as does the applied load at buckling if b is measured parallel to the transverse edge. If b is measured parallel to the transverse edge, the plate perimeter remains constant as α increases. This means that for critical buckling load comparisons between skew angle, which have to be made for plates with aspect ratios defined using b measured normal to the longitudinal plate edge, the total length (and possibly mass, if a constant density per unit length is assumed) of the supporting structure of the plate increases as the angle of skew of the plate increases.

The buckling curves presented in terms of constant planform area are presented in Figures 4.15 to 4.17. The figures show the critical buckling load of the skew plates for each individual boundary condition and all the skew angles considered on one graph to allow easy comparison of the effect of skew angle on the buckling load of the plate. The figures are arranged in the same logical order as the set of buckle curves for the original aspect ratio definition. Fewer buckling curves dealing with rotational restraint are shown on the buckle curves to prevent the figures from becoming congested, but are sufficient to show the effect of rotational stiffness. Note that to improve clarity, the range of the ordinate for the boundary cases that converge to the same buckling solution when $a/b' \rightarrow \infty$ (*i.e.* Cases 4-2 and 1-2) is half that of the other cases.

The constant planform area representation of the curves, by observation of the factors applied to produce them, results in the cusps appearing flatter. In the case of Case 2-1, which is the boundary condition that, in comparison to the other boundary condition cases results in a buckling mode with more half-wavelengths than the other boundary conditions, the buckle curves are almost flat at $a/b' = 3.5$. Convergence to the same theoretical rectangular plate values are observed as discussed in section 4.4.1.

The cusp location in the curves follows a distinct pattern when making comparisons between different skew angles. It shifts to the right on the abscissa as the skew angle increases. This shift is solely a result of increasing the skew angle of the plate and can be explained using a similar analogy as was used to describe the sweeping patterns of the cusps as a result of changing boundary conditions. The skew edge of the plate resists buckling in the acute corners of the plate, forcing the buckle to move towards its centre. As a result, the aspect ratio at which a change in buckling mode increases with skew angle. This change in cusp location is also observed in rectangular plates that have increasing orthotropy [9]. These changes in buckling mode are readily apparent in the buckling modes shown in Figure 4.18 for aspect ratio $a/b' = 1.5$, $\alpha = 15°$, $30°$ and $45°$ and boundary condition cases 1-1 and 4-4 (all edges simply supported and all edges clamped respectively). The figures show that the acute corners of the skew plate resist buckling and therefore the area of the plate in which buckling occurs is reduced with increasing skew angle. Note that the spacing of the contour lines is constant for all the mode plots in Figure 4.18 in order that the relative changes in buckling mode can be observed, remembering that deflections obtained from eigenvalue analyses are normalised. Vertical or near vertical lines running across the plate to and from opposite longitudinal edges in the cases where the buckling mode comprises two half-wavelengths correspond to nodal lines.

The buckling curves in the figures show that the strength gains associated with skew are not as large as the previous aspect ratio definition suggests. In some cases, asynchronous buckling mode changes and cusping lead to instances when plates with a smaller skew angle are marginally more buckling resistant than the equivalent plate with a larger skew angle which is an important design issue if the skew angle of plates is being taken into account at design stage.

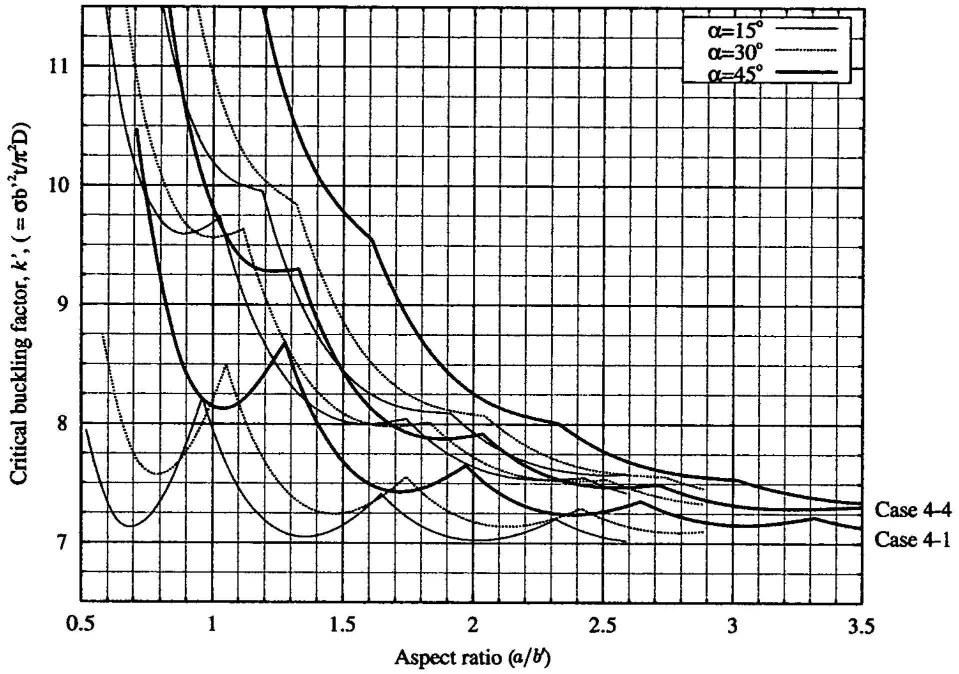

(a) Case 4-2 (Longitudinal edges clamped and skew, transverse edges elastically rotationally restrained). The intermediate buckling curves are for $\kappa = 10$.

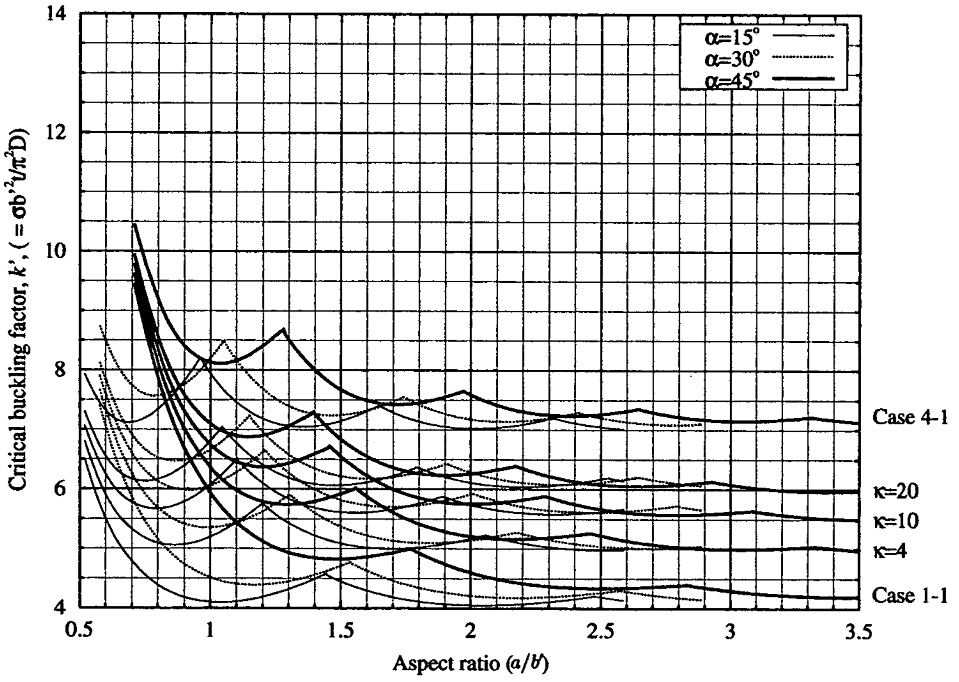

(b) Case 2-1 (longitudinal edges elastically, rotationally restrained and skew, transverse edges simply supported)

Figure 4.15: Combined buckling mode curves for all skew angles combined represented in terms of constant plan area. Boundary condition cases Case 4-2 and Case 2-1.

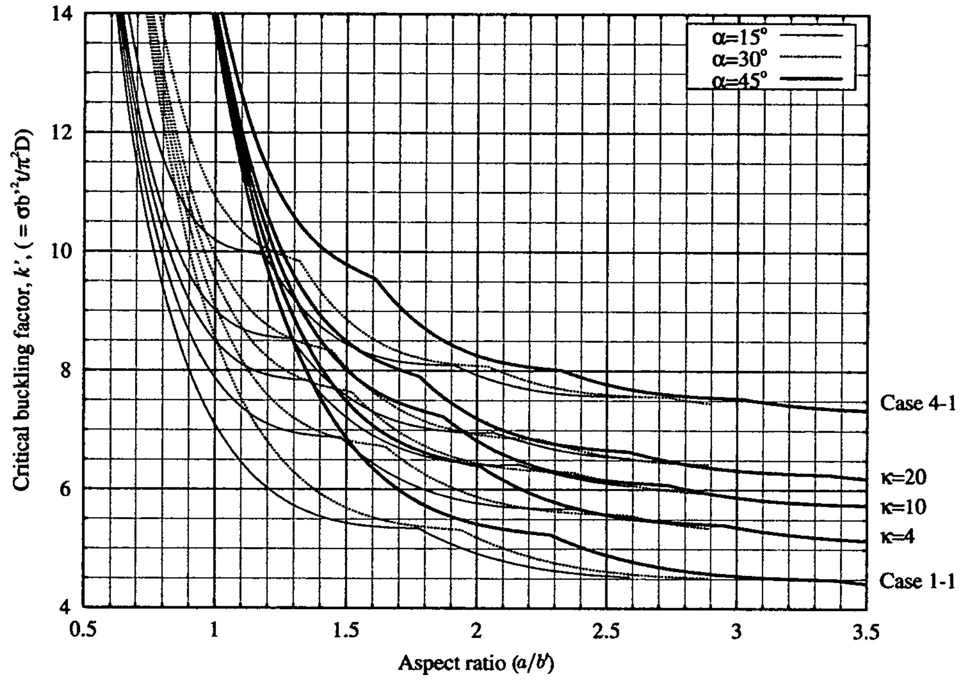

(a) Case 2-4: longitudinal edges rotationally restrained and skew, transverse edges clamped.

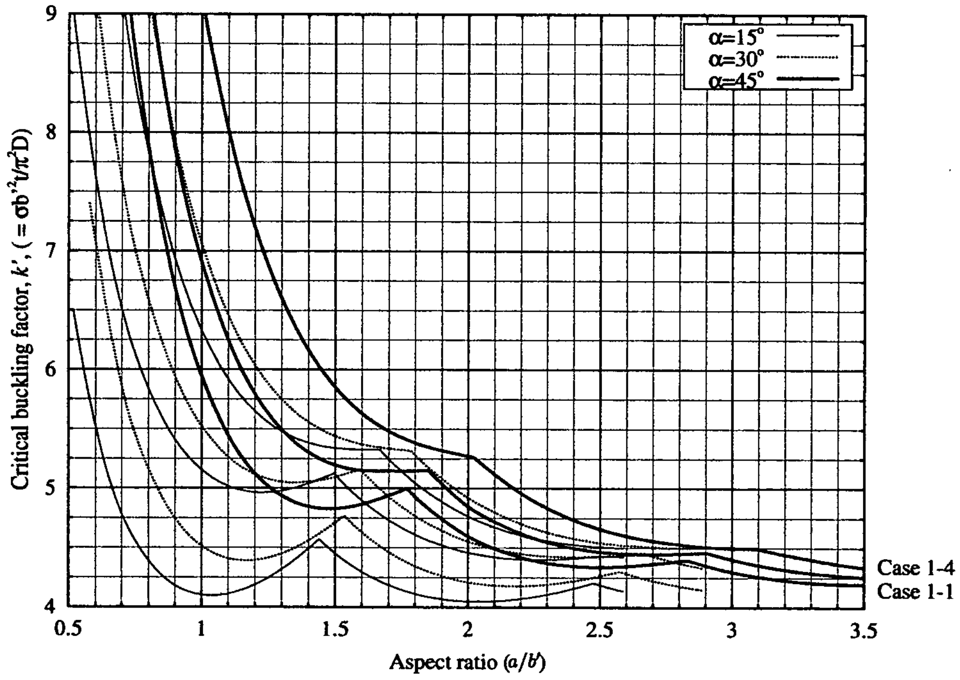

(b) Case 1-2: longitudinal edge simply supported, skew, transverse edges elastically rotational restrained. The intermediate buckling curves are for $\kappa = 10$.

Figure 4.16: Combined buckling mode curves for all skew angles combined represented in terms of constant plan area. Boundary condition cases Case 2-4 and Case 1-2.

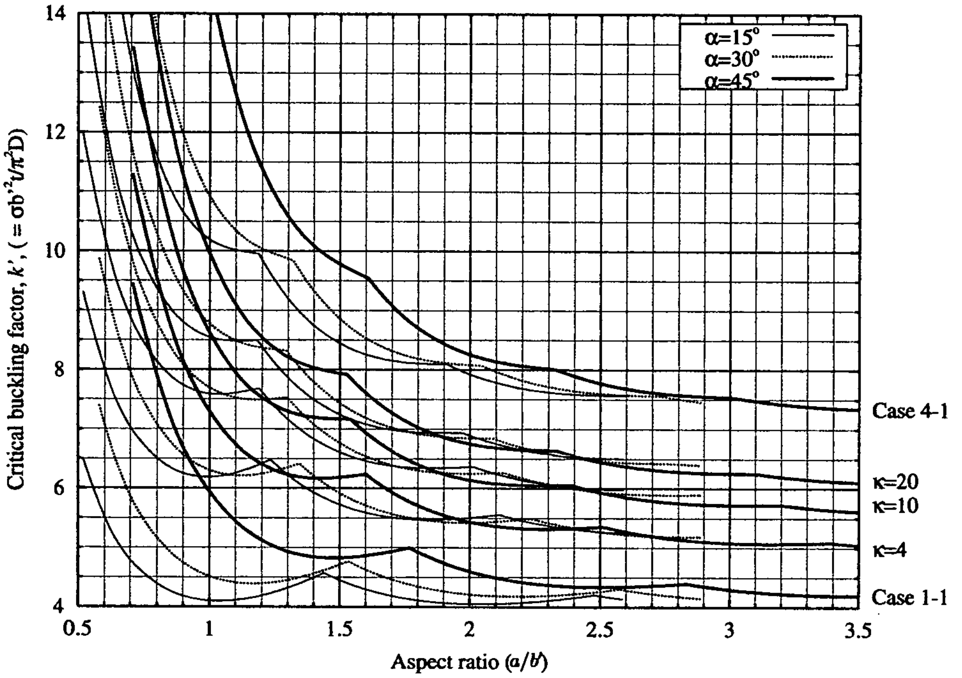

(a) Case 2-2: All edges have elastic rotational restraint

Figure 4.17: Combined buckling mode curves for all skew angles combined represented in terms of constant plan area. Boundary condition cases Case 2-2.

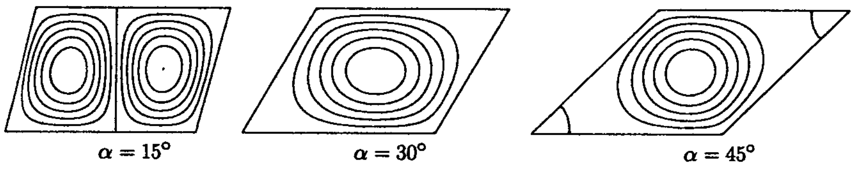

(a) Case 1-1, all four edges simply supported.

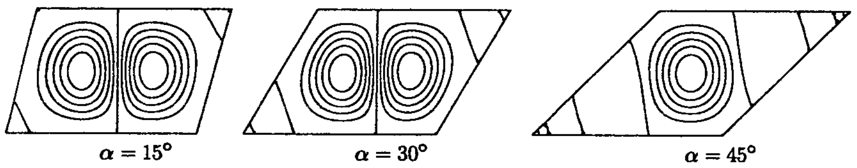

(b) Case 4-4, all four edges clamped

Figure 4.18: Typical buckling modes for skew plates having (*a*) all four edges simply supported and (*b*) all four edges clamped for $a/b' = 1.5$. The contours of all the plots have the same spacing and so accurately show the relative deflections between the plates. The vertical or near vertical lines in the cases where the buckle comprises two half-wavelengths represent the point of zero displacement or nodal line.

4.7 Plates with unsymmetrical boundary conditons

Analysis of the skew plates in the preceeding sections deals with plates that have symmetrical combinations of rotational restraint applied to the plate edges. This section considers the effect on the buckling load of plates with non-symmetrical boundary conditions (*i.e.* different values of rotational stiffness) on the unloaded edges *i.e.* that of a plate with boundary conditon Case 2-1 (see figure 4.1).

4.7.1 Background

Lunquist and Stowell [56] considered this problem when compiling buckling curves for rectangular plates having, unloaded, longitudinal edges rotationally restrained and loaded, transverse edges simply supported. This section determines whether Lunquist and Stowell's approximate methods are applicable to skew plates. Two methods of approximation are suggested by Lundquist and Stowell [56] and use the buckling curves of plates having symmetrical degrees of rotational stiffness along the longitudinal edges. The first is to take the arithmetical average of the buckle loads for plates with symmetrical rotational stiffnesses equal to the rotational stiffness, κ_1 and κ_2 on the edges of the plate with unsymmetrical boundary conditons. The arithmetic mean is given by:

$$k = \frac{k_1 + k_2}{2} \tag{4.3}$$

Where, k_1 and k_2 are the buckle loads for a plate with magnitudes of rotational stiffness, κ_1 and κ_2 on both the unloaded plate edges.

The second is to take the geometric mean of the plate buckling loads, k_1 and k_2 defined previously given by:

$$k = \sqrt{k_1 k_2} \tag{4.4}$$

The relative merits of making such approximations are easy to see, it requires only the production of buckling curves for plates with symmetrical boundary conditons, as has already been done.

Lunquist and Stowell showed that the methods gave accurate buckling predictions with the arithmetic mean giving more conservative approximations. Typical errors are reported as being less than 3%.

4.7.2 Numerical Validation

A quantitative test is carried out to determine the validity of these approximations when applied to skew plates. The buckling curves, previously compiled are used to determine the buckling loads of plates with case 2-1 type boundary conditions and different magnitudes of rotational restraint applied to the longitudinal edges. This boundary conditon is chosen to determine the effectiveness of the arithmetic and geometric mean approximations because it is seen in figure 4.9 to be more influential on the critical plate buckling load when the plate aspect ratios are larger than $a/b = 1.0$. All skew angles previously considered are analysed as well as rectangular plates ($\alpha = 0°$) which are used to verify Lundquist and Stowell's results against the current finite element analysis.

Finite element analyses are carried out to determine the critical buckling loads of plates having all combinations of magnitudes of rotational stiffness previously considered, for aspect ratios $a/b' = 1.0, 2.0$. Note that the aspect ratio is defined as in section 4.6 (*i.e.* the plates have a planform area that is not dependent on skew angle). Further economies in calculation are made by making use of the fact that a magnitude of rotational spring stiffness κ_1 applied to the top plate edge and κ_2 to the bottom edge will give the same critical buckling load if they are interchanged.

Results are given in Figures 4.19 and 4.20 and Tables B.1 - B.16 in Appendix B for both aspect ratios, mean approximations and all four skew angles.

The graphs in Figures 4.19 and 4.20 show buckling coefficient Vs rotational stiffness for each of the aspect ratios and skew angles. Each curve on the graph gives the buckling coefficient for a plate with a different value of rotational stiffness along one edge, whilst the abscissa gives the rotational stiffness along the opposite edge. The buckling curves relating aspect ratio and buckling coefficient can be found in Figure 4.15(b). Comparison of the geometric and arithmetic mean results are shown as discrete results on the curves.

Tables B.1 - B.16 in Appendix B show buckling predictions for the plates numerically. Each table is split into two sections either side of the leading diagonal which give the finite element buckling predictions for plates having symmetrical combinations of rotational restraint. Figures above the leading diagonal give the finite element buckling predictions for plates with combinations of rotational stiffness shown in the table column and row headings. Figures below the leading diagonal give the mean approximation (either geometric or arithmetic as noted in the table caption). The italic data next to the mean approximations give the percentage error between the finite element prediction and the applicable mean approximation. A negative difference infers that the mean approximation is lower than the actual predicted buckle load of the plate.

It can be seen from both the tabulated data and the figures that the method of taking the arithmetic and geometric mean provide good approximations to the buckling load of the plates for all the skew angles and aspect ratios considered. The geometric mean gives the better approximation, in respect of the fact that it generally underestimates the critical buckling load of the plates with $\alpha = 0°, 15°$. At higher skew angles however, both approximations tend to overestimate the plate buckling load and should therefore be used with caution in a design situation. The arithmetic mean gives buckling predictions higher than the geometric mean, which in many cases will overestimate the buckling load of the plate. This is true for all cases when $a/b' = 1.0$ and for $\alpha = 45°$ when $a/b' = 2.0$. It is noted that the approximation is very good for the case when $a/b' = 2.0$ and $\alpha = 0°$.

The greatest difference between the approximate methods and the actual predicted buckling load is for plates having the largest difference in spring stiffness along the edges (*i.e.* a simply supported and clamped edge). In these cases, the approximate method should be used with caution as these cases predict the greatest overestimate of plate buckling strength.

4.8 Conclusions

A comprehensive set of buckling curves has been presented for the buckling assessment of isotropic skew plates under uniform, uni-axial, compression load. The new curves illustrate the changes in buckling strength arising from the addition of symmetric combinations of elastic edge restraints against rotation for a wide range of aspect ratios and skew angles.

The new curves provide a greater insight into the buckling behaviour of skew plates and continuous structures. They permit a more appropriate choice of aspect ratio to exploit strength gains when elastic restraint against rotation or continuity exists in a structure, which could otherwise not be used to advantage, because the information is unavailable in the open literature.

The buckling curves have also, as is rarely the case, been presented in terms of maintaining a constant planform area independent of the skew angle of the plate. The results allow the comparison of buckling strength between plates as a result of skew angle. The results show that buckling strength gains are not as great as the often used presentation of analyses suggests.

Finally, the buckling predictions obtained for skew plates with equal magnitudes of elastic rotational restraint applied along the longitudinal plate edges are used to assess the accuracy of predicting buckling

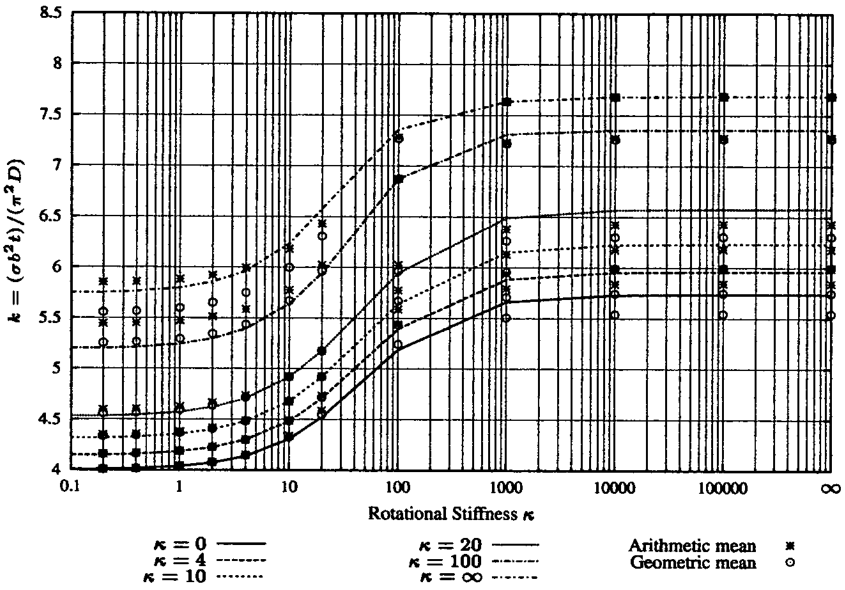

(a) $\alpha = 0°$

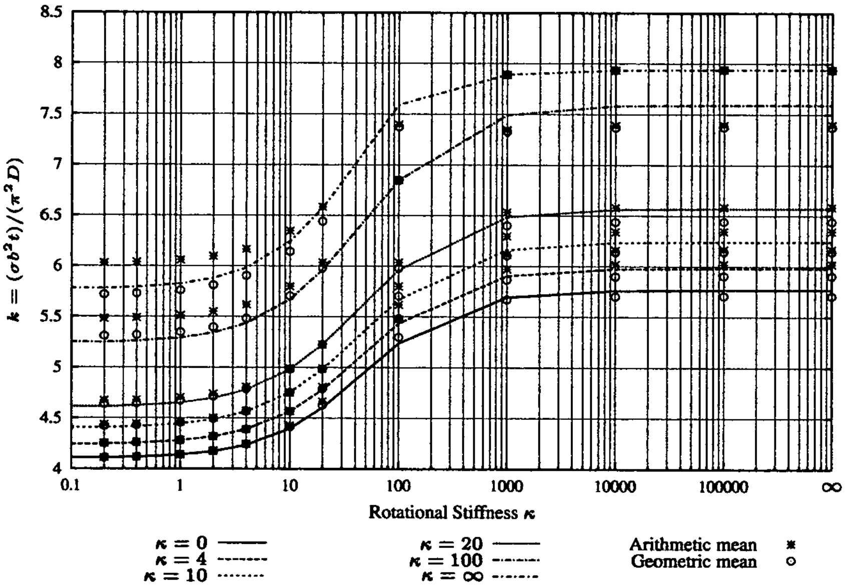

(b) $\alpha = 15°$

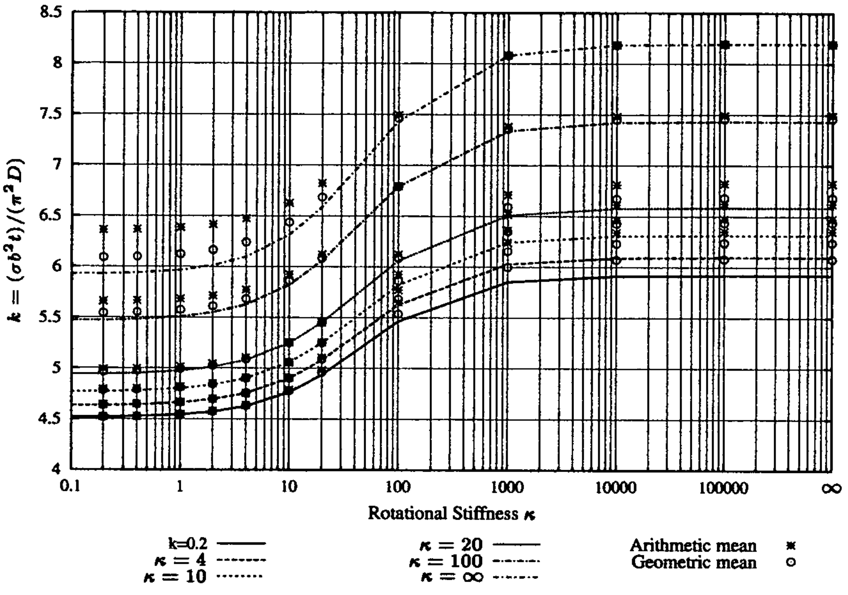

(c) $\alpha = 30°$

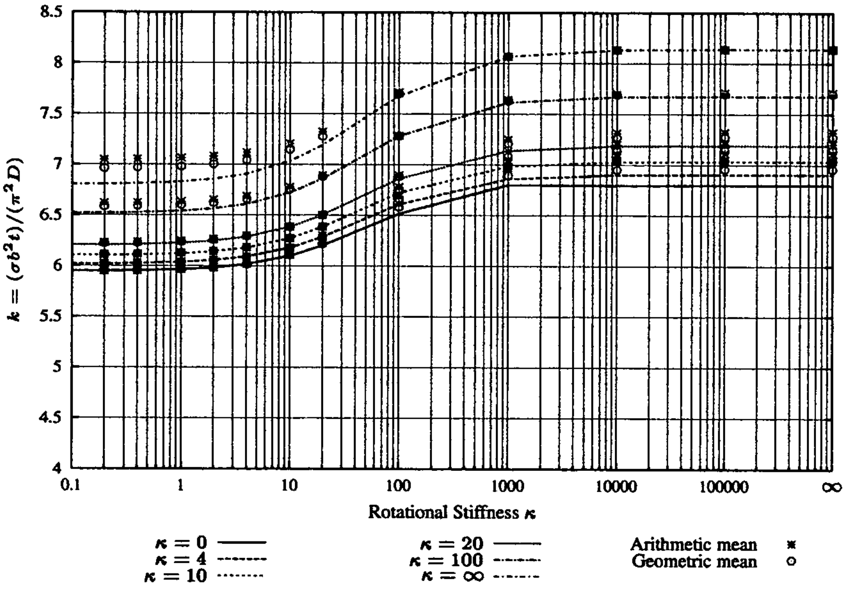

(d) $\alpha = 45°$

Figure 4.19: Graphical comparison of the geometric and arithmetic approximations to determine the buckling coefficient of a skew plate, with a uniform in-plane compression along simply supported transverse edges having different degrees of rotational stiffness along the top and bottom longitudinal edges. The plate has an aspect ratio $a/b' = 1.0$

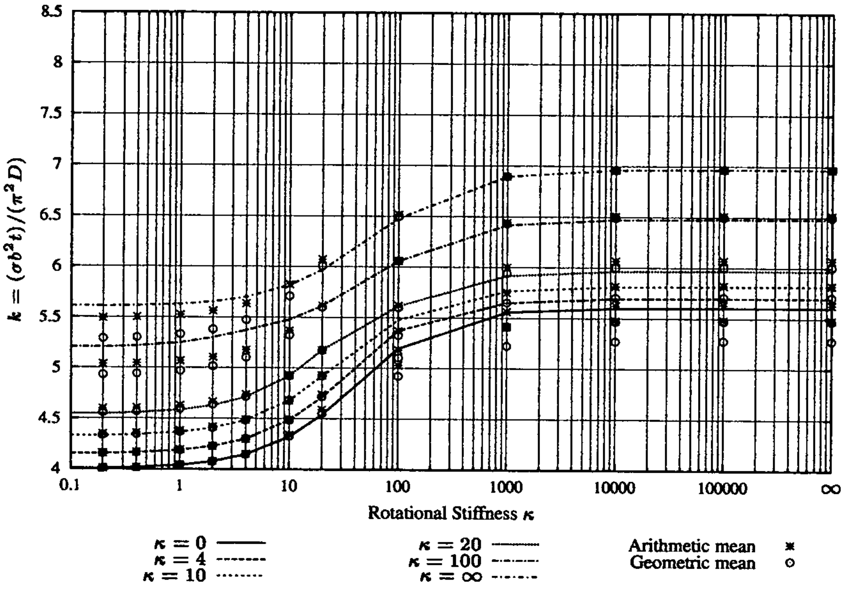

(a) $\alpha = 0°$

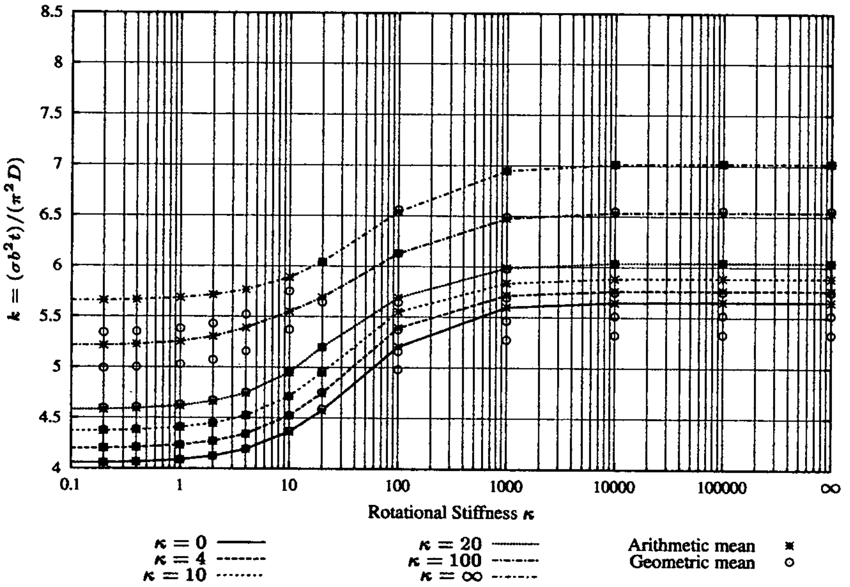

(b) $\alpha = 15°$

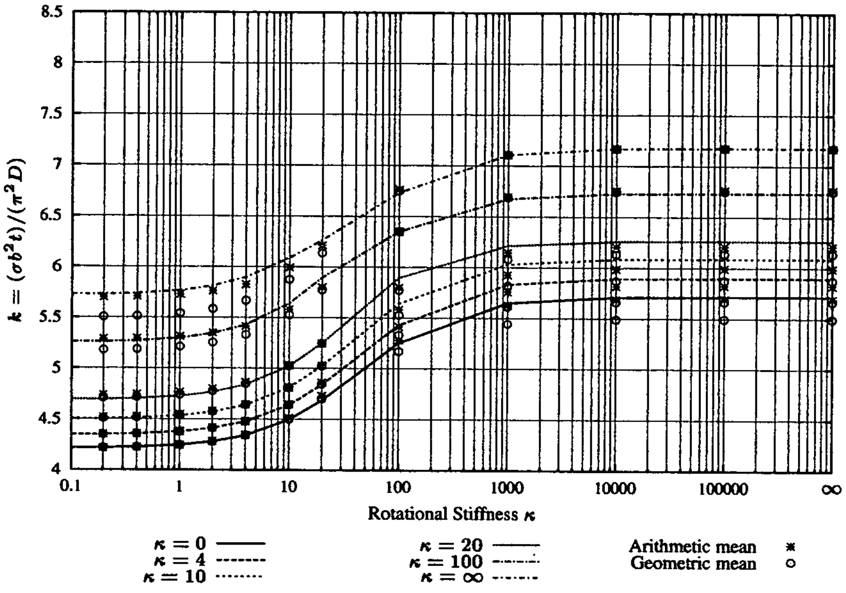

(c) $\alpha = 30°$

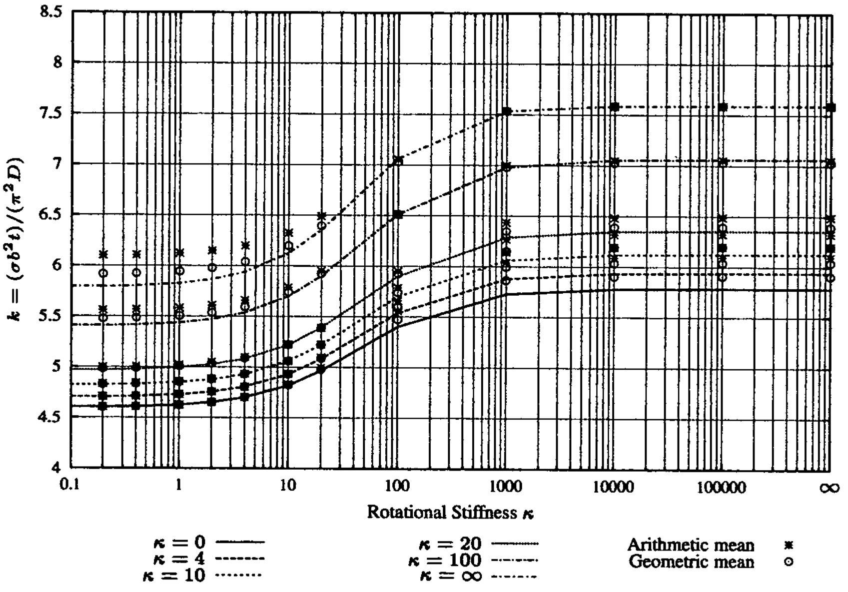

(d) $\alpha = 45°$

Figure 4.20: Graphical comparison of the geometric and arithmetic approximations to determine the buckling coefficient of a skew plate, with a uniform in-plane compression along simply supported transverse edges having different degrees of rotational stiffness along the top and bottom longitudinal edges. The plate has an aspect ratio $a/b' = 1.0$

loads of plates having unequal values of elastic restraint applied along the longitudinal edges. The results suggest that good buckling predictions can be made using the approximations.

Chapter 5

Elastic Buckling of Continuous Skew Plates

5.1 Introduction

The aim of this chapter is to present a method that uses ABAQUS finite element code to model the buckling strength of an infinite plate assembly continuous over simply supported skew bays. Thus, buckling modes may extend over many bays. The buckling predictions will provide a set of results comparable with the continuous buckling predictions published results of York [112] using VICONOPT described in Chapter 2. These results were also used for comparison in chapter 4. The chapter builds on these results and provides further verification of them.

In addition to the continuity results by York [112], Anderson [5], also produced buckling predictions for skew plates that are continuous in both the longitudinal and transverse directions. He solved the buckling problem using a Raleigh-Ritz implementation described in section 5.3.2.

5.2 Modelling

The result of incorporating continuity in the analysis of an infinite plate split into equal skew bays causes the critical buckling mode of the plates to increase in complexity and it may repeat over many bays. The critical buckling load can be significantly higher than for a simply supported isolated plate because the

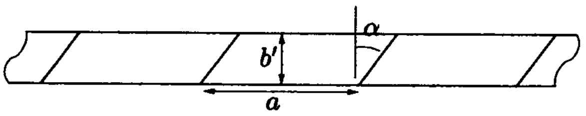

(a) Uni-axial continuity

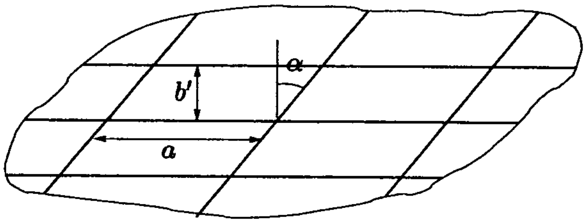

(b) Bi-axial continuity

Figure 5.1: Schematic showing definition of (a) uni-axial continuity and (b) biaxial continuity. In all cases, the plate outlines also correspond to a simply supported edge. The bays have a longitudinal length, a, transverse width b' and skew angle α.

continuity provides some rotational restraint its edges. The aim of the chapter is to present a method using finite element analysis to model a plate array sufficiently large to capture the entire critical buckling mode and to apply boundary conditions along the edge of the plate that accurately model continuity between adjacent plates. Determining the critical buckling stress of the plate involves a process of trial and error to model the required size of the plate array. The analysis of plates that are infinite in length only, termed *uni-axially continuous* (Figure 5.1(a)), with simply supported longitudinal edges and plates that are infinite in width and length, termed *bi-axially continuous* (Figure 5.1(b)), are both considered. In the former case, the buckling load of arrays of 'n' bays of plates in length are analysed and the result compared to the analysis of an array of $n + 1$ bays and the published continuity solutions by York [112]. In the case of bi-axial continuity, a similar method is followed, however two dimensional arrays of plates are required to model the infinite width assumption. Because the size of the model increases in proportion to the number of bays modelled, the maximum number of bays modelled is restricted to five to keep the size of the model analysis within the limits of the available computational resources. The finite element model will therefore only provide an approximation to the buckling load for an infinite plate, if the buckling mode relating to the critical buckling load repeats over more than five bays.

The plate model used in the finite element analysis is the same as that used in the previous chapter and comprises a uniform mesh of 900 (30 × 30) elements for a plate with an aspect ratio (ratio of width and length) of 1. This uniform mesh increases in proportion with the aspect ratio of the plate. ABAQUS type

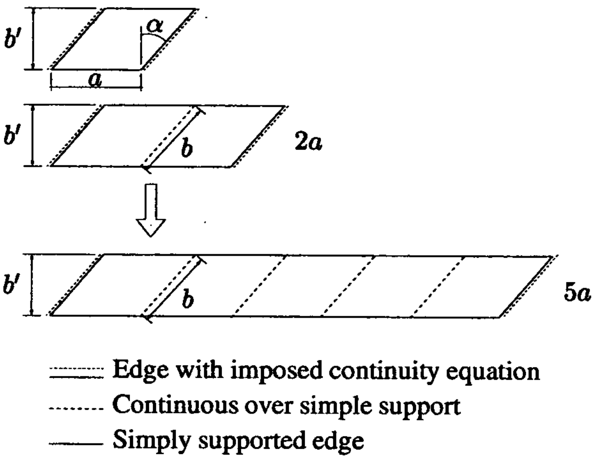

Figure 5.2: Typical plate arrays used in the uni-axial continuity finite element analysis showing nomenclature used throughout the chapter. Bays have a longitudinal length, a transverse width (normal to the plate longitudinal edge), b' and skew angle, α. Imposed continuity equations are given in equation. (5.3) and (5.5). Note that $b' = b\cos\alpha$

S8R5 [3] (see Appendix A) thin-shell elements are used with a width to thickness ratio of 1000 to ensure convergence on a thin-plate solution.

Figure 5.2 clarifies the approach for the uni-axial continuity case and defines the nomenclature used throughout the remainder of the chapter.

Plate arrays having a skew angle, $\alpha = 15°, 30°$ and $45°$ and aspect ratios, $0.5 \leq a/b \leq 2.5$ are analysed because results for comparison with previous continuity studies [5, 112] exist. Note that the results are presented in terms of plate width, b (where b is used for consistency with the preceeding chapter), is defined parallel to the skew edge of the plate. This results in plates with the same aspect ratio having a different planform area if the skew angle is changed. b' is defined as the width of the plate normal to the longitudinal edge, hence $b' = b\cos\alpha$. The use of b means that maintaining a constant stress to the plate causes the preload to change with skew angle and that direct comparison of changes in buckling strength with skew angle are not valid. Measuring b parallel to the skew edge is preferred because the results in the open literature are presented in the same manner and it therefore makes comparison easy.

5.2.1 Boundary Conditions

It is convenient to adopt a local 'skew' coordinate system to describe the boundary conditions that are applied to plate edges to model continuity over a number of adjacent panels, n. This local coordinate system is shown in Figure 5.3 from which it is clear that,

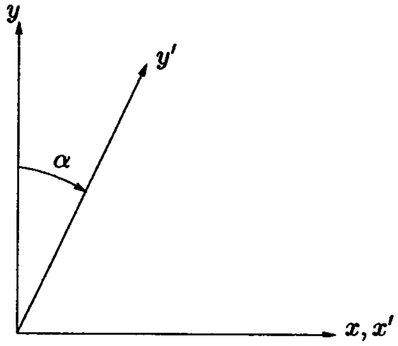

Figure 5.3: Definition of local skew axis system

$$x' = x - y \tan \alpha \tag{5.1}$$

$$y' = y \sec \alpha \tag{5.2}$$

Uni-axial Continuity

Continuity requires that displacement and differentials of displacement (rotations) are equal at the edges of adjacent plates. This condition is implicitly satisfied along the internal transverse edges of adjacent plates. At the outer transverse edges, (*i.e.* at $x = 0, na$) continuity is defined using sets a linear equations applied to the nodes that define the plate edge. It is possible to set one of four equations to enforce the boundary condition depending on whether the mode is symmetrical or unsymmetrical about the centre of the array and whether there are an even or odd number of plates in the array.

In the following equations, rotations are assumed to follow the sign convention dictated by the right-hand screw rule. The equations used are:

when n is even,

$$\frac{\partial w}{\partial x'}^{x'=0} \mp \frac{\partial w}{\partial x'}^{x'=na} = 0 \tag{5.3}$$

$$\frac{\partial w}{\partial y'}^{x'=0} \mp \frac{\partial w}{\partial y'}^{x'=na} = 0 \tag{5.4}$$

where w is out-of-plane displacement and x', y', z' correspond to the local skew coordinate system. The superscript in the equations shows the boundary on which the conditon is enforced. The $\mp$ corresponds to the equations that are required to represent buckling modes that are: (-) antisymmetrical about the centre of the array; (+) symmetrical about the centre of the array. For arrays that have an even number of bays in them, the '+' version of the equations does not make any real sense and would only be possible if the number of half-wavelengths in the outer bays were odd in one and even in the other.

A similar equation is used to enforce continuity for plate arrays that have an odd number of bays,

$$\frac{\partial w}{\partial x'}^{x'=0} \pm \frac{\partial w}{\partial x'}^{x'=na} = 0 \tag{5.5}$$

$$\frac{\partial w}{\partial y'}^{x'=0} \pm \frac{\partial w}{\partial y'}^{x'=na} = 0 \tag{5.6}$$

In this latter case, the ± correspond to the cases when the buckling mode gives: (+) have a buckling mode that is symmetric about the centre of the array and; (-) a buckling mode that is antisymmetric about the array centre. Both of these boundary condition cases are plausible. The latter describes a buckling mode that repeats over the 'n' bays. The former describes half a buckling mode that is symmetrical about one edge of the modelled array.

Figure 5.4 shows the basis for these equations.

The following boundary conditions are implicitly satisfied, and apply to the simply supported longitudinal edge.

$$w = 0 \quad \text{at} \quad x' = 0, a, 2a, \ldots, na \quad \text{and} \quad y' = 0, b\sec\alpha \tag{5.7}$$

Bi-axial Continuity

Similar boundary conditions can be applied to longitudinal edge of the plate to obtain the bi-axial continuity result.

Assuming that the uni-axial equations are also applied,

$$\frac{\partial w}{\partial x'}^{y'=0} \pm \frac{\partial w}{\partial x'}^{y'=mb\cos\alpha} = 0 \tag{5.8}$$

$$\frac{\partial w}{\partial y'}^{y'=0} \pm \frac{\partial w}{\partial y'}^{y'=mb\cos\alpha} = 0 \tag{5.9}$$

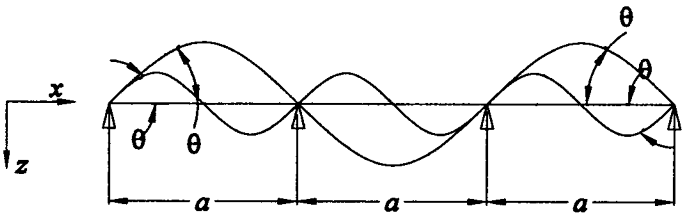

(a) Example buckling modes for an array with an odd number of equally sized bays.

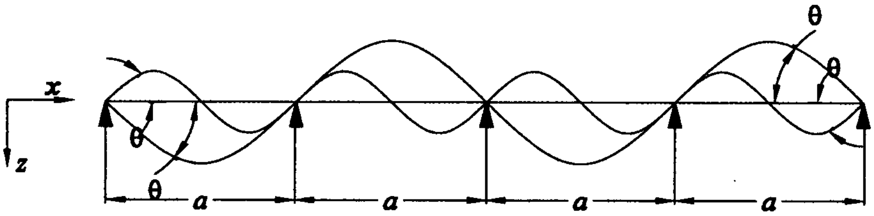

(b) Example buckling modes for an array with an even number of equally sized bays.

Figure 5.4: Example buckling modes over (a) an odd number of bays and (b) an even number of bays. In (a), the large wavelength (symmetrical buckling about the centre of the array) is resolved using the boundary condition imposed by the '+' case of Eqn. (5.5). The smaller wavelength buckling mode is antisymmetric about the array centre and therefore Eqn. (5.5) using the '-' case is used to make rotations along the transverse edge of the plate equal and opposite. In (b) both the large and small wavelength shown correspond to buckling modes that are antisymmetrical about the centre of the array and require that the rotations at the tranverse edge of the plate array are equal and opposite (the '-' case of Eqn. (5.3)). The '+' case of Eqn. (5.3) inferring that transverse edge rotations be equal and in the same direction would require that the two outer panels buckle with a different number of half-wavelengths.

where m is the number of tranverse bays that make up the array.

In the case of bi-axial continuity, there is a conflict when modelling the corner nodes; two constraints cannot be applied to the same node. A compromise must therefore be met in which the corner nodes are assumed to span in one direction only, or are omitted completely from the continuity equations. Tests confirmed that the effect of these corner nodes were negligible. The corner nodes are made to couple longitudinal arrays of bays in the following analysis.

The plate arrays are restricted to a maximum number of five bays because of limited computer resources.

5.2.2 Loading

Only one loadcase, that of a uniform, in-plane compressive stress acting along the skew, transverse edges is considered in keeping with the loading in the previous chapter.

5.3 Results

Results are presented in a tabular format to allow comparison with the continuity results (York [112]) in detail. Successful modelling using the finite element model should predict buckling loads that are in agreement with these results if arrays of no more than five plates are required to model the solution. If the solution requires more than five bays to modelled, the finite element solution will give an upper bound solution for the problem.

Results are presented for plates with aspect ratios $a/b = 0.5, 0.6, \ldots, 2.5$ for both the uni-axial and bi-axially continuity cases to allow comparison with the continuity results by York [112] which are presented for a definition of aspect ratio in which b is defined parallel to the y' axis of Figure 5.3. Buckling predictions for all of these aspect ratios are produced for $\alpha = 15°, 30°, 45°$. Note that the buckling stress of square or rectangular plate ($\alpha = 0°$) is omitted from the study because continuity in this case causes a buckling mode that is the same as a simply supported, isolated plate. In this case there are no strength gains associated with continuity of the plate over simple supports.

The critical buckling load is presented using the same dimensionless coefficient, k, as in the previous chapter,

$$k = \frac{\sigma b^2 t}{\pi^2 D} \tag{5.10}$$

where b is as previously defined (see Figure 5.2), t is the plate thickness and D is the plate flexural rigidity.

The plate buckling predictions are presented in Tables 5.1 and 5.2 together with the comparison continuity results. The tables show only the critical buckling predictions for the infinite plate analysis together with the value of ξ (and in the case of bi-axial continuity ξ and g) used to obtain them in the case of the continuous analysis and the number of bays, n, for the current finite element analysis. The definition of ξ and g are not important here (they are explained in full in the section 2.5), but they correspond to the half–wavelengths of the critical buckling mode given in Table 5.3.

All the results for arrays having an odd number of plates are obtained using the negative ('-') version on equation (5.5). For arrays with an even number of equal bays, the negative ('-') version of equation (5.3) is used. These boundary conditions constraints gave the lowest buckling loads for the plates arrays. In the case of $n = 1$ for the uni-axial continuity case there was an exception to this finding. In this case if the buckling mode is repetitive over one bay, the buckling load for the negative version of equation (5.5) gives higher buckling loads than the positive version. The true buckling load of the uni-axial continuous plate in this case is given by the $n = 2$ array in Table 5.2 and, predictably, is the same as analysis of an $n = 1$ array with the positive version of equation (5.5). When the buckling load repeats over two bays for the uni-axial continuity case, both the $n = 1$ array with the negative version of the boundary conditon (equation (5.5)) and the $n = 2$ array with the negative boundary condition give the same buckling load. This is because the critical buckling modes are anti–symmetrical about the centre of the plate array and the buckling mode of the plate is therefore captured in both analyses.

5.3.1 A note on the VICON [112] comparisons

The continuous comparison taken from the open literature after York [112] are obtain using the VICON buckling routine in VICONOPT, an account of which is given for completeness in section 2.5.

VICON assumes that the critical buckling mode, leading to the critical buckling load of the plate repeats over M bays *i.e.* over a length Ma. VICON produces buckling solutions for each possible buckling mode, m where $m = n + qM, (q = 0, \pm 1, \pm 2, \ldots, q_{max})$ and is the number of full wavelengths making up the buckling mode. All modes are obtained by solving the eigenvalue equation for each 'n' in the previous equation given by,

$$-M'' \leq n \leq M' \qquad (5.11)$$

where M'' and M are the integer parts of $(M - 1)/2$ and $M/2$. Solutions for a number of M bays will yield the lower boundary buckling result required provided that M is large enough. This is synonymous

Table 5.1: Comparison of critical buckling loads, given as the buckling factor, $k = (\sigma b'^2 t)/(\pi^2 D)$, for uni-axially continuous skew plates for VICON and the current finite element analysis. ξ relates to the critical half-wavelength of the buckling mode in the VICON analysis and is defined in section 2.5 and Table 5.3. The n in the table relates to the current analysis and gives the number of plates in the analysed array used to obtain the buckling prediction. Note that the aspect ratio is given in terms on b (*i.e.* plate transverse width measured parallel to the longitudinal edge).

	$\alpha = 15°$				$\alpha = 30°$				$\alpha = 45°$			
	VICON†		Current		VICON†		Current		VICON†		Current	
$a\cos\alpha/b'$	k	ξ	k	n	k	ξ	k	n	k	ξ	k	n
0.5	6.913	1.0	6.917	1.0	9.295	1.0	9.318	1	14.949	0.6	15.302	1
0.6	5.709	1.0	5.712	1.0	7.739	1.0	7.759	1	12.117	0.2	12.746	1
0.7	5.043	1.0	5.046	1.0	6.840	1.0	6.858	1	10.266	0.0	10.295	2
0.8	4.676	1.0	4.678	1.0	6.291	1.0	6.306	1	8.831	0.0	8.904	2
0.9	4.490	1.0	4.492	1.0	5.946	1.0	5.958	1	7.620	0.0	7.682	2
1.0	4.425	1.0	4.426	1.0	5.725	1.0	5.736	1	6.772	0.1	6.821	2
1.1	4.445	1.0	4.446	1.0	5.589	1.0	5.597	1	6.188	0.1	6.225	2
1.2	4.530	1.0	4.531	1.0	5.507	1.0	5.513	1	5.776	0.9	5.797	2
1.3	4.666	1.0	4.667	1.0	5.433	0.4	5.436	3	5.492	0.9	5.504	2
1.4	4.721	0.0	4.722	2.0	5.288	0.0	5.290	2	5.312	1.0	5.318	2
1.5	4.535	0.0	4.536	2.0	5.084	0.0	5.084	2	5.199	1.0	5.200	2
1.6	4.400	0.0	4.400	2.0	4.923	0.0	4.923	2	5.099	0.9	5.106	2
1.7	4.305	0.0	4.306	2.0	4.799	0.0	4.799	2	4.904	0.9	4.909	1
1.8	4.245	0.0	4.245	2.0	4.706	0.0	4.705	2	4.760	0.9	4.763	1
1.9	4.212	0.0	4.212	2.0	4.638	0.1	4.637	2	4.656	0.9	4.657	2
2.0	4.202	0.0	4.202	2.0	4.591	0.1	4.589	2	4.578	0.1	4.579	2
2.1	4.212	0.0	4.212	2.0	4.559	0.1	4.557	2	4.526	0.1	4.526	2
2.2	4.239	0.0	4.238	2.0	4.536	0.5	4.536	3	4.492	0.1	4.492	2
2.3	4.280	0.0	4.280	2.0	4.515	1.0	4.515	2	4.469	0.0	4.469	2
2.4	4.303	1.0	4.302	1.0	4.479	1.0	4.479	2	4.436	0.1	4.434	2
2.5	4.241	1.0	4.240	1.0	4.424	1.0	4.424	2	4.381	0.1	4.379	2

† After York [112]

Table 5.2: Comparison of critical buckling loads, given as the buckling factor, $k = (\sigma b'^2 t)/(\pi^2 D)$, for bi-axially continuous skew plates for VICON and the current finite element analysis. ξ relates to the critical half-wavelength of the buckling mode in the VICON analysis and is defined in section 2.5 and Table 5.3. The n in the table relates to the current analysis and gives the number of plates in the analysed array used to obtain the buckling prediction.

	$\alpha = 15°$				$\alpha = 30°$				$\alpha = 45°$			
	VICON†		Current		VICON†		Current		VICON†		Current	
a/b'	k	ξ, g	k	n, m	k	ξ, g	k	n	k	ξ	k	n
0.5	6.969	1.0,1.0	6.969	1,1	9.569	1.0,1.0	9.562	1,1	15.794	0.5,2.0	16.014	1,1
0.6	5.776	1.0,1.0	5.776	1,1	8.064	1.0,1.0	8.064	1,1	12.790	0.3,2.0	12.912	3,2
0.7	5.125	1.0,1.0	5.125	1,1	7.237	1.0,1.0	7.237	1,1	10.979	0.2,2.0	11.116	3,2
0.8	4.772	1.0,1.0	4.773	1,1	6.782	1.0,1.0	6.782	1,1	9.572	0.0,2.0	9.573	2,2
0.9	4.603	1.0,1.0	4.603	1,1	6.558	1.0,1.0	6.558	1,1	8.673	0.1,2.0	8.695	2,2
1.0	4.555	1.0,1.0	4.555	1,1	6.490	1.0,1.0	6.490	1,1	7.941	0.2,2.0	7.976	3,2
1.1	4.594	1.0,1.0	4.594	1,1	6.537	1.0,1.0	6.537	1,1	7.370	0.4,2.0	7.366	3,2
1.2	4.700	1.0,1.0	4.699	1,1	6.515	0.2,2.0	6.668	1,1	6.912	0.5,2.0	6.944	1,3
1.3	4.857	1.0,1.0	4.857	1,1	6.311	0.4,2.0	6.413	2,2	6.545	0.6,2.0	6.542	1,3
1.4	5.060	1.0,1.0	5.059	1,1	6.124	0.6,2.0	6.211	3,2	6.238	0.8,2.0	6.274	1,2
1.5	4.874	1.0,2.0	4.874	2,1	5.963	0.8,2.0	5.991	1,2	5.961	1.0,2.0	5.961	1,2
1.6	4.733	1.0,2.0	4.733	2,1	5.818	1.0,2.0	5.818	1,2	5.760	1.0,2.0	5.760	1,2
1.7	4.636	1.0,2.0	4.636	2,1	5.668	1.0,2.0	5.667	1,2	5.614	0.8,2.0	5.642	1,2
1.8	4.575	1.0,2.0	4.574	2,1	5.567	1.0,2.0	5.567	1,2	5.369	0.2,2.0	5.532	1,2
1.9	4.542	1.0,2.0	4.541	2,1	5.478	0.5,2.0	5.501	1,2	5.218	0.2,2.0	5.429	1,2
2.0	4.534	1.0,2.0	4.533	2,1	5.410	0.5,2.0	4.929	1,3	5.042	0.2,2.0	5.214	3,2
2.1	4.546	1.0,2.0	4.546	2,1	5.343	0.3,2.0	4.868	1,3	5.023	0.2,2.0	5.107,	3,2
2.2	4.577	1.0,2.0	4.577	2,1	5.284	0.2,2.0	4.831	1,3	4.953	0.2,2.0	5.008	2,2
2.3	4.624	1.0,2.0	4.624	2,1	5.231	0.0,2.0	4.808	1,3	4.874	0.2,2.0	4.921	2,2
2.4	4.686	1.0,2.0	4.685	2,1	5.174	0.0,2.0	4.798	1,3	4.806	0.2,2.0	4.978	1,3
2.5	4.653	1.0,1.0	4.652	1,1	5.133	0.2,2.0	4.778	1,3	4.819	0.1,2.0	4.905	1,2

† After York [112]

Table 5.3: Half-wavelengths, λ corresponding to the ξ values used in the VICON analysis used for comparison with the ABAQUS continuous solution. Maximum values of m are given by $q_{\text{max}} = 10$. After York [112]

ξ	M	n	$m = qM$	$\lambda_m = Ma/2m$
0	1	0	$0; 1; 2; \ldots, 10$	$\infty; a/2; a/4; \ldots; a/20$
0.1	20	1	$1; 21; -19; 41; -39; \ldots; 201; -199$	$10a; 10a/21; -10a/19; 10a/41; -10a/39; \ldots; 10a/201; -10a/199$
0.2	10	1	$1; 11; -9; 21; -19; \ldots; 101; -99$	$5a; 5a/11; -5a/9; 5a/21; -5a/19; \ldots; 5a/101; -5a/99$
0.3	20	3	$3; 23; -17; 43; -37; \ldots; 203; -197$	$10a/3; 10a/23; -10a/17; 10a/43; -10a/37; \ldots; 10a/203; -10a/197$
0.4	5	1	$1; 6; -4; 11; -9; \ldots; 51; -49$	$5a/2; 5a/12; -5a/8; 5a/22; -5a/18; \ldots; 5a/102; -5a/98$
0.5	4	1	$1; 5; -3; 9; -7; \ldots; 41; -39$	$2a; 2a/5; -2a/3; 2a/9; -2a/7; \ldots; 2a/41; -2a/39$
0.6	10	3	$3; 13; -7; 23; -17; \ldots; 103; -97$	$5a/3; 5a/13; -5a/7; 5a/23;$ dat$-5a/17; \ldots; 5a/103; -5a/97$
0.7	20	7	$7; 27; -13; 47; -33; \ldots; 207; -193$	$10a/7; 10a/27; -10a/13; 10a/47; -10a/33; \ldots; 10a/207; -10a/193$
0.8	5	2	$2; 7; -3; 12; -8; \ldots; 52; -48$	$5a/2; 5a/7; -5a/3; 5a/12; -5a/8; \ldots; 5a/52; -5a/48$
0.9	20	9	$9; 29; -11; 49; -31; \ldots; 209; -191$	$10a/9; 10a/29; -10a/11; 10a/49; -10a/31; \ldots; 10a/209; -10a/191$
1.0	2	1	$1; 3; 5; \ldots; 21$	$a; a/3; a/5\ a/21$

with the finite element solution, in which a sufficiently large plate array has to be analysed to converge on the exact VICON solution.

Transverse repetition, *i.e.* to produce bi-axially continuous results, is modelled using similar assumptions about the possible buckling modes made in the previous paragraphs. The transverse buckling mode is assumed to repeat over a number of repeating transverse bays, P. The length over which the buckling mode repeats is therefore Pb, if b' is assumed to be a width of the plate (normal to the longitudinal edge). Hence the eigenvalue solutions are found for each tranverse wavelength, λ_T, given by,

$$\lambda_T = Pb/g \qquad g = -(P-1), \ldots, -1, 0, 1, \ldots, P \tag{5.12}$$

The presented VICON results consider the maximum value of q, $q_{max} = 10$, $0.0 \leq \xi \leq 1.0$ and $P \leq 2$. The number of bays, M, over which the buckling mode was assumed to repeat for each value of ξ is given in Table 5.3 together with values for n and the half-wavelengths, λ_m.

5.3.2 Results by Anderson [5]

A brief overview of the method used by Anderson to produce bi-axially continuous buckling solutions for infinite skew plates is given in this section. The results of his analysis are compared with the current solution and the continuous buckling prediction using VICONOPT (by York [112]). Anderson provides a simple expression for the deflected shape of the buckled plate. His predicted buckling mode is compared with that obtained from the current finite element solution.

Anderson [5] produced results for a bi-axially continuous plate using a simplified approximate method and a more exact method using the Raleigh-Ritz method to minimize the governing energy equations. In the first case, Anderson assumes a deflection function composed of two separate terms, w_1 and w_2 below,

$$w_1 = \sin\frac{p\pi x'}{Na}\sin\frac{q\pi y'}{Mb} \tag{5.13}$$

$$w_2 = \cos\frac{j\pi}{Na}\left(x' \pm \frac{Na}{Mb}y'\right) \tag{5.14}$$

where x' and y' are x and y in the local coordinate system given in Figure 5.3 and b is the skew transverse plate width parallel to the edge (*i.e.* in the local coordinate system). The complete deflection function is the product of w_1 and w_2 (*i.e.* $w = w_1 \times w_2$). The first part of the deflection function, w_1 is synonymous with the deflection function for a simply supported square or rectangular plate written using skew coordinates with p/N and q/M being integers. p/N and q/M describe the number of half–wavelengths that make up the buckling pattern in the longitudinal and transverse plate direction respectively. The second term in the deflection function (w_2 part) produces nodal lines (when $w_2 = 0$) in the buckling patterns at a spacing governed by the ratio of the constants j/N and with a slope N/M.

The deflection function is used to minimise the energy equations, written in terms of the local skew coordinates, with resect to the coefficients described in the previous paragraph (p/N, q/M, j/N and N/m), thus finding a value for the critical buckling load of the plate. Solutions for the coefficients are used to determine whether the critical buckling mode of the plate is of one of the forms given in Table 5.4.

More exact analysis is carried out for discrete plate parameters using the form of the buckling mode from the approximate analysis to construct a deflection function as a trigonometric series having 3 terms. The energy equations are now solved using the Rayleigh-Ritz method. The trigonometric series has to satisfy the chosen boundary conditions of zero deflection and continuity of differentials for each term and is given by,

Table 5.4: Values of $S_{1,2,3,4}$ for the trigonometric series in Eqn.(5.15) [5]

Form of buckling mode	S_1	S_2	S_3	S_4
symmetric and periodic over a, b'	$2,4,6$	$2,4,6$	$1,3,5$	$1,3,5$
symmetric and periodic over $2a, 2b'$	$1,3,5$	$1,3,5$	$2,4,6$	$2,4,6$
antisymmetric and periodic over $a, 2b'$	$2,4,6$	$1,3,5$	$1,3,5$	$2,4,6$
antisymmetric and periodic over $2a, b'$	$1,3,5$	$2,4,6$	$2,4,6$	$1,3,5$

$$\begin{aligned} w &= \sum_{m=S_1}^{\infty} \sum_{n=S_2}^{\infty} a_{mn} \sin \frac{m\pi x'}{a} \sin n\pi y' b' + \\ &+ \sum_{m=S_3}^{\infty} \sum_{n=S_4}^{\infty} b_{mn} \left[\cos \frac{(m-1)\pi x'}{a} - \cos \frac{(m+1)\pi x'}{a} \right] \times \\ &\times \left[\cos \frac{(n-1)\pi x'}{b'} - \cos \frac{(n+1)\pi x'}{b'} \right] \end{aligned} \tag{5.15}$$

where $S_{1,2,3,4}$ depend on the form of the deflection function and are, for completeness, given in Table 5.4.

Typical buckling modes given by solutions to equations (5.13) and (5.14) that correspond to aspect ratios at which Anderson [5] provides calculations using the above analysis are compared to the comparable current finite element solution in Figures 5.5 - 5.9. Values of the constants in the result to produce the buckling plots are included in the relevant figure caption.

Tabulated buckling predictions results from Anderson's more exact analysis are given in Table 4.4 in Chapter 4.

5.4 Discussion of Results

Generally there is excellent correlation between the results obtained using the VICON and finite element analysis, although it is clear that in some cases, a larger number of bays are required to be modelled to achieve the continuous results. Discussion of the results for the uni-axial and bi-axial cases are considered separately below together with a quantitative account of the differences between the sets of buckling predictions.

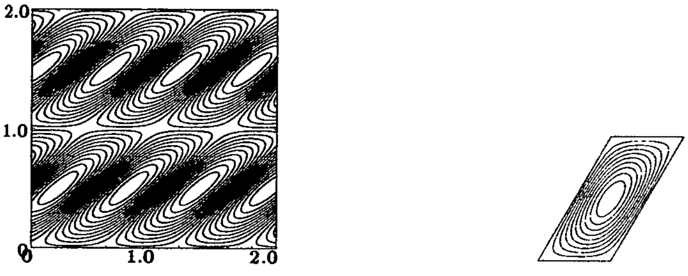

(a) (b)

Figure 5.5: Buckling mode for a bi-axial continuous plate, predicted by: Anderson (a) (the buckling mode is periodic over $2a$ and $2b'$); and finite element (b) (the critical solution is given for an array of $n = 1$, $m = 2$), for $\alpha = 30°$, $a/b = 0.577 = a\cos\alpha/b = 0.5$. Buckling factors are given as $k = 9.60$ for Anderson's solution, $k = 9.562$ for finite element and $k = 9.569$ for VICON. Factors in eq. (5.13) and (5.14) used to produce Anderson's buckling pattern are: $p/N = q/M = 1.0, j/N = j/M = 0.0$.

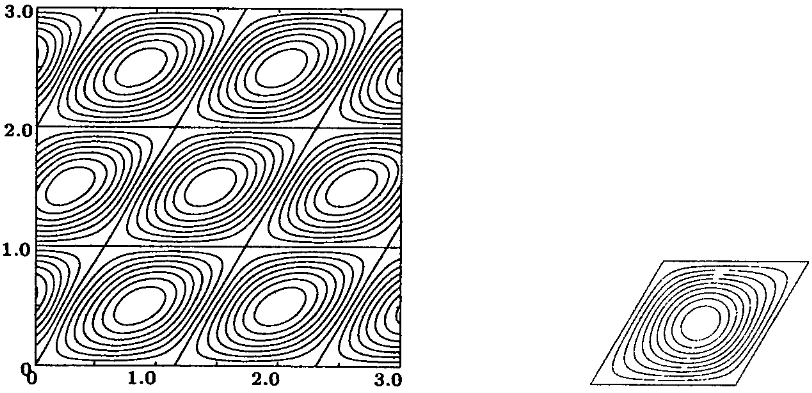

(a) (b)

Figure 5.6: Buckling mode for a bi-axial continuous plate, predicted by: Anderson (a) (The buckling mode is periodic over $2a$ and $2b'$); and finite element (b) (The critical solution is given for $n = 1$, $m = 1$), for $\alpha = 30°$, $a/b = 1.0$. Buckling factors are given as $k = 6.62$ for Anderson's solution, $k = 6.490$ for finite element and $k = 6.490$ for VICON. Factors in eq. (5.13) and (5.14) used to produce Anderson's buckling pattern are:
$p/N = q/M = 1.0, j/N = j/M = 0.0$.

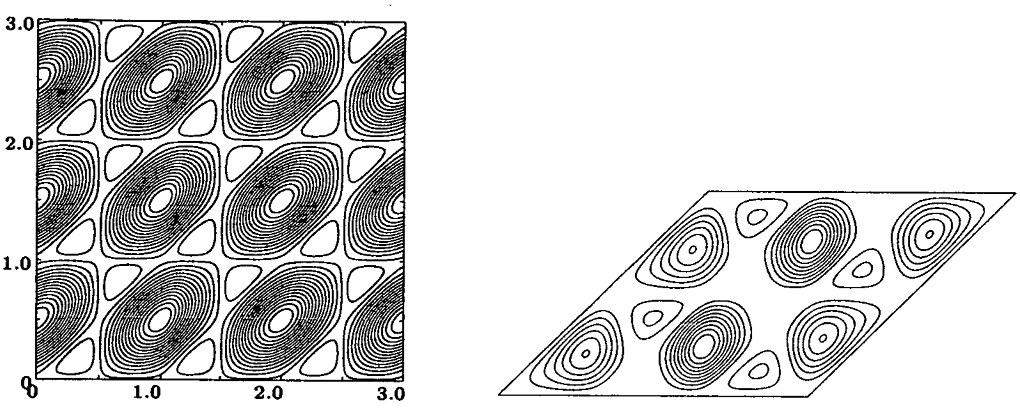

(a) (b)

Figure 5.7: Buckling mode for a bi-axial continuous plate, predicted by Anderson (a) (the buckling mode is periodic over a and b), for $\alpha = 45°$, $a/b = 1.0$ giving $k = 11.46$. Comparison is made with the finite element solution (b) (the critical buckling prediction is made with an array $n = 3$, $m = 2$) for $\alpha = 45°$, $a/b = 0.990 = 0.7/cos\alpha$ for which Anderson's buckling mode is valid. The critical buckling load predicted by the finite element model is given by $k = 11.116$ and the VICON result for this same case is $k = 10.979$. Factors used in eq. (5.13) and (5.14) to produce Anderson's buckling pattern are $p/N = q/M = j/N = j/M = 1.0$.

5.4.1 Uni-axial Continuity Results

Buckling curves for the uni-axial continuity case are shown in Figure 5.10(a) for the VICON and finite element solutions. For the 15° uni-axial continuity results, finite element and VICON results agree to 3 d.p. over the range of aspect ratios considered. In the case of the finite element model, this result is achieved by considering arrays of only 1 or 2 plates corresponding to a buckling mode that is repetitive over 1 or 2 bays. The buckling mode is repetitive over two bays if the critical buckling load of the plates is given by analysis of a plate array with $n = 1$ and over one bay if the critical buckling load is given by an array with $n = 1$. The transition at which the continuous solution is obtained by using either of these arrays is determined when the critical buckling mode changes from being comprised of an odd number of wavelengths to being an even number of wavelengths. As discussed previously, the boundary conditions pertain to buckling modes that are symmetrical or anti-symmetrical about the centre of the plate array, producing rotations at the transverse edges that are equal and opposite or equal respectively. Consideration of Figure 5.10(a) shows that buckling mode changes at $a\cos\alpha/b = 1.3 - 1.4$ and $a\cos\alpha/b = 2.3 - 2.4$ coincide with the change in array size required to model the continuous solution by VICONOPT.

Figure 5.11 shows graphically, the difference between the continuous VICONOPT and finite element so-

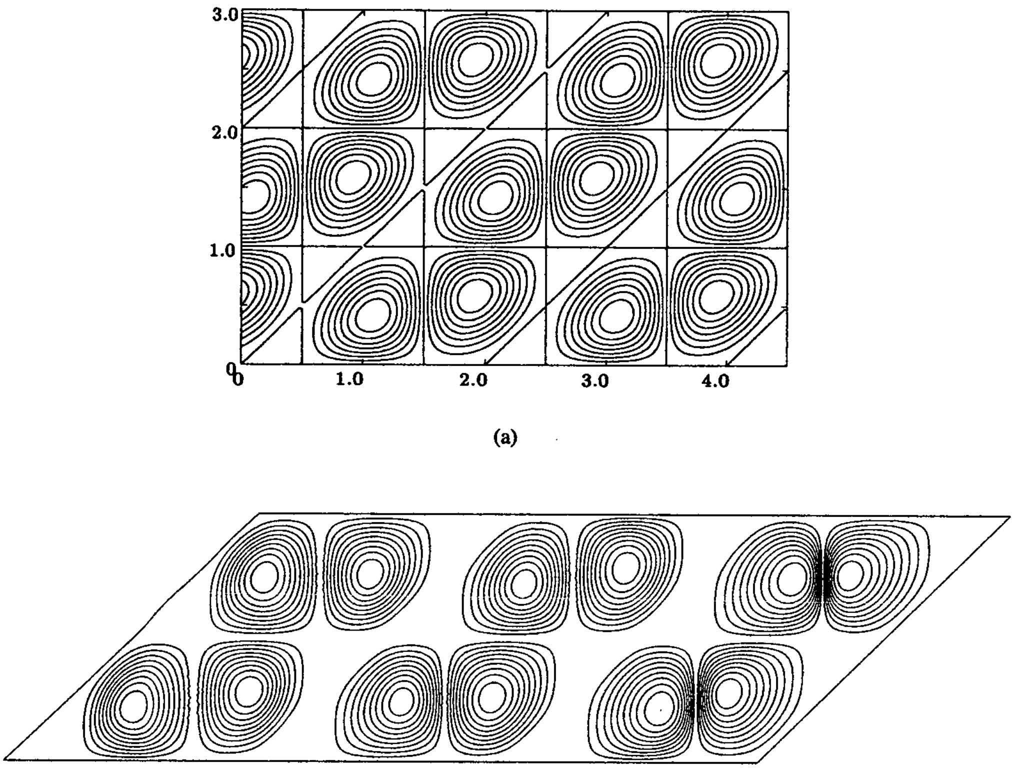

(b)

Figure 5.8: Buckling mode for a bi-axial continuous plate, predicted by Anderson (a) (the buckling mode is periodic over $2a$ and b), for $\alpha = 45°$, $a/b = 2.0$ giving $k = 6.36$. Comparison is made with the finite element solution (b) (the critical buckling predication is made with array size, $n = 1$, $m = 2$) for $\alpha = 45°$, $a/b = 1.980 = 1.5/cos\alpha$ for which Anderson's buckling mode is valid. The critical buckling load predicted by the finite element model is given by $k = 6.274$ and the VICON result for this same case is $k = 6.238$. Factors used in eq. (5.13) and (5.14) to produce Anderson's buckling pattern are $p/N = q/M = j/M = 1.0$, $j/N = 2.0$

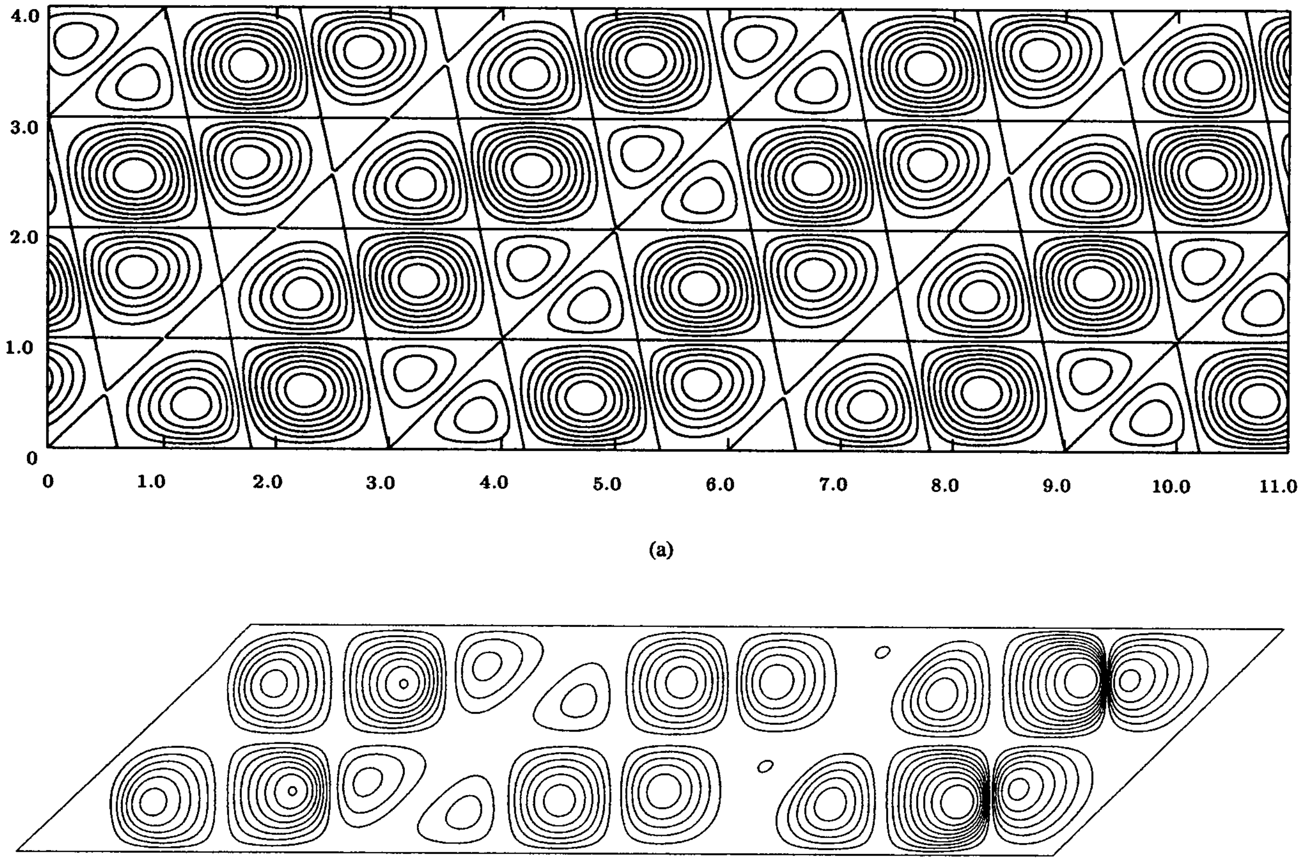

(b)

Figure 5.9: Buckling mode for a bi-axial continuous plate, predicted by Anderson (a) (the buckling mode is periodic over a and b), for $\alpha = 45°$, $a/b = 3.0$, $k = 5.11$. Comparison is made with the finite element solution (b) (the critical buckling prediction is made with array size, $n = 3$, $m = 2$) for $\alpha = 45°$, $a/b = 2.970 = 2.1/cos\alpha$ for which Anderson's buckling mode is valid. The critical buckling load predicted by the finite element model is given by $k = 5.107$ and the VICON result for this same case is $k = 5.023$. Factors used in eq. (5.13) and (5.14) to produce Anderson's buckling pattern are $p/N = q/M = j/M = 1.0$. $j/N = 2.0$

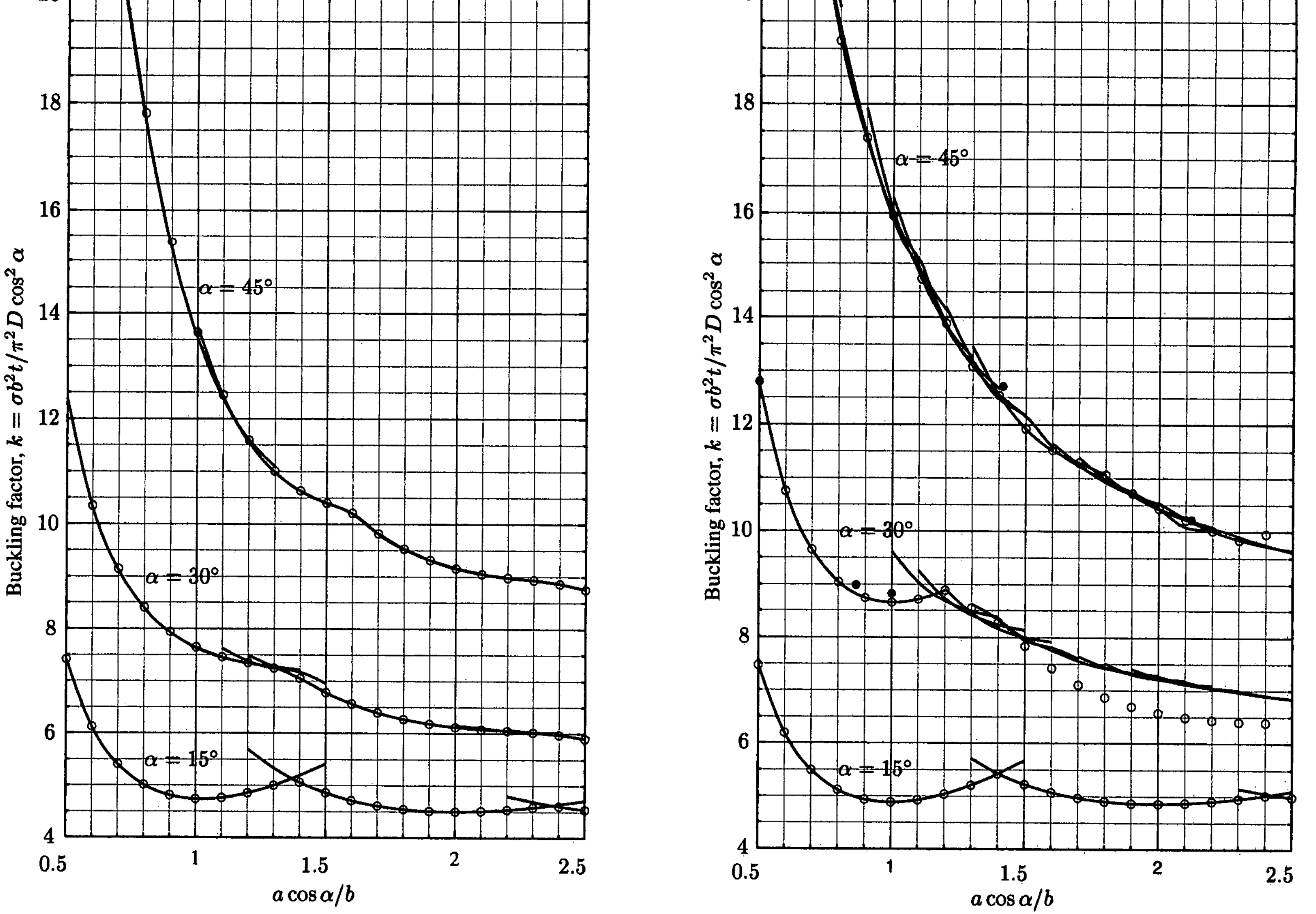

(a) Uni-axial Continuity Case

(b) Bi-axial Continuity Case

Figure 5.10: Buckle plots from VICON (lines) compared with the critical buckling load from the finite element solution (○) and Anderson [5] (●). In order to spread the curves for each of the skew angles, the buckling factor has been divided by $\cos^2 \alpha$. This effectively presents the buckling factor in terms of b (*i.e.* the breadth of the plate measured parallel to the skew edge). The aspect ratio has been multiplied by $\cos \alpha$, which is therefore also effectively written in terms of b.

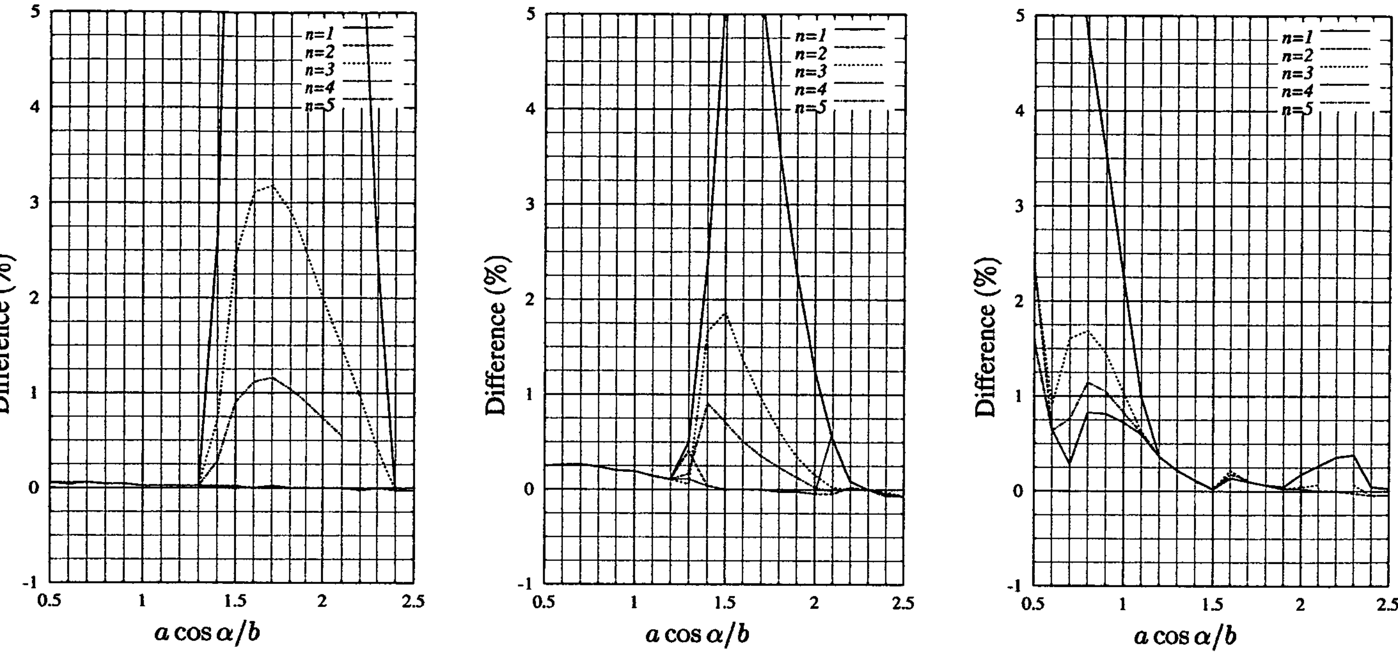

(a) $\alpha = 15°$

(b) $\alpha = 30°$

(c) $\alpha = 45°$

Figure 5.11: Graphical representation of the difference between VICON and finite element results for the uni-axial continuity case shown as a percentage for each value of 'n' used in the finite element analysis. A positive difference infers that the finite element results is greater than the VICON result.

lution for all values of 'n' making up the uni-axial plate array and skew angles, α. From the figure, it can clearly be seen that the buckling stress predictions for the other two skew angles are within 1% of the VICON solution. These buckling predictions are generally made by consideration of a plate array no larger than 2 bays.

In cases where the critical buckling mode repeats exactly over a set number of bay lengths, a plate array with a factor of this array will buckle with the same critical buckling factor. For example in the 45° case, at some aspect ratios, plate arrays with $n = 2$ and $n = 4$ have buckling modes that repeat over exactly two bays and hence the same critical buckling load. These solutions could potentially give the critical buckling factor for the continuous problem and it is this repetitious calculation that VICONOPT avoids by solving only for half-wavelengths chosen using the method in section 5.3.1. The fact that the two array sizes, which are factors of each other, give the same buckling predictions proves that the solution has converged.

Although not included in the tabulated results, it is of interest to note that analysis of the plate arrays using the opposite equation to that which was found to give the lowest buckling load (*i.e.* equations which impose rotations equal and opposite for an array having an even number of bays instead of equal and of the same sign), gave higher buckling values except in the cases previously discussed. The difference between the critical buckling load using both sets of equations decreased as the number of bays in the array increased. This result infers that as the plate array increases in size, the edge boundary conditions on the array have a diminishing effect on the plate buckling load. This observation serves to validate the continuous result given in the previous chapter for which the critical buckling load for a continuous plate predicted by VICON was approximated using an array of seven plates with clamped transverse edges. Obviously, the analysis employed herein is far more effective in that it is efficient in the plate array needed to give sufficient accuracy. Further in some cases, it can give critical buckling loads that are exactly the same as the critical buckling loads predicted by VICON to an accuracy of three decimal places.

5.4.2 Bi-axial Continuity

The complexity of the buckling mode increases when bi-axial continuity is considered especially when the skew angle of the plate increases. However, the finite element results are seen to generally be in good agreement with the VICON results for smaller angles of skew. Figure 5.12 shows the difference between the VICON and finite element results in the same graphical format as for the uni-axial continuous case. The figure shows that in all cases, a buckling predictions are made within 2% of that predicted by the published continuity solutions.

For plates with $\alpha = 15°$, which show the closest correlation, plate arrays having $n = 1, m = 1$ and $n = 2, m = 1$ produce buckling solutions in agreement to 3 d.p. with the VICON solution. The point at which the array size needed to model the VICON results shifts from being $n = 1, m = 1$ to $n = 2, m = 1$ is given by the cusp on the buckling curve for the bi-axial continuity case shown in figure 5.10(b) for the buckling mode shifting from comprising one half-wavelength to two half-wavelengths at $a/b \approx 1.35$. When three half-wavelengths make up the critical mode, the single bay ($n = 1, m = 1$) models the critical buckling mode as is expected. This second cusp occurs at $a/b \approx 2.4$.

Interesting results are obtained for the 30° case. From the Figure 5.12 the finite element and published continuity results are in good agreement for $a/b \leq 1.2$. There is a slight increase in the difference between the two sets of results until $a/b = 1.5$ when the finite element solution is lower than the published continuity solution for the remaining aspect ratio considered. The finite element array producing these results has $n = 1, m = 3$. Therefore, the finite element model considers a buckling mode, symmetrical about an outer transverse edge and hence is repetitive over six bays. In the continuous analysis, it was assumed that the transverse buckling mode would repeat over no more then 2 bays. These finite element solutions would

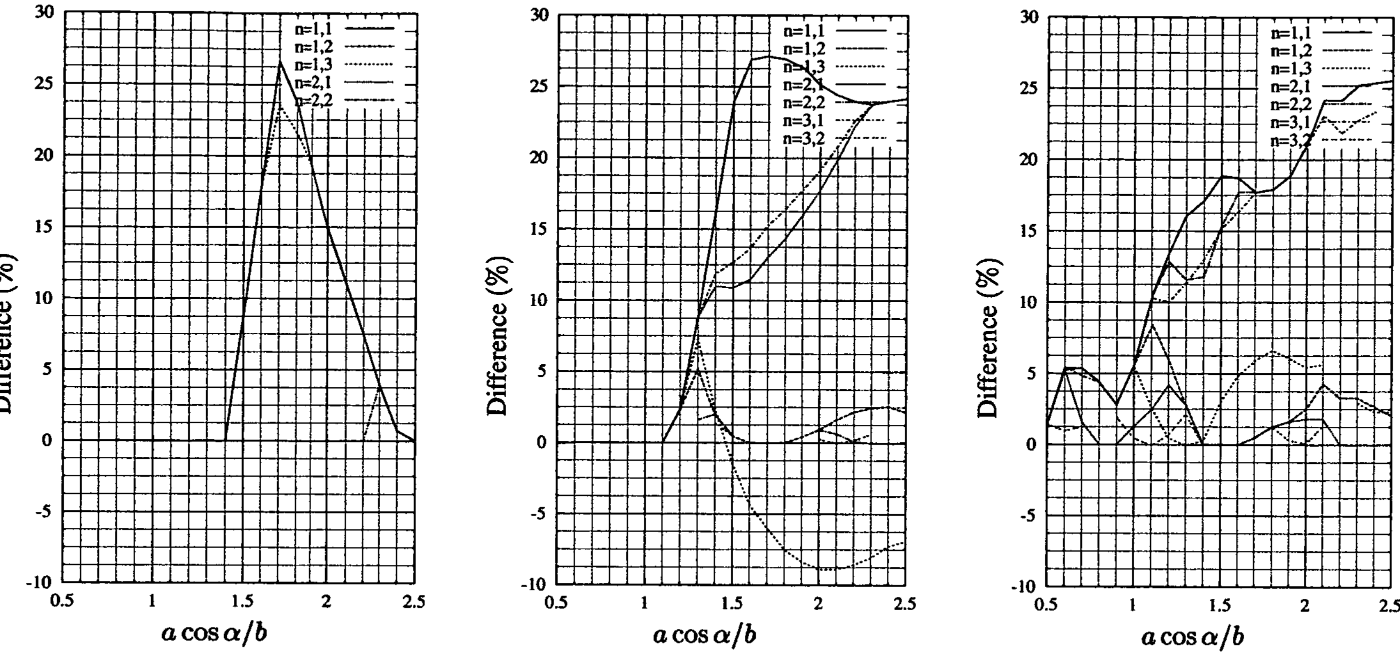

(a) $\alpha = 15°$ (b) $\alpha = 30°$ (c) $\alpha = 45°$

Figure 5.12: Graphical representation of the difference between VICON and finite element results for the bi-axial continuity case shown as a percentage for each value of 'n' used in the finite element analysis. A positive difference infers that the finite element results is greater than the VICON result.

imply that this assumption is wrong. These finite element solutions also fit well on the buckling curves of Figure 5.10(b) where they are shown as discrete points.

The correlation between the published continuity results for $\alpha = 45°$ and the finite element solutions, is the worst of all the cases considered in the study. This is because of the increasing complexity of the modes which repeat over more bays than the maximum array sizes used in the study. Hence larger arrays are required to obtain good correlation with the continuous solutions. It is however clear from the previous results that the methodology employed to obtain the results is correct. The finite element results are however still generally less than 2% inaccurate for this worst case.

The complexity of the buckling modes at these higher skew angles is shown in the example buckling modes given to compare Anderson's solution with the finite element buckling prediction, previously mentioned, in Figures 5.5 – 5.9. The figures show the buckling mode associated with Anderson's approximate solution at the same aspect ratios at which he also produced a solution, using this buckling mode as a basis for trigonometric series given in equation (5.15) to increase accuracy. The buckling modes are seen to accurately match the finite element predicted buckling mode, although there is greater difference between

Anderson's and York's [112] VICONOPT continuity solutions than the finite element and the published VICONOPT solution. Because of the different definition of aspect ratio, the VICONOPT and Anderson solutions do not always allow for direct comparisons to be made.

5.4.3 Bi-axial continuity for $\alpha = 30°$ case

The finite element buckling predictions, suggest that the buckling mode corresponding to the critical buckling load repeats over more than two transverse bays as was assumed in the published VICONOPT solution used for comparison. To confirm the finite element results, the bi-axial continuity problem was re–analysed using an extended range of wavelengths. As a further check, all the skew angles in the study are considered.The buckling curves are presented in Figure 5.13. The Figures show the published VICONOPT solution by York [112], the critical buckling loads obtained using the finite element models and the critical buckling loads obtained from the rerun of the VICONOPT analysis for wavelengths corresponding to repetition over mode than two transverse bay widths.

The analysis is carried out for values of $0.0 \leq \xi \leq 1.0$ and $0.0 \leq g \leq 1.0$. The previous analysis considered the possibility of the transverse wavelength being equal to twice the width of the plate assembly.

The new VICONOPT buckling predictions show that the assumption that the transverse wavelength of the buckling mode will be twice the transverse width does not always yield critical buckling loads. For plates with skew angles of 15° or 45°, the critical buckling loads are predicted by the published VICONOPT solution, except for a discrepancy when $a/b > 2.2$ and $\alpha = 15°$. For the 30° which prompted the reanalysis, the buckling predictions using the finite element formulation match the new VICONOPT ones for $a/b \geq 1.6$. An over prediction by the published VICONOPT results is highlighted between $1.0 \leq a/b \leq 1.5$. This was not predicted by the finite element formulation. Critical bucking factors for each of analyses are reproduced in Table for $\alpha = 30°$ for completeness together with the relevant wavelength parameters for the buckling mode.

5.5 Conclusions

The finite element solution and continuous VICONOPT solution agree well over the range of aspect ratios and skew angles considered in the study. There is a larger margin of difference as the skew angle increases and when bi-axial continuity is considered, as these boundary conditions give rise to complex buckle modes which may repeat over many bays more than was used in the finite element analysis. The

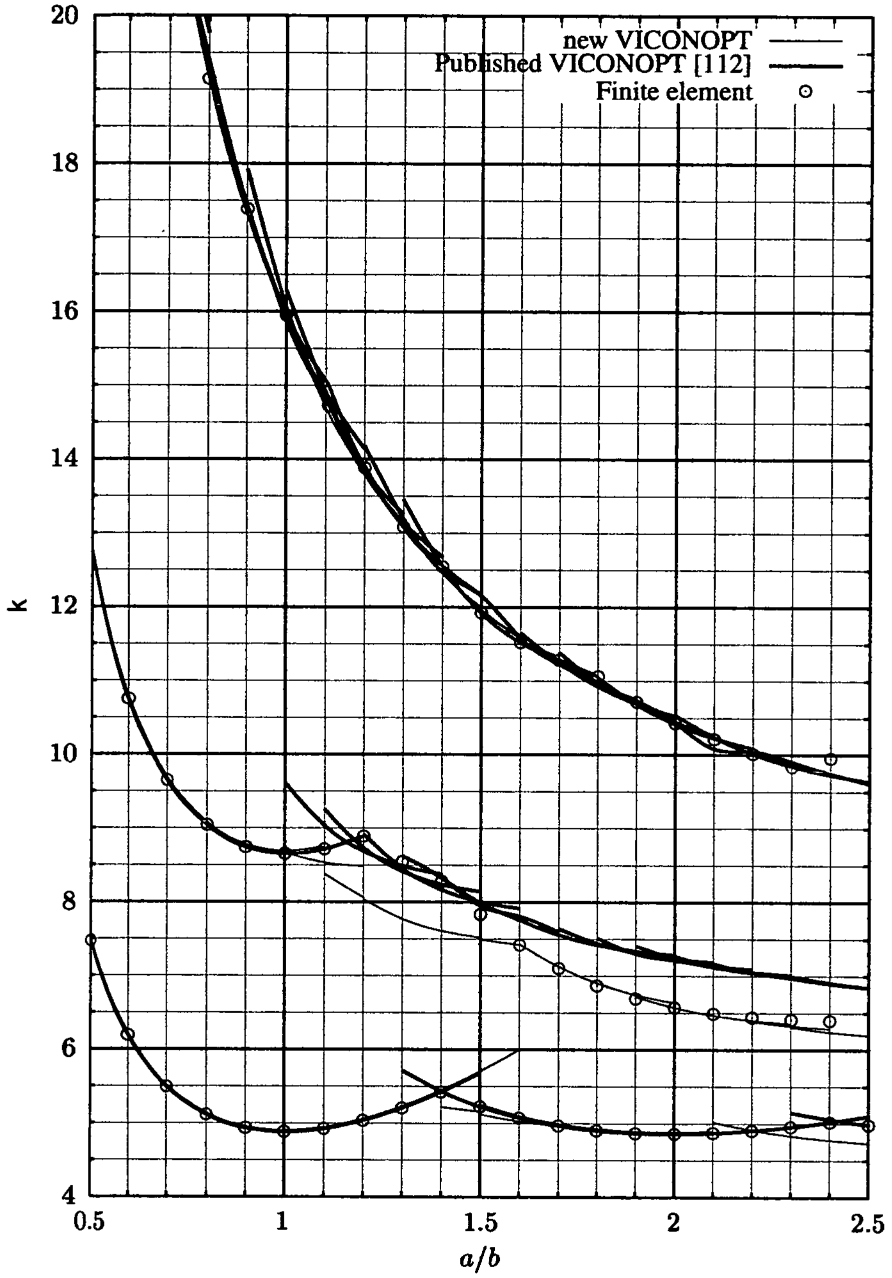

Figure 5.13: Buckling curves for bi-axially continuous plates for $\alpha = 15°, 30°$ and $45°$. The buckling curves show: the published bi-axially continuous VICONOPT buckling solutions by York [112] with the assumption the buckling mode is repetitive over no more than two bays; the finite element model of the bi–axial continuity case and; the re–run of the VICONOPT buckling solutions

Table 5.5: Critical buckling loads for skew plates with $\alpha = 30°$ and bi-axial continuity. The table shows buckling predictions from: VICONOPT published in the open literature (reference [112]); VICONOPT with a larger range of wavelengths and; the finite element model previously described. The buckling load, $k = (\sigma b^2 t)/(\pi^2 D)$ is presented with the transverse plate width, b, measured parallel to the skew edge.

	Published VICONOPT [112]		Finite Element		New VICONOPT	
a/b	k	ξ, g	k	n, m	k	ξ, g
0.5	12.76	1.0, 1.0	12.75	1, 1	12.8	1.0, 1.0
0.6	10.75	1.0, 1.0	10.75	1, 1	10.8	1.0, 1.0
0.7	9.65	1.0, 1.0	9.65	1, 1	9.69	1.0, 1.0
0.8	9.04	1.0, 1.0	9.04	1, 1	9.08	1.0, 1.0
0.9	8.74	1.0, 1.0	8.74	1, 1	8.78	1.0, 1.0
1.0	8.65	1.0, 1.0	8.65	1, 1	8.67	0.6, 0.7
1.1	8.72	1.0, 1.0	8.72	1, 1	8.38	0.2, 0.5
1.2	8.69	0.2, 2.0	8.89	1, 1	8.03	0.1, 0.5
1.3	8.41	0.4, 2.0	8.55	2, 2	7.77	0.1, 0.5
1.4	8.17	0.6, 2.0	8.28	3, 2	7.61	0.1, 0.5
1.5	7.95	0.8, 2.0	7.99	1, 2	7.49	0.1, 0.6
1.6	7.76	1.0, 2.0	7.76	1, 2	7.42	0.1, 0.6
1.7	7.56	1.0, 2.0	7.56	1, 2	7.13	0.1, 0.3
1.8	7.42	1.0, 2.0	7.42	1, 2	6.91	0.1, 0.3
1.9	7.30	0.5, 2.0	7.33	1, 2	6.72	0.1, 0.4
2.0	7.21	0.5, 2.0	6.57	1, 3	6.57	0.1, 0.4
2.1	7.12	0.3, 2.0	6.49	1, 3	6.47	0.1, 0.4
2.2	7.05	0.2, 2.0	6.44	1, 3	6.38	0.9, 0.4
2.3	6.97	0.0, 2.0	6.41	1, 3	6.31	0.7, 0.4
2.4	6.90	0.0, 2.0	6.4	1, 3	6.24	0.4, 0.7
2.5	6.84	0.2, 2.0	6.37	1, 3	6.18	0.5, 0.4

VICON predictions consider buckling repetition over an infinite number of bays compared with the finite element which considers plate arrays of up to five bays.

The buckling predictions for bi-axial continuity for $\alpha = 30°$ show that the assumption that buckle modes repeat over no more than two transverse bays used in the published VICONOPT solutions is not correct. Transverse repetition over more than 2 bays needs to be considered. This was proved using the finite element buckling predictions in which plate arrays with more than two transverse bays produced buckling loads upto 9% lower than predicted using VICONOPT. The finite element solutions were verified by rerunning the VICONOPT analysis with a greater range of transverse half-wavelengths.

Chapter 6

Orthotropic Stiffened Skew Plates and Panels

6.1 Introduction

A large and comprehensive body of both numerical [13, 61, 36, 55] and experimental work [35, 42, 2] dealing with the structural stability of rectangular stiffened plates (from now on refered to as panels) exists. In contrast, similar work on skew panels is rarely encountered. This chapter investigates the buckling behaviour of highly orthotropic skew plates by conducting a study into the buckling capacity of a set of well known benchmark stiffened panels and to expand on the previous work dealing with skew plates in the previous chapters.

Researchers testing new numerical codes [107, 72, 14, 114, 115, 112] have used the square benchmark stiffened panels first investigated by Stroud *et al.* [85]. Given that there are buckling predictions available, these panels are used as a basis for conducting the current research into skew plates. The chapter is split into two distinct sections, the first of which uses the current finite element tool, ABAQUS, to model all the square panels and compares the results the published ones to verify the numerical approach. Secondly, a selection of these panels are then used as the basis for further investigation if they are skew.

Analysis of stiffened panels is important because when used in aerospace application, plates will generally be stiffened to increase their buckling capacity and maximum span.

6.2 Background to the Benchmark Panels

Seven different stiffened panels were used by Stroud *et al.* [85] in a study to overcome a limitation of VIPASA, a buckling routine used in a panel design code, PASCO (Panel Analysis and Sizing Code). The limitation of VIPASA (Vibration and Instability of Plate Assemblies including Shear an Anisotropy) is that the transverse edge boundary conditions cannot be specified and that stiffeners must run longitudinally along the panel. The analysis produces a continuous plate buckling prediction with simply supported transverse edges. When dealing with rectangular panels under uniform compression, these limitations are of little concern because the transverse boundary conditions, caused by the occurrence of a nodal line at the panel support, are essentially those of a simple support. However, when dealing with shear loading or anisotropy, the nodal lines become skew and VIPASA underestimates the true buckling load of the panel. This predicted buckling load becomes increasingly more conservative as the half wavelength of the buckling mode of the panel approaches the panel length. This is because it is more dependant on the transverse edge boundary condition. Stroud *et al.* suggest that the VIPASA buckle solution is too conservative for practical use when the buckling mode has more than 3 half-wavelengths running parallel to the stiffeners. The theory relating to VIPASA has been discussed at length in chapter 2.

Stroud *et al.* assume that satisfying the boundary condition along the panel edge normal to the stiffener direction is more important than the boundary condition along the edge parallel to it. Two reasons are given for this: nodal lines tend to run parallel to the stiffeners; and critical modes tend to have smaller half wavelengths normal to the stiffener direction. VIPASA can enforce any boundary condition along the longitudinal edge of a panel so it is argued that a better solution for the critical buckling load of a panel will be predicted by VIPASA if the stiffeners run transversely across the panel. Because VIPASA cannot model stiffeners that run transversely across to the panel, Stroud *et al.* compare the critical buckling loads for plates of constant thickness that have an equivalent orthotropy to the stiffened panel. These equivalent orthotropic plates can be analysed by VIPASA with the orthotropic properties rotated through 90°. Hence, the problematic panel boundary corresponds to the longitudinal edge and can be enforced exactly. This should result in better buckling predictions if the assumptions about the importance of the transverse edge put forward by Stroud *et al.* are satisfied.

There is the prerequisite that the panels must buckle in an 'overall' manner for the solution to be correct because the smeared stiffener model used by Stroud *et al.* cannot model a local buckling type failure. The results by VIPASA using this method are compared with a finite element analysis using EAL (Engineering Analysis Language) and STAGS (STructural Analysis of General Shells) for verification.

6.3 The Benchmark Panels

The seven panels are made from a homogenous material with the properties of aluminium, or a graphite-epoxy composite laminate stacked in symmetric, balanced layers. Each panel is stiffened using either a blade, 'J' or hat stiffener. One panel is exceptional in that it is a composite, corrugated sheet. This panel is not considered further because it is generally not applicable to wing and fuselage panels that form the subject of the thesis. The panels are numbered 1-7 as follows:

1. Composite blade-stiffened panel;
2. Aluminium blade-stiffened panel;
3. High buckling strength composite blade-stiffened panel;
4. Metal blade stiffened panel with thin skin;
5. Composite hat-stiffened panel;
6. composite corrugated panel (ignored in the remainder of this discussion);
7. Metal 'J'-stiffened panel.

All the panels are $760mm$ square and have six equally spaced stiffeners at $127mm$ intervals. The plate therefore has six equal, adjacent cross sections which are shown in Figures 6.2 - 6.6. The panels are subject to varying combinations of in-plane shear and compression that enable interaction diagrams to be compiled showing critical buckling loads of the panels for combinations of shear and compression.

6.3.1 Analysis of the Panels using other codes

The set of panels has been used to determine the effectiveness of a set of other buckling codes. Consequently, there exists a small body of work that consider some or all of the panels in the open literature. This section outlines previous work relating to the panels.

Wittrick and Horsingham [107] investigated the buckling behaviour of the panels using the computer code CASEOPIA (Compression And Shear Instability of Orthotropic Panels) written with the specific objective of predicting the buckling strength of any prismatic assembly of plate strips. The method is based on an exact solution for the classical governing differential equation of equilibrium for thin plates and is solved using energy methods (Rayleigh–Ritz solution) using a deflection function assumed to be sinusoidal in shape. CASEOPIA assumes that the panels are purely orthotropic and error is introduced (0.1 – 0.2%) for the benchmark panels) as result of not considering anisotropy in the case of the laminated panels.

Peshkam and Dawe [72, 26] analysed the panels using two computer codes, BAVAMPAS and BAVAMPAC [25]. BAVAMPAS (Buckling And Vibration Analysis of Multi-term Plate Assemblies using Shear deformation plate theory) incorporates shear deformation theory as the expansion of the acronym suggests and is therefore applicable to thicker plate assemblies. BAVAMPAC in comparison does not account for shear deformation and produces a classical thin-plate buckling prediction. The panels are analysed using both sets of code and the results suggest that the use of classical plate theory to model the critical buckling stresses of the panels is justified, with both sets of buckling predictions being very close. This could have been predicted because the breadth to thickness ratios of the plate which are quite high, even if a local buckling mode is critical (b/t is typically greater than 60 for local buckling).

Bedair [14] used the aluminium blade stiffened panel (Panel 2) under an in-plane compression loading to test a computer code incorporating SQO (Sequential Quadratic Optimisation) [12] to find suitable non-linear deflection functions to solve the governing thin plate differential equations using the Rayleigh Ritz energy method.

York and Williams [115, 116] used VICON to model a representative section of the panels. A detailed account of VICON is given in chapter 2. VICON can analyse any prismatic assembly of panels and plates including those that are not necessarily rectangular but skew, or any other tessellating polygon. The code also has the ability to include the possibility a panel assembly being infinite in width as well as length. York and Williams present interaction buckling curves for four of the panels: composite blade-stiffened (example 1); aluminum blade-stiffened (example 2); composite hat-stiffened (example 5) and; aluminium 'J' stiffened (example 7) in reference [115] for skew angles $-60^\circ \leq \alpha \leq 60^\circ$. In reference [116], analysis of a single repeating section of each of the four panels with appropriate boundary conditions is compared to a rigorous analysis of the entire panel to ascertain the decreased accuracy using the former method in comparison with its reduction in analysis time over that of the rigorous analysis.

York [112] discussed the effect of continuity on each of the four panels made skew (using the same definitions as in Chapters 4 and 5. The effect of continuity of the panels is compared with the effect of continuity on similarly sized isotropic plates. It is concluded that the increase in buckling capacity of the skew panels moving from the uni-axial to the biaxial continuity case is very small in for the panel analysis, but significant in the plate analysis. These results confirm the assumptions made by Stroud *et al.* used to justify the use of the smeared stiffness model, that satisfying the boundary condition normal to the direction of high orthotropy is paramount in obtaining an accurate buckling prediction.

6.4 Other Modelling and Investigations into the Stability of Skew Panels

The work of York [112] and York and Williams [115, 116] described in the previous section represents almost all the work treating skew stiffened panels avaliable in the open literature. Other work has been carried out by Mizusawa *et al.* [65] and Mukhopadhyay and Mukherjee [69].

Mizusawa *et al.* [65] used the a Raleigh–Ritz method with B-Spline functions to the buckling load of a panel with stiffeners running parallel to both the longitudinal and transverse plate edges, having varying flexural and torsional stiffnesses. The panels are assumed to have simply supported edges and three plate aspect ratios are considered, $a/b = 0.5, 1.0, 1.5$. The results show that there is considerable increase in the buckling load of the panels originating from an increase in the flexural rigidity of the stiffeners. The panel stiffeners are all concentric.

The skew plate analysis by Mizusawa *et al.* [65] was later used as the basis of a verification exercise by Mukhopadhyay and Mukherjee [69] for their finite element formulation. The results compare favorably, with the finite element solution giving higher buckling predictions for the $\alpha = 0°$ case and lower buckling predictions for the $\alpha = 45°$ case.

Other work dealing with orthotropy in skew plates has considered composite plates that are orthotropic or anisotropic to varying degrees. Typically, orthotropic ratios, D_{11}/D_{22} for composite laminated plates are many times less than for a stiffened panel.

Krishna Reddy and Palaninathan [53] used a high precision triangular finite element formulation to study the effect of orthotropy in the range $D_{11}/D_{22} = 10, D_{12}/D_{22} = 0.5$ for uni-axial and bi-axial in-plane orthogonal loading as well as the effect on the buckling load of skew plates having arbitrary antisymmetric laminate orientations. All the analysis was based on simply supported plates with aspect ratios, $a/b = 1.0$. Some of the first work considering orthotropy in skew plates was published by Durvasula *et al.* [29] using the Raleigh–Ritz method. Buckling results were given for all the three skew angles, $\alpha = 15°, 30°$ and $45°$) as well as for a square case. All the plates had sides of equal length and symmetrical combinations of clamped and simple supported were considered. The degrees of orthotropy (D_{11}/D_{22} were very small, being 1.265 (corresponding to a grooved steel plate) and 2.963 (corresponding to a fibre-glass epoxy composite) respectively. Results were also produced for natural frequencies of vibration of the plates.

Thangam Babu and Reddy [87] used a finite strip method to find critical buckling stresses for skew orthotropic plates. The results were used to produce buckling curves showing critical buckling load versus aspect ratio (a/b) for isotropic and orthotropic plates with $D_{11}/D_{22} = 2.67$.

Jaunky, Knight and Ambur [44] used the Raleigh–Ritz method to produce a limited set of buckling predictions for skew plates that are orthotropic and anisotropic for a number of combinations of in-plane shear and compression loading. All plates have an aspect ratio, $a/b = 1.0$ and both simply supported and clamped boundary conditions are considered. Verification of the results was carried out using VICONOPT and STAGS.

Wang [97] formulated a Raleigh–Ritz method with B-Spline functions to study the buckling characteristics of skew, laminated plates with skew angles, $\alpha = 0°, 15°, 30°, 45°$ and aspect ratio $a/b = 1.0$. Both simply supported and clamped plate edges were considered as well as skew orientated and orthogonal in-plane shear, uni-axial and bi-axal compression loading. Critical buckling loads are predicted for plates having one layer of fibre-reinforced material orientated at either $0°, 30°$ or $45°$. The layer has an orthotropy ratio $D_{11}/D_{22} = 10$. Buckling predictions for skew plates having anti-symmetrical cross-ply laminates comprising 2 layers and 4 layers. Finally, consideration is given to plates having anti-symmetric, 45° angle-ply lay-ups with 2 and 4 layers.

The account of previous work on orthotropic and anisotropic skew plates shows the limited scope and results published in the literature for plates and panels that are skew. Especially for panels which have a degree of orthotropy far higher that for the work dealing with laminated plates.

6.5 Finite Element Modelling of the Benchmark Panels

All the panels are modelled, with exception of the corrugated (panel 6) and hat–stiffened panel (panel 5) using ABAQUS finite element code. These models are used for verification to establish the effectiveness of the finite element code and modelling assumptions. Two of the panels are given a skew planform geometry and used in a comprehensive study. There are no analyses of isolated skew panels in the open literature with which to compare the results and the analysis presented in this chapter is therefore unique. The buckling behaviour of the panels is considered as the panel orthotropy factor increases from being a flat plate to having an orthotropy equivalent to that of the Stroud *et al.* model. A smeared stiffener solution, similar to

Stroud *et al.* is also modelled to establish the validity of this approach and also to ascertain the effects of the stiffeners on the buckling strength of the panels.

Thin plate theory is assumed to be adequate to give accurate buckling predictions. This assumption is justified by the large breadth to thickness ratio of panels (even if a local buckling mode is prevalent) and the previous work on the panels by Peshkam and Dawe [72] comparing the use of thick-plate shear deformation theory and classical thin-plate theory. Accordingly suitable elements are chosen from the ABAQUS library; S4R type elements are used. These four noded, first order elements are valid for both thin and thick plate analysis (see Appendix A).

A detailed mesh convergence analysis is carried out to establish a suitable mesh size to give accurate results. Convergence for the models was based on a skew panel, $\alpha = 45°$ so that the models used in the preliminary method verification tests would be valid for use in the work considered later in the chapter with an aspect ratio $a/b' = 1.0$ (Note the use of the constant planform area definition to preserve the stiffener spacing). Convergence within 1% of the converged mesh result was obtained using 60 × 60 elements for the skin (3600 in total) and the same element density along the stiffener and 4 elements deep. The mesh is larger than that used by Stroud *et al.* for the STAGS and EAL analysis of the panels because convergence is based on a skew panel. The EAL finite element results are obtained with a mesh on the skin of 24 × 36 4-noded plate elements and in the case of the STAGS analysis a 39 × 80 element mesh of 3-noded triangular plate elements. Example convergence tests for both models 2 and 4 (used for further later in the chapter) are reproduced in Tables 6.1.

In keeping with the analysis procedures adopted by other researchers, the eccentricity between the middle of the panel skin and joint of the panel stiffener to the skin is ignored. Hence the skin and blade are joined by a set of common nodes.

6.5.1 Boundary conditions and pre-loading

Loading to the square benchmark panels includes pure in-plane shear and uni-axial compression loading and combinations of both. The results are used to draw interaction diagrams showing critical combinations of in-plane shear and compression.

Boundary conditions

For the Stroud *et al.* comparison models, the panel boundary in all cases is a simple support. The schematic in Figure C.1 shows the loading, panel dimensions and orthogonal axis system. Using this nomenclature

Mesh (skin) Mesh (stiffeners)	20 × 24 20 × 2	40 × 40 40 × 4	60 × 60 60 × 4	120 × 120 120 × 4
Buckling factor	0.9842	0.9410	0.9377	0.9375
Difference (%)	—	4.591	0.3519	0.0213

(a) Panel 2

Mesh (skin) Mesh (stiffeners)	20 × 24 20 × 2	40 × 40 40 × 4	60 × 60 60 × 4	120 × 120 120 × 4
Buckling factor	0.3290	0.3093	0.3072	0.3071
Difference (%)	—	6.3692	0.6836	0.0326

(b) Panel 4

Table 6.1: Convergence study for panels 2 and 4 for the uni-axial compression loading case (Case 7 in the NASA study). The 'Difference (%)' row shows the percentage difference between adjacent mesh increments. All the meshes are uniform with the number of elements (ABAQUS type S4R) in the longitudinal direction given first.

and the definition of panel deflections u, v, w in the x, y, z directions described respectively, the boundary conditions applied to the panel to obtain the simple support are:

At $x = 0, a; w = 0$

At $y = 0, b; w = 0$

A diaphragm end support is sought and accordingly, the transverse edges of the blades satisfy the condition $v = 0$.

These boundary conditions are comparable to those used in the other finite element analyses of the panels.

In-plane uni-axial compression

In-plane uni-axial preloading to the panels provides a uniform, longitudinal strain and is described in reference [84] and shown in Figure 6.1. Calculations for the applied loading are given in Appendix C for completeness.

6.6 Finite Element Method Verification Results

Results for the current finite element study are shown in Figures 6.2 - 6.6 in which the interaction curves given by Stroud are superimposed on the current finite element analysis solution, VICON [116] solution

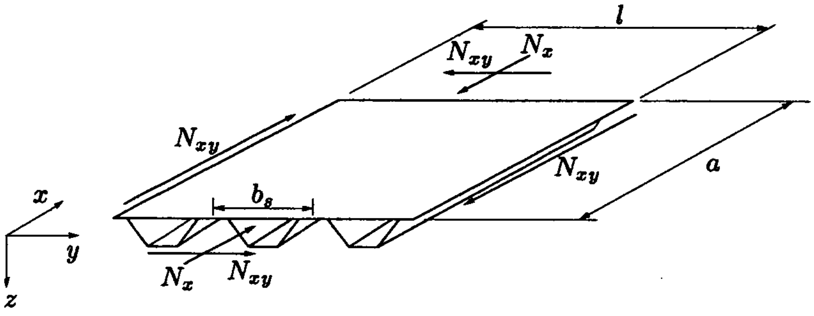

Figure 6.1: Typical section of stiffened panel showing loading considered in the analysis

and BAVAMPAC and BAVAMPAS [72] solutions and are largely complete. The figures also give the dimensions of a repeating section of the panel and show a typical compression case buckling mode for each panel. Ply-layup and material properties for the panel material are given in the captions of each of the figures where applicable. The material properties for the aluminium and graphite epoxy composite used in the modelling are:

Graphite-epoxy composite:

E_{11}	$131.0GPa$
E_{22}	$13.0GPa$
G_{12}	$6.41GPa$
ν_{12}	0.38
ν_{21}	0.0378

Aluminum:

E	$72.4GPa$
G	$27.42GPa$
ν	0.32

The numerical buckling factors for each panel are given together with further, incomplete sets of data (CASEOPEIA [107], STAGS [85] and SQL [14]) for all the current work on the panels discussed in section 6.3.1 in Tables 6.2 - 6.6.

The current ABAQUS finite element results do not compare very favourably with the previous analyses. Some panels compare more favourably than others and the pure shear buckling results compare better than the pure compression results. As the proportion of the load applied that is compression increases, so does (with the exception of model 1) the difference between the EAL and ABAQUS buckling predictions.

Table 6.7 shows the percentage difference between the ABAQUS and EAL buckling predictions for the considered panels. The panels that fail with a local mode under pure compression (panels 4 and 7) show a larger difference compared to EAL than the other panels that fail in an overall mode. The reasoning why the ABAQUS and EAL buckling solutions are different and why the amount by which they vary is different for pure shear, pure compression and the panel type is not clear. The ABAQUS models used were the same in every case, with the various changes in geometry and material properties applied.

Table 6.2: Buckling factor for current and previous analysis of model 1; composite blade stiffened panel. See Figure 6.2

LOADCASE	1	2	3	4	5	6
N_x (kN/m)	0.0	35.03	87.57	175.13	350.26	175.13
N_{xy} (kN/m)	175.13	175.13	175.13	175.13	175.13	0.0
EAL [85]	1.5525	1.3985	1.2060	0.8397	0.4764	1.0030
CURRENT	1.5310	1.3795	1.1903	0.8289	0.4702	0.9904
VICON [116]	1.6587	1.5006	1.2820	0.9256	1.4901	1.0005
BAVAMPAC[72]	1.5548	1.4000	1.2069	0.8383	0.4754	1.0005
BAVAMPAS[72]	1.5497	1.3958	1.2037	0.8376	0.4751	1.0002
VIPASA [85]	1.4683	1.3098	1.1222	0.8222	0.4690	0.9970
CASEOPIA[107]	1.5600	–	–	–	–	–
STAGS [85]	1.5565	–	–	–	–	–

Table 6.3: Buckling factor for current and previous analysis of model 2; aluminium blade stiffened panel. See Figure 6.3.

LOADCASE	1	2	3	4	5	6
N_x (kN/m)	0.0	70.05	175.13	350.26	875.65	175.13
N_{xy} (kN/m)	175.13	175.13	175.13	175.13	175.13	0.0
EAL [85]	0.8138	0.7195	0.6061	0.4444	0.1929	0.9759
CURRENT	0.8183	0.7077	0.5803	0.4400	0.1836	0.9291
VICON [116]	0.8429	0.7504	0.6307	0.4619	0.1932	0.9710
BAVAMPAC[72]	0.8130	0.7187	0.6068	0.4446	0.1919	0.9710
BAVAMPAS[72]	0.8121	0.7180	0.6063	0.4443	0.1919	0.9709
VIPASA [85]	0.9823	0.8423	0.6879	0.4637	0.1975	0.9969
CASEOPIA[107]	0.8302	–	–	–	–	–
STAGS [85]	0.8179	–	–	–	–	–
SQO [14]	–	–	–	–	–	0.9591

Table 6.4: Buckling factor for current and previous analysis of model 3; heavily loaded composite blade stiffened panel. See Figure 6.4.

LOADCASE	1	2	3	4	5	6
N_x (kN/m)	0.0	70.05	175.13	350.26	700.52	175.13
N_{xy} (kN/m)	175.13	175.13	175.13	175.13	175.13	0.0
EAL [85]	6.4424	5.7530	5.1630	4.1240	2.4543	10.0760
CURRENT	6.4016	5.6509	5.0202	3.9509	2.3656	9.6855
BAVAMPAC[72]	6.4484	5.7572	5.1658	4.1168	2.4300	9.9724
BAVAMPAS[72]	6.3150	5.6403	5.0618	4.0422	2.4249	9.9596
VIPASA [85]	9.2435	8.0628	6.7945	4.8627	2.6424	10.7300
CASEOPIA[107]	6.5020	–	–	–	–	–
STAGS [85]	6.4700	–	–	–	–	–

Table 6.5: Buckling factor for current and previous analysis of model 4; thin-skin aluminium blade stiffened panel. See Figure 6.5.

LOADCASE	1	2	3	4	5	6
N_x (kN/m)	0.0	70.05	175.13	350.26	700.52	175.13
N_{xy} (kN/m)	175.13	175.13	175.13	175.13	175.13	0.0
EAL [85]	0.2767	0.2491	0.1881	0.1253	0.0706	0.2965
CURRENT	0.2827	0.2553	0.1874	0.1204	0.0651	0.2690
BAVAMPAC[72]	0.2773	0.2474	0.1875	0.1254	0.0706	0.2958
BAVAMPAS[72]	0.2768	0.2465	0.1867	0.1248	0.0703	0.2944
VIPASA [85]	0.2961	0.2428	0.1840	0.1227	0.06984	0.2958
CASEOPIA[107]	0.2792	–	–	–	–	–
STAGS [85]	0.2773	–	–	–	–	–

Table 6.6: Buckling factor for current and previous analysis of model 7; aluminium 'J'-stiffened panel. See Figure 6.6.

LOADCASE	1	2	3	4	5	6
N_x (kN/m)	0.0	70.05	175.13	175.13	175.13	175.13
N_{xy} (kN/m)	175.13	175.13	175.13	87.67	35.03	0.0
EAL [85]	1.0420	0.9480	0.8250	1.1460	1.3150	1.3560
CURRENT	1.0680	0.9288	0.7811	1.0935	1.2305	1.2549
VICON [116]	1.1160	1.0140	0.8561	1.1437	1.3116	1.3503
BAVAMPAC[72]	1.0414	0.9479	0.8250	1.1420	1.3124	1.3503
BAVAMPAS[72]	1.0396	0.9463	0.8235	1.1375	1.3075	1.3454
VIPASA [85]	1.6050	1.4343	1.1966	1.7501	1.9579	1.9768

Table 6.7: Percentage difference between ABAQUS and EAL buckling predictions for panels 1,2,3,4, and 7.

	Percentage difference compared to EAL	
	Pure shear (LC 1)	Pure compression (LC 7)
Model 1	-1.40	-1.27
Model 2	+0.55	-5.03
Model 3	-0.64	-4.03
Model 4	+2.12	-10.22
Model 7	+2.50	-8.05

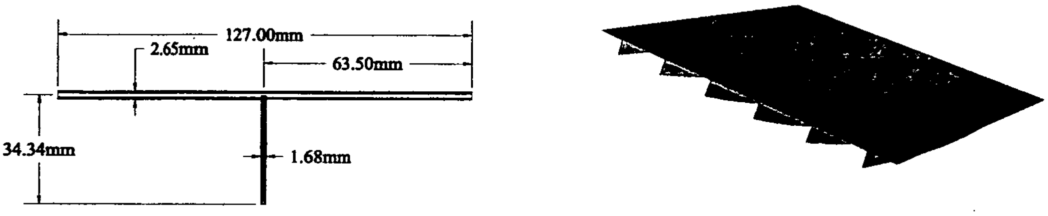

(a) Repeating section through Model 1

(b) Critical buckling mode for the pure compression loading case

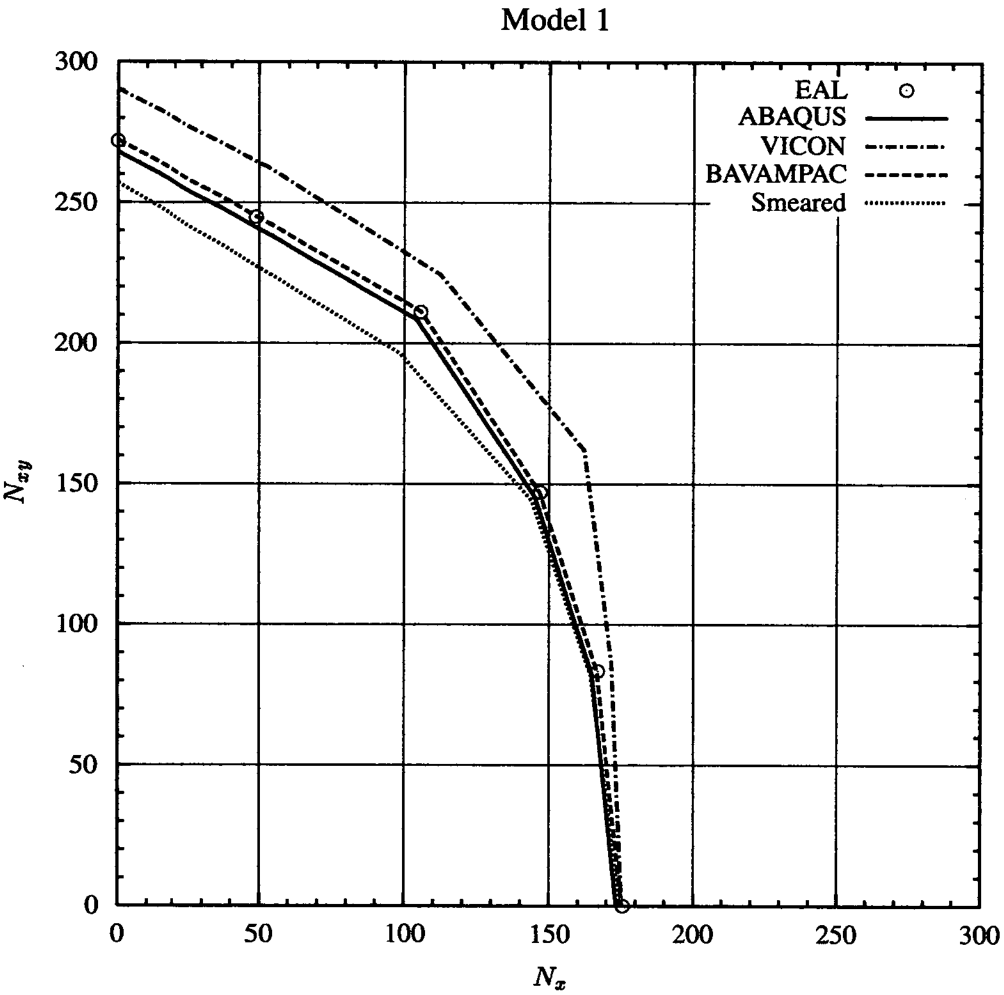

(c) Interaction curve, Model 1

Figure 6.2: Model 1 - Blade stiffened composite panel. The stacking sequence for the skin is $[\pm 45/\mp 45/0/90]_S$ plies are all $0.1397mm$ thick except for the middle ply, which is $1.2573mm$. The blade has a stacking sequence $[\pm 45/\mp 45/0]_S]$ and ply thicknesses of $0.1397mm$ except for the middle ply which is $0.2794mm$ thick.

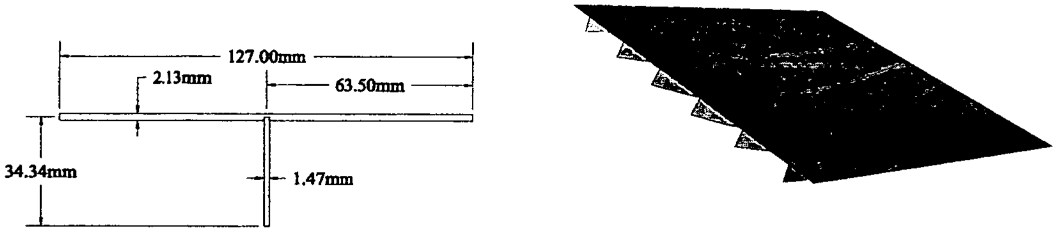

(a) Repeating section through Model 2

(b) Critical buckling mode for the pure compression loading case

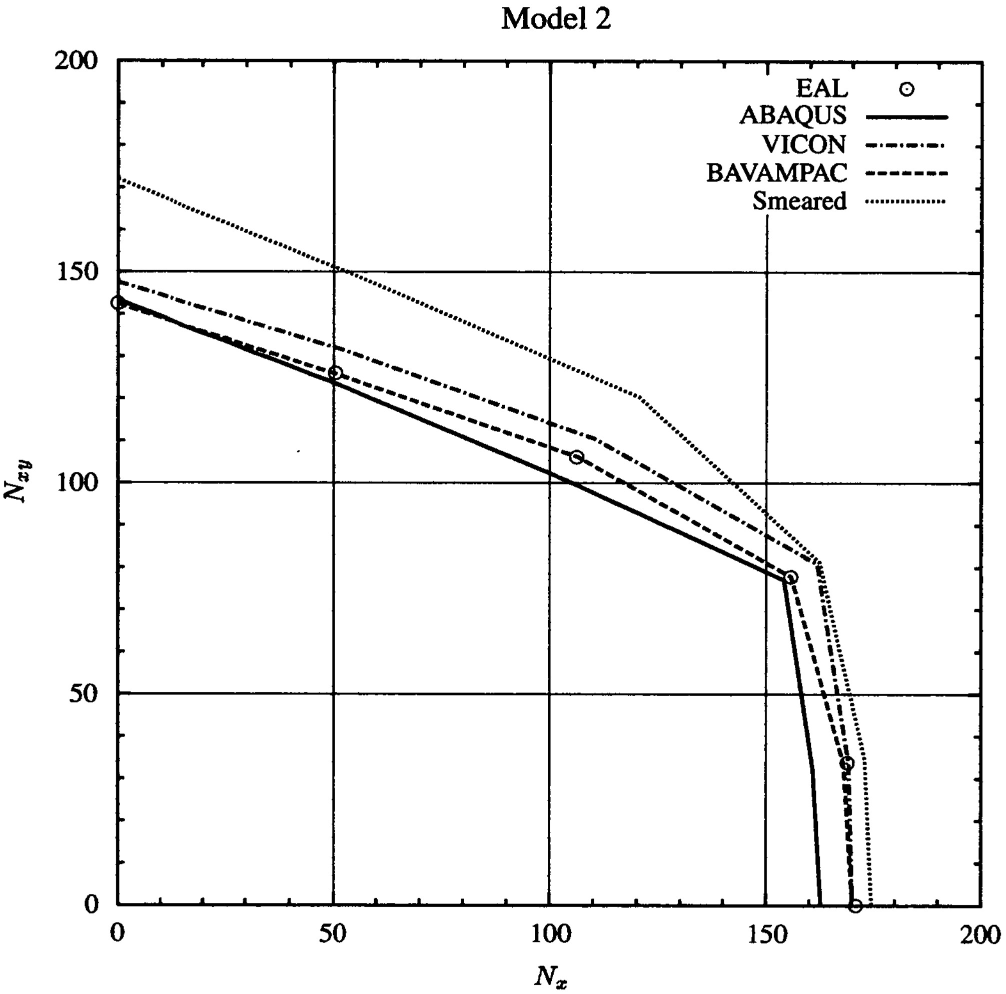

(c) Interaction curve, Model 2

Figure 6.3: Model 2 - Blade stiffened isotropic panel.

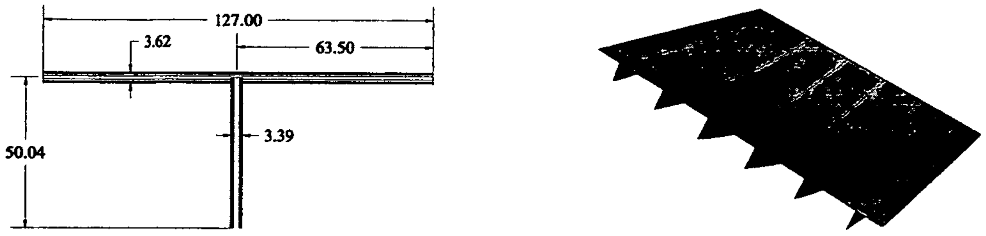

(a) Repeating section through Model 3

(b) Critical buckling mode for the pure compression loading case

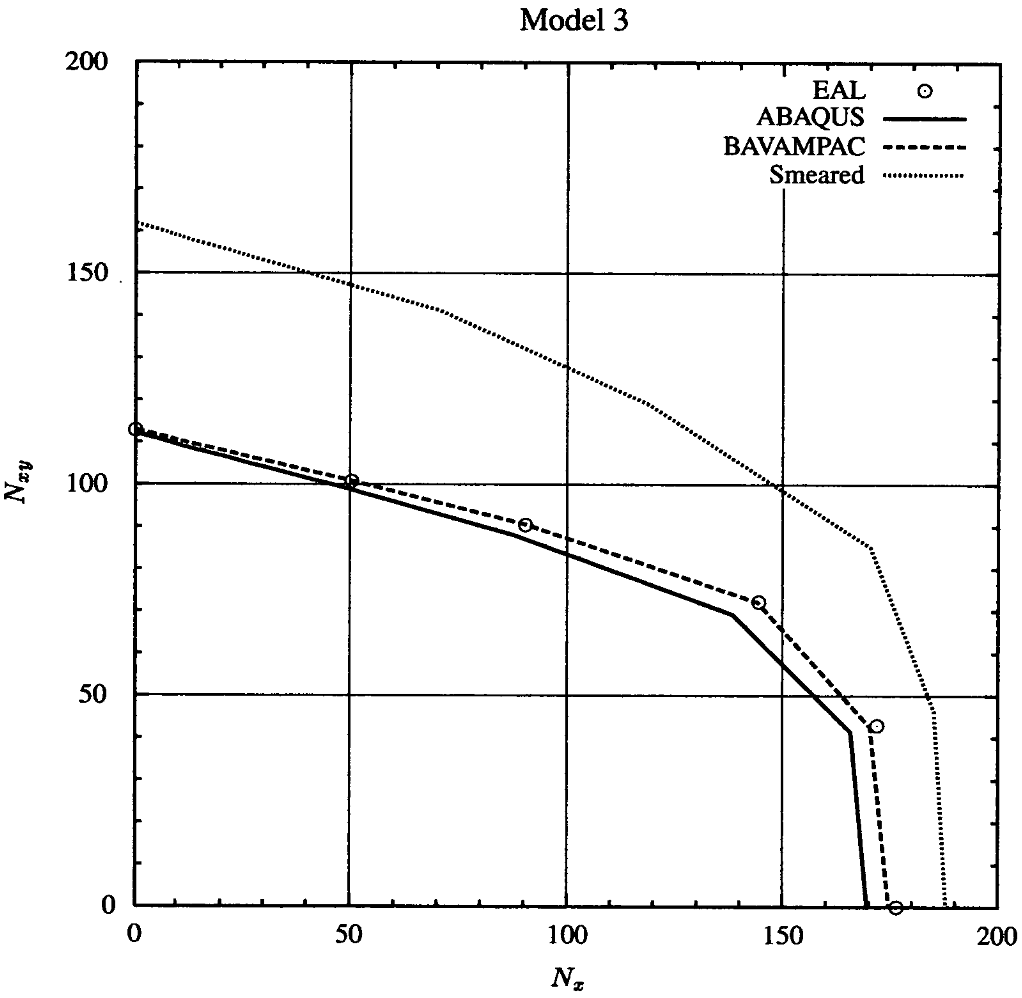

(c) Interaction curve, Model 3

Figure 6.4: Model 3 - Composite blade stiffened, high load panel. The stacking sequence for the panel skin is $[\pm45/\mp45/0/90]_S$ where the $\mp45°$ plies have a thickness of $0.1618mm$, the $0°$ plies a thickness of $0.6325mm$ and the $90°$ plies a thickness of $1.0566mm$.

6.7 Skew Stiffened Panels

The current finite element models are used to investigate the buckling behaviour of skew panels. Two panels, the blade stiffened aluminum panels (2 and 4) are investigated further because they have the largest difference in orthotropic properties and different buckling modes for the square case. Panel 4 buckles in a local manner and panel 2 in overall manner.

The following parameters are investigated in the study:

1. Aspect ratio of the panel $0.5 \leq 2.5$
2. Skew angle of the plate, $\alpha = 15°, 30°, 45°$
3. Orthotropy, which is changed by reducing the depth of the stiffener.
4. Boundary condition along the panel skin edge.

The aspect ratios considered are commensurate with those considered previously for plates and encompass those most often encountered in the open literature, this argument is also applicable to the choice of skew angles. The degree of orthotropy, *i.e.* the ratio of D_{11}/D_{22} is changed by considering panels with stiffeners $1/4$, $1/2$, $3/4$ and the full depth of the those on the benchmark panels. Comparison will also be made with the isotopic plate solution. A smeared stiffness analysis will also be carried out for a plate with constant thickness having identical orthotropic properties to the panels.

The same boundary conditons are used as described in Section 6.5.1 to provide a lower bound simply supported buckling prediction and an upper-bound fully clamped solution is obtained by preventing rotations along the panel skin edges.

A schematic of typical skew panel analysed in the study showing the relevant nomenclature is given in figure 6.7.

6.7.1 Stiffened Panel Properties

Tables 6.8 and 6.9 categorises and identifies the geometric panel properties for each of the stiffener depths described above. The categorisation of the panels given in the table will be adhered to throughout the remainder of the chapter. In addition to the 4 categories for varying stiffener depths, there is an additional category, 'E', which represents an isotropic plate of the kind analysed in Chapter 4.

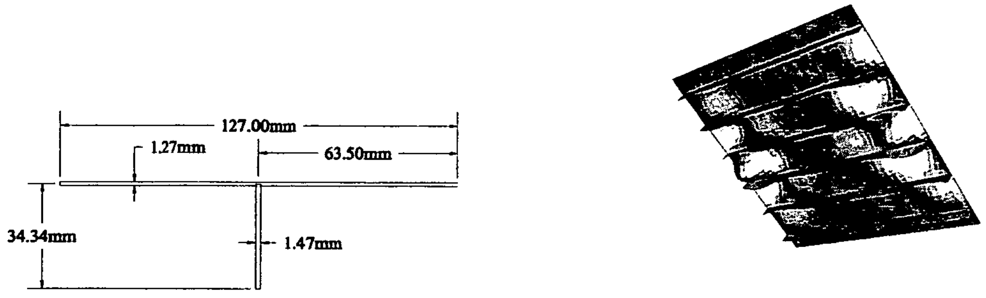

(a) Repeating section through Model 4

(b) Critical buckling mode for the pure compression loading case

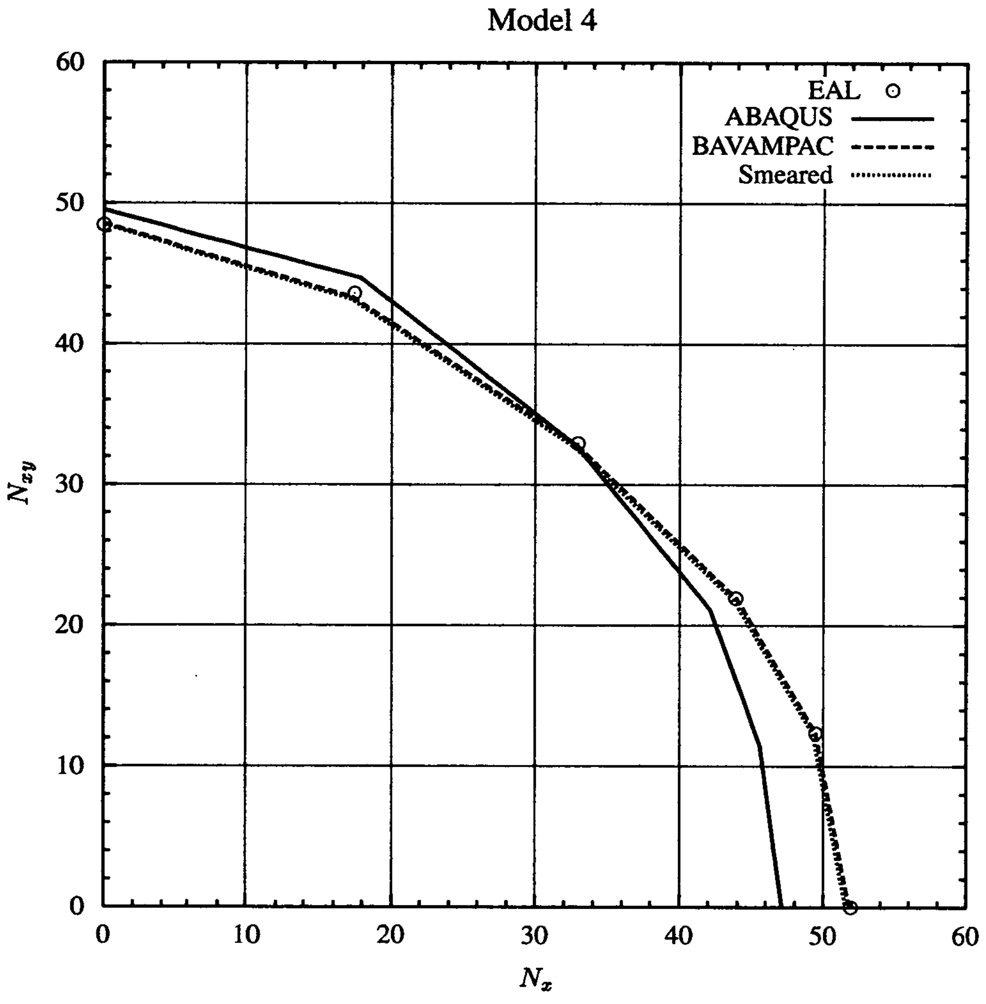
Model 4

(c) Interaction curve, Model 4

Figure 6.5: Model 4 - Blade stiffened isotropic panel with thin skin.

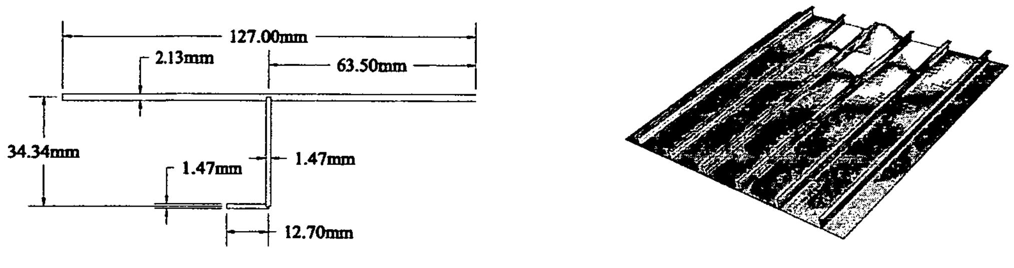

(a) Repeating section through Model 7

(b) Critical buckling mode for the pure compression loading case

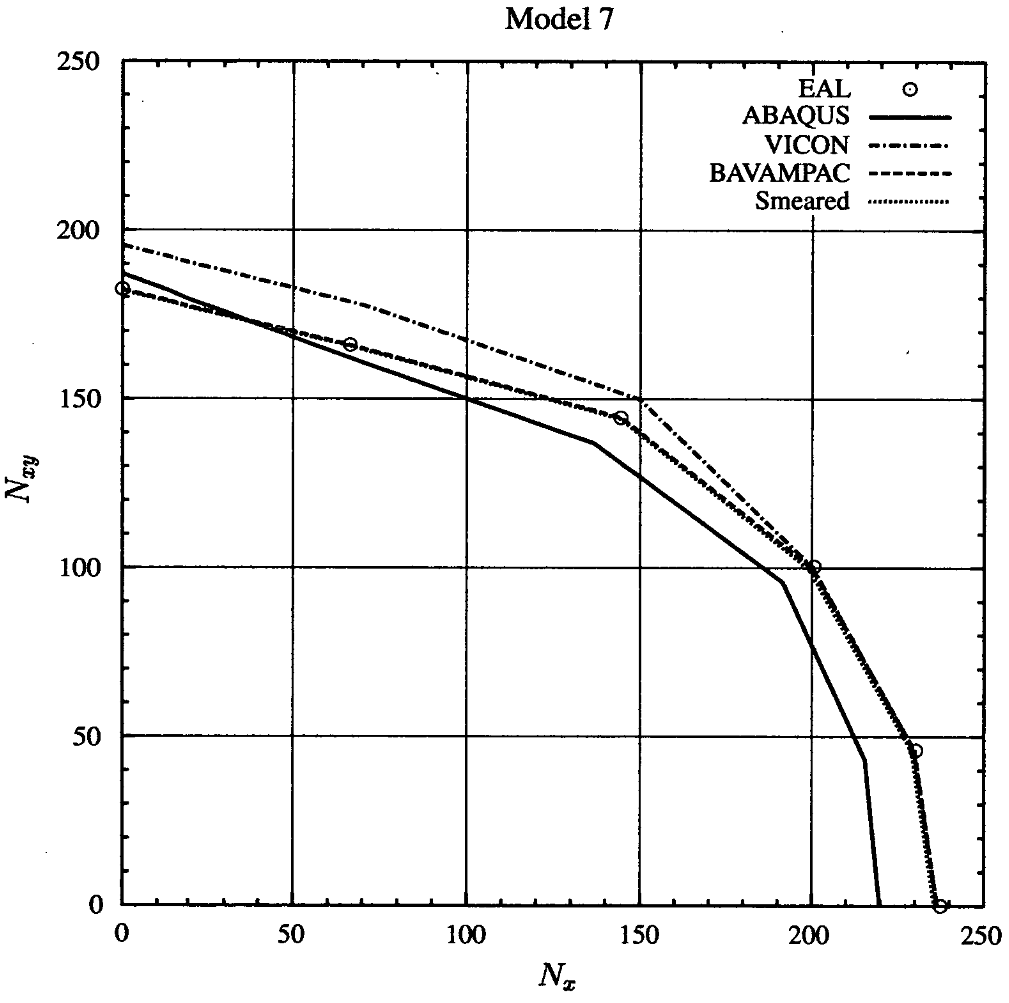

(c) Interaction curve, Model 7

Figure 6.6: Model 7 - 'J' Blade stiffened isotropic panel.

Table 6.8: Geometric properties of Panel 2. Subscript 'stiff' corresponds to the stiffener and subscript 's' to the repeating section of the panel. The sketch at the base of the table provides scale sketches of a repeating panel section with the stiffener heights that categorise the panels.

				Stiffener Properties			Panel section properties	
Category	Stiffener Depth (mm)	b_{stiff}/b_s	A_{stiff}/A_s	I_{xx} (mm^4)	$(EI_{xx})/(b_sD)$	J_{xx} (mm^4)	I_{xx} (mm^4)	$(EI_{xx})/(bD)$
A	34.34	0.27	0.16	4960.98	489.86	36.361	17609.45	153.77
B	25.76	0.2	0.12	2092.91	275.54	27.271	7704.7	67.28
C	17.17	0.14	0.09	620.12	122.46	18.181	2424.76	21.17
D	8.59	0.07	0.04	77.52	30.62	9.090	402.5	3.51

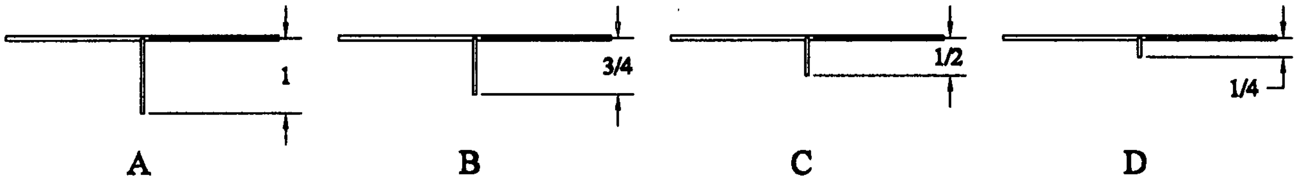

Table 6.9: Geometric properties of Panel 4. Subscript 'stiff' corresponds to the stiffener and subscript 's' to the repeating section of the panel. The sketch at the base of the table provides scale sketches of a repeating panel section with the stiffener heights that categorise the panels.

				Stiffener Properties			Panel section properties	
Category	Stiffener Depth (mm)	b_{stiff}/b_s	A_{stiff}/A_s	I_{xx} (mm^4)	$(EI_{xx})/(b_s D)$	J_{xx} (mm^4)	I_{xx} (mm^4)	$(EI_{xx})/(bD)$
A	34.34	0.27	0.24	4960.98	489.86	36.361	16317.87	675.64
B	25.76	0.2	0.19	2092.91	275.54	27.271	7199.67	298.1
C	17.17	0.14	0.14	620.12	122.46	18.181	2250.43	93.18
D	8.59	0.07	0.07	77.52	30.62	9.090	314.86	13.04

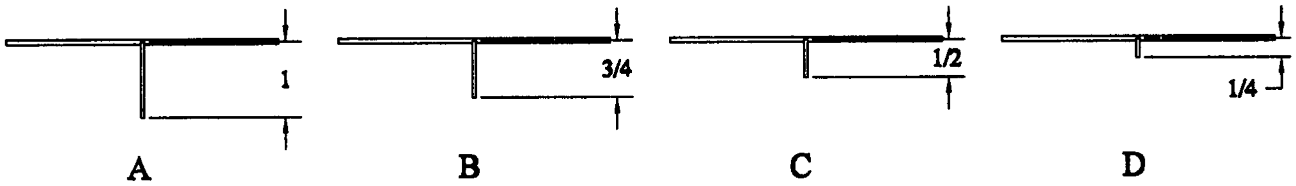

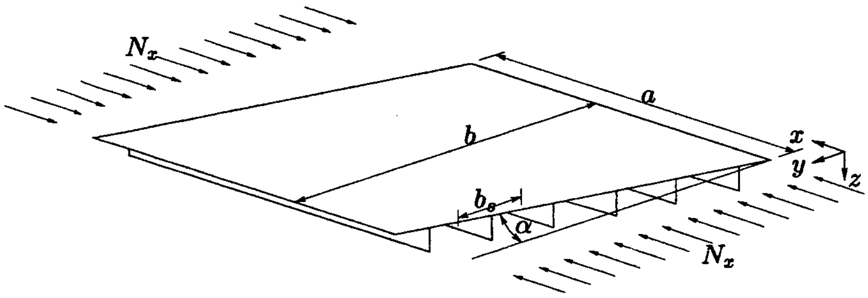

Figure 6.7: A typical skew panel, showing: longitudinal length, a; transverse width normal to the longitudinal edge, b; in-plane uniform compression load, N_x and; repeating panel section, b_s.

6.8 Smeared Stiffener Solution

A smeared stiffener solution is also produced for each of the panel analyses to determine the effect of the stiffeners on the buckling load of the panel. The analysis of such panels is advantageous because it is generally much easier: it requires only a change to the material stiffness matrix with no increase in the number of elements required for modelling. For the simply supported square and rectangular plate cases, closed-form solutions to the problem also exist.

A comparison with the current finite element analysis of the panels is made by modelling a uniformly thick (but still classically thin) plate with orthotropic properties equivalent to those of the panels. Orthotropy of the current panels in the two cases considered is due entirely to panel geometry, that is the material is isotropic, but the second moment of area about the x and y orthogonal axes are different. The orthotropic properties for each panel are calculated using a method similar to that in reference [84], an account of which is given in 6.8.1.

6.8.1 Smeared Stiffener Solution Stiffener Properties

Smeared stiffness are calculated for bending about the panel section major axis (D_{11}) and minor panel section axis (D_{22}) and twisting (D_{33}).

D_{11} Stiffness

This is an EI type stiffness and is given by:

$$D_{11} = \frac{1}{b_s}\sum_{i=1}^{i=n}\left(A_{11_i} - \frac{A_{12_i}^2}{A_{22_i}}\right)\left(b_i z_i^2 + \frac{b_i^3}{12}\sin^2\theta\right) + b_i D_{11_i}\cos^2\theta \tag{6.1}$$

where:

D_{11} is the flexural rigidity of the plate in the x direction;

i is an element making up the repeating section of the panel;

z_i is the distance between the centroid of the section i and the centroid of the entire repeating section;

b_s is the width of the repeating section;

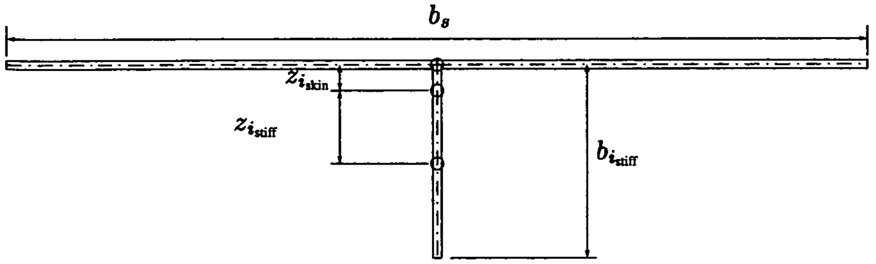

Figure 6.8: Section through a typical repeating section of blade stiffened plate showing the nomenclature used in Eqn (6.1) to derive an equivalent D_{11} stiffness for the panel. The unfilled circles represent (working form the top of the figure to the bottom) the centroids of the panel skin, repeating section and blade stiffener respectively.

$A_{11} - (A_{12}^2/A_{22})$ is the stiffness of element i per unit length;

θ is the angle that the panel element makes with the horizontal. In the case of the panels used in the study therefore, θ is 0° for all the skin sections and 90° for all the blade stiffeners.

This nomenclature is shown in Figure 6.8.

D_{22} Stiffness

This stiffness is given by the flexural rigidity of the panel skin because no stiffeners run transversely across the panel, hence;

$$D_{22} = \frac{Et^3}{12(1-\nu^2)} \tag{6.2}$$

D_{33} Stiffness

The twisting portion of the **D** matrix is given by;

$$D_{33} = \frac{1}{b_s}\sum_{i=1}^{i=n} b_i \left(\frac{1}{2}D_{12_i} + D_{66_i}\right) \tag{6.3}$$

hence,

$$D_{12} = \frac{1}{2b_s}\sum_{i=1}^{i=n} D_{12_i} b_i \tag{6.4}$$

and

$$D_{66} = \frac{1}{b_s}\sum_{i=1}^{i=n} D_{66_i} b_i \tag{6.5}$$

given that the equation for lateral loading of the plate is governed by;

$$q = D_{11}\frac{\partial^4 w}{\partial x^4} + 4(D_{33})\frac{\partial^4 w}{\partial x^2 \partial y^2} + D_{22}\frac{\partial^4 w}{\partial} \tag{6.6}$$

Comparative Young's Modulus to obtain the smeared stiffness solutions

Using the constitutive relationships for the material property matrices relating plate bending, but ignoring transverse shear and normal deformation [92];

$$D_{11} = \frac{E_{11}t^3}{12(1-\nu_{12}\nu_{21})} \tag{6.7}$$

$$D_{22} = \frac{E_{22}t^3}{12(1-\nu_{21}\nu_{12})} \tag{6.8}$$

$$D_{12} = D_{11}\nu_{21} = D_{22}\nu_{12} \tag{6.9}$$

$$D_{66} = \frac{G_{12}t^3}{12} \tag{6.10}$$

Hence, given the above relationships between **D** and **A**, given a plate thickness valid for a thin plate solution, values for E_{11}, E_{22}, D_{12} and G_{12} can be calculated.

Tabulated values for the material orthotropy as a result of the geometric orthotropy are given in Table 6.10.

6.9 Results

Buckling predictions for each of the models are presented as a series of buckling curves for each panel showing its buckling load, as a non-dimensional coefficient, plotted against aspect ratio. A spline curve is fitted between the buckling predictions made at intervals of 0.1 × a/b and the location of coincident buckling loads obtained to determine the critical aspect ratios at which buckling mode changes occur. The spline curves are cropped above the point of a cusp location. The non-dimensional buckling coefficient is given by,

Table 6.10: Bending stiffnesses of the smeared stiffener solution for each category of each panel. The ratio of D_{11}/D_{22} is included and gives the degree of orthotropy of the panel.

		Stiffener depth category			
		A	B	C	D
Panel 2	D_{11} $kNmm$	10045.5	1643.4	501.5	115.1
	D_{22} $kNmm$	65.3	65.3	65.3	65.3
	D_{33} $kNmm$	902.4	884.1	865.8	847.5
	D_{11}/D_{22}	154.2	67.8	20.5	3.6
Panel 4	D_{11} $kNmm$	9303.9	4096.0	1272.9	180.6
	D_{22} $kNmm$	13.8	113.8	113.8	113.8
	D_{33} $kNmm$	248.2	229.9	211.5	193.2
	D_{11}/D_{22}	675.7	297.5	92.5	13.1

$$k = \frac{\sigma b^2 t}{\pi^2 D_{22}} = \frac{F b^2}{\pi^2 D_{22}} \tag{6.11}$$

where:

σ, F is the critical buckling stress and buckling force respectively for the panel. σ is used to classify the buckling load for the smeared stiffness solution and F the buckling load for the panels;

b is the transverse panel width normal to the longitudinal edge of the plate;

t is the plate thickness;

D_{22} is the panel bending stiffness about the weaker axis and is a constant value for all the panels with the same skin thickness.

The buckling curves for the panels are shown in Figures 6.9 – 6.14. Figures 6.9 – 6.11 relate to panel 2 and show: buckling curves for the panel analysis showing comparison between the simply supported and fully clamped plate boundary condition; buckling curves comparing the simply supported panel analysis and the simply supported smeared stiffener model and; buckling curves comparing fully clamped panel analysis with the fully clamped smeared stiffener model respectively. Figures 6.12 – 6.14 show the same curves for panel 4.

Each curve on the set of figures represents one of the panel analyses and is categorised according to the stiffener depth or, in the case of the smeared stiffness solution, a plate with an equivalent orthotropy. The curves are categorised according to stiffener depths using the labels in Tables 6.8, 6.9 and 6.10. An additional category, 'E' represents an equivalent isotropic panel. The letter 'P' against a curve represent buckling predictions obtained by analysis of the panels and 'S' a buckle prediction using the smeared stiffener model. A number '1' represents simply supported boundary conditions and '4' the clamped skin edge boundary conditons.

The smeared stiffener solutions accurately model the panels when the buckling mode of failure is an overall type. At low aspect ratios both panels analysed buckle in a local manner. The aspect ratios $0.5 \leq a/b \leq 2.5$ captures this local buckling failure. Clearly, this range of aspect ratios is not large enough to capture the buckling behaviour of the skew panels and plates because the buckling load for the panels and plates is still decreasing with an increase in aspect ratio. As a result, and because of the apparent accuracy of the smeared stiffener model for the panels chosen for further analysis, it is used to extended the buckling curves in Figures 6.15 and 6.16 over the range $0.5 \leq a/b \leq 5.0$. In the chapter 4 it was shown that the initial range of aspect ratios ($0.5 \leq a/b \leq 2.5$) is sufficient to model the buckling characteristics of the skew plate. When $a/b > 2.5$ the buckling stress of a skew plate is sufficiently converged on the buckling load of a rectangular plate to use a rectangular plate model to predict the buckling load of a skew plate with good accuracy. The comparison buckle curve for an isotropic plate is therefore not continued further and is stopped short in the analysis (this can be seen in the graphs of the results) after which the critical buckling load of the isotropic can be taken to be that of the lower-bound rectangular plate solution.

The extended buckling curves are compared with the theoretical minimum buckling load for a rectangular orthotropic plate calculated using an affine transformation of the closed-form solution for a simply supported isotropic rectangular plate. An outline of this affine transformation is given in Appendix D. Critical buckling loads are presented in Table 6.11 which show the minimum critical buckling load and the first aspect ratio at which it occurs for the smeared stiffener model of the panels. This comparison serves two purposes: it establishes the accuracy of using a rectangular plate to approximate the buckling load of one that is skew; and because in the preceeding chapters, it has been shown that the skew transverse panel edge has a diminishing influence on the plate buckling load with an increase in aspect ratio, it gives a lower–bound buckling load for a simply supported skew orthotropic plate with high aspect ratio. The closed-form solution for the simply supported rectangular orthotropic plate is shown in Figures 6.15 and 6.16 by a dashed horizontal line.

The extended buckling curves flatten very quickly at high aspect ratios and the buckling load of the plates converge on that of the minimum buckling load predicted by the closed-form solution of a rectangular plate. It is therefore concluded that the aspect ratio range considered is sufficient to highlight the behaviour characteristics of the skew panels.

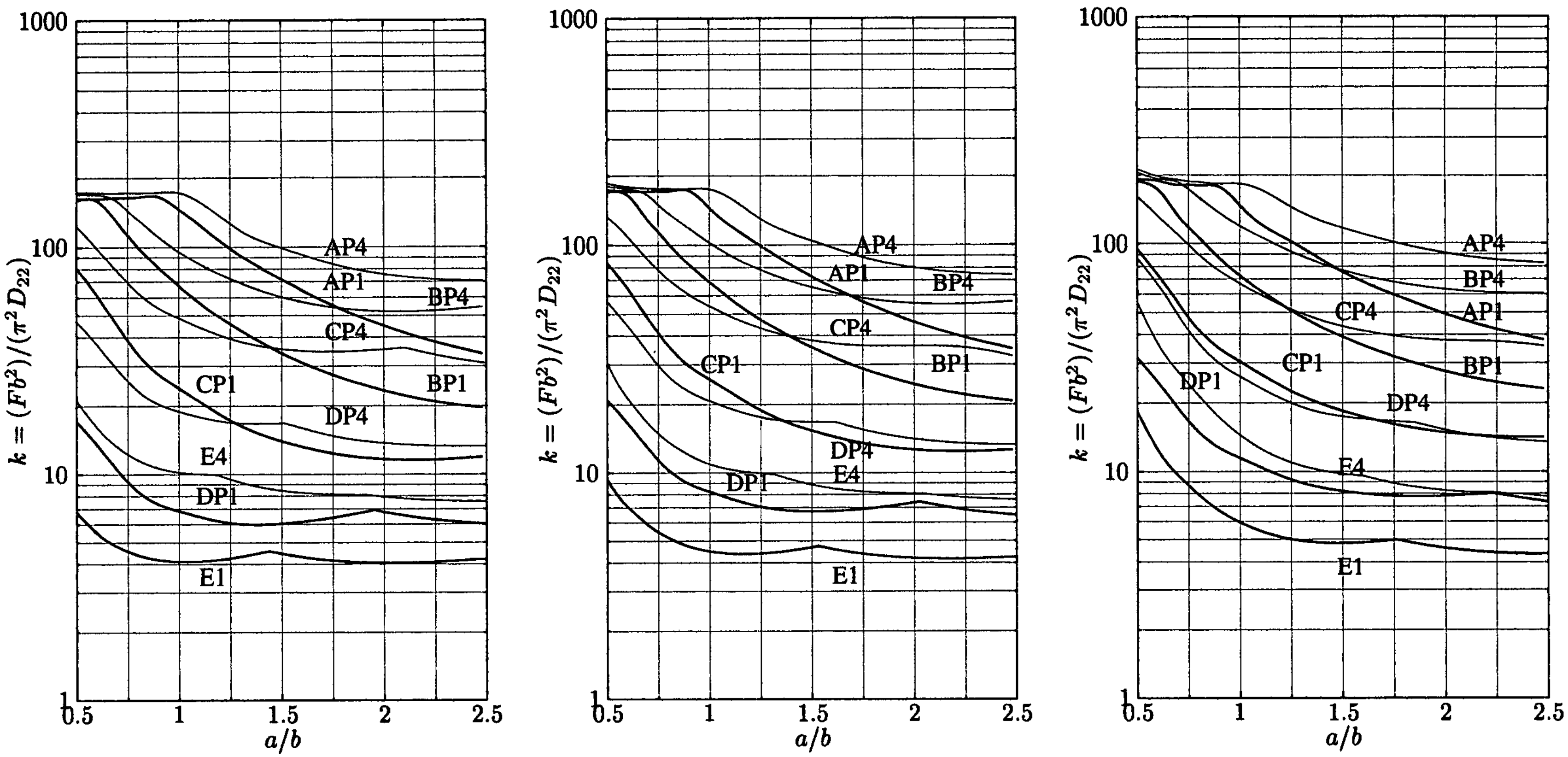

(a) Model 2: $\alpha = 15°$

(b) Model 2: $\alpha = 30°$

(c) Model 2: $\alpha = 45°$

Figure 6.9: Buckling curves for Model 2 blade stiffened panel showing analysis of the panels with simply supported and clamped boundary conditions. The curves are identified using the 3 figure code given in the text and by the line type, where a thick line gives the simply supported actual panel analysis and the light solid line the clamped panel analysis. To recap: the first letter of the line label gives the category of orthotropy of the panel (A-E); the second the actual panel analysis (P) and; 1 represents simply supported boundary conditons and 4 fully clamped boundary conditions.

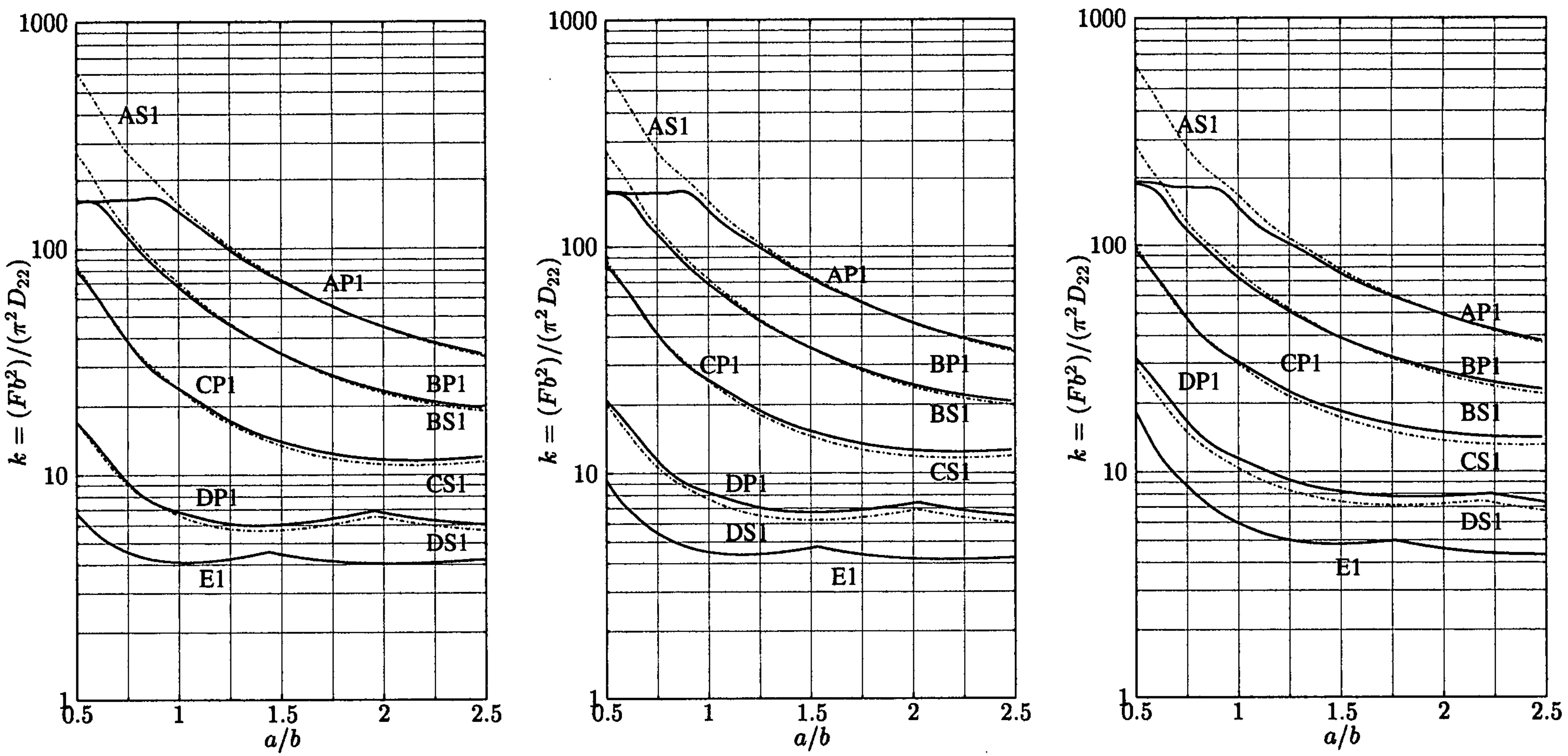

(a) Model 2: $\alpha = 15°$

(b) Model 2: $\alpha = 30°$

(c) Model 2: $\alpha = 45°$

Figure 6.10: Buckling curves for Model 2 blade stiffened panel comparing the actual panel analysis with the equivalent smeared stiffness analysis with simply supported boundary conditons. The curves are identified using the 3 figure code given in the text and by the line type, where a thick line gives the simply supported actual panel analysis and the dashed line the simply supported smear stiffener solution. To recap: the first letter of the line label gives the category of orthotropy of the panel (A-E); the second the actual panel analysis (P) or the smeared stiffness analysis (S) and; 1 represents simply supported boundary conditons and 4 fully clamped boundary conditions.

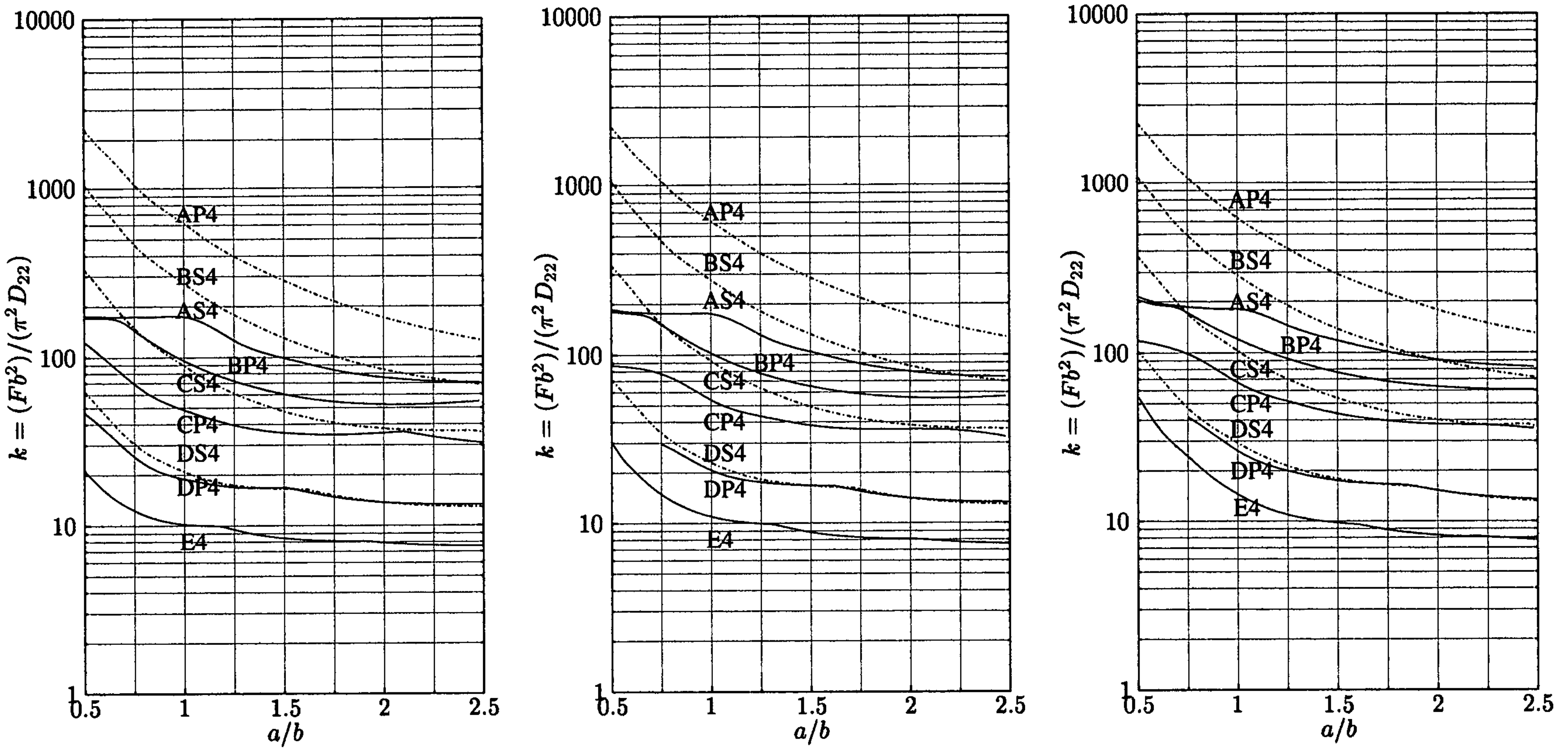

(a) Model 2: $\alpha = 15°$ (b) Model 2: $\alpha = 30°$ (c) Model 2: $\alpha = 45°$

Figure 6.11: Buckling curves for Model 2 blade stiffened panel comparing the analysis of the panel with the smeared stiffener model for clamped boundary conditons. The curves are identified using the 3 figure code given in the text and by the line type. The solid line gives the panel analysis buckling load and the dashed line the equivalent smeared stiffener one. To recap: the first letter of the line label gives the category of orthotropy of the panel (A-E); the second the actual panel analysis (P) or the smeared stiffness analysis (S) and; 1 represents simply supported boundary conditons and 4 fully clamped boundary conditions.

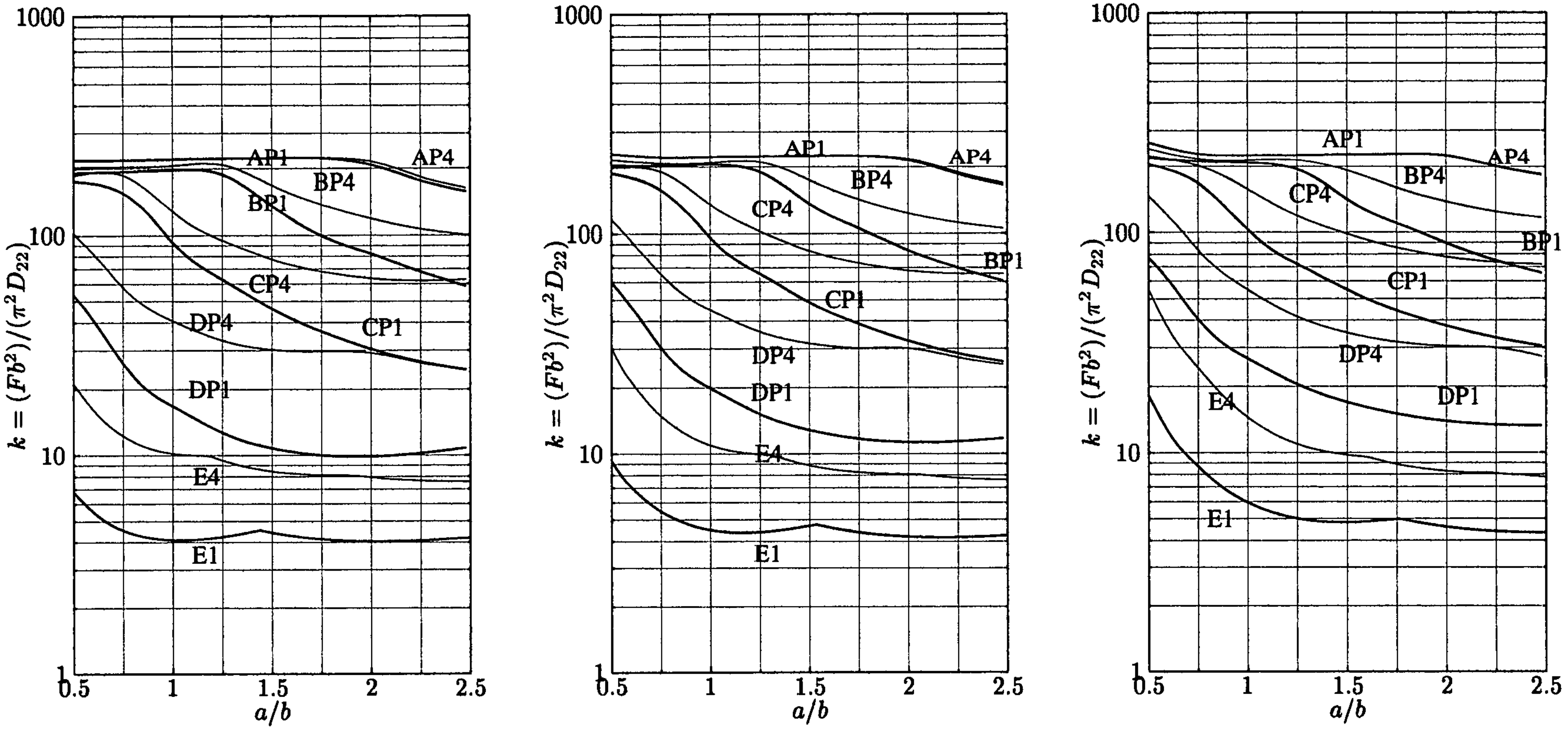

(a) Model 4: $\alpha = 15°$

(b) Model 4: $\alpha = 30°$

(c) Model 4: $\alpha = 45°$

Figure 6.12: Buckling curves for Model 4 blade stiffened panel with simply supported and clamped boundary conditions. The curves are identified using the 3 figure code given in the text and by the line type, where a thick line gives the simply supported actual panel analysis and the light solid line the clamped panel analysis. To recap: the first letter of the line label gives the category of orthotropy of the panel (A-E); the second the actual panel analysis (P) or the smeared stiffness analysis (S) and; 1 represents simply supported boundary conditons and 4 fully clamped boundary conditions.

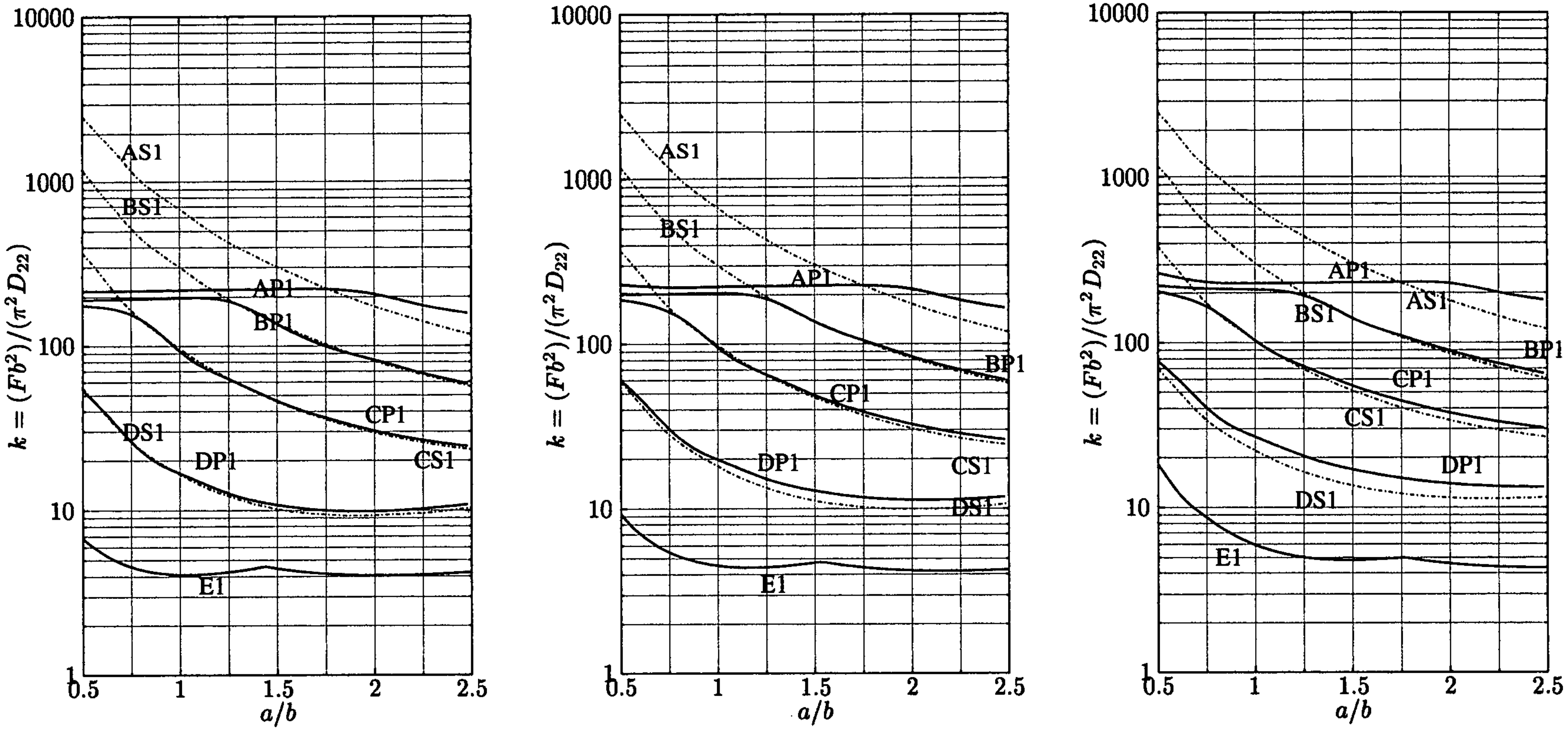

(a) Model 4: $\alpha = 15°$

(b) Model 4: $\alpha = 30°$

(c) Model 4: $\alpha = 45°$

Figure 6.13: Buckling curves for Model 4 blade stiffened panel comparing the panel analysis and the equivalent smeared stiffener analysis for the simply supported boundary condition case. The curves are identified using the 3 figure code given in the text and by the line type, where a thick line gives the simply supported actual panel analysis and the dashed line the simply supported smear stiffener solution. To recap: the first letter of the line label gives the category of orthotropy of the panel (A-E); the second the actual panel analysis (P) or the smeared stiffness analysis (S) and; 1 represents simply supported boundary conditons and 4 fully clamped boundary conditions.

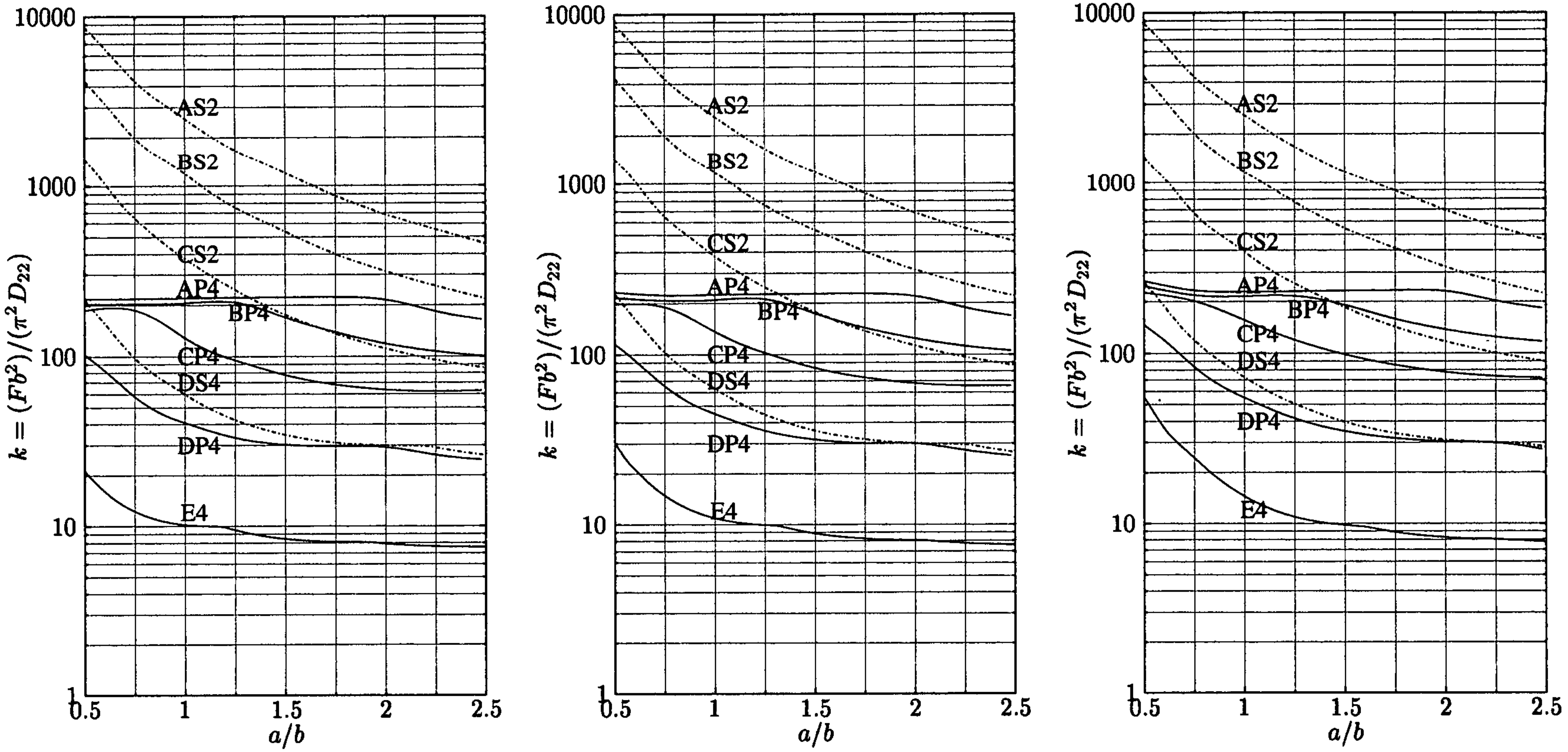

(a) Model 4: $\alpha = 15°$

(b) Model 4: $\alpha = 30°$

(c) Model 4: $\alpha = 45°$

Figure 6.14: Buckling curves for Model 4 blade stiffened panel comparing the analysis of the panel with the smeared stiffener model for the clamped boundary conditon case. The curves are identified using the 3 figure code given in the text and by the line type. The solid line gives the panel analysis buckling load and the dashed line the equivalent smeared stiffener one. To recap: the first letter of the line label gives the category of orthotropy of the panel (A-E); the second the actual panel analysis (P) or the smeared stiffness analysis (S) and; 1 represents simply supported boundary conditons and 4 fully clamped boundary conditions.

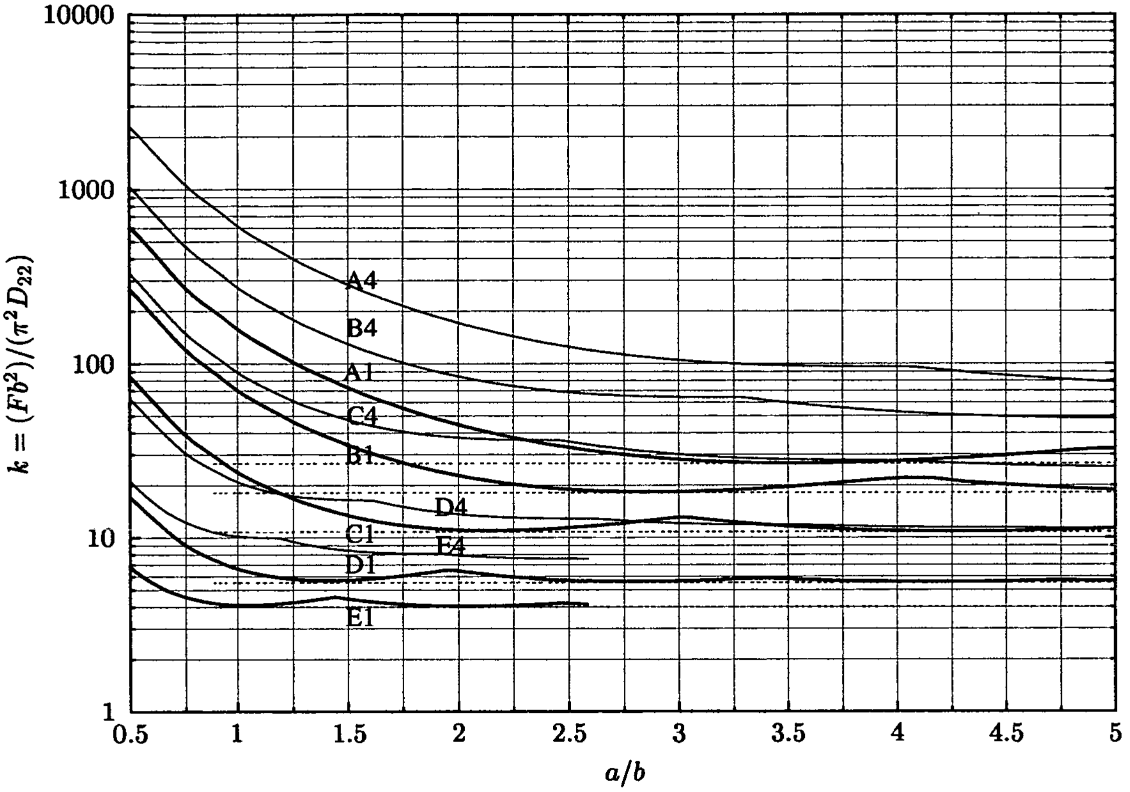

(a) Model 2: $\alpha = 15°$

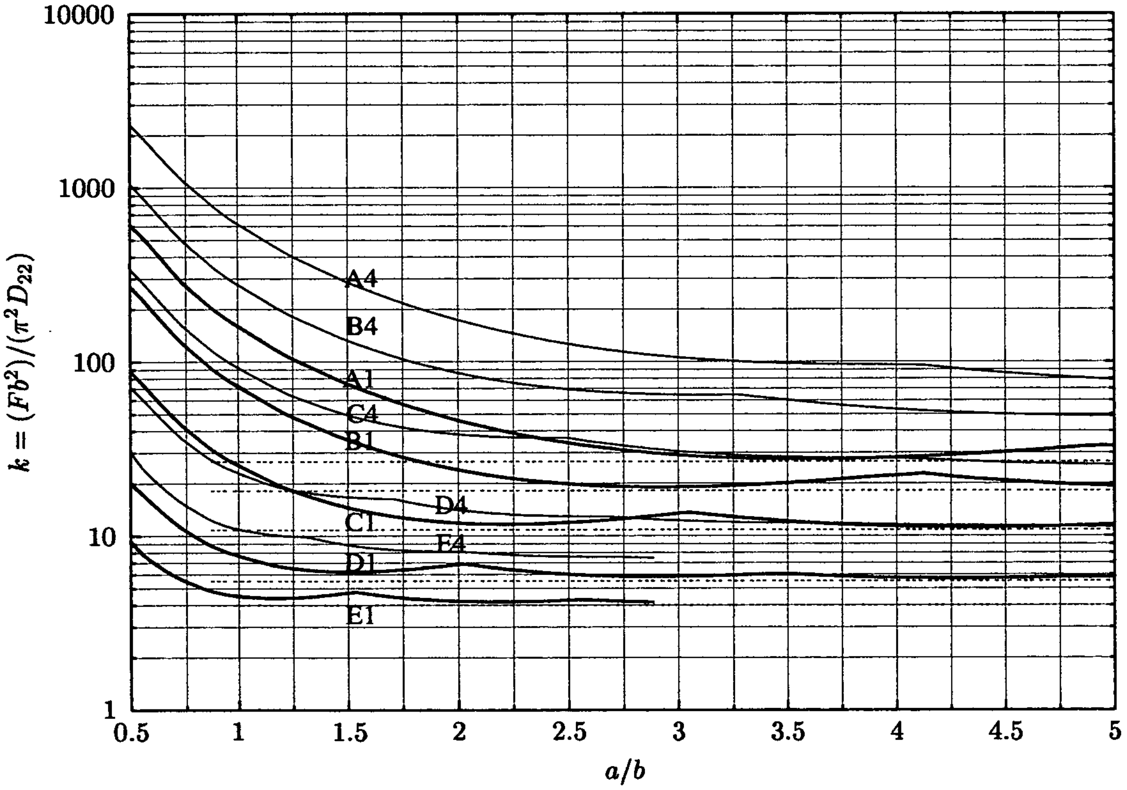

(b) Model 2: $\alpha = 30°$

continued overleaf

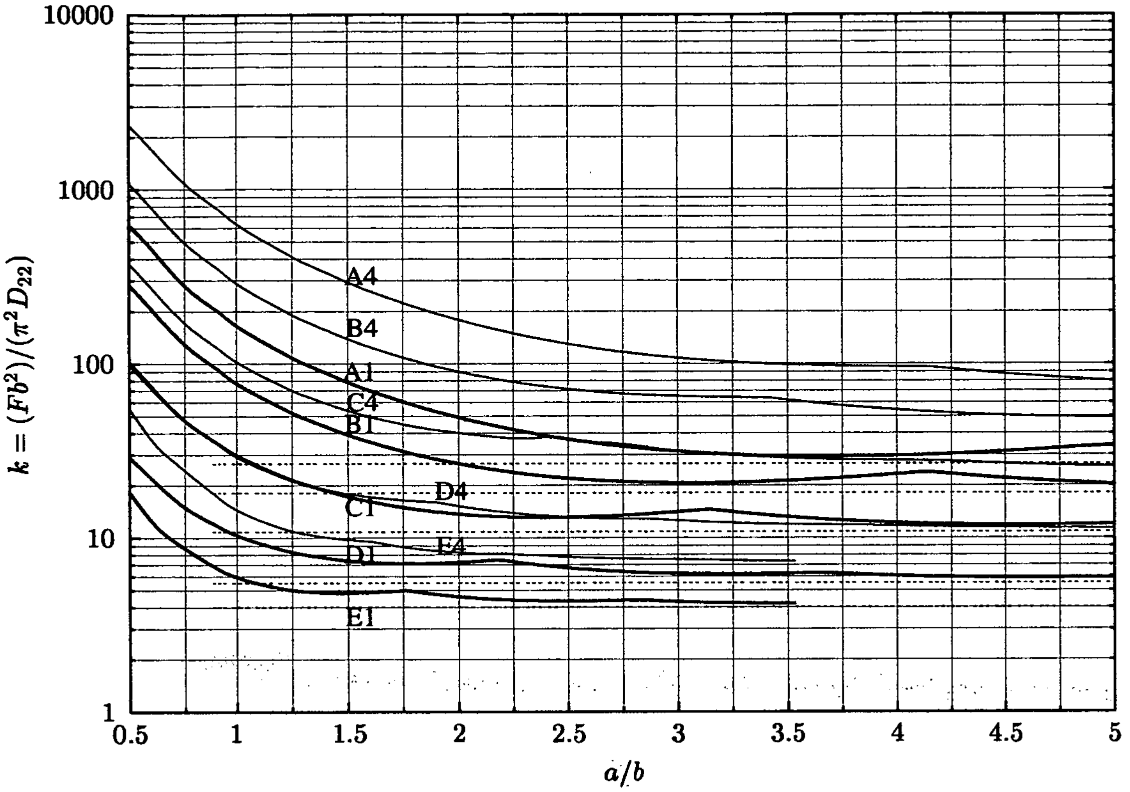

(c) model 2: $\alpha = 45°$

Figure 6.15: Smeared stiffener solution extended to consider $0.5 \leq a/b/ \leq 5.0$. The thick solid line gives the simply supported boundary conditon result, the thin solid line gives the clamped buckling results and the dashed horizontal line give the theoretical minimum buckling load for a simply supported rectangular plate

Table 6.11: Theoretical asymptotic buckling loads for specially orthotropic skew plates. The buckling load is calculated using a rectangular solution of the governing equation of equilibrium for specially orthotropic plates using the affine transform method outlined in Appendix D. Buckling loads are given in terms of $k = (Fb^2)/(\pi^2 D_{22})$

	Model 2		Model 4	
Category	a/b	k	a/b	k
A	3.52	26.67	5.10	54.43
B	2.85	18.14	4.16	36.74
C	2.13	10.81	3.10	21.28
D	1.49	5.51	1.90	9.11
E	1.0	4.0	1.0	4.0

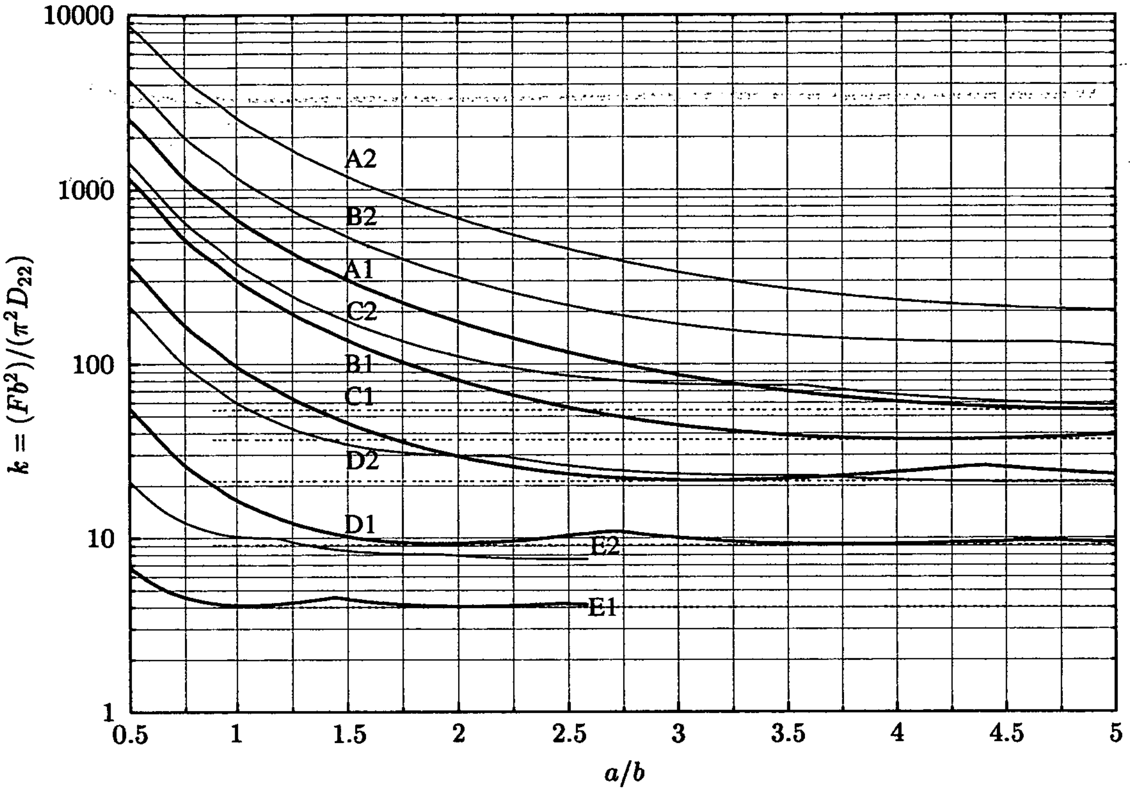

(a) Model 4: $\alpha = 15°$

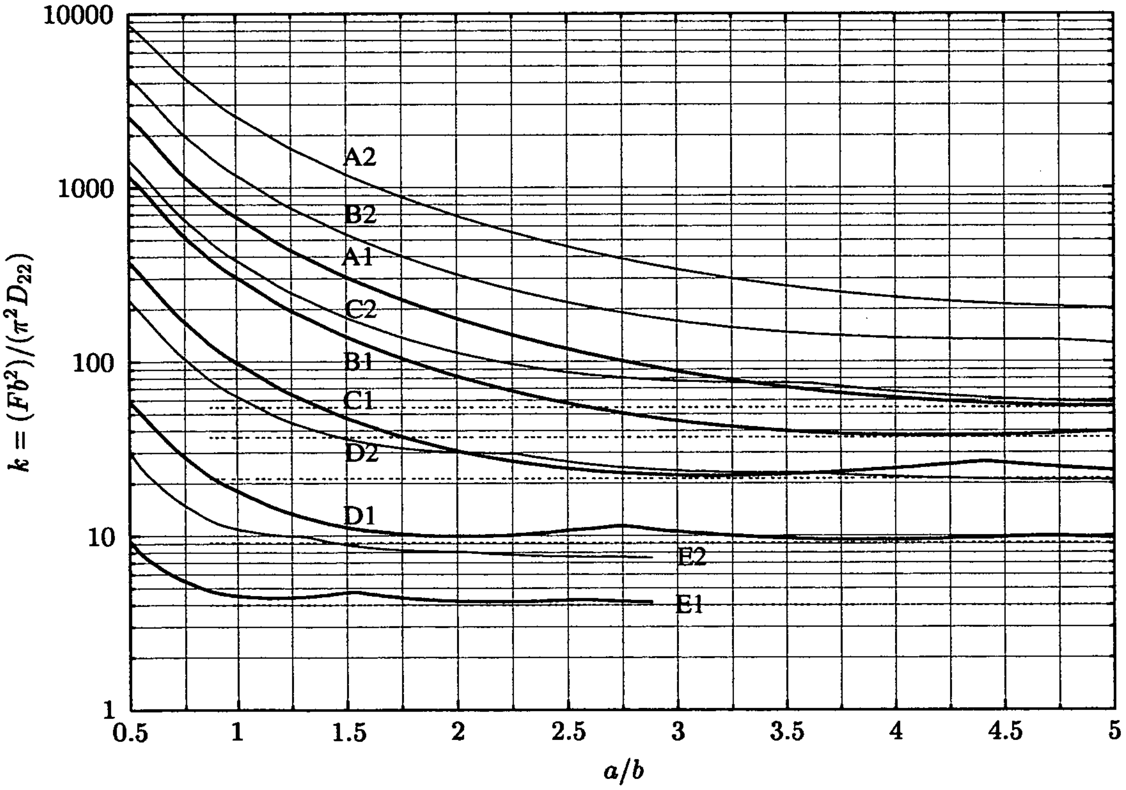

(b) Model 4: $\alpha = 30°$

continued overleaf

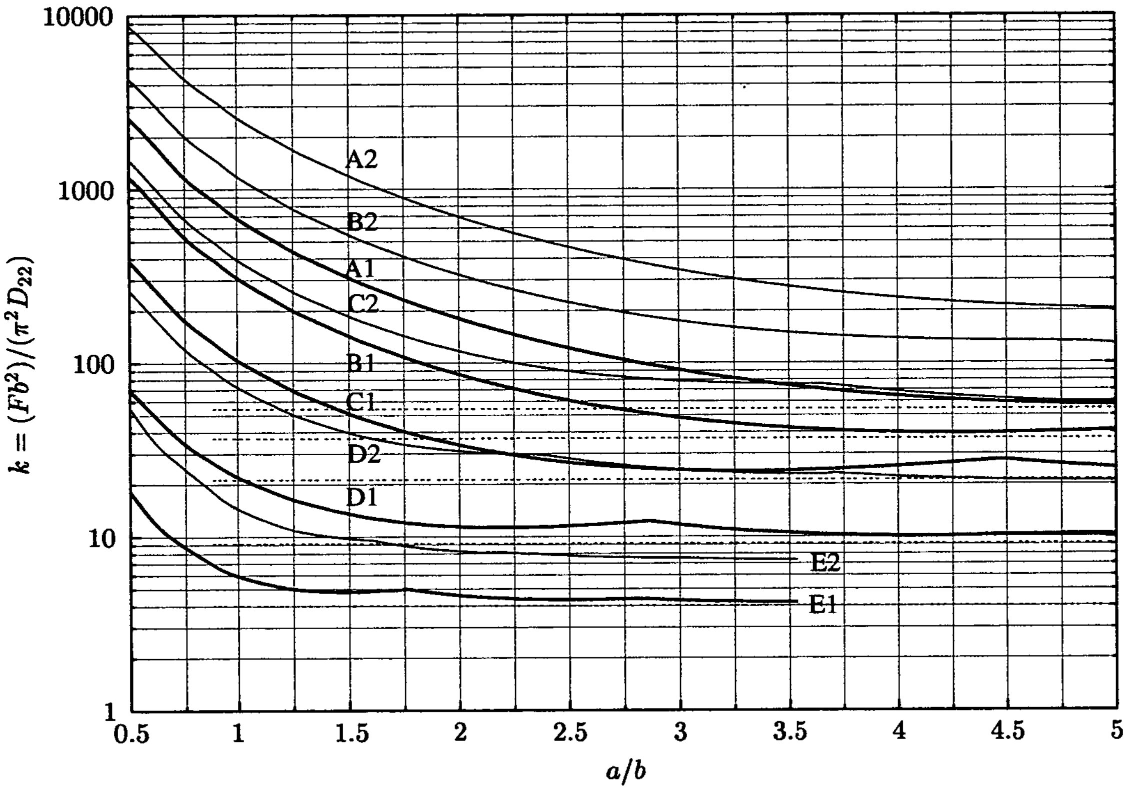

(c) model 4: $\alpha = 45°$

Figure 6.16: Smeared stiffener solution extended to consider $0.5 \leq a/b/ \leq 5.0$. The thick solid line gives the simply supported boundary conditon result, the thin solid line gives the clamped buckling results and the dashed horizontal line gives the theoretical minimum buckling load for a simply supported rectangular plate

6.10 Discussion

6.10.1 General Remarks

The buckling curves of Figures 6.9 to 6.13 resemble those for the isotropic panels in which the buckling load of the plate and/or panel decreases with aspect ratio and cusps form at aspect ratios with coincident buckling loads and different buckling modes. An increase in the orthotropy of the plate increases its buckling load, as does the addition of clamped supports on the panel skin edge. Model 4 appears to carry the higher buckling load in general, but care needs to be made when making this comparison because the bending stiffness for Model 4 is much lower ($13.8kNmm$ compared with $65.3kNmm$ for panels 4 and 2 respectively) and the buckling load is defined as a factor of this constant.

The smeared stiffener buckling prediction is seen to accurately match that of the panel solution if the panel buckles in an overall manner and the stiffeners are closely spaced so that there is no localised, torsional buckling. This is true for panels with simply supported edges, the smeared stiffener solution gives an accurate buckling prediction for the panel. Comparison of the clamped smeared stiffener and clamped panel are not so conclusive. The smeared stiffener solution predicts higher buckling loads than analysis of the panel, but it converges on the panel solution as the aspect ratio of the panel and orthotropy decreases. For panels with the highest orthotropy, the smeared stiffener solution is higher than the panel analysis over the range of aspect ratios used in the study. Because the orthotropy ratio for panel 4 is higher than panel 2, the smeared stiffener buckling predictions are not as accurate. The reasoning for the difference is due to localised buckling modes occurring over the aspect ratio range. Hence, the smeared stiffener and panel buckling mode are not equivalent.

6.10.2 Buckling load increases arising from skew angle

Using the closed-form solution to give a buckling prediction for a rectangular orthotropic plate, the increase in buckling load resulting from the skew angle of the orthotropic plates (smeared stiffener solution) is presented in graphical form in figure 6.17 and 6.18 for model 2 and 4 respectively (they are separated by model number for clarity). To preserve clarity, the range of the buckling strength increase is different for each skew angle.

The buckling strength increases are highest at low aspect ratios which correspond to aspect ratios at which there may be a local mode at failure. In this case, the smeared stiffener model is not valid. The curves therefore need to be read in conjunction with Figures 6.9 and 6.12 to check their applicability.

The curves show buckling strength increases that are erratic over the range of aspect ratios due to asynchronous mode changes. These asynchronous mode changes occur because by considering the affine transformation used to obtain the rectangular plate buckling load, the effect of increasing special orthotropy is to apply a scaling factor to the plate aspect ratio.

A number of observations can be made about the figures:

- there is an increase in buckling strength over that of the rectangular plate (this buckling strength increase for the isotropic case has been presented in Chapter 4);
- the buckling strength increases diminish with an increase in orthotropy. The figures show that the panels that have the highest buckling strength increase over a rectangular plate are those that also have the lowest orthotropy ratio (category D).
- higher buckling strength increases are seen in the Model 2 case compared with the Model 4 case. This can be explained by the fact that the degree of orthotropy is higher in Model 4 than in Model 2 because of the thinner skin on the panel (see Table 6.10). This agrees with the previous point *i.e.* that the higher the orthotropy of the plate, the lower the buckling strength increase as a result of an increase in skew angle.

These results suggest that as the orthotropy of a panel increases, considering the skew angle of the transverse edges may well not lead to very significant increases in the buckling load: the buckling load increases for the category A panels show very small, typically less than 5% for the 45° skew angle plate and much less for the other values of α considered.

6.10.3 Local Buckling

The buckling curves of the stiffened panels are flat at low aspect ratios for the highest degrees of orthotropy. This is due to local buckling of the panel skin. This different buckling mode explains the large difference in buckling load predicted by the smeared stiffener solution and the panel analysis. In the local buckling case, the skin buckles into a number of subpanels of width equal to the distance between the stiffeners and a length, in the case of the panels made from an isotropic material like the models considered herein, approximately equal to this width. The half-wavelength of the mode must be a factor of the length of the panel if the transverse edge is square and simply supported. Hence for a rectangular stiffened panel, the panel skin will tend to buckle into a number of equal rectangles of width equal to the stiffener spacing.

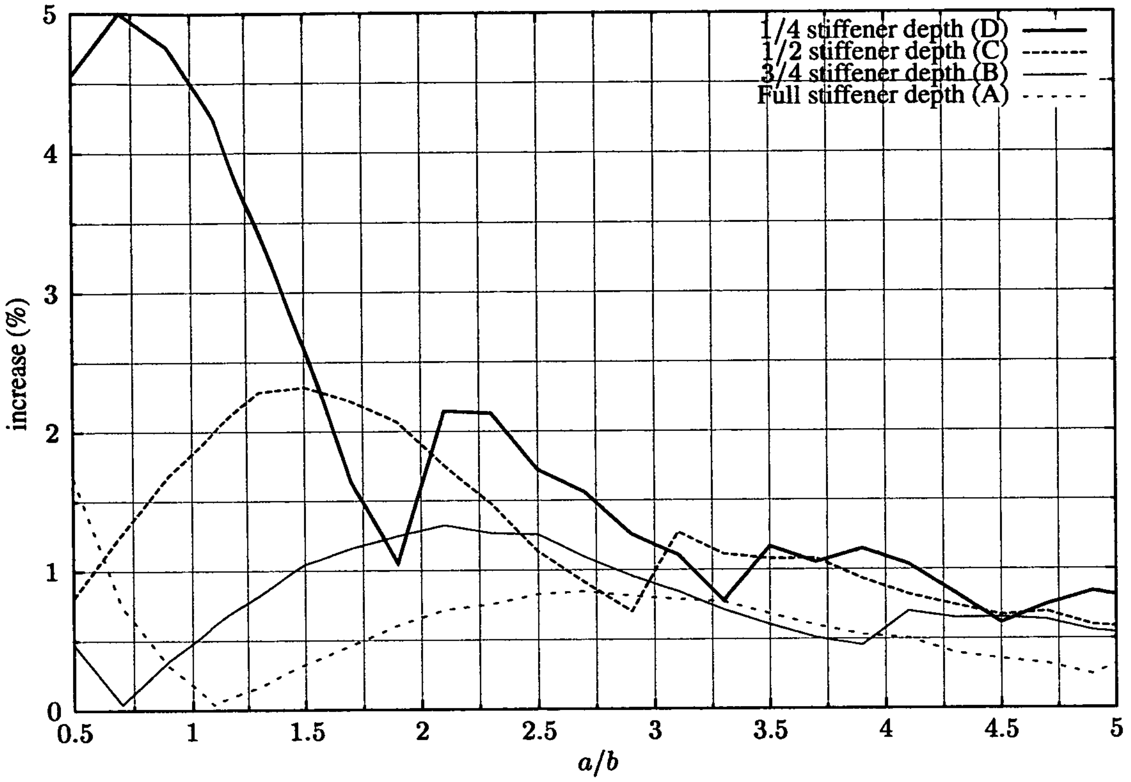

(a) $\alpha = 15°$

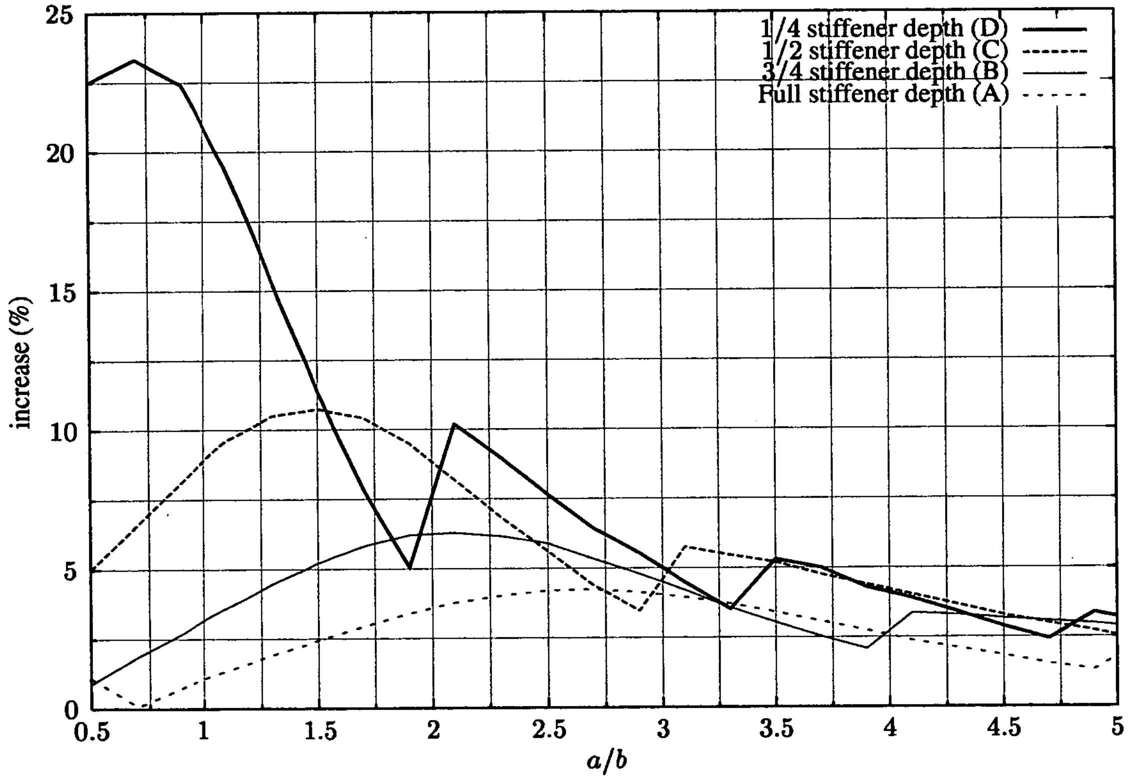

(b) $\alpha = 30°$

continued overleaf

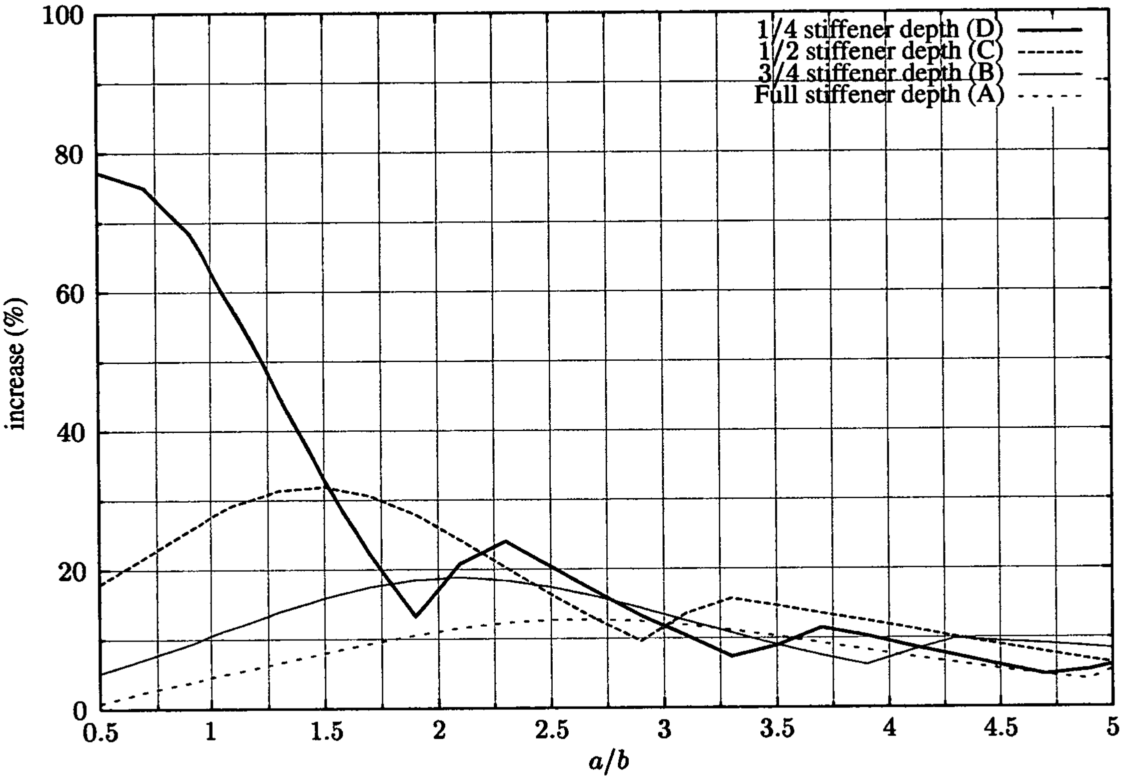

(c) $\alpha = 45°$

Figure 6.17: Model 2: Comparison of buckling loads (shown as percentage increase) resulting from an increase in orthotropy for: (a) $\alpha = 15°$; (b) $\alpha = 30°$ and; (c) $\alpha = 45°$. Note that the letters in the key correspond to the panel category, where A,B,C,D are orthotropic panels with material orthotropy equivalent to the geometric orthotropy for Panel 2 with stiffener depths, $d = 34.34mm, 25.76mm, 17.17mm, 8.59mm$ respectively. Increase is defined as $(k_(\alpha)/k_(\alpha = 0°) - 1).100$ where k is the buckling load of the panel with skew angle α.

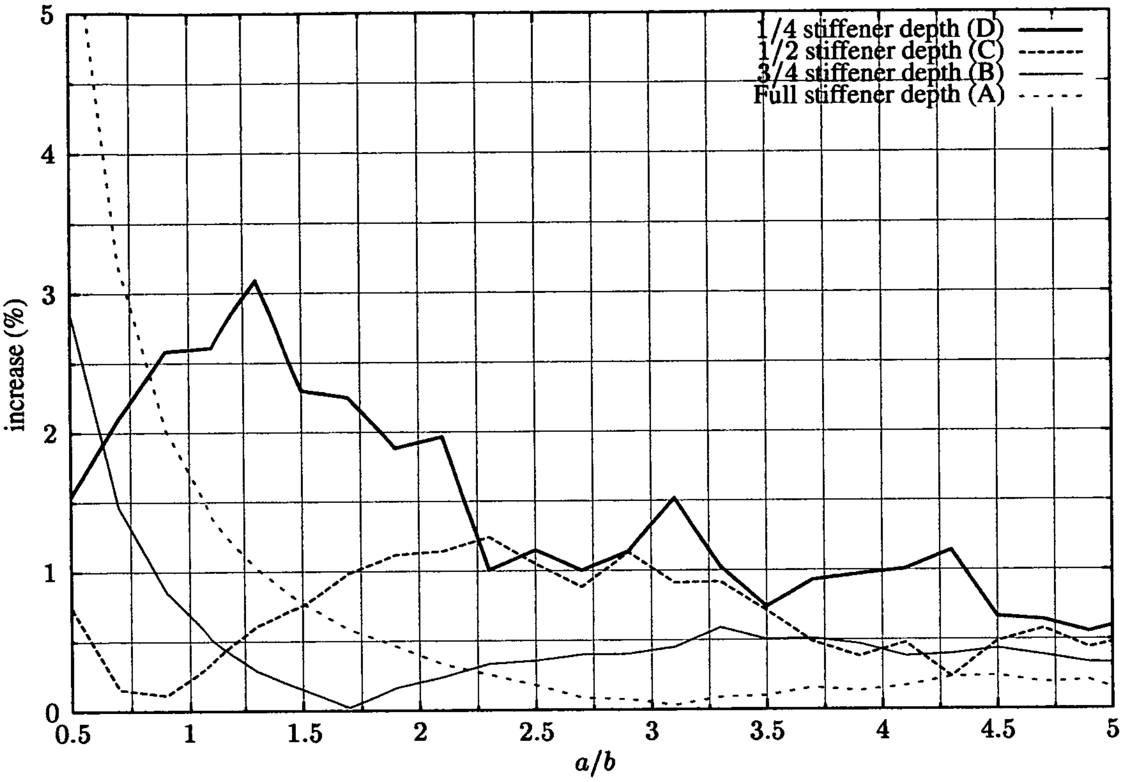

(a) Model 4: $\alpha = 15°$

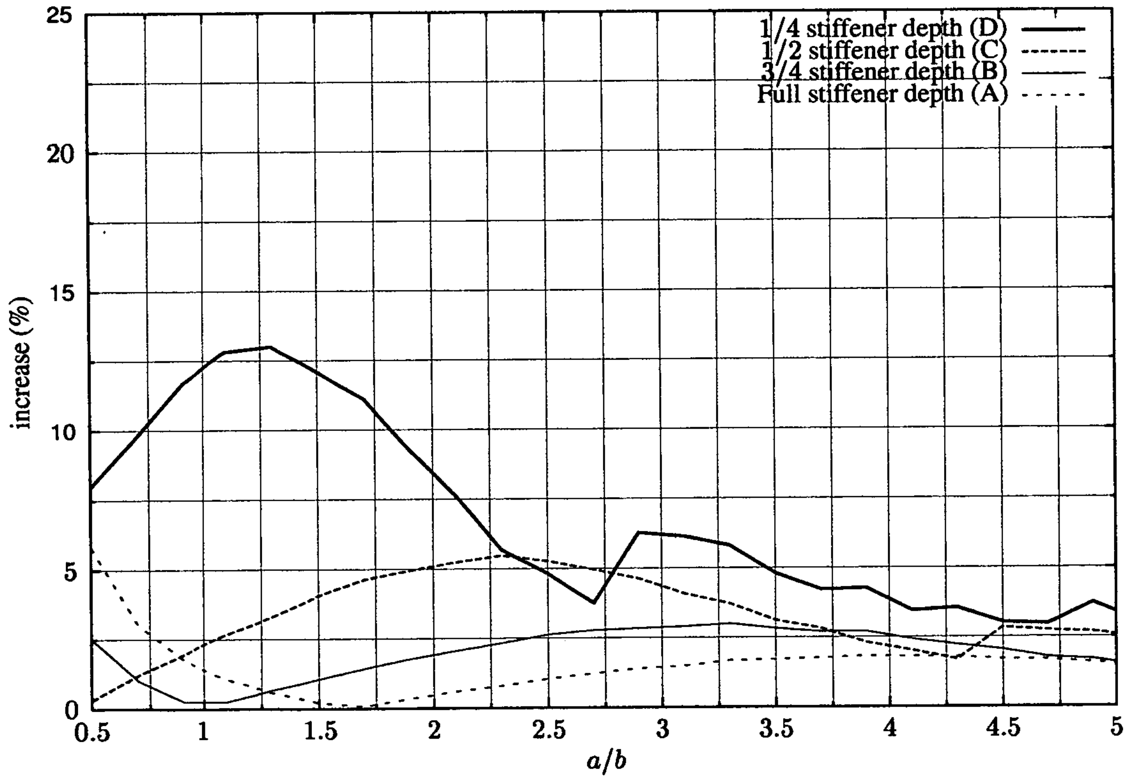

(b) Model 4: $\alpha = 30°$

continued overleaf

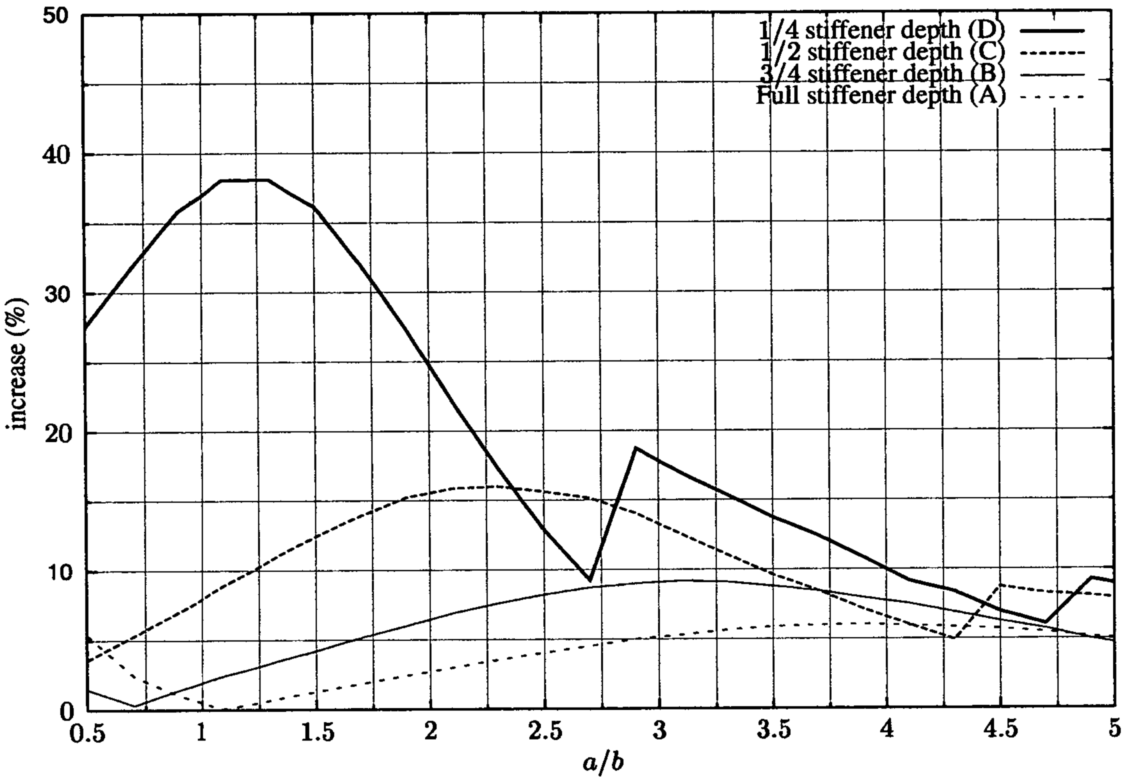

(c) Model 4: $\alpha = 45°$

Figure 6.18: Model 4: Comparison of buckling loads (shown as percentage increase) resulting from an increase in orthotropy for: (a) $\alpha = 15°$; (b) $\alpha = 30°$ and; (c) $\alpha = 45°$. Note that the letters in the key correspond to the panel category, where A,B,C,D are orthotropic panels with material orthotropy equivalent to the geometric orthotropy for Panel 2 with stiffener depths, $d = 34.34mm, 25.76mm, 17.17mm, 8.59mm$ respectively. Increase is defined as $(k_(\alpha)/k_(\alpha = 0°) - 1).100$ where k is the buckling load of the panel with skew angle α.

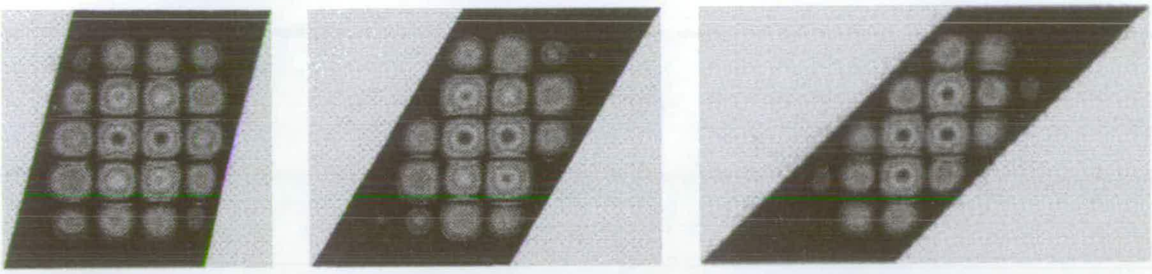
(a) $\alpha = 15°$ (b) $\alpha = 30°$ (c) $\alpha = 45°$

Figure 6.19: Typical local buckling modes for panels with aspect ratio $a/b = 0.75$ and skew angles $\alpha = 15°, 30°$ and $45°$

When a skew transverse edge is introduced in the panel, this local buckling pattern becomes distorted and the local buckling mode for a skew panel comprises a number of strips, each of width equal to the stiffener spacing and longitudinally like a long plate with a rotational restraint along the longitudinal edges. The panel resists buckling at the acute panel corners, in a similar manner to the isotropic solutions. When the local mode governs panel failure, the buckling strength of the panel is equivalent to the buckling strength of the panel skin and there is no appreciable variation buckling strength with an increase in aspect ratio until the overall mode becomes critical. For the same reasons, the boundary conditons applied to the panel along the skin edge also have little effect of the total buckling load and this is confirmed by the analysis. The effect of applying clamped boundary conditons along the panel edges is to increase the range of aspect ratios at which the local buckling mode prevails, but is not accompanied by any significant increase in buckling load over that of the simple supported panel. This is also true of the effect of the skew angle on the panels. The transition from local to overall mode occurs when the buckling load for local buckling is higher than that of the overall mode. This point of transition represents the theoretical optimal panel size for the applied loading and both buckling of the stiffeners and the panel skin occurs simultaneously.

Local modes for Panel 2 with clamped boundary conditons are shown in Figure 6.19 for each skew angle with an aspect ratio, $a/b = 0.75$. The buckling mode plots show the effect of skew angle on the local mode.

The effect of skew angle on the buckling load of the panel can be investigated by comparing the buckling factors of the skin. These are shown in Table 6.12 for Model 4 for which the local buckling mode is more dominant over the range of aspect ratios considered because it has a much thinner skin than Model 2. The table shows the buckling factor for the skin calculated by considering the total load carried by the panel at buckling and scaling this in proportion with the preload applied. The skin buckling factor,

α	Category	Boundary Condition	Min.	Max.	Mean	Std Dev.
15°	A	Simply Supported	4.59	4.70	4.65	0.05
	B	Simply Supported	4.33	4.45	4.39	0.06
	C	Simply Supported	4.25	4.25	4.25	Only Result
30°	A	Simply Supported	4.70	4.88	4.77	0.06
	B	Simply Supported	4.56	4.62	4.59	0.03
	C	Simply Supported	4.51	4.51	4.51	Only Result
45°	A	Simply Supported	4.86	5.62	5.03	0.29
	B	Simply Supported	4.71	4.98	4.82	0.14
	C	Simply Supported	4.92	4.92	4.92	Only Result
15°	A	Clamped	4.60	4.71	4.66	0.05
	B	Clamped	4.57	4.63	4.59	0.03
	C	Clamped	4.49	4.49	4.49	Only Result
30°	A	Clamped	4.70	4.88	4.77	0.07
	B	Clamped	4.25	4.66	4.51	0.18
	C	Clamped	4.25	4.77	4.53	0.19
45°	A	Clamped	4.86	5.62	5.03	0.29
	B	Clamped	4.85	5.58	5.12	0.4
	C	Clamped	5.45	5.45	5.45	Only Result

Table 6.12: Minimum, maximum, mean and standard deviation in skin buckling factors ($k = (\sigma b^2 t)/(\pi^2 D_{22})$) for model 4 for the range of aspect ratios over which local buckling is the dominant mode of buckling (Refer to figure 6.13 for this range.

$k = (\sigma b^2 t)/(\pi^2 D)$, is calculated by taking: σ to be the stress on the skin at buckling; b equal to the stiffener spacing (b_s) and; the flexural rigidity of the panel skin equivalent to D_{22} for the panel. The table shows the minimum, maximum and mean buckling factor for the panel skin for each discrete buckling calculation over the range of aspect ratios where local buckling is dominant. The standard deviation for this set of data is also included to give some indication of the variability of these buckling values where more than one discrete buckling prediction has been obtained.

A number of observations can be made from the buckling results in Table 6.12:

- the buckling load for the panel skin must be higher than the buckling load for a simply supported square plate, implying that the buckling factor must be equal to or higher than 4 as in the table;
- the buckling factors for the skin increase with an increase in skew angle. This is attributed to the more complex buckling mode shapes that form;
- comparison of the clamped and simply supported edge boundary condition, shows that in the case of the panels with the highest orthotropic stiffnesses, the buckling load is affected less when a clamped edge boundary condition is applied than in the cases of panels that have the lowest orthotropy. This can be explained by the increased torsional stiffness of the supporting stiffeners (given in Table 6.9).

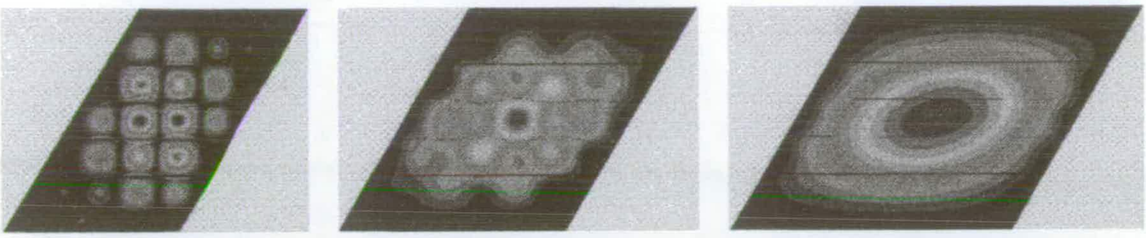

(a) $a/b = 0.75$ (b) $a/b = 1.0$ (c) $a/b - 1.25$

Figure 6.20: Buckling modes showing the transition from the local mode (a) to the fully overall mode (c) via a transitional, torsional mode (b) caused by buckling of the skin and stiffeners.

The torsional stiffness increases the rotational restraint along the longitudinal edge of the subpanels, effectively elongating it. This has the effect of reducing the sensitivity of the transverse edge on the buckling load of the plate;

- the panels with low orthotropy (category C), also have stiffeners with the lowest torsional stiffness and the boundary conditons applied to the longitudinal edge of the subpanel approach those of a simple support. The effect of the clamped edge is therefore more pronounced in this case.

6.10.4 Transition from local to overall buckling

The panel buckling curves in Figures 6.9 - 6.13 show that the panel changes from failing in a local manner to an overall manner when the buckling load (load applied to the panel skin) of the panel skin is lower than that of the equivalent orthotropic panel. This section presents a selection of buckling mode contour plots showing the transformation from local to overall buckling. Both transition from local to overall buckling as a result of increasing aspect ratio and increasing orthotropy at a fixed aspect ratio is considered.

Buckling modes in Figure 6.20 show the transition from local to overall buckling as the panel aspect ratio increases for panel 2 with clamped edges and $\alpha = 30°$. The figure shows that the transition between local and overall buckling is not sudden, but that an intermediate mode form (Figure 6.20(b)). The transitional mode forms because the stiffeners buckle in a torsional manner together with the panel skin.

Buckling modes in Figure 6.21 show the transition from the local to overall buckling mode for Panel 2 with clamped edges as the orthotropy of the panel increases from that of category D panel (1/4 full stiffener depth) to that of the category A panel (full stiffener depth). The panel has an aspect ratio of $a/b = 0.5$ and skew angle, $\alpha = 45°$. A torsional buckling mode, similar to that in Figure 6.20(b) in which both the

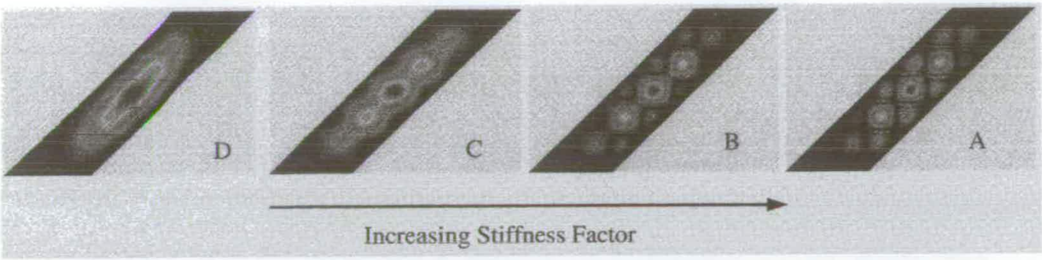

Figure 6.21: Transition from overall to local buckling as the orthotropy of the Panel 2 increases from being of category D (1/4 full stiffener depth) to that of category A (full stiffener depth). The buckle plots are for Panel 2 with clamped skin boundaries, aspect ratio of 0.5 and skew angle $\alpha = 45°$. The letters next to the buckle plot correspond to the panel category.

stiffeners and plate buckle is seen in the second mode plot.

6.11 Conclusions

This chapter presents a comprehensive study on the critical buckling load of skew, stiffened panels. The study considers the effect of aspect ratio, stiffener depth and edge boundary conditon on benchmark panels, originally presented by Stroud *et al.* [85], that are made skew.

The benchmark panels are square and these panels are analysed using ABAQUS finite element code and compared against other results in the open literature as a verification exercise. The results also provide a further set of buckling predictions.

Two of the aluminium, blade stiffened benchmark panels are investigated further and buckling curves are drawn showing the relationship between panel buckling and aspect ratio as the depth of the stiffeners on the benchmark panel increase. The buckling curves identify the critical aspect ratios at which local buckling mode failure is superceded by an 'overall' mode. Both boundary conditons of all edges simply supported and all edges fully clamped are considered in the study to give upper– and lower– buckling loads for the panels.

An equivalent 'smeared stiffener' model of the benchmark panels is presented. The smeared stiffener model gives very accurate buckling predictions for a panel that is simply supported along all edges when the mode of failure of the panel and 'smeared stiffener' plate are the same (*i.e.* of the overall type). The smeared stiffener model does not produce good buckling predictions for the panel when its edges are fully clamped. In this case, the plate model overestimates the buckling load of the plate. This overestimation is explained by a difference in edge boundary conditon between the two structures.

The buckling strength increase of a skew panel over an equivalent rectangular panel is calculated using the 'smeared stiffener' models for the simply supported boundary conditon. The comparisons show that when $\alpha = 45°$, the buckling strength advantages of considering skew planform geometry can be as high as 10%. The comparison shows that there are potentially economic savings to be made by considering the skew planform geometry of a panel at the design stage rather than making a crude rectangular approximation.

At low aspect ratios, when the buckling strength of the panel skin governs the critical buckling load of the panels (*i.e.* a local buckling mode), skew edges do not result in significant buckling strength increases. Instead, the buckling strength of the panel skin is governed by the torsional stiffness of the stiffener which is effectively applying a rotational restraint along the longitudinal edges of the plate running between the stiffeners.

The effect that skew has on the buckling loads of skew panels is extended in chapter 8 to include the effects of a planform taper.

Chapter 7

Buckling of isotropic skew plates tapered in planform

7.1 Introduction

Plates and panels used in aircraft applications, especially in wing panels, are often not only skew or rectangular, but also tapered in planform area. Given the frequency with which this plan geometry is encountered, it is surprising to find that little work at all has considered plates and panels tapered in planform and none which include skew and planform taper. The published work in the open literature is discussed in Section 7.1.1.

This chapter adds to the limited research in this area and logically extends the previous work on skew plates and panels to plates that are skew and tapered in planform. A comprehensive parametric study is presented to determine the buckling load for tapered plates and the results are compared with those for skew plates previously obtained and discussed. As with the previous work, analysis is carried out using finite element code, ABAQUS [3] (see Appendix A).

7.1.1 Background

The following section presents a comprehensive summary of work on elastic buckling of plates tapered in planform in the open literature.

The first work dealing with tapered plates is given by Klein [49] in which design curves are presented for varying aspect ratios and degrees of taper using a collocation method. Klein's tapered plate has the geometry of an incomplete isosceles triangle, with taper being defined as the angle at the apex of the complete triangle. Loading to the plate is a pure in-plane, uni-axial compressive stress, with a shear stress applied along the longitudinal, tapered edges to preserve global equilibrium. Klein's work is extended to include pure shear loading [52] and in-plane bi-axial compression loading [50].

Pope [73] used the Raleigh-Ritz method with a deflection function in the form of a trigonometric series. He assumed that the buckling mode laterally across the plate would be the same as that for a rectangular plate. Pure in-plane compression loading is considered with either a shear flow or in-plane restraint applied to the tapered longitudinal edges to preserve global equilibrium. Buckling predictions are made for varying ratios of in-plane compression applied to the transverse edges as well as combinations of clamped and simply supported edges on opposite sides of the plate. Pope's work is incorporated into the current design charts produced by ESDU [1]. In general, Pope predicts critical buckling loads that are lower that those of Klein's.

More recent work on plates tapered in planform has been carried out by Radloff, Hyer and Nemeth [74]. Radloff *et al.* present a closed form solution for predicting buckling loads for simply supported plates made from symmetric laminated composites under an in-plane, pure compression loading. The closed form solution is verified using ABAQUS finite element code and finally, experimentally validated. Isotropic plates are also treated and used as a basis from which the effect of symmetric laminates can be seen. All the laminates are specially orthotropic or anisotropic. The geometry of the tapered panels is the same as that used by both Klein and Pope and is a truncated isosceles triangle.

Herdi and Tutuncu [41] provide buckling predictions for tapered plates using a finite element formulation. The plates have the same geometry as that considered by the previous authors and are compression loaded. The boundary conditions are of limited use in aerospace applications because the tapered longitudinal edges are assumed to be free with only the transverse edges simply supported. The buckling predictions are made for symmetric laminated composites and no isotropic buckling solutions are given.

All the authors typically use the plate geometry, often described in different ways, using different nomenclature. A typical plate is shown in Figure 7.1(a).

All authors predict an increase in buckling load with an increase in taper and it would seem that sensible, cost effective design of tapered plates should make use of this observed strength increase.

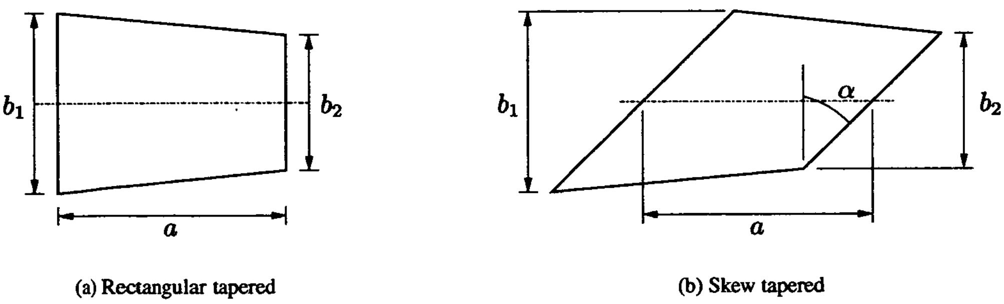

(a) Rectangular tapered

(b) Skew tapered

Figure 7.1: Planform geometry of a rectangular tapered plate (a) and a skew tapered plate (b). The figure shows plates of length, a, transverse width, b_1 and b_2, and for the skew plate, a skew angle, α. Taper is defined as the ratio b_2/b_1 and aspect ratio the ratio of plate length and widest transverse width, b_1 *i.e.* a/b_1

7.2 Aims and Objectives

The aim of the chapter is to establish the buckling strength characteristics of tapered plates as the transverse edges become skew. A parametric study of the type used so far relating the buckling strength and aspect ratio of the plates will be carried out. The following subsections describe the choice of plate geometry, edge boundary conditions and loading used throughout the study.

7.2.1 Geometry

The geometry used for the plates is that of a truncated isosceles triangle, hence there is symmetry about the plate centre line when the panel isn't skew. Rectangular tapered plates are made skew by introducing a skew of $\alpha°$ about the intersection of the plate centre line with the transverse plate edge. Figure 7.1 shows a typical plate geometry for a rectangular tapered panel (a) and a skew tapered panel (b). The rectangular tapered plates are of similar geometry to those treated in previous work discussed in section 7.1.1 This geometry and nomenclature is adopted to allow for comparison with other work.

Aspect ratio is defined as the ratio between the longitudinal distance along the centreline of the plate, a, and the longer transverse width of the plate, b_1. Hence aspect ratio is equal to a/b_1. Taper, β, is defined as the ratio of the narrower, transverse edge to the larger transverse edge, *i.e.* $\beta = b_2/b_1$. This definition of taper, which is consistent with Pope's [73], means that the internal angle of the plate varies as the aspect ratio of the plate changes.

Further discussion is given to the choice of geometry in Section 7.2.4 (Parameters used in the Study).

7.2.2 Edge Boundary Conditions

Boundary conditions are chosen to give upper– and lower– bounds to the problem and consider combinations of clamped and simple supports on opposing edges. Hence there are 4 possible combinations. These are:

1. all edges simply supported (absolute lower bound) [Case 1-1];
2. all edges clamped (absolute upper bound) [Case 4-4];
3. longitudinal edges simply supported and transverse edges clamped [Case 1-4];
4. longitudinal edges clamped and transverse edges simply supported [Case 4-1].

Each boundary condition is given a 2 digit code in keeping with the nomenclature used to describe boundary conditions in previous chapters. Hence, the boundary condition is Case $x - y'$ where x describes the boundary condition along the longitudinal tapered plate edges and y' the boundary condition along the transverse plate edges. x and y' take the value 1 if the edges are simply supported or 4 if the edges are clamped. The cases relating to each boundary condition case are given in square brackets in the previous listing.

7.2.3 Loading

Loading to the plates is a pure in-plane compression load. To preserve global equilibrium, this compression is also applied along the tapered longitudinal edges of the plate and the material is under a constant uniaxial stress. For comparison with other results, analyses of plates with $\alpha = 0°$ are run with a uniform shear applied along the tapered longitudinal edges of the plates. A shear along the tapered longitudinal edges is omitted from the loading for the study on skew plates because, when the plates become skew, the shear load causes bending in the plate. The chosen loading simplifies the analysis, but enables conclusions about the behaviour of the skew tapered plates to be made.

Schematics of the applied loading are given in Figure 7.2 for pure in-plane compression (a) and an in-plane compression load with shear applied along the tapered edge (b) as adopted by Klein [49] and Pope [73].

7.2.4 Parameters used in the study

This section describes the parameters used in the study and uses the nomenclature defined in the previous sections.

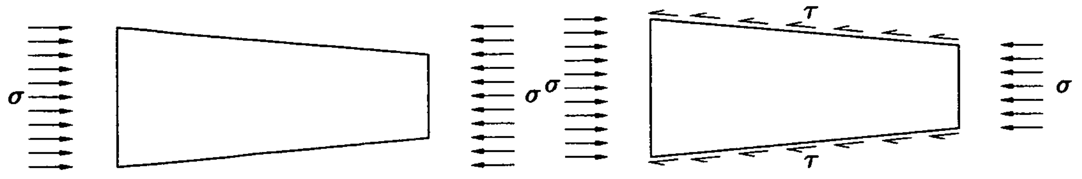

(a) Pure in-plane compression loading

(b) In-plane compression loading with shear applied to the longitudinal tapered edge

Figure 7.2: Loading to the plate: (a) a uniform compression loading applied along the transverse edges and where necessary, the longitudinal ones as well; and (b) a uniform compression loading applied along the transverse plate edges and a shear load applied along the longitudinal tapered edges. This latter loading condition is considered only for plates with $\alpha = 0°$ and is used for comparison and verification purposes.

The four parameters used in the study are:

1. aspect ratio, $0.5 \leq a/b_1 \leq 2.5$;
2. skew angle, $\alpha = 0°, 15°, 30°, 45°$;
3. taper, $\beta = 1.0, 0.8, 0.6, 0.4$;
4. boundary conditions, Case 1-1, Case 1-4, Case 4-1, Case 4-4 (As discussed in section 7.2.2.

The parameters are the same as those used in the previous chapters of the thesis and therefore allow comparisons to be made with these previous results. The parameters are also comparable to those used to compile the results in the existing literature.

Figure 7.3 shows a plate with $a/b_1 = 1$ for all the combinations of skew angle and taper used in the study. It shows the effect of taper and skew angle on the planform area of the plate. The figure shows the logical transformation of rectangular plate or rectangular tapered plate into a skew and/or tapered plate reading from left to right. Reading from top to bottom, the figure shows the logical transformation of a rectangular or skew plate into a rectangular and/or skew tapered plate.

The figure also shows that the planform area of the plate decreases as β decreases according to,

$$A = \frac{b_1 a}{2}[1 + \beta] \tag{7.1}$$

Thus comparisons made between plates having different values of β also have different area which translates into masses if the plate material has a constant density and thickness. The plate perimeter also in-

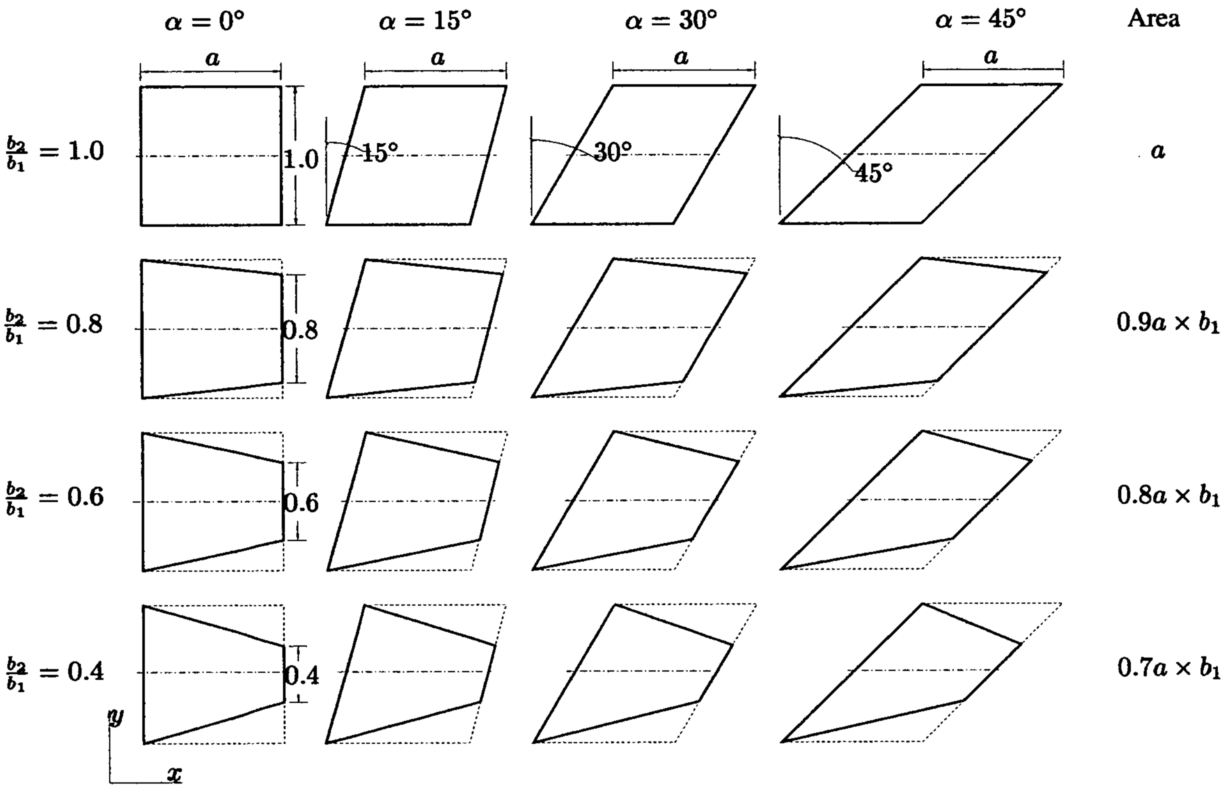

Figure 7.3: Schematic showing the geometry resulting from the parameters chosen in the study. The figure shows the logical transformation of a rectangular and/or tapered plate becoming increasingly skew reading from left to right and a rectangular or skew plate becoming increasingly tapered reading from top to bottom. The far most right column gives the planform area of the plates as the degree of taper, β, increases. The planform area of the plate decreases as the degree of taper increases, but remains constant as the angle of skew increases. The dashed outline of the rectangular skew plate superimposed over the tapered plates highlights this area decrease.

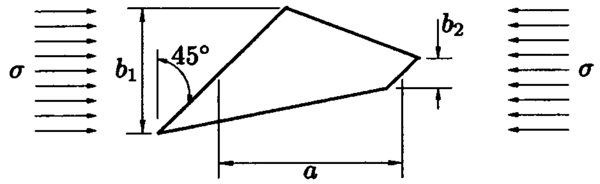

Mesh	10 x 10	20 x 20	30 x 30	40 x 40	60 x 60
D.O.F.	4205	17405	39605	70805	160205
$k = (\sigma b^2 t)/(\pi^2 D)$	10.359	9.897	8.759	8.756	8.755
Difference (%)	—	4.668	2.126	0.0310	0.0103

Table 7.1: Convergence study for S8R5 type ABAQUS element for a skew, tapered plate with $\alpha = 45°$, $\beta = 0.4$, $a/b = 1.0$ and simply supported boundary conditons. All the meshes were uniform. The 'Difference (%)' row gives the percentage difference between each successive mesh refinement.

creases with skew angle, implying that a larger supporting structure would be necessary for the plate, but decreases with taper.

Using the definitions of geometry adopted for the parametric study, and keeping b_1 constant throughout, the total preloading applied to the plate is constant and it is therefore valid to make comparisons about the relative buckling load increases over the entire range of panels adopted.

7.3 ABAQUS Modelling

The elastic buckling strength of the plates is computed using finite element package, ABAQUS. A mesh convergence study showed that good accuracy (to within 1 percent of the converged solution) in buckling strength predictions can be obtained using a 30 $\times$ 30 mesh as in the previous analyses of skew plates. Similarly, the mesh density was kept uniform and constant over the range of plates studied.

Table 7.1 shows the results of the convergence study for a the simply supported skew, tapered plate with $\alpha = 45°, \beta = 0.4$ and $a/b = 1.0$.

ABAQUS type S8R5 elements [3] are used throughout to predict the critical buckling load of a classically 'thin-plate' at discrete intervals of $0.1 \times a/b_1$.

7.3.1 Model Verification

The ABAQUS model has been previously used and verified against other, previous work in the preceeding chapters for plates that are skew and not tapered. It has also been shown that the ABAQUS model also predicts the correct closed-form solutions for square and rectangular plates.

To verify the use of the model for plates that are tapered in planform, plates that have the same loading used by Klein [49] and Pope [73] (*i.e.* a uniform compressive stress applied to the transverse plate edges and an equilibrating shear to the longitudinal ones) are analysed. Comparisons between Pope's results and the current ABAQUS results are presented in Table 7.2 for verification purposes and give the difference (given as percentage) between the two. Because Pope's results give consistently lower buckling predictions than Klein's, Klein's results are omitted from the comparison. Klein's results are also presented using different nomenclature to define the plate geometry which makes comparison difficult. Both Pope's and Klein's results predict the closed-form solutions for simply supported rectangular plates exactly (Rad *et al.* [74] observations about this are incorrect).

Buckling predictions obtained using ABAQUS are close to those made by Pope, although they are in general marginally lower. This finding is consistent with a better approximation of the buckled form of the plate that should be achieved with the high number of degrees of freedom in the ABAQUS mesh. The ABAQUS model gives confidence in the analysis by Pope and the current ESDU [1] data sheet.

ABAQUS results in the table are given to 3 d.p. in order that they could be used for further verification purposes. Pope's results are obtained by reading from his design charts [1] and are therefore only given to one decimal place. Note that reading from Pope's design charts may lead to further error.

7.4 Results

Results are presented as buckling curves for each of the boundary condition cases and skew angles considered in the study. Separate figures are used for each skew angle. Each figure is split into four sub-figures which give the buckling curve for each angle of skew treated (including $\alpha = 0°$). The buckling load of the plates is given using the now familiar buckling coefficient,

$$k = \frac{\sigma b_1^2}{\pi^2 D} \tag{7.2}$$

Table 7.2: Comparison between ABAQUS and Pope [73] buckling predictions for skew tapered plates for boundary condition cases: (a) 1-1; (b) 4-4; (c) 1-4; and (d) 4-1. Buckling strengths are given in terms of the critical buckling factor coefficient, $k = \sigma b_1^2 t/\pi^2 D$ (see Eqn (7.4)). A negative difference indicates that the buckling results from ABAQUS are higher than those of Pope.

	$\beta = 0.8$				$\beta = 0.6$				$\beta = 0.4$			
a/b_1	1.0	1.5	2.0	2.5	1.0	1.5	2.0	2.5	1.0	1.5	2.0	2.5
ABAQUS	5.017	4.939	4.722	4.623	6.343	5.621	5.262	5.060	7.609	6.364	5.807	5.483
Pope	5.0	4.9	4.6	4.6	6.3	5.6	5.2	5.1	7.7	6.3	5.9	5.4
Difference (%)	-0.3	-0.8	-2.79	-0.5	-0.7	0.4	-1.2	0.8	1.2	-1.0	1.6	-1.5

(a) Comparison results for all plate edges simply supported (Case 1-1)

	$\beta = 0.8$				$\beta = 0.6$				$\beta = 0.4$			
a/b_1	1.0	1.5	2.0	2.5	1.0	1.5	2.0	2.5	1.0	1.5	2.0	2.5
ABAQUS	12.225	9.986	9.285	9.743	14.296	11.875	10.824	10.207	17.270	13.895	12.341	10.500
Pope	13.4	10.1	9.4	9.0	15.4	12.1	11.0	10.3	17.7	14.2	12.5	10.5
Difference (%)	9.6	1.1	1.2	-8.3	7.7	1.9	1.6	0.9	2.9	2.2	1.3	0.0

(b) Comparison results for all plate edges clamped (Case 4-4)

	$\beta = 0.8$				$\beta = 0.6$				$\beta = 0.4$			
a/b_1	1.0	1.5	2.0	2.5	1.0	1.5	2.0	2.5	1.0	1.5	2.0	2.5
ABAQUS	7.654	6.599	5.677	5.406	9.202	7.575	6.709	6.268	11.529	8.937	7.797	7.138
Pope	7.7	6.6	5.7	5.4	9.2	7.6	6.7	6.3	-	8.9	7.8	7.1
Difference (%)	0.6	0.0	0.4	-0.1	0.0	0.3	-0.1	0.5	-	-0.4	0.0	-0.5

(c) Comparison results for tapered longitudinal edges simply supported and transverse edge clamped (Case 1-4)

	$\beta = 0.8$				$\beta = 0.6$				$\beta = 0.4$			
a/b_1	1.0	1.5	2.0	2.5	1.0	1.5	2.0	2.5	1.0	1.5	2.0	2.5
ABAQUS	8.787	8.310	8.020	7.858	10.268	9.280	8.779	8.480	12.038	10.316	9.533	9.078
Pope	9.1	8.4	8.1	8.0	10.1	9.3	8.9	8.5	11.9	10.4	9.7	9.2
Difference (%)	3.6	1.1	1.0	1.8	-1.7	0.2	1.4	0.2	-1.2	0.8	1.8	1.3

(d) Comparison results for tapered longitudinal edges clamped and transverse edges simply supported (Case 4-1) where:

σ is the critical buckling stress applied to the plate;

b_1 is as previously defined;

D is the flexural rigidity of the plate.

The bucking curves are presented in Figures 7.4 - 7.7 where: Figure 7.4 shows buckling curves for Case 1-1 boundary conditons; Figure 7.5 for Case 1-4; Figure 7.6 for Case 4-1; and Figure 7.7 for Case 4-4. Each of the figures is split into four sub-figures each of which relate to one of the skew angles ($\alpha = 0°, 15°, 30°$ and 45°) used in the study.

There is a marked difference in the appearance of the curves when comparing them to buckling curves for skew and rectangular plates. The current curves do not take on the classical garland form of buckling curves although distinct peaks in the buckling load often accompany a buckling mode change. The behaviour of the plate around such peaks is discussed in section 7.5.1.

Clearly, the buckling load of a plate increases as the degree of taper increases (which corresponds to a reduction in β). Buckling strength increases are considered in further detail in sections 7.5.2 and 7.5.3.

7.5 Discussion of Results

7.5.1 Buckle mode changes

Splines are drawn through the buckling curves in Figures 7.4 – 7.7. The cusps that are seen in previous buckling curves for plates that are skew or rectangular are not present, but peaks in the buckling load of the plates do occur which correspond to changes in buckle mode. These peaks are predictably more pronounced and numerous in the boundary conditon case that has clamped longitudinal edges and simply supported transverse edges (Case 4-1). The complete set of buckling curves for this case are given in Figure 7.6. To show what happens in the region of these peaks, a representative buckling curve, that of $\beta = 0.8, \alpha = 0°$, is chosen for further analysis. This curve is chosen because it has more clearly defined peaks than curves with smaller values of β. This analysis is presented in the remainder of this section.

Figure 7.8 shows the representative buckling curve. Two curves are given: one for the critical buckling load (1^{st} eigenvalue) and one for the second most critical state of equilibrium (2^{nd} eigenvlaue). The curves

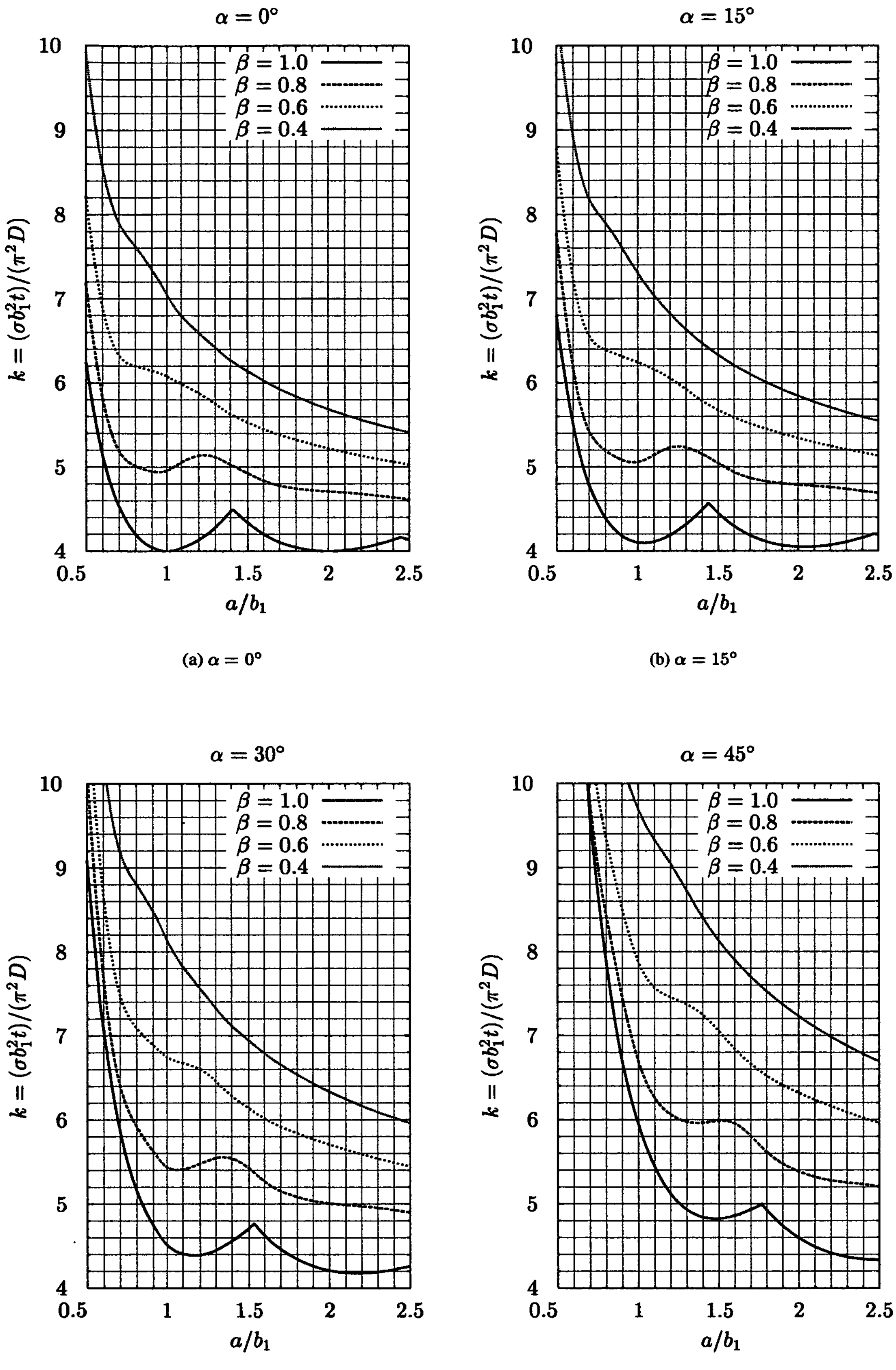

(a) $\alpha = 0°$

(b) $\alpha = 15°$

(c) $\alpha = 30°$

(d) $\alpha = 45°$

Figure 7.4: Buckling curves for Case 1-1 (All plate edges simply supported)

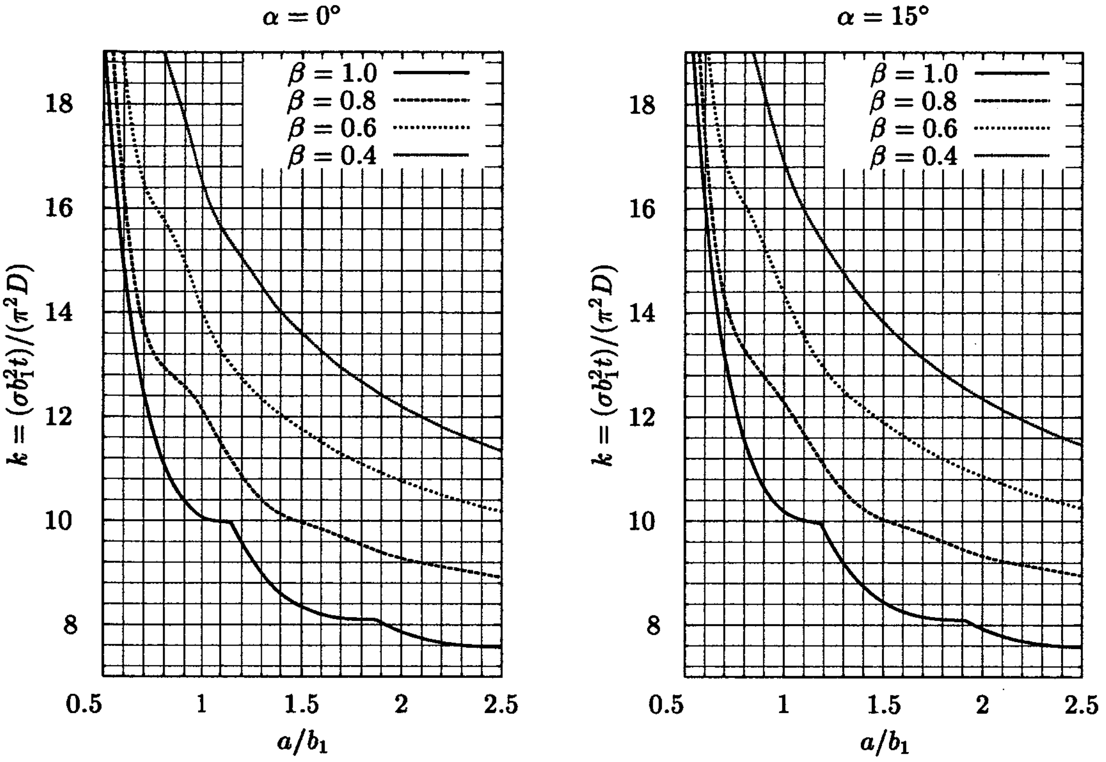

(a) $\alpha = 0°$

(b) $\alpha = 15°$

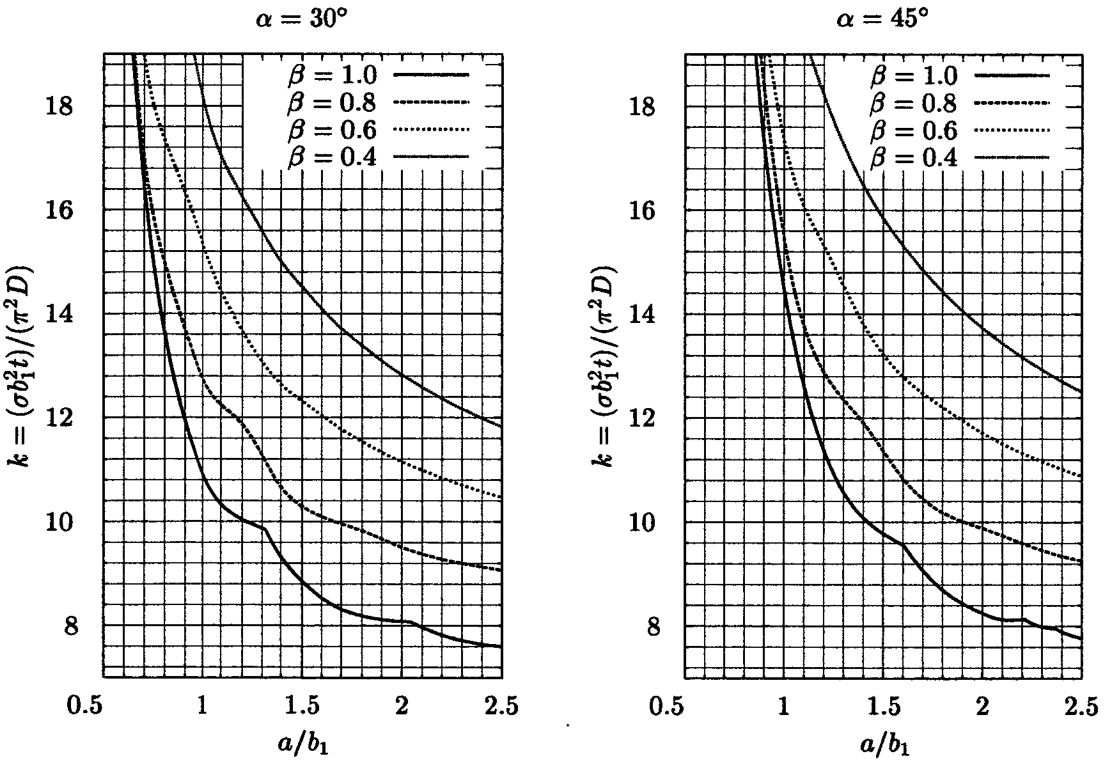

(c) $\alpha = 30°$

(d) $\alpha = 45°$

Figure 7.7: Buckling curves for Case 4-4 (All edges clamped)

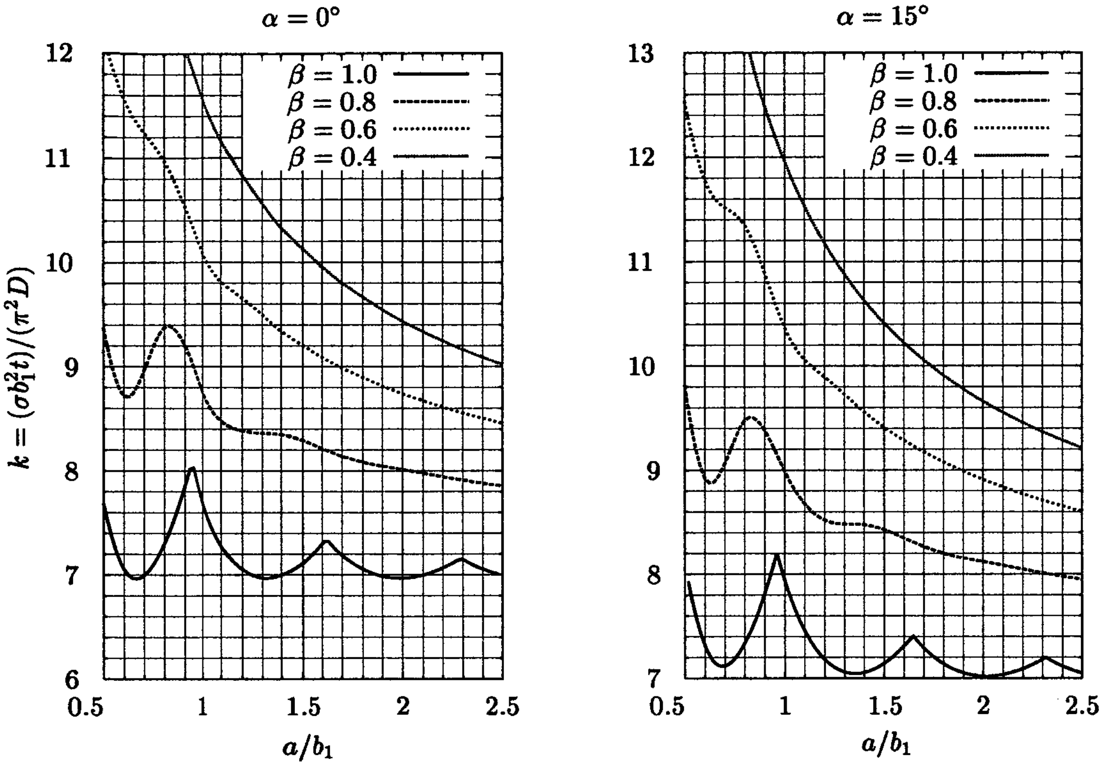

(a) $\alpha = 0°$

(b) $\alpha = 15°$

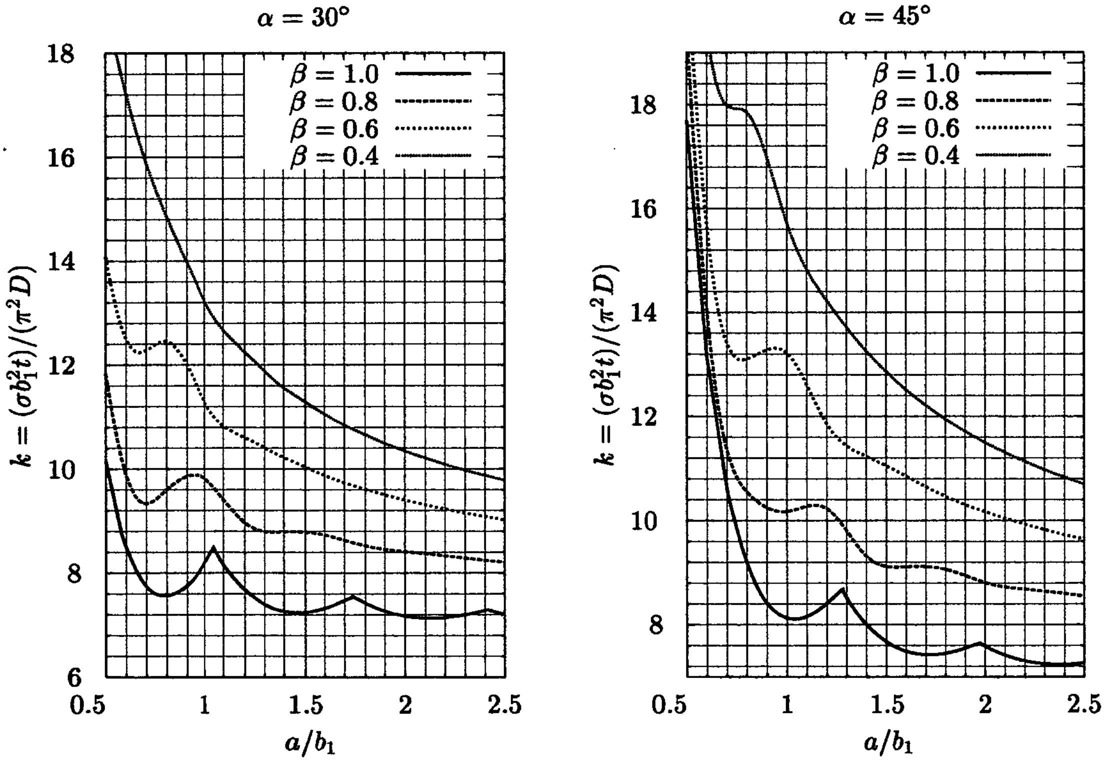

(c) $\alpha = 30°$

(d) $\alpha = 45°$

Figure 7.6: Buckling curves for Case 4-1 (Longitudinal edges clamped and transverse edges simply supported)

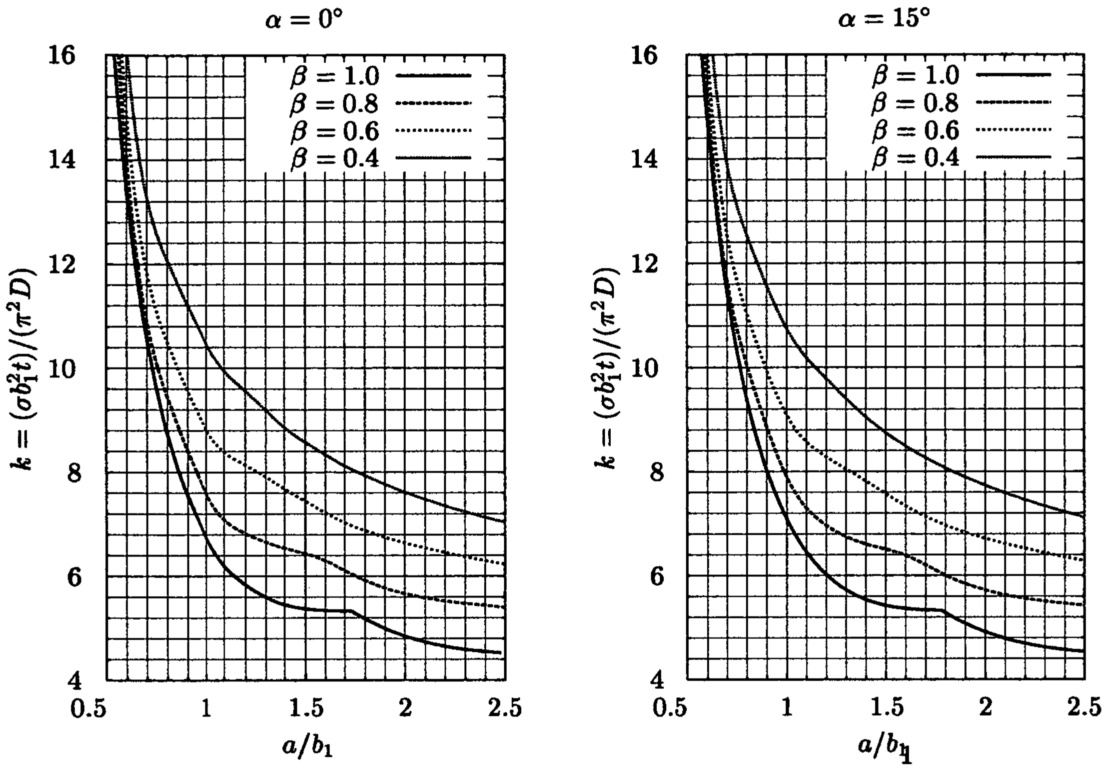

(a) $\alpha = 0°$

(b) $\alpha = 15°$

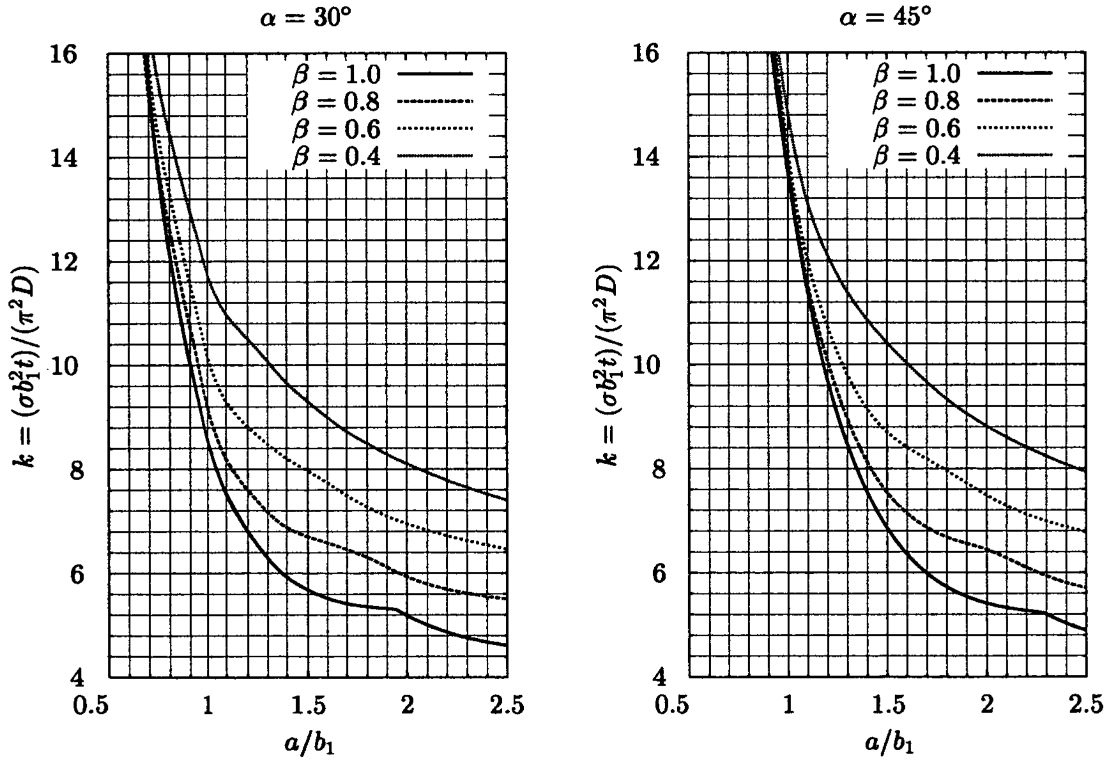

(c) $\alpha = 30°$

(d) $\alpha = 45°$

Figure 7.5: Buckling curves for Case 1-4 (Longitudinal edges simply supported and transverse edges clamped)

show the discrete points at which the buckling loads were calculated and the spline which was generated through them. The critical buckling curve (1^{st} eigenvalue) shows two peaks that in the case of rectangular or skew geometry plates would lead one to predict that distinct cusps will form between $a/b_1 = 0.8$ and $a/b_1 = 0.9$ and $a/b_1 = 1.4$ and $a/b_1 = 1.5$. However, the second eigenvalue around these peaks does not converge on the critical buckle load prediction as would be expected. Extra discrete results produced at intervals of $a/b_1 = 0.02$ between $a/b_1 = 0.8$ and $a/b_1 = 0.9$ show that the critical buckling load curve peaks smoothly around the location of this first peak and that the second eigenvalue produces a smooth trough between these two critical aspect ratios. The difference between the critical and second eigenvalue is approximately 15%. A cusp forms because the second most critical buckling factor converges on that of the critical buckling value at some aspect ratio, after which the critical buckle mode of a plate changes.

The critical mode after the cusp relates to the mode which previously produced the second most critical buckling load. That is the buckling mode changes from having n half-wavelengths to one having $n + 1$ half-wavelengths. In the case of the tapered plate, this clearly defined change in buckling mode does not occur.

To check that the absence of clearly defined buckling mode changes are not a consequence of the adopted plate geometry used throughout the study, which causes the angle of tapered edge to decrease with aspect ratio, an alternative plate geometry is analysed about the aspect ratios corresponding to the first peak on the curve ($a/b_1 = 0.8, 0.9$). The alternative plate geometry maintains a constant angle of taper measured relative to the centreline of the plate as shown in Figure 7.9. This angle is defined as γ. For this alternative geometry, γ is calculated from the first discrete result made at the start of the peak, $a/b_1 = 0.8$ for $\beta = 0.8$, giving $\gamma = 7.25°$. Further discrete critical buckling load predictions are made at discrete intervals of $a/b_1 = 0.02$ up to $a/b_1 = 0.9$ which signifies the last discrete result initially obtained after the curve using the original geometry. These points are plotted onto Figure 7.8 (labeled as 'Constant angle of taper'). These discrete results, although giving marginally higher buckling predictions, as would be expected because b_1/b_2 decreases (*i.e.* taper increases) with aspect ratio, show a similar relationship between the first and second eigenvalues as with the adopted geometry. That is, the eigenvalues are far-spaced and a cusp is not a characteristic of the buckling curve. This is also a characteristic of the loading configuration used in Pope's analysis, where a shear force was applied along the tapered edge to maintain equilibrium. Buckling predictions for this load case are produced in Table 7.2 for model verification purposes.

Figures 7.10 and 7.11 show buckling modes of the first four eigenvalues for the 'adopted' and 'constant angle of taper' geometry. The first two eigenvalues are given to determine whether there is a switch in buckling modes over the aspect ratio range and the third and fourth eigen-modes for interest. They are

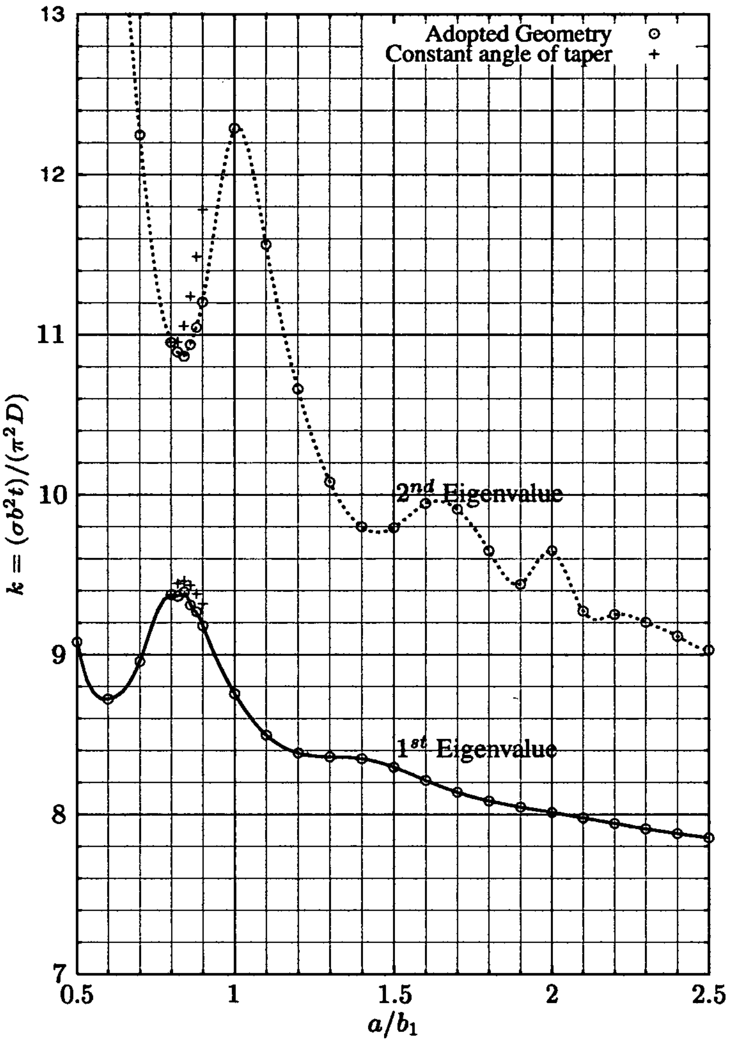

Figure 7.8: Example buckle curve for $\beta = 0.8, \alpha = 0°$ which is used in the discussion given in section 7.5.1. It shows both the first and second critical eigenvalue solutions for plate buckling as well as the same solutions for a tapered plate having a constant angle of taper (Figure 7.9). This constant angle of taper, γ, is the same as the angle of taper for a plate with $\beta = 0.8, a/b_1 = 0.8$ which is calculated to be 7.125°. The buckling curve shows one distinct peak that correspond to a change in the number of half-waves forming the buckle mode. This peak occurs between $a/b_1 = 0.8$ and $a/b_1 = 0.9$. The complete curves from which this buckle curve is extracted are given in Figure 7.6(a).

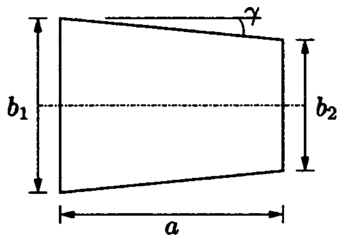

Figure 7.9: Schematic showing the alternative geometry used to check that the absence of clearly defined cusps on the buckle curves is not due to the adopted plate geometry definition. The figure shows a tapered plate, without skew ($\alpha = 0°$) and tapered defined as the angle that the tapered longitudinal edge makes with the plate centre-line, γ. Using this alternative definition of geometry, the ratio b_2/b_1 changes as the aspect ratio of the plate (b_1/b_2) is varied and γ remains constant

not significant in determining the critical buckling load of the plate. The two figures allow comparison of the buckling modes for the two different geometries. The figures each contain four sub-figures which relate to aspect ratios, $a/b_1 = 0.8, 0.84, 0.86$ and 0.9. The first and last $a/b_1 = 0.8, 0.9$ correspond to those surrounding the peak which were originally obtained in the study and the middle two modes, $a/b_1 = 0.84, 0.86$, relate to the two modes obtained for the more closely spaced analysis surrounding a buckling mode change. Sub-figure (a) (for $a/b_1 = 0.8$) in both figures relates to the same plate and is therefore the same.

A buckling mode change is identified between $a/b_1 = 0.84$ and $a/b_1 = 0.86$ in both cases. Using the contour plots to determine when this buckle mode takes place however is not conclusive. Because the out-of-plane deflection is small, the plate appears to be un-displaced at the narrowed edge. A plot of the deflection along the centreline of the plate (included next to the contour plot) reveals that there is a slight negative deflection when $a/b_1 = 0.86$ and that deflection is entirely positive when $a/b_1 = 0.84$, hence that there is a change in mode between these two aspect ratios.

The contour plots for plate geometry around the first peak on the buckling curve show that the second eigen-mode is not the same as the eigen-mode for the first eigenvalue after a change in mode. In the case of $a/b_1 = 0.84, 0.86$, the second eigen-modes are the same and comprise of a distinct buckle biased towards the narrow end of the plate, with little out-of-plane deflection at the wider end of the plate. This buckling mode is different to the first eigen-mode in which the main out-of-plane displacement occurs at the wide end of the plate and little displacement at the narrow edge.

Figure 7.12 shows the first two buckling modes of the tapered plate either side of the peak in the buckling curve at $a/b_1 = 1.4, 1.5$. Comparison with the second eigenvalue in Figure 7.8 shows that plates with aspect ratios either side of the peak do not share similar eigen-modes as they would if a distinct cusp is to

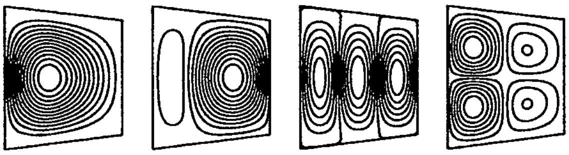

(a) First four critical buckle modes for $a/b_1 = 0.8$ using the adopted definition of geometry for $\beta = 0.8$. Critical buckling factors are $k = 8.4726, 9.8991, 15.893, 23.354$. This figure is used as the base for comparison with the alternative geometry shown in Figure 7.11.

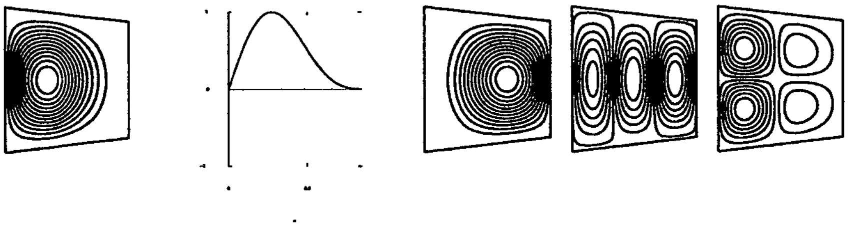

(b) First four buckling modes for $a/b_1 = 0.84$ using the adopted definition of geometry for $\beta = 0.8$. Critical buckling factors are $k = 8.5504, 9.9918, 14.833, 23.445$ respectively. A plot of the deflected shape for the plate is given for the critical buckling mode, which clearly shows the buckle mode change when compared with the same plot for $a.b_1 = 0.86$ in (c)

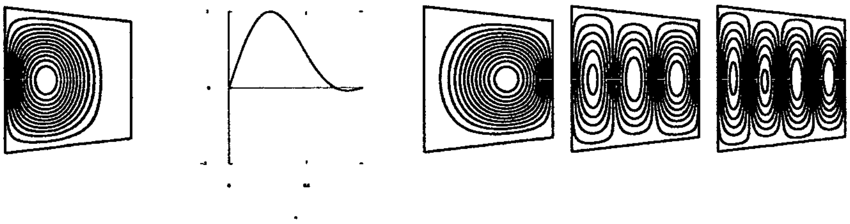

(c) First four buckling modes for $a/b_1 = 0.86$ using the adopted definition of geometry for $\beta = 0.8$. Critical buckling factors are $k = 8.4138, 9.8861, 14.287, 22.501$ respectively. The buckling mode attributed to the critical buckling load changes between this aspect ratio and that in the previous subfigure for aspect ratio $a/b_1 = 0.86$. A plot of the deflected shape for the plate is given for the critical buckling mode, which clearly shows the buckle mode change when compared with the same plot for $a.b_1 = 0.84$ in (b)

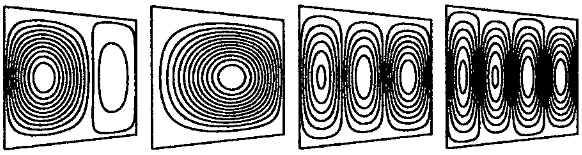

(d) First four buckling modes for $a/b_1 = 0.9$ using the adopted definition of geometry for $\beta = 0.8$. Critical buckling factors are $8.2967, 10.126, 13.398, 20.842$ respectively. These buckling modes should be compared to those for the alternative constant angle tapered definition used for comparison given in Figure 7.11(d).

Figure 7.10: Buckling modes for the adopted geometry around the peak on the buckle curves a/b=0.8, 0.9 which corresponds to the first peak in Figure 7.8

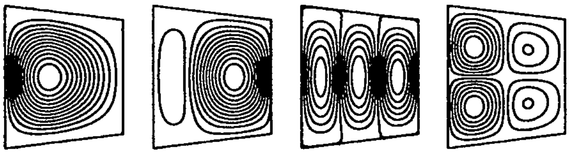

(a) First four critical buckling modes for $a/b_1 = 0.8$ using the adopted geometry for the study. Buckling factors for the modes are $k = 8.4726, 9.8991, 18.893, 23.354$ respectively.

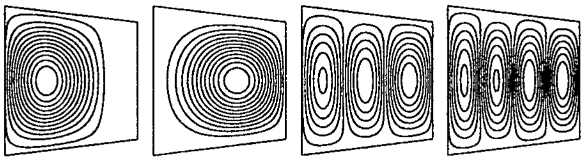

(b) First four critical buckling modes for $a/b_1 = 0.84$ using a tapered geometry defined using a constant angle of slope between the tapered edge and plate centre-line. Buckling factors for the modes are $k = 8.5255, 10.159, 14.368, 22.569$ respectively.

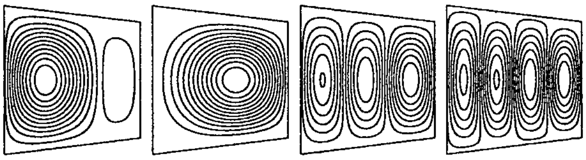

(c) First four critical buckling modes for $a/b_1 = 0.88$ using a tapered geometry defined using a constant angle of slope between the tapered edge and plate centre-line. Buckling factors for the buckle modes are $k = 8.5255, 10.159, 14.368, 22.569$ respectively. Note that there is a mode change between this aspect ratios and $a/b_1 = 0.84$ in subfigure (b) above

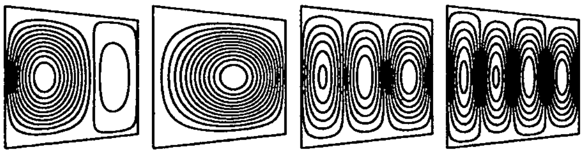

(d) First four buckling modes for $a.b_1 = 0.9$ using a tapered geometry defined using a constant angle of slope between the tapered edge and plate centre-line. Buckling factors for the modes are $k = 8.4212$, $k = 10.650$, $k = 13.553$ and $k = 20.961$.

Figure 7.11: Buckling modes for an alternative geometry which defines taper using the angle that the tapered longitudinal edge makes with the plate centre-line, γ. γ is derived for a plate having $\beta = 0.8$ and $a/b_1 = 0.8$, hence this angle is 7.125°. The figure shows the change in buckle mode for the critical buckle factor occurring between $a/b_1 = 0.86$ and $a/b_1 = 0.88$.

(a) $a/b_1 = 1.4$, $\beta = 0.8$. First and second buckling modes having buckling factor, $k = 7.5452$ and $k = 8.8566$ respectively.

(b) $a/b_1 = 1.5$, $\beta = 0.8$. First and second buckling modes having buckling factor, $k = 7.4968$ and $k = 8.8511$ respectively.

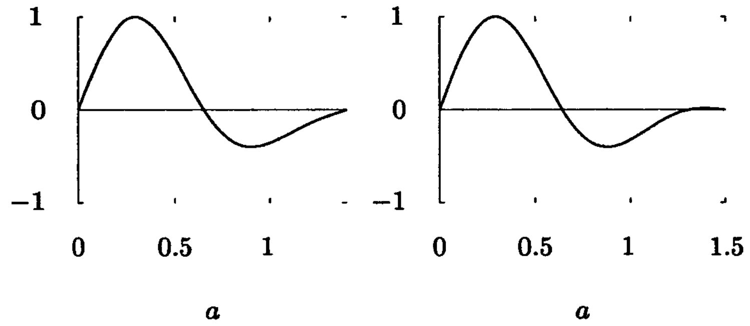

(c) Plot through centreline of the critical buckling mode shown in (a)

(d) Plot through centreline of the critical buckling mode shown in (b)

Figure 7.12: Buckling modes showing the transition between a change in mode at aspect ratio $a/b_1 = 1.4, 1.5$ corresponding to the first cusp on the buckling curve in Figure 7.8. The first and second most critical modes are included as contour plots to show that they do not interchange at a critical aspect ratio *i.e.* shows that cusps will not form. Plots of displacement through the centreline of the plate are shown in (c) and (d) in which the buckling mode can be seen to have changed, but that the change is not sudden and that the blank section of the contour plot in (b) actually contains a transverse displacement so that the mode comprises of 3 half-wavelengths. The y-axis in the displacement plots measures a normalised (and non-dimensional) displacement.

(a) $a/b_1 = 2.1$, $\beta = 0.8$. First and second buckling modes having buckling factor, $k = 7.2107$ and $k = 8.3791$ respectively.

(b) $a/b_1 = 2.2$, $\beta = 0.8$. First and second buckling modes having buckling factor, $k = 7.1790$ and $k = 8.3618$ respectively.

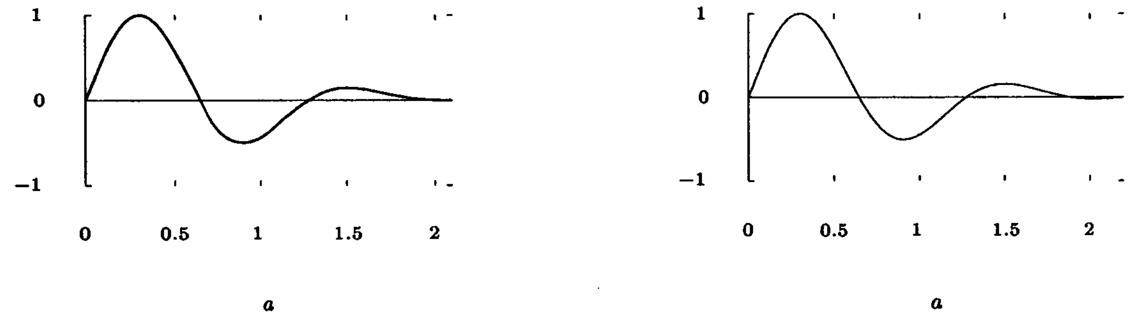

(c)

Figure 7.13: Buckling modes showing the transition between a change in mode at aspect ratio $a/b_1 = 2.1, 2.2$ which relates to the second peak on the buckling curve shown in figure 7.8 on page 185. See caption in Figure 7.12 for further explanation.

form as in the case of a rectangular plate. The figure also shows a plot of the deflected shape through the centre-line of the plate, where the changes in buckling mode are more obvious than in the contour plots in which they are impossible to see.

There is a further change in buckling mode before $a/b_1 = 2, 5$, in which there are four half-wavelengths. Inspection of the buckle modes for the plates in the region $a/b_1 = 2.0$ to $a/b_1 = 2.5$ reveals that this buckling mode occurs between $a/b_1 = 2.1$ and $a/b_1 = 2.2$. The first two eigen-modes for these aspect ratios are shown in Figure 7.13. This mode change is not accompanied by an appreciable peak in buckling strength and is therefore almost unidentifiable without inspection of the mode contour and cross-section plots.

In all cases, the buckling mode changes in the planform tapered plates are gradual. Higher ratios of b_2/b_1 are seen to give higher peaks in the buckling stress accompanied by mode changes. As the taper of the plate increases, peaks in buckling load are reduced and the mode changes are more gradual leading to smooth buckling curves that do not have appreciable peaks where there are mode changes.

These observations are not consistent with the results of Pope who shows clearly defined cusps in his buckling curves although there is no specific dependence on the number of half-wavelengths defined in the deflection functions used. In contrast, Klein does not show clearly defined cusping in his buckling curves. Radhoff [74], using a constant end-shorting load distribution, does. This constant end-shortening loading distribution is not considered in this chapter.

7.5.2 Effect of Taper

The effect of taper on the buckling load of the plate is shown graphically in figures 7.14 - 7.17. They show the buckling strength of a plate having a fixed skew angle and taper ratio less than 1.0 as a percentage of that of a plate with the same skew angle and the taper ratio, $\beta = 1.0$ (*i.e.* an equivalent rectangle or square plate). Each figure represents a different skew angle and each sub-figure a different boundary condition case.

The figures show, that there are significant buckling increases associated with an increase in taper along the longitudinal edge of the plate for the range of aspect ratios in the study. This strength increases with increased taper and is clearly seen on the buckling curves. The erratic nature of the curves is due to the asynchronous mode changes between plates with different taper. The erratic nature of the curves is increased because plates with higher taper ratios have more prominent peaks than those with lower taper ratios.

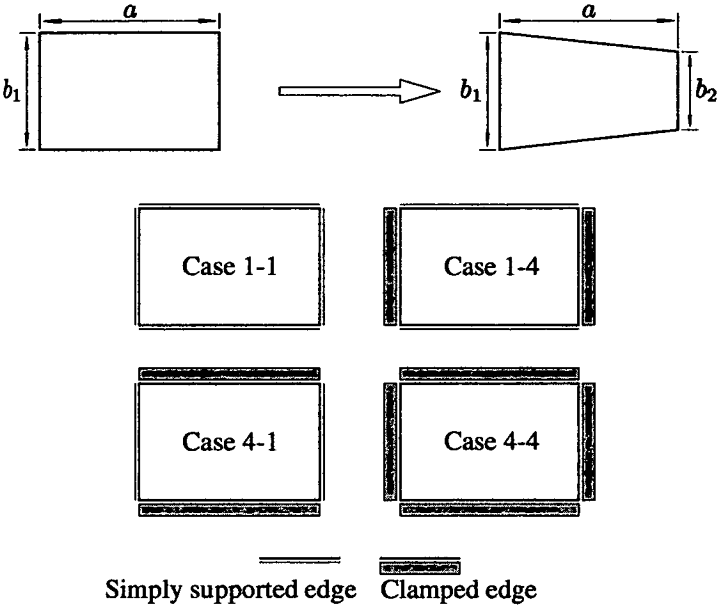

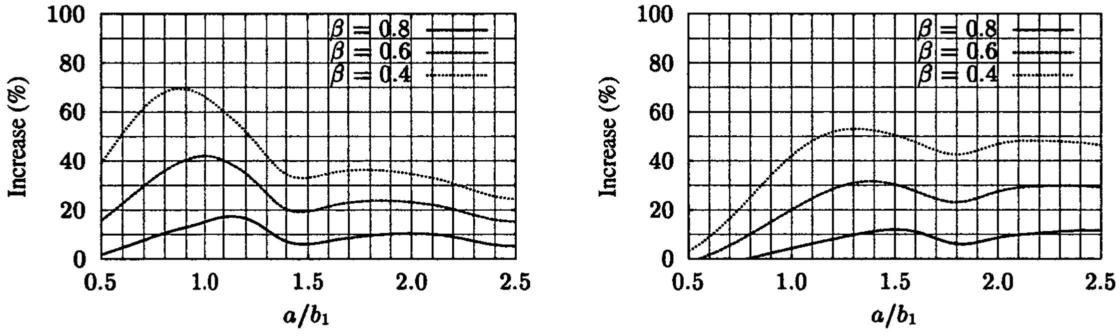

(a) Case 1-1

(b) Case 1-4

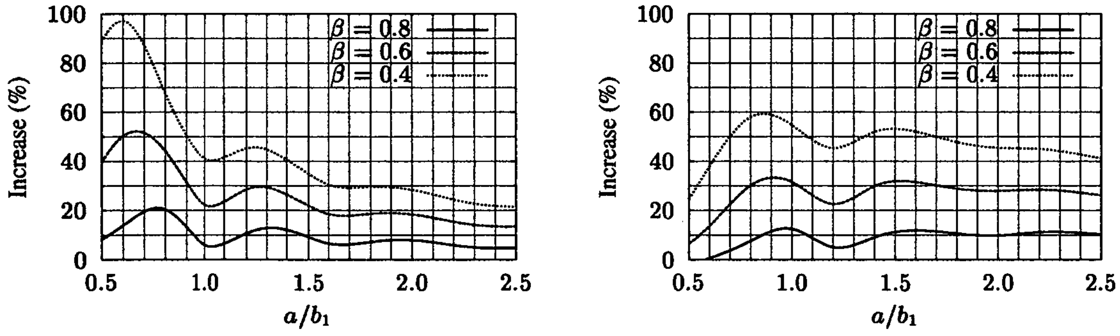

(c) Case 4-1

(d) Case 4-4

Figure 7.14: Buckling strength increase resulting from taper for plates with skew angle, $\alpha = 0°$.

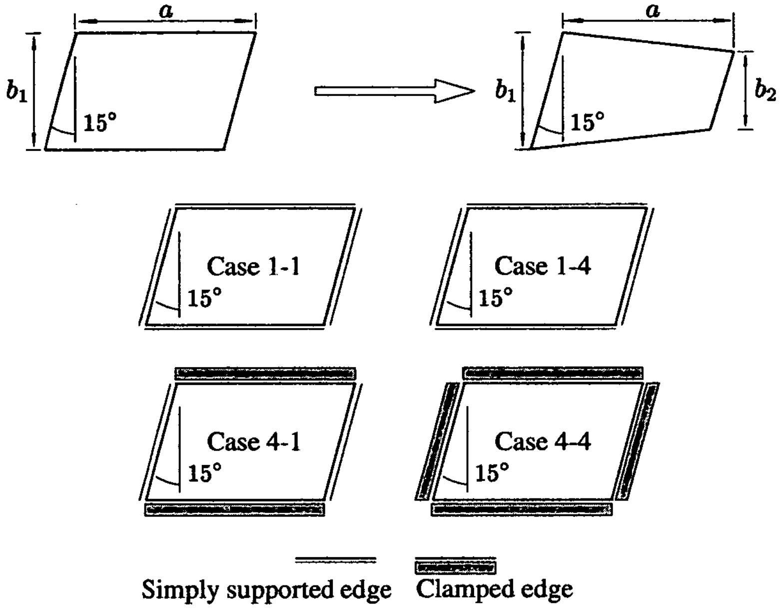

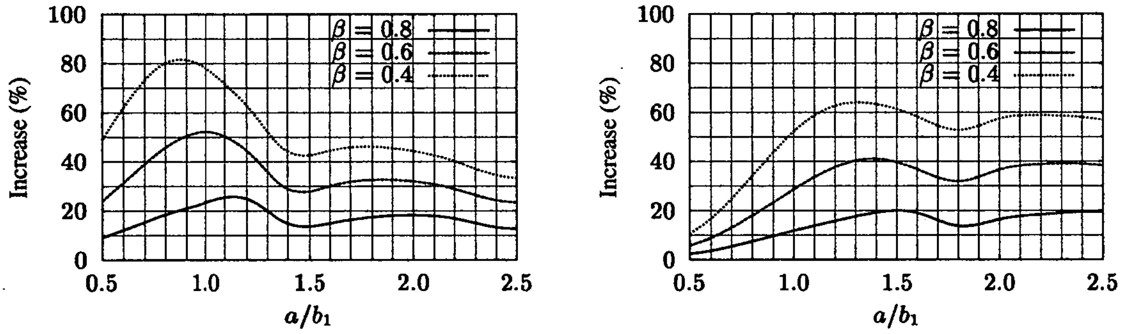

(a) Case 1-1

(b) Case 1-4

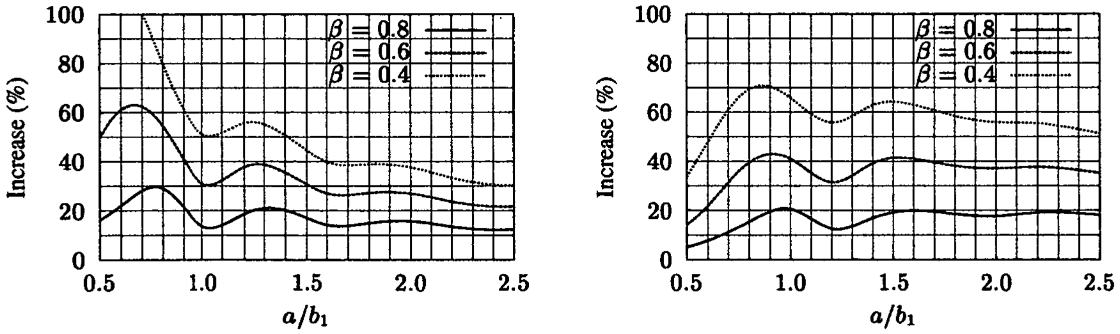

(c) Case 4-1

(d) Case 4-4

Figure 7.15: Buckling strength increase resulting from taper for plates with skew angle, $\alpha = 15°$.

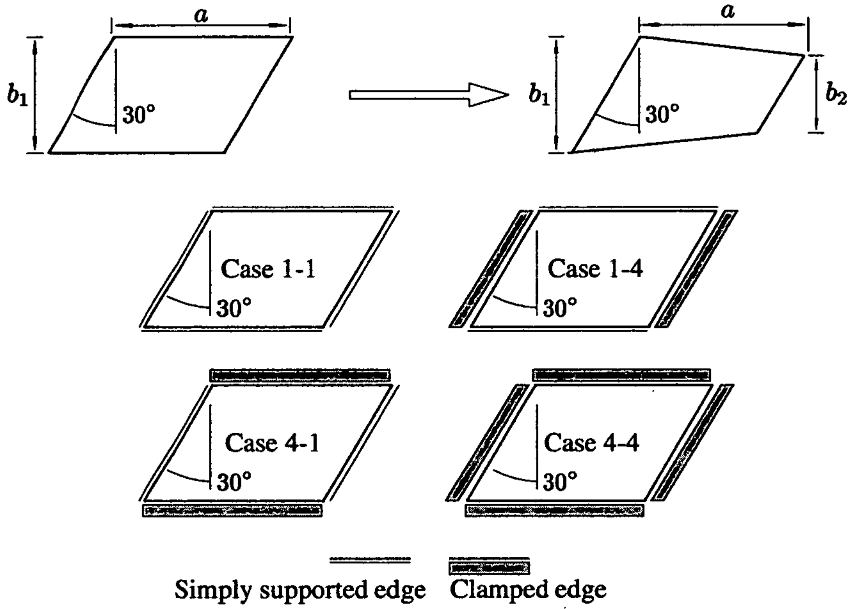

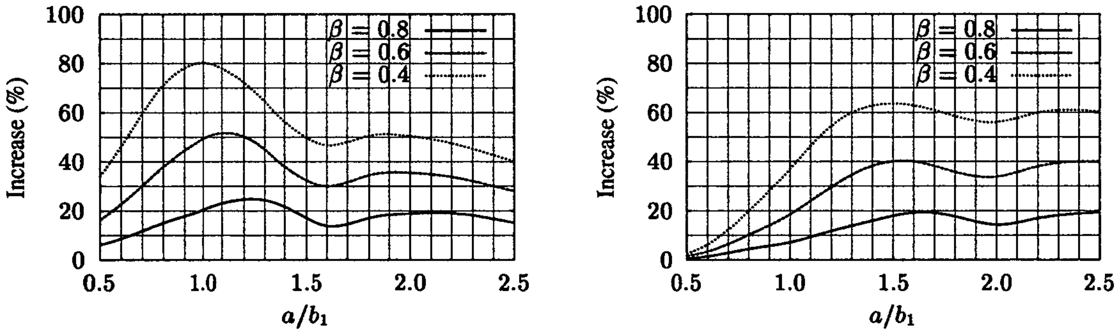

(a) Case 1-1

(b) Case 1-4

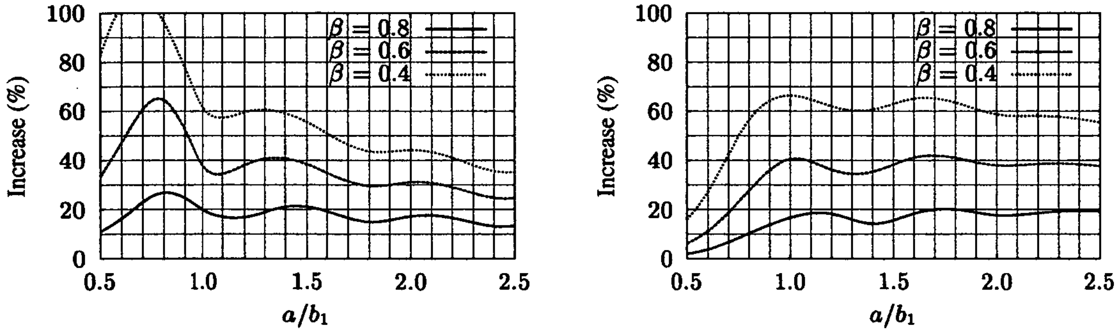

(c) Case 4-1

(d) Case 4-4

Figure 7.16: Buckling strength increase resulting from taper for plates with skew angle, $\alpha = 30°$.

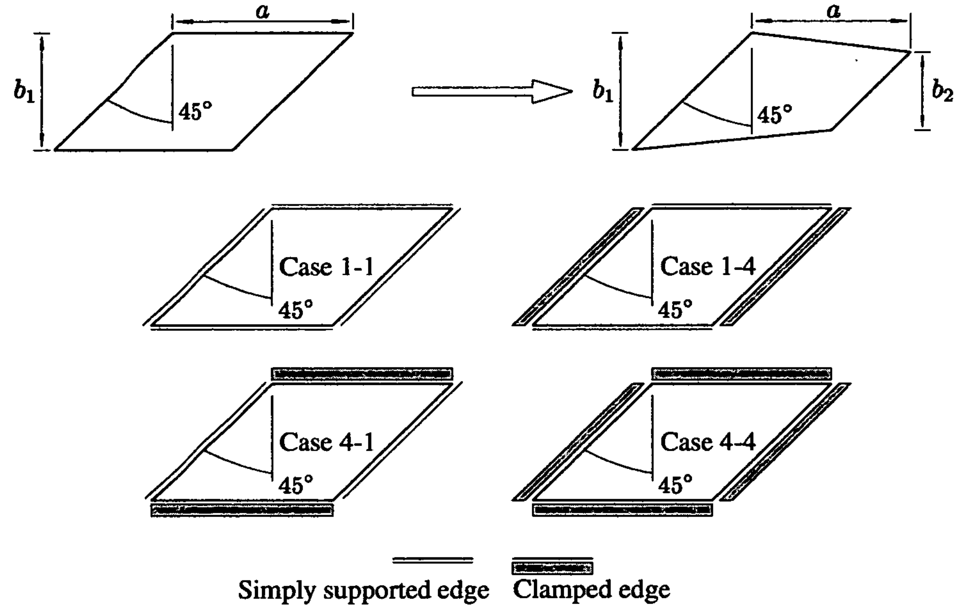

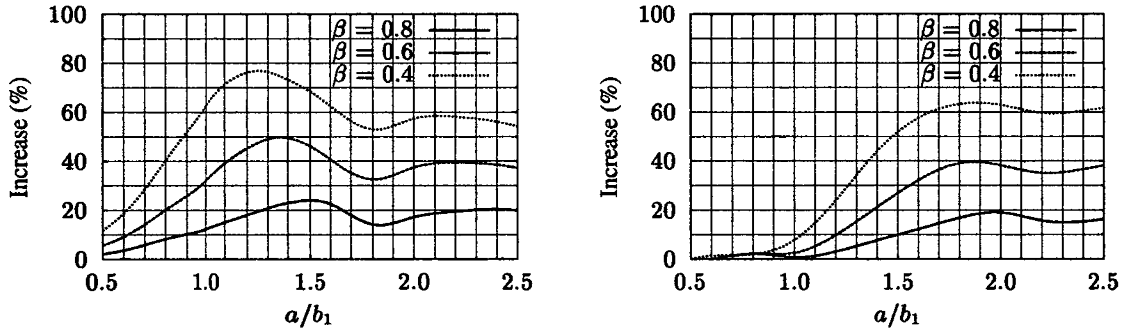

(a) Case 1-1

(b) Case 1-4

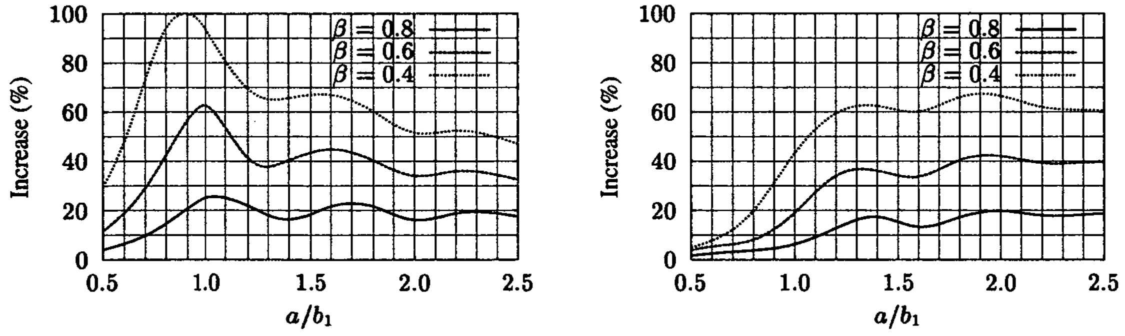

(c) Case 4-1

(d) Case 4-4

Figure 7.17: Buckling strength increase resulting from taper for plates with skew angle, $\alpha = 45°$.

Buckling load increases are smaller for small aspect ratios when the plate has a clamped transverse edge (Case 1-4 or Case 4-4) than for plates with simply supported transverse edges. This can be explained by making comparison with the set of buckling curves for each boundary condition case. Plates with clamped transverse edges appear to be relatively insensitive to taper at small aspect ratios where the buckle strength of the plate is governed by the moment resisting buckling along the transverse plate edge. For the case of a simply supported longitudinal edge, the overriding factor governing the buckle strength of the plate is the taper of the longitudinal edge and consequently this leads to a higher buckling strength increase at low aspect ratios. At higher aspect ratios, the tapered edge and the boundary condition along the longitudinal edge has a more dominant effect on the buckling load of the plate and consequently, the curves showing buckling strength increase flatten out.

The plate skew angle causes the buckling curves to shift to the right along the aspect ratio axis and the buckling curves become bunched together at low aspect ratios for boundary condition cases in which the transverse plate edges are clamped. This is because of the dominating effect of the clamped transverse edge which governs the critical buckling load of the plate. For this reason buckle strength increases are minimal for low aspect ratio plates with clamped transverse edges and the range of aspect ratios over which a small increase is found increases with an increase in skew angle. This is seen in an extreme case in figure 7.17(b). It shows the buckling strength increases for an increase in taper of plate with $\alpha = 45^\circ$ and boundary condition Case 1-4. The curves show that there is no significant buckling strength increase when the aspect ratio of the plates is less than $a/b_1 = 1.0$.

The figures show that substantial buckling strength increase arise from applying a taper along the longitudinal plate edge. These buckling strength increases exist at the highest aspect ratios used in the study, whereas it has been shown previously that there is little strength advantage to be gained in skew plates with aspect ratios greater than $a/b_1 = 2.5$. At $a/b_1 = 2.5$, the buckling strength of the tapered plates has not converged on that of a infinite rectangular plate as would be expected using the geometric definition of taper used in the study. The buckling strength increase arising from taper is typically greater than 10% for a tapered plate with $\alpha = 0^\circ, a/b_1 = 2.5$ and can be seen to be as high as 60% for the fully clamped (Case 4-4) when $\alpha = 45^\circ$ and $\beta = 0.4$ (Figure 7.17(d)).

7.5.3 Effect of Skew Angle

The previous section (section 7.5.2) discussed the effect of taper on the buckling load of plates. This section considers the buckling strength increases arising from changes in the skew angle of the plate, α. Buckling strength increase curves are drawn in a similar manner to those used in the previous section, but show the buckling strength increase for each value of taper (β) and skew angle as a percentage of that over an equivalent plate with $\alpha = 0°$. The buckling strength increase curves are shown in figures 7.18 - 7.21 for each value of β, including the rectangular configuration of $\beta = 1.0$. Each sub-figure gives the buckling strength increase curves for each boundary condition case.

The buckling strength increase curves are markedly different in appearance to the curves showing the buckling strength increase of the plates due to taper. As predicted from the buckling curves for skew plates obtained and discussed in previous chapters, there is an increase in the buckling strength of the plate as the skew angle of the plate increases. Generally, all the curves show that increasing the skew angle of the plate leads to significant increases in buckling strength at low aspect ratios, but this buckling strength increase rapidly diminishes as the aspect ratio of the plates increases. When the aspect ratio of the plate reaches the maximum used in the study ($a/b_1 = 2.5$), the buckling strength increase as a result of skew is generally less than 5%. Slightly higher buckling strength increases are seen for boundary condition cases in which there are simply supported longitudinal (tapered) edges. The curves show that the buckling strength of the plate is greatly influenced by the transverse edge at small aspect ratio and that this influence is quickly lost. This is consistent with the observations made regarding skew plates and panels in Chapters 2-4.

The curves show that the buckling strength of the plates increase marginally as the value of β falls.

7.6 Buckling at High Aspect Ratio

In section 7.5.2 when $a/b_1 = 2.5$, the bucking strength of the tapered plate is seen to be significantly higher than for an equivalent rectangular plate. At infinite aspect ratios, because the definition of taper is given as the ratio of transverse edges, the buckling load of the plate will converge on that of an infinite rectangular plate. This rectangular buckling solution will give lower–bound buckling values for the tapered plates (note that a triangular plate will give the upper bound value).

Additional buckling predictions are generated for plates with aspect ratios, $a/b_1 = 5, 10$ and 20, to determine the sensitivity of the analysis past the maximum aspect ratio used in the study. The buckling predictions are made for all the boundary condition cases, aspect ratios and skew angles considered in the study. The buckling predictions are tabulated in Table 7.3, where for clarity, buckling predictions for intermediate skew angles $\alpha = 15°, 30°$ are omitted. Curves for these intermediate skew angles nest between the curves for $\alpha = 0°$ and $\alpha = 45°$.

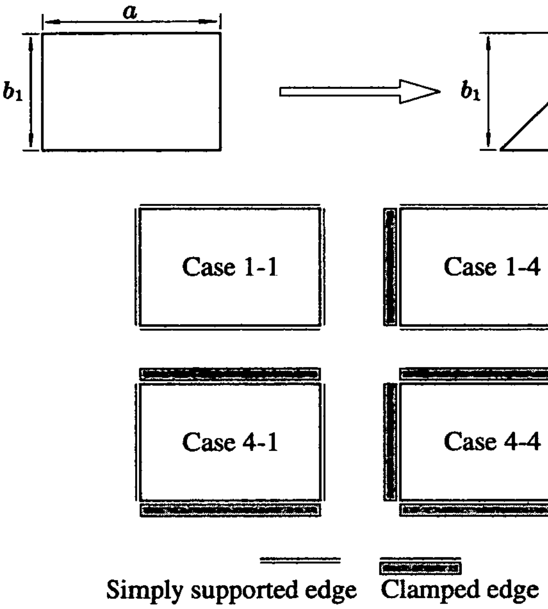

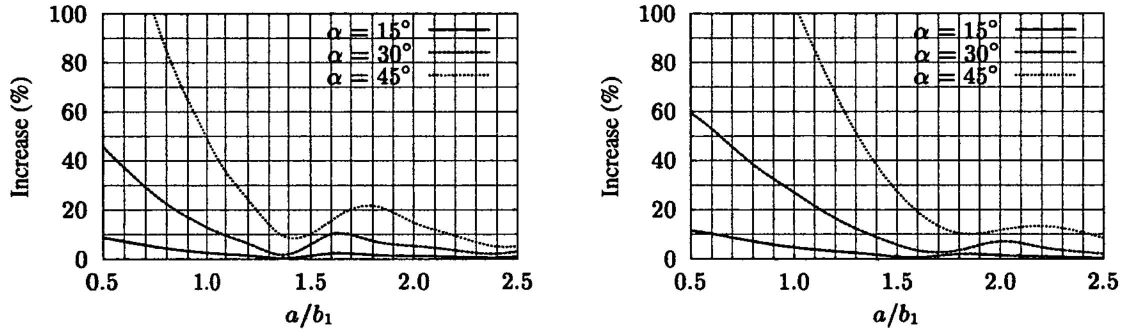

(a) Case 1-1

(b) Case 1-4

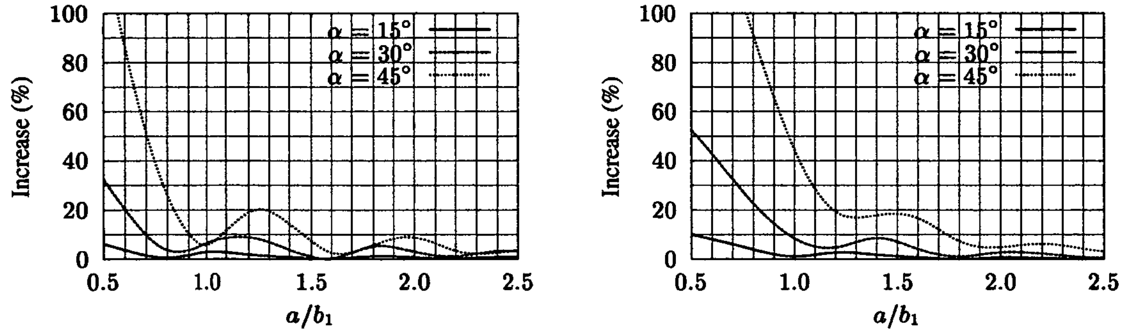

(c) Case 4-1

(d) Case 4-4

Figure 7.18: Buckling strength increase resulting from skew angle of the plates with taper, $\beta = 1.0$.

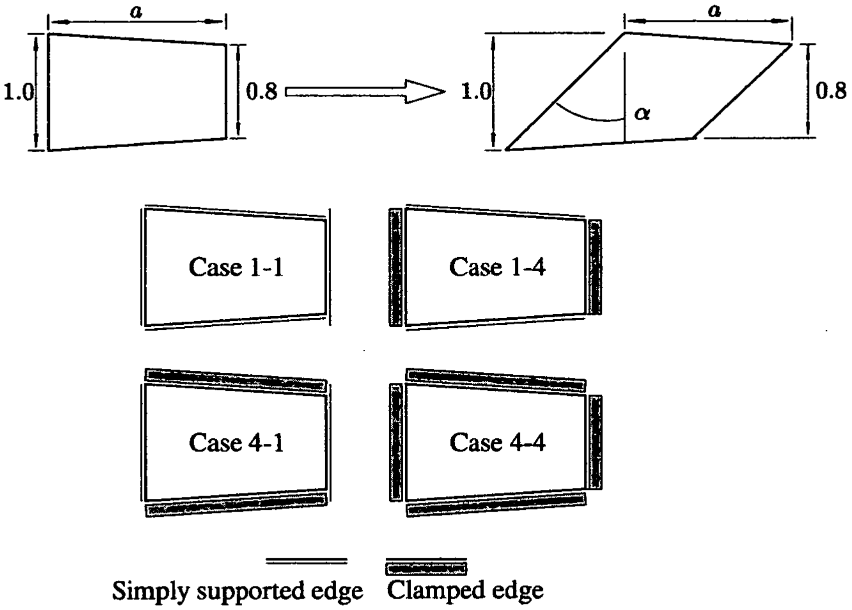

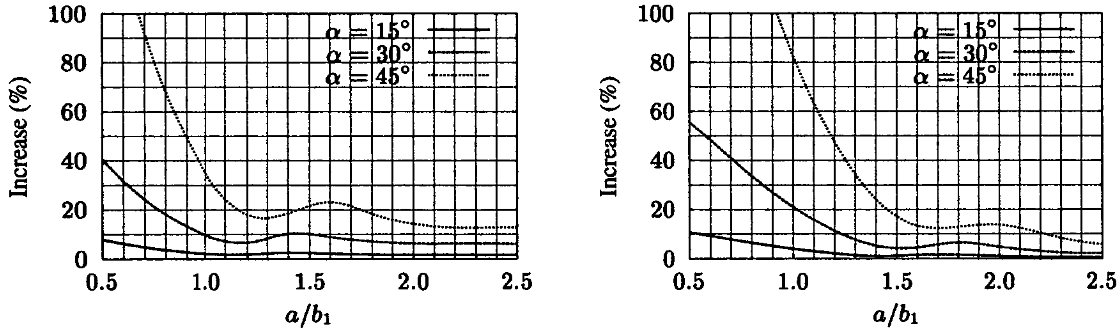

(a) Case 1-1

(b) Case 1-4

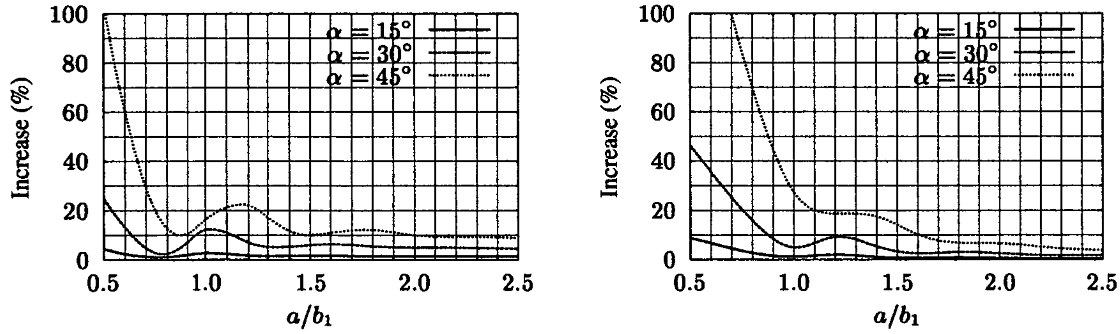

(c) Case 4-1

(d) Case 4-4

Figure 7.19: Buckling strength increase resulting from skew angle of the plates with taper, $\beta = 0.8$.

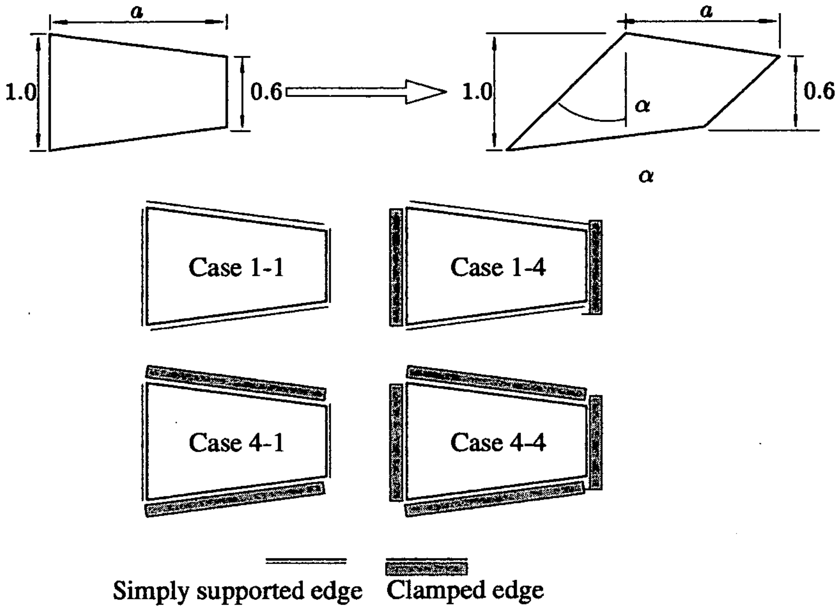

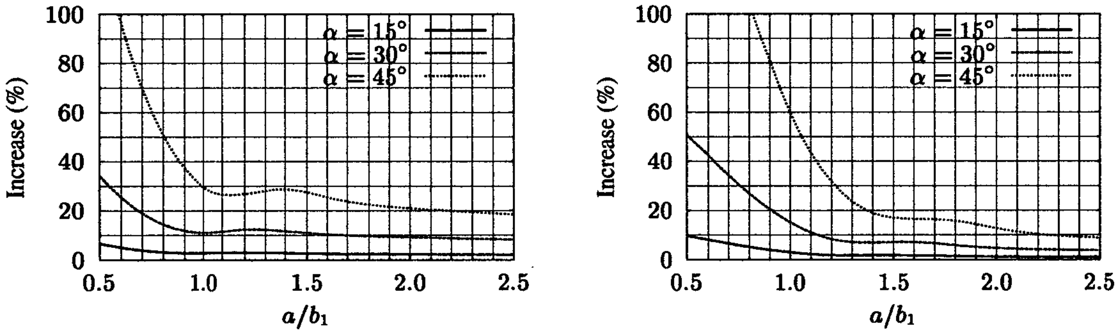

(a) Case 1-1

(b) Case 1-4

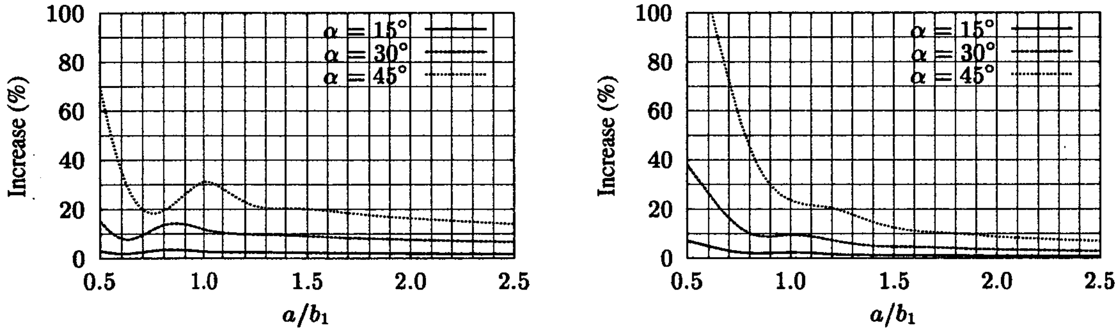

(c) Case 4-1

(d) Case 4-4

Figure 7.20: Buckling strength increase resulting from skew angle of the plates with taper, $\beta = 0.6$.

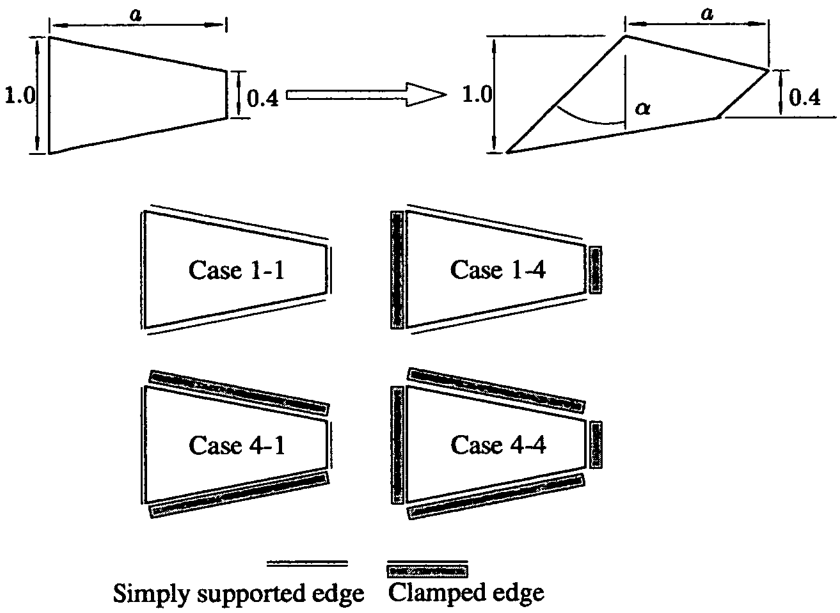

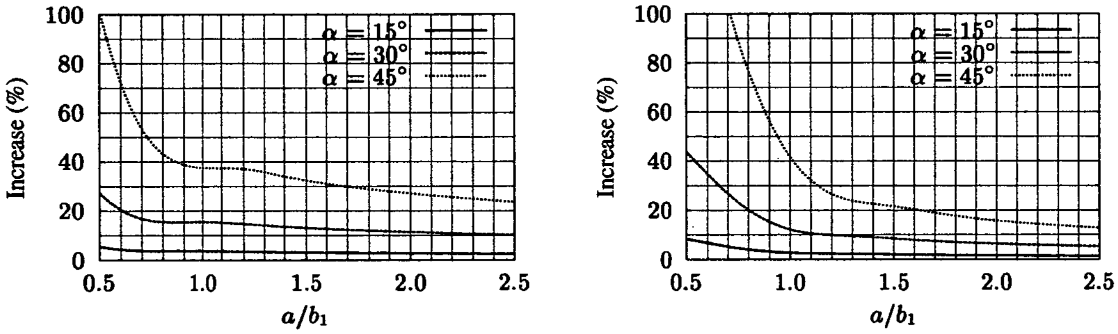

(a) Case 1-1 (b) Case 1-4

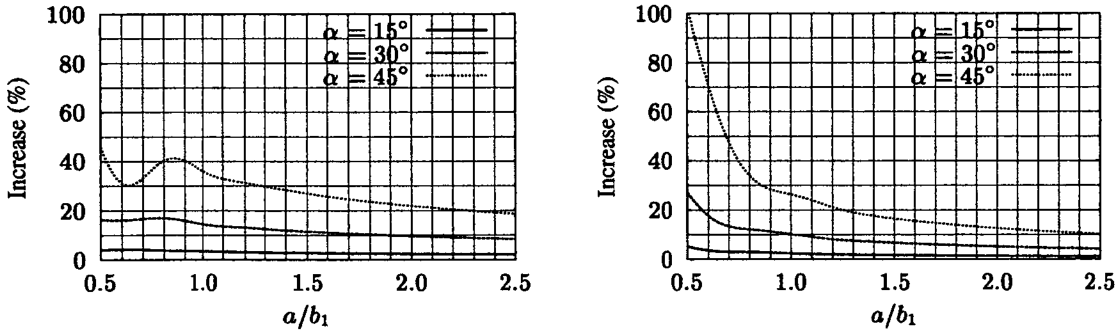

(c) Case 4-1 (d) Case 4-4

Figure 7.21: Buckling strength increase resulting from skew angle of the plates with taper, $\beta = 0.4$.

Table 7.3: Buckling predictions in terms of buckling coefficient, $k = (\sigma b_1^2 t)/(\pi^2 D)$, for tapered plates with aspect ratios of 2.6, 5.0, 10.0 and 20.0. For comparison purposes, the critical buckling coefficient for an infinitely long rectangular plate simply supported on transverse edges is 4.0 (Cases 1-1 and 1-4 in (a) and (b)) and for a plate with clamped longitudinal edges 6.97 [70] (Cases 4-1 and 4-4 in (c) and (d)).

β	1.0		0.8		0.6		0.4	
a/b_1 / α	0	45	0	45	0	45	0	45
2.6	4.0745	4.3551	4.5957	5.1719	4.9989	5.8978	5.3679	6.6063
5	4.0004	4.1243	4.3761	4.7244	4.6219	5.1795	4.8456	5.5940
10	4.0004	4.0357	4.2314	4.4546	4.3761	4.7244	4.5034	4.9602
20	4.0005	4.0099	4.1438	4.2886	4.2314	4.4546	4.3070	4.5960

(a) Case 1-1

β	1.0		0.8		0.6		0.4	
a/b_1 / α	0	45	0	45	0	45	0	45
2.6	4.5078	4.7837	5.3523	5.6267	6.1601	6.6907	6.9406	7.7961
5	4.1550	4.1794	4.8230	4.9341	5.3473	5.5878	5.8185	6.2062
10	4.0401	4.0428	4.5102	4.5621	4.8229	4.9329	5.0953	5.2683
20	4.0105	4.0112	4.3190	4.3441	4.5102	4.5621	4.6740	4.7542

(b) Case 1-4

β	1.0		0.8		0.6		0.4	
a/b_1 / α	0	45	0	45	0	45	0	45
2.6	6.9738	7.3293	7.8291	8.4935	8.4116	9.5567	8.9553	10.5779
5	7.0019	7.0600	7.5121	7.9314	7.8627	8.5477	8.1807	9.1187
10	6.9738	7.0063	7.3050	7.5721	7.5122	7.9316	7.6938	8.2504
20	6.9766	6.9826	7.1793	7.3538	7.3050	7.5722	7.4132	7.7599

(c) Case 4-1

β	1.0		0.8		0.6		0.4	
a/b_1 / α	0	45	0	45	0	45	0	45
2.6	7.5142	7.6935	8.8535	9.1935	10.082	10.756	11.213	12.316
5	7.1197	7.1576	8.1618	8.3088	8.9138	9.2309	9.5851	10.092
10	7.0116	7.0149	7.7108	7.7809	8.1618	8.3088	8.5531	8.7828
20	6.9828	6.9839	7.4343	7.4684	7.7108	7.7812	7.9470	8.0551

(d) Case 4-4

The buckling predictions in Table 7.3 will converge on the critical buckling load of an infinite rectangular plate giving buckling factors of $k = 4.0$ or 6.97 for simply supported or clamped longitudinal edges respectively. The simply supported case refers to Case 1-1 and 1-4 (parts (a) and (b) in Table 7.3) and the clamped case to Case 4-1 and 4-4 (parts (c) and (d) Table 7.3). The buckling predictions in the table converge towards these values, and in the case of the rectangular or skew plates to have converged on the minimum buckling values. The tapered plates are not converged at an aspect ratio of $a/b_1 = 20$. Figure 7.22 shows the buckling strength increase of the tapered plate for each boundary case, as in Figures 7.14 - 7.17 except that the datum is the applicable theoretical minimum buckling load of the infinitely long rectangular plate. These datum buckling loads are $k = 4$ and $k = 6.97$ when the longitudinal edges of the plates are simply supported and clamped respectively. Two skew angles: $\alpha = 0°$ which gives a datum case and; 45° which gives the extreme upper bound are both considered. Intermediate results are omitted to preserve clarity.

The figure shows that even at high aspect ratios the tapered plates are not well converged on the theoretical minimum buckling load and that significant buckling strength increases exist for the higher degrees of taper. For the cases with clamped longitudinal edges, the difference between the actual and converged plate buckling strength is as high as 20%. The rectangular ($\alpha = 0°$) cases are well converged at $a/b_1 = 2.5 - 5$ as has been previously shown in chapter 4. Convergence follows the expected trend of decreasing as the degree of taper increases (β decreases). For cases when the transverse edge boundary condition is simply supported, it is often the case that the 45° case for one degree of taper is higher than a 0° for a higher degree of taper. This is due to the insensitivity to buckling load variation caused by the clamped transverse edge.

Example buckling modes for these high aspect ratio are given in Figures 7.23 and 7.24. The figures show representative buckling modes for high aspect ratio plates with all four edges simply supported and all four clamped respectively. The figures compare the buckling modes for plates that are rectangular or have a skew angle of e $\alpha = 45°$ for an intermediate degree of taper $\beta = 0.6$. The plates have simply supported edges (Figure 7.23) or fully clamped edges (Figure 7.24). Both contour plots and cross–sections of the deflected plate through its centreline are shown.

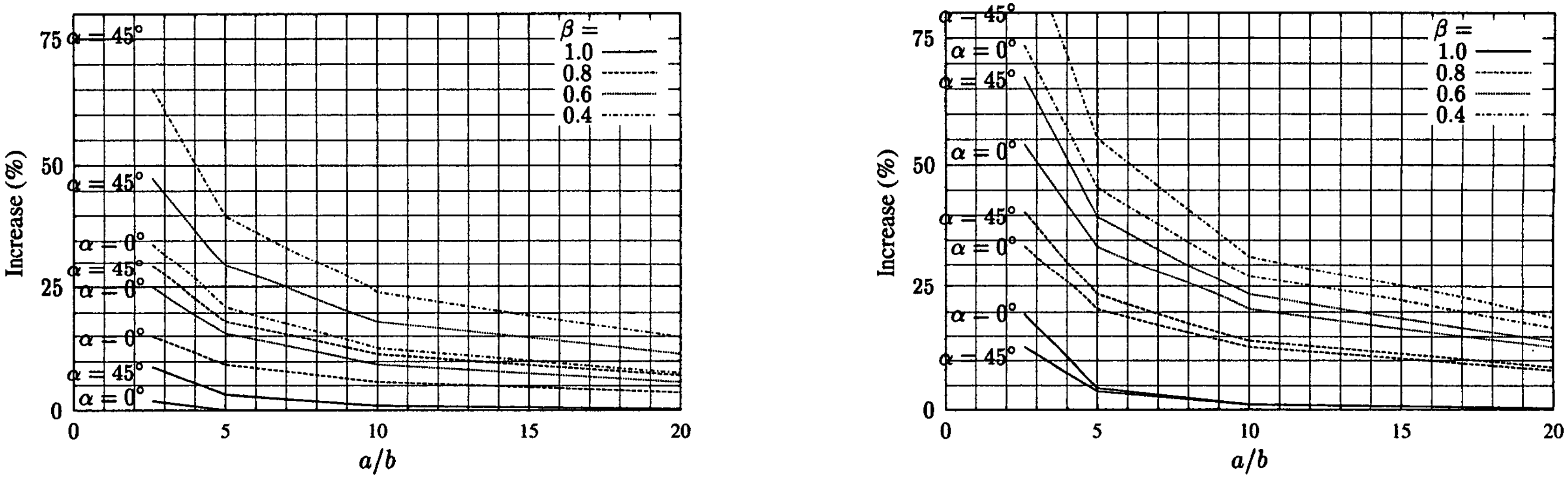

(a) Case 1-1

(b) Case 1-4

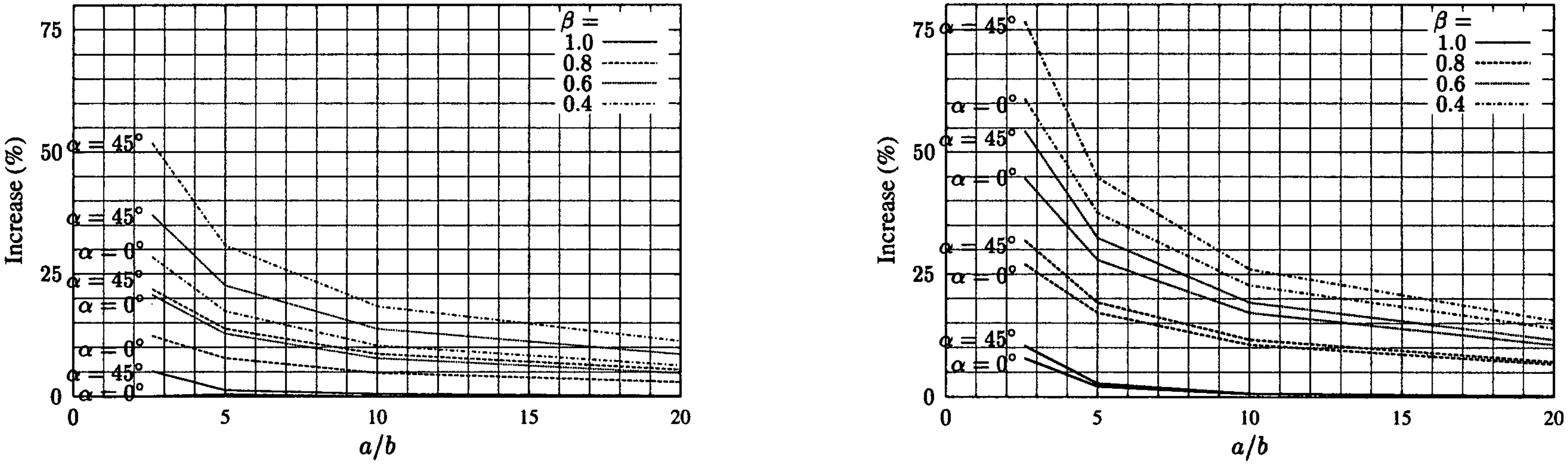

(c) Case 4-1

(d) Case 4-4

Figure 7.22: Tapered plate buckling prediction as percentage over that of the theoretical buckling load for an infinitely long rectangular plate for the tapered and skew plates used in the study. A 0% increase represents the fully converged case.

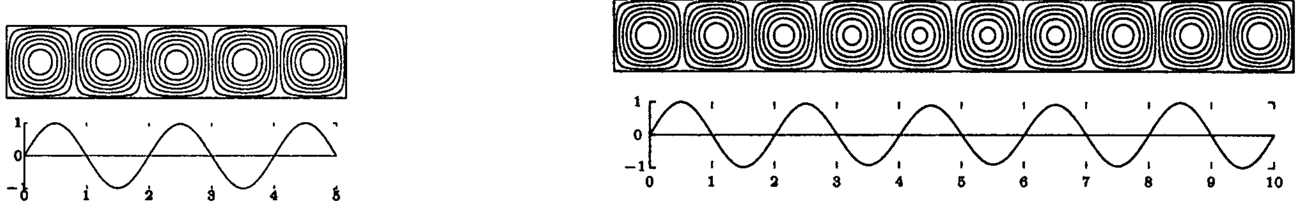

(a) $a/b = 5, \alpha = 0°$ (b) $a/b = 10, \alpha = 0°$

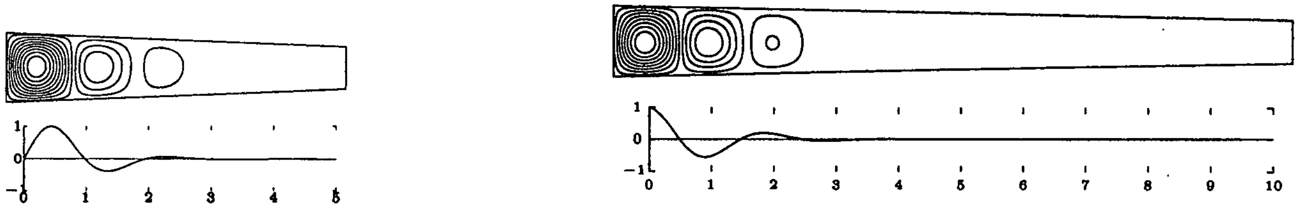

(c) $a/b = 5, \alpha = 0°, b_2/b_1 = 0.6$ (d) $a/b = 10, \alpha = 0°, b_2/b_1 = 0.6$

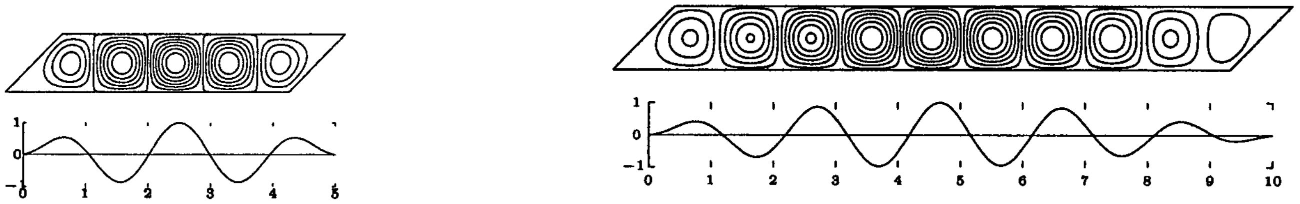

(e) $a/b = 5, \alpha = 45°, b_2/b_1 = 1.0$ (f) $a/b = 10, \alpha = 45°, b_2/b_1 = 1.0$

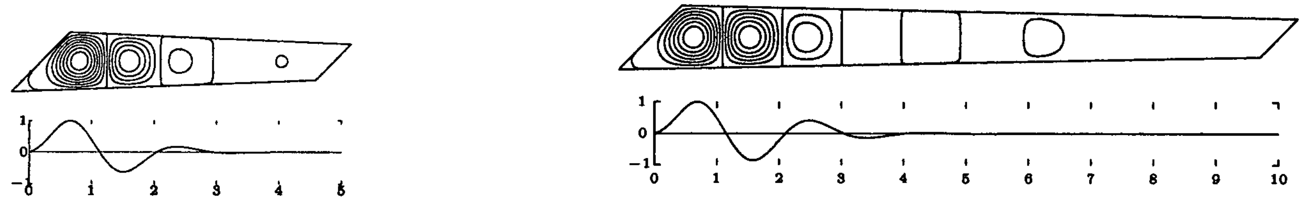

(g) $a/b = 5, \alpha = 45°, b_2/b_1 = 0.6$ (h) $a/b = 10, \alpha = 45°, b_2/b_1 = 0.6$

Figure 7.23: Contour plots and buckling modes (relative displacement through longitudinal centreline of plate) for simply supported plates with aspect ratios $a/b_1 = 5$ (left-hand side) and 10 (right-hand side).

The buckling modes in Figure 7.23 parts (a) and (b) are for a long, simply supported plate [88], have a half-wavelength equal to the width of the plate. The buckling mode is a series of equal sinusoidal buckles. The tapered counterpart (part (c) and (d)), has a much higher buckling load and does not have a buckling mode comprising of many half-wavelengths: 3 are visible in the contour plot and four in the deflection plot (the contour plot is not as sensitive as the deflection plot). This is true for both aspect ratios.

The long skew simply supported plates (parts (e) and (f)) have a different buckling mode compared to the equivalent rectangular plate. The modes that form have the same number of longitudinal half-wavelengths, but the skew transverse edge shifts the buckling pattern away from the transverse edge. The half-wavelengths of the buckles are necessarily shorter and vary along the plate resulting in a modulated deflected shape plot. The tapered skew plate for this case is similar to the $\beta = 1.0$ plot, but the first buckle is not sinusoidal.

The clamped buckling modes shown in Figure 7.24 differ from the simply supported plots. In general, they comprise of more half–wavelengths along the plate length. This is a results of the longitudinal edge, which being clamped, causes the plates to buckle with modes that are similar to a simply supported plate with a higher aspect ratio. The rectangular plate with $a/b_1 = 10$ for example has a buckled form comprising 15 half–wavelengths in the longitudinal direction compared to 10 in the simply supported equivalent (Figure 7.23 (b)). The deflected shape in this case is symmetrical about the plate centre as opposed to being antisymmetric as in the simply supported case and the amplitude of the mode modulates over the plate length. The tapered comparisons to these rectangular plates (parts (d) and (e)) have six distinct buckles in the wide end of the plate compared to only four in the simply supported equivalent. Obviously no symmetry (or antisymmetry) exists in the tapered example because the geometry of the plate has no longitudinal symmetry. The skew plate (parts (e) and (f)) can be compared in a similar manner, however, because the clamped, skew transverse edges shift the mode away from it, the number of half–wavelengths reduces by two, to thirteen, in comparison to its rectangular equivalent. The amplitude of the cross–section mode plots modulate in both cases over the plate length. The tapered comparison (parts (g) and (h) are similar to the skew equivalents in parts (c) and (d), but the first half–wavelength of the mode is shifted further away from the transverse edge by the skew geometry.

7.7 Concluding Remarks

The chapter presents a detailed study on the linear-elastic buckling strength of thin plates tapered in plan-form and extends the currently limited knowledge of their behaviour. The results are presented as a series

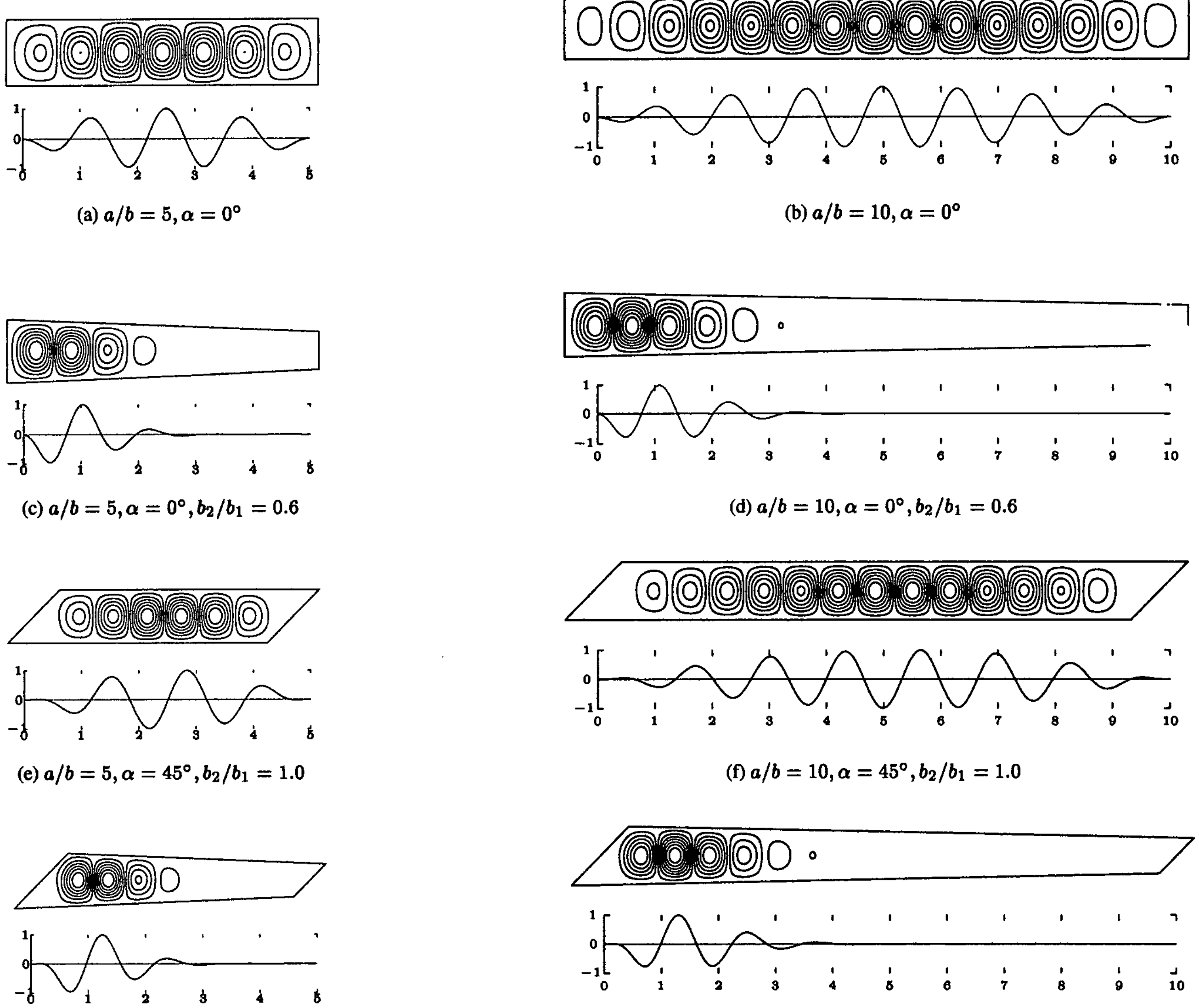

(a) $a/b = 5, \alpha = 0°$

(b) $a/b = 10, \alpha = 0°$

(c) $a/b = 5, \alpha = 0°, b_2/b_1 = 0.6$

(d) $a/b = 10, \alpha = 0°, b_2/b_1 = 0.6$

(e) $a/b = 5, \alpha = 45°, b_2/b_1 = 1.0$

(f) $a/b = 10, \alpha = 45°, b_2/b_1 = 1.0$

(g) $a/b = 5, \alpha = 45°, b_2/b_1 = 0.6$

(h) $a/b = 10, \alpha = 45°, b_2/b_1 = 0.6$

Figure 7.24: Contour plots and buckling modes (relative displacement through longitudinal centreline of plate) for fully clamped plates with aspect ratios $a/b_1 = 5$ (left-hand side) and 10 (right-hand side).

of buckling curves showing the relationship between plate buckling strength and plate aspect ratio.

The study shows that the buckling strength of plates that are tapered in planform are significantly stronger than a rectangular plate with the same aspect ratio. These strength gains are prominent not only over a small range of aspect ratios as is the case of skew plates, but also over much higher aspect ratios because the geometry of the longitudinal plate edge is changed. At the highest aspect ratios ($a/b_1 = 20$) in the study, there are significant strength gains over an equivalent rectangular or skew plate. These gains are as high as 15% when $\beta = 0.4$.

The buckling strength increase curves have shown that when the aspect ratio of a plate is small (less than one), buckling strength increases are largely the result of a skew tranverse edge. For aspect ratios higher than one, buckling strength increases are attributed to the tapered longitudinal edges. This is a significant observation because in practice wing panels and plates will typically have aspect ratio higher than one.

The buckling curves for the tapered plates are very different in appearance than for a skew or rectangular plate with equivalent aspect ratio. The study proves that the existence of cusps arising from clear and distinct buckle mode changes do not occur in the case of plates that are tapered. The narrowed edge of the plate restricts buckling deflection, with the result that the mode change is forced to occur gradually as the plate aspect ratio increases and that where cusps would be expected to form in the case of rectangular and skew plates, now smoothly defined peak occurs. These peaks decrease in magnitude both with an increase in aspect ratio and also as the taper of the plate increases. This latter observation leads to very smooth buckle curves for plates at very high taper.

Making simplifying assumptions as to the geometry of plates when designing them, for example by assuming that they are rectangular when they are in fact tapered, can lead to large strength advantages being disregarded. For the tapered plates considered in the chapter a 60% increase in buckling strength is attributed to taper for a plate with $\alpha = 45°$ and aspect ratio, $a/b_1 = 2.5$ (Figure 7.17 (d)).

The results of making simplifying assumptions is discussed in the following chapter where the work contained in this chapter is extended to cover composite laminated panels and an example is used to quantify possible strength advantages of using the correct geometry to design wing panels.

Chapter 8

Skew-tapered panels in a swept aircraft wing

8.1 Introduction

The previous chapters have considered the buckling strength of skew plates and panels and plates that are both skew and tapered. The previous chapters have shown that invariably, buckling strength increases occur when the geometry of the plate changes to one of these configurations compared to a similarly sized rectangular plate. This chapter discuses the effect that panel taper, skew and edge rotational restraint have on the buckling strength of wing panels taken from an actual aircraft wing structure.

The aircraft wing adopted is 'swept' and tapered with the result that the panels forming the wing are both skew and tapered in planform. The effect on the buckling prediction of the wing panels if simplifying assumptions are made with respect to the planform geometry of the panel and rectangular approximations are made instead of considering the actual skew-tapered planform geometry are investigated. Rectangular approximations are used extensively in aircraft design because of the availability of design data relating to rectangular plates and panels, for example those by ESDU (Engineering Science Data Unit). Previous results in the thesis suggest that using rectangular approximation leads to 'over design' because plates with more complicated skew and tapered geometry are stronger in buckling for the in-plane compression loading cases considered.

8.2 Example Wing Panels

A benchmark wing provided by Dornier is used to provide the practical problem. The wing is constructed from eight individual panels that are skew–tapered in planform. Each of the panels has three equally spaced stiffeners. The panels are made from a symmetric balanced CFRP (carbon reinforces plastic) laminate. The panels are supported on three spars and five ribs which are also tapered in depth. The spars and ribs are constructed from the same CFRP laminate as the panels.

Figure 8.1 shows: (top) a plan on the wing showing all eight wing panels and a local Cartesian coordinate system with the x–axis along the central spar; (centre) an isometric view of the three individual spars which provide the supporting structure for the wing: and (bottom) an isometric of the wing without wing panels showing supporting ribs and spars.

The wing is taken from an optimisation study by the GARTEUR Action Group. Results for the optimised configurations of the panels are avaliable in the open literature by York *et al.* [117]. The study, for which results are available, optimised each wing panel separately for combinations of bi-axial in-plane compression loading and shear using an optimisation code VICONOPT (VICON with OPTimisation) [103, 102]. The optimisation provides a minimum weight design for the prescribed magnitudes of loading using ply thickness as design variables (stacked symmetrically with fixed orientations $[\pm 45°, 0°, 90°]_S$. VICONOPT uses VICON [101, 4, 114] [1] to provide buckling predictions for plates which are then used in an optimisation routine.

Rectangular approximations of the actual panels are used for optimisation, and the results of the analysis and the practical problem therefore provide an ideal platform to ascertain the effect on the panel buckling of changing the geometry of the plate, from the rectangular approximation to more accurate approximations until the actual planform geometry is analysed. Each of the wing panels have a skew angle of 45° and a constant angle of taper along one edge.

8.2.1 Minimum weight optimised panels

The ply lay-ups used in the study are taken from the results of the optimised rectangular approximation of the wing panels. They are not necessarily typical of a fabricated structure in which there may be additional constraints for economy reasons, for example for ply thicknesses to be multiple integers of the lamina thickness. Results for two wing panels are reported in York *et al.* [117] which are the panels having the

---

[1] VICONOPT can alternatively use VIPASA instead of VICON to provide buckling predictions, but all analyses by VICONOPT considered herein are conducted using buckling predictions by VICON

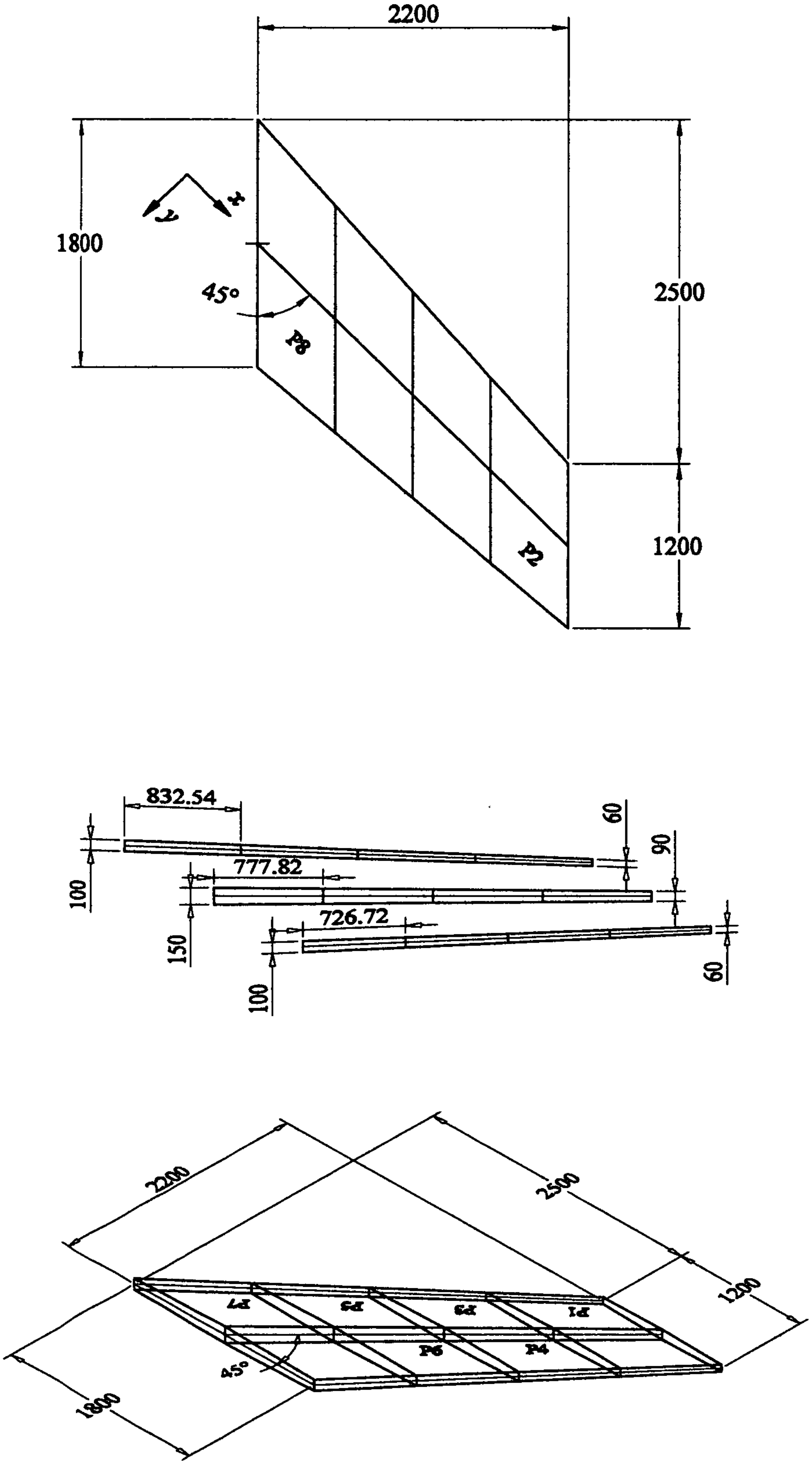

Figure 8.1: The wing used in the study. The figure shows: (top) a plan on the wing showing the individual wing panels, highlights the wing panels used for the study (Panels 2 and 8) and defines a local Cartesian coordinate system used throughout; (centre) the spars supported in the panels with dimensions; and (bottom) the wing structure used to support the panels comprising the three spars and five ribs. (All dimensions in mm)

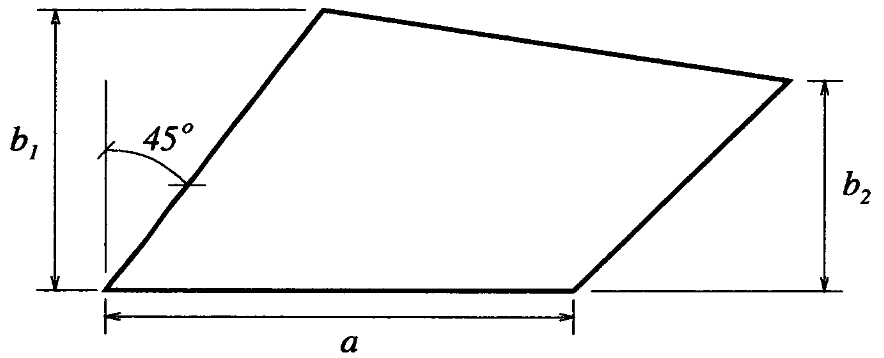

Figure 8.2: Nomenclature used to describe the geometry of the plate. The figure shows the actual skew-tapered geometry of a panel having a length a along the bottom of the panel which coincides with the $x - axis$ in Figure 8.1 parallel to the central spar. Transverse widths b_1 and b_2 are measured normal to the central spar and the panels have a skew angle of 45°. Aspect ratio is taken to be the ratio of longitudinal panel length and the mean transverse edge widths, $b' = (b_1 + b_2)/2$ and taper the ratio of the transverse edge widths, b_2/b_1.

lowest and highest predefined loading. By coincidence, these panels also have the largest difference in geometry and are adopted for use in the study. These two panels are Panels 2 and 8 shown in Figure 8.1.

The panels in the study by York *et al.* [117] are approximated by taking the mean longitudinal and transverse panel dimensions parallel and normal to the coordinate system given in Figure 8.1. The current study considers three possible planform geometries of the panel:

1. the rectangular geometry as used in the previous optimisation study;
2. a skew geometry approximated using the rectangular dimensions, with the transverse panel edge skewed through 45°;
3. the actual skew-tapered geometry.

It is convenient to adopt a nomenclature based on the work in the previous chapters to discuss the panel geometry and permit comparisons to be made. This nomenclature is given in Figure 8.2. The figure shows the skew-tapered plate having a longitudinal length, a, along the x−axis. This reference axis lies along the central spar of the wing, with the consequence that all the panels in the wing share this same length which is $777.8mm$. The transverse widths of the panels are labeled, b_1 and b_2 for the widest and narrowest edge respectively. The skew angle, α is a constant 45° for all the panels in the wing.

Table 8.1: Geometry and dimensions of the two panels used in the study, giving aspect ratio and taper of the panels

Panel	b_1 (mm)	b_2 (mm)	(b_2/b_1)	$(b_1+b_2)/2=b'$	l_{top} (mm)	l_{bot} (mm)	a/b_1	Plan Area (mm^2)	Stiffener Depth mm
2	477.4	424.3	0.89	450.9	724.8	777.8	1.72	327632.7	32.5
8	636.4	583.4	0.92	609.9	724.8	777.8	1.22	443214.33	47.5

8.2.2 Geometry of the Panels used in the study

The geometry of the panels is described using the nomenclature above. The geometry and dimensions for each panel are given in Figure 8.3 and 8.4 for panels 2 and 8 respectively. The figures also give a lateral cross section through the panels showing stiffener depths as well as the ply lay-up for each panel. The basis used to obtain the dimensions in the figure are given below.

Rectangular

The rectangular geometry uses the longitudinal length, a, along the $x-$axis ($777.8mm$) and the average of the transverse widths to give the transverse width *i.e.* $(b_1 + b_2)/2$. This average transverse width is termed b'. Stiffeners run parallel to the $x - axis$ and are equally spaced at a distance of $(b_1 + b_2)/8 = b'/4$.

Skew

The skew approximation uses the longitudinal and transverse dimensions in the rectangular case, but a skew angle of 45° is applied to the transverse edge.

Actual Configuration

The actual panel geometry shown in Figures 8.3 or 8.4 is adopted in this analysis. The stiffeners are taken to run parallel to the $x - axis$ and are equally spaced at $b_1/4$. The spacing is taken to be $b_1/4$ (α in Figure 8.2).

Using the definitions for geometry given above, all the panels have an equal weight and planform area. Table 8.1 summarises the geometry of the Panels 2 and 8 and introduces definitions for: aspect ratio, taken to be a/b' and taper, taken as $\beta = (b_2/b_1)$. Panel 2 has an aspect ratio of 1.72 and a taper of 0.89 and panel 8 has an aspect ratio of 1.22 and a taper of 0.92.

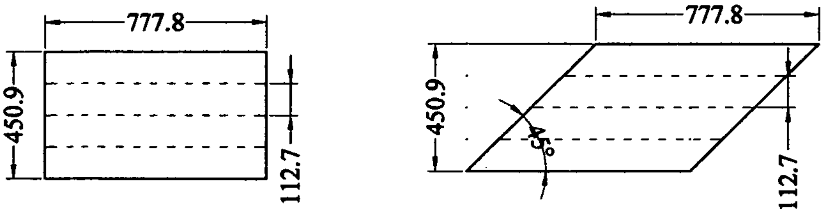

P-2 Rectangular

P-2 Skew

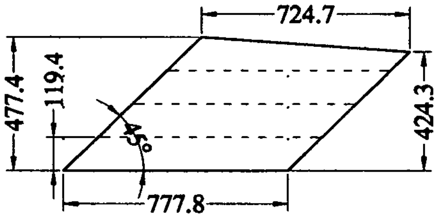

P-2 Tapered

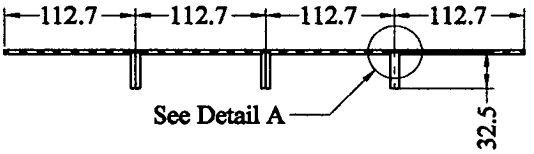

P-2 Section

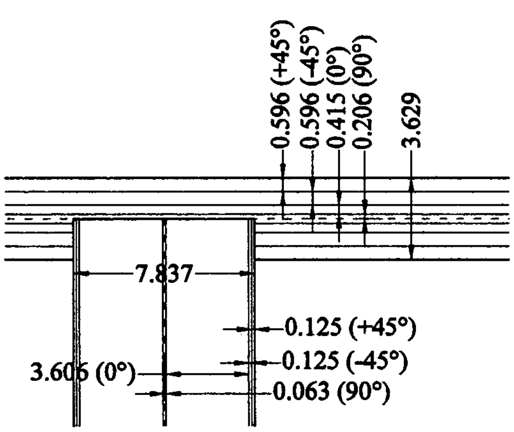

Detail A
Ply layup

Figure 8.3: Panel 2: dimensions of the wing panels for each of the geometries considered in the study, cross section though the panel showing stiffener spacing and stiffener depths and ply lay-up. The orientation for the plies is given with respect to the local coordinate system defined in figure 8.1 (top). The dashed lines on the wing panels identify the stiffener location. (All dimensions in mm)

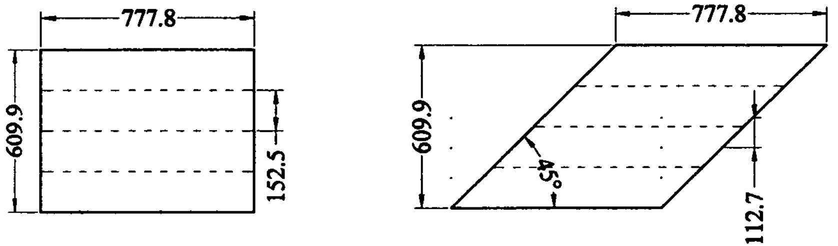

P-8 Rectangular

P-8 Skew

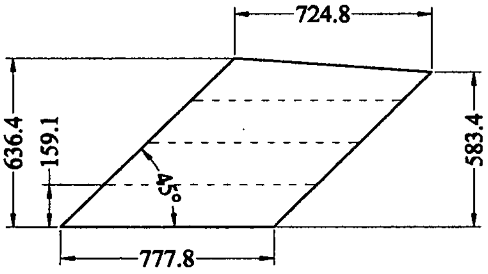

P-8 Tapered

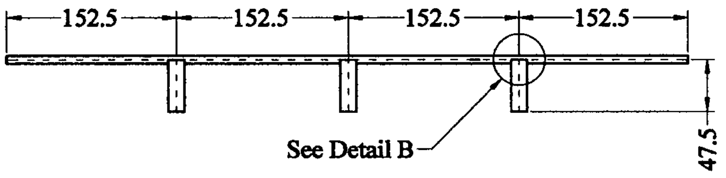

P-8 Section

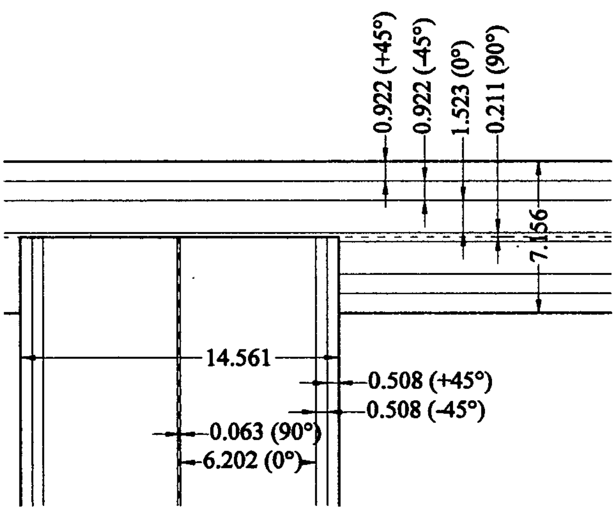

Detail B
Ply layup

Figure 8.4: Panel 8: dimensions of the wing panels for each of the geometries considered in the study, cross section though the panel showing stiffener spacing and stiffener depths and ply lay-up. The orientation for the plies is given with respect to the local coordinate system defined in figure 8.1 (top). The dashed lines on the wing panels identify the stiffener location. (All dimensions in mm)

Table 8.2: Load distributed based on an applied load to the rectangular and skew configurations of 100kN/m. For the tapered configuration, this load is reduced by the factor b'/b_1 to ensure that the total preloading applied to all the panels is the same and that eigenvalue predictions can be compared between the sets of analyses.

	Rectangular and Skew		Tapered	
	Panel 2	Panel 8	Panel 2	Panel 8
Skin	46.95	55.89	44.83	54.56
Stiffener	250.02	188.84	243.38	193.52

8.3 Loading and Panel Properties

Loading to the panels is in keeping with the loading regimes used in the rest of the thesis *i.e.* an in-plane, uni-axial compression applied along the transverse edges of the panel. The load is distributed over the panel skin and stiffeners to apply a uniform, uni-axial compression using the methods outlines in appendix C and reference [84]. This panel load is distributed in proportion to the values of $(A_{11} - (A_{12}^2/A_{22}))$ for the panel skin and stiffeners. The loading has to address two issues: to apply this uniform, uniaxial strain; and to preserve global equilibrium. Equilibrium is automatically satisfied in the case of the rectangular and skew panel configurations. For the tapered configurations, a load is also applied along the tapered edge. In addition, to make valid comparisons between the buckling loads of the panels, the preloading applied to the panels should be the same because the eigenvalue, λ, is a factor of the applied loading, P, hence the buckling load of the panel is λP. An arbitrary loading $N_x = 100kN/m$ length of the transverse edge is taken as the datum loading. The eigenvalues, calculated in the analysis therefore give a factor of this arbitrary load that will cause buckling of the panel. Because the tapered panel has slightly wider transverse edges than that used to obtain the rectangular and skew geometry, the applied loading to the tapered panel is reduced accordingly so that $N_x' = (b'/b_1)N_x$ to ensure that the total preloading applied to the panels is the same. The load distribution applied to the panels is given in Table 8.2

The material properties for the CFRP laminate are:

$$\begin{array}{rclrcl}
E_{11} & = & 125GNm^{-2}, & Q_{11} & = & 126GNm^{-2} \\
E_{22} & = & 8.8GNm^{-2}, & Q_{22} & = & 8.88GNm^{-2} \\
G_{12} & = & 5.3GNm^{-2}, & Q_{12} & = & 3.11GNm^{-2} \\
\nu_{12} & = & 0.35, & Q_{66} & = & 5.30GNm^{-2} \\
\nu_{21} & = & 0.0246 & & &
\end{array}$$

Table 8.3: Ply lay-ups for the each panel. The ply lay-up is balanced symmetrical and so only half is shown here. The lay-up is shown graphically in figures 8.3 and fig:6:P8 for panels 2 and 8.

Layer No.	Ply Orientation (Degrees)	Ply Thickness Skin (mm)	Ply Thickness Stiffener (mm)
1	+45	0.5960	0.1250
2	-45	0.5960	0.1250
3	0	0.4150	3.6060
4	90	0.2075	0.0625
		3.6290	7.8370

(a) Ply lay-up for Panel 2

Layer No.	Ply Orientation (Degrees)	Ply Thickness Skin (mm)	Ply Thickness Stiffener (mm)
1	+45	0.9220	0.5080
2	-45	0.9220	0.5080
3	0	1.5230	6.2020
4	90	0.2110	0.0625
		7.1560	14.5610

(b) Ply lay-up for Panel 8

Table 8.3 gives the ply lay-up for each panel and overall stiffnesses for the panels are given in Tables 8.4 and 8.5 for panels 2 and 8 respectively. Bending and membrane stiffnesses for the panel stiffeners and skin are calculated according to the well-known methods used in reference [92]. The non-dimensional coefficient D_{11}/D_{22} for the entire panel, is calculated using an EI type stiffness according to the methods outlined in chapter 6 and reference [84] to allow comparison with the orthotropic plates treated in chapter 6. These coefficients are included in the captions of the tabulated data.

8.4 Boundary Conditions

The panels are initially modelled as being simply supported an all four edges. These buckling results provide a datum with which to make comparisons about the effect of changing boundary conditions. This simply supported case, does not give consideration to buckling strength increases that will be obtained by an imposed rotational stiffness arising from continuity and the spars. The effects of applying a rotational restraint of constant magnitude along the panel edges is therefore also considered in a similar manner to

Table 8.4: Membrane and Bending stiffnesses for Panel 2 CRFP laminate. See caption in Table 8.5 for Σ. The overall orthotropic stiffness of the panel are: $D_{11} = 151.101 \times 10^3$NM; and $D_{22} = 157.326$NM, giving $D_{11}/D_{22} = 960.45$.

	Transformed Reduced Stiffnesses (GNm^{-1})				Membrane stiffnesses (MNm^{-1})				Bending Stiffnesses (Nm)			
Layer	$\overline{Q}_{11}$	$\overline{Q}_{22}$	$\overline{Q}_{12}$	$\overline{Q}_{66}$	A_{11}	A_{22}	A_{12}	A_{66}	D_{11}	D_{22}	D_{12}	D_{66}
1	40.594	40.594	29.994	32.188	24.194	24.194	17.877	19.184	169.072	169.072	124.924	134.059
2	40.594	40.594	29.994	32.188	24.194	24.194	17.877	19.184	63.649	63.649	47.029	50.468
3	126.087	8.877	3.107	5.300	52.326	3.684	1.289	2.200	30.415	2.141	0.749	1.278
4	8.877	126.087	3.107	5.300	1.842	26.163	0.645	1.100	0.079	1.126	0.028	0.047
				Σ	205.113	156.471	75.375	83.334	175.477	157.326	115.154	123.902

(a) Panel 2 - Skin

	Transformed Reduced Stiffnesses (GNm^{-2})				Membrane stiffnesses (MNm^{-1})				Bending Stiffnesses (Nm)			
Layer	$\overline{Q}_{11}$	$\overline{Q}_{22}$	$\overline{Q}_{12}$	$\overline{Q}_{66}$	A_{11}	A_{22}	A_{12}	A_{66}	D_{11}	D_{22}	D_{12}	D_{66}
1	40.594	40.594	29.994	32.188	5.074	5.074	3.749	4.023	226.365	226.365	167.257	179.486
2	40.594	40.594	29.994	32.188	5.074	5.074	3.749	4.023	211.928	211.928	156.589	168.039
3	126.087	8.877	3.107	5.300	454.67	32.009	11.203	19.112	6224.92	438.236	153.382	261.661
4	8.877	126.087	3.107	5.300	0.555	7.880	0.194	0.331	0.002	0.031	0.001	0.001
				Σ	930.749	100.076	37.792	54.980	4442.155	584.373	318.153	406.125

(b) Panel 2 - Stiffener

Table 8.5: Membrane and Bending stiffnesses for Panel 8 CFRP laminate. For this table and Table 8.4 Σ gives the membrane and bending stiffnesses for the entire section. For membrane stiffness, $\Sigma = \Sigma_k^n A_{ij}(z_k - z_{k-1})$ and for bending stiffness, $\Sigma = \frac{1}{3}\Sigma_k^n D_{ij}(z_k^3 - z_{k-1}^3)$ [92]. In both cases n is the number of layers making up the laminate, k is the layer number and z is the through thickness from the centre of the laminate. The overall orthotropic stiffness of the panel are: $D_{11} = 1868 \times 10^3$Nm; and $D_{22} = 1130.185$NM, giving $D_{11}/D_{22} = 1652.8$.

	Transformed Reduced Stiffnesses (GNm^{-1})				Membrane stiffnesses (MNm^{-1})				Bending Stiffnesses (Nm)			
Layer	$\overline{Q}_{11}$	$\overline{Q}_{22}$	$\overline{Q}_{12}$	$\overline{Q}_{66}$	A_{11}	A_{22}	A_{12}	A_{66}	D_{11}	D_{22}	D_{12}	D_{66}
1	40.594	40.594	29.994	32.188	37.428	37.428	27.655	29.677	1098.871	1098.871	811.934	871.303
2	40.594	40.594	29.994	32.188	37.428	37.428	27.655	29.677	548.942	548.942	405.602	435.260
3	126.087	8.877	3.107	5.300	192.031	13.519	4.732	8.072	657.384	46.280	16.198	27.633
4	8.877	126.087	3.107	5.300	1.873	26.604	0.656	1.118	0.083	1.184	0.029	0.050
				Σ	537.520	229.959	121.394	137.088	1536.853	1130.185	822.509	889.497

(a) Panel 8 Skin

	Transformed Reduced Stiffnesses (Nm^{-1})				Membrane stiffnesses (Nm^{-1})				Bending Stiffnesses (Nm)			
Layer	$\overline{Q}_{11}$	$\overline{Q}_{22}$	$\overline{Q}_{12}$	$\overline{Q}_{66}$	A_{11}	A_{22}	A_{12}	A_{66}	D_{11}	D_{22}	D_{12}	D_{66}
1	40.594	40.594	29.994	32.188	20.622	20.622	15.237	16.351	10011.910	10011.910	7397.601	7938.518
2	40.594	40.594	29.994	32.188	251.766	251.766	186.025	199.627	68670.268	68670.268	50739.095	54449.168
3	126.087	8.877	3.107	5.300	781.994	55.052	19.268	32.871	30997.768	2182.243	763.785	1302.971
4	8.877	126.087	3.107	5.300	0.555	7.880	0.194	0.331	0.002	0.031	0.001	0.001
				Σ	2109.874	670.642	441.450	498.361	73119.966	53909.635	39266.988	42460.439

(b) Panel 8 Stiffeners

that used in chapter 4 for skew plates. A comparison between this simplified rotational restraint and the actual rotational restraint provided by the spars is also considered in the study. Discussion relating to the modelling procedure for this aspect of the study is given in section 8.7.4.

The common nomenclature describing the boundary conditions is the same as that used in the preceeding chapters of the thesis where the boundary condition is given a Case $x - y$. x gives the boundary condition applied along the longitudinal panel edge and the y the boundary condition applied along the transverse plate edge. x and y take on the values given below representing the appropriate boundary condition relating to:

1. a simply supported panel edge;
2. a rotationally restrained panel edge and;
4. a fully clamped edge.[2]

Rotational stiffness is measured using the dimensionless coefficient, κ,

$$\kappa = \frac{\beta b'}{D} \tag{8.1}$$

where:

β is the spring stiffness of the torsional support (Moment per unit rotation);

b' is the average panel breadth $((b_1 + b_2)/2$ in Figure 8.2;

D is the flexural rigidly of the panel skin to which the rotational stiffness is applied.

The flexural rigidity of the panel skin is measured normal to the panel edge and the bending stiffness of the plate is also recalculated normal to the edge by applying a rotation to the ply layers. Hence, the stiffness is calculated about a local axis with minor axis orientated along the panel edge and minor axis located normal to this edge. This procedure is applicable to both the skew transverse panel edges and the top edge of the tapered panel.

The boundary conditions are illustrated in Figure 8.5. Each of the nine configurations represent the possible combinations which have an equal rotational stiffness on opposite edges.

Note that a value of rotational stiffness, $\kappa = 0$ is synonymous with a simple support and $\kappa = \infty$ is synonymous with a clamped edge.

---

[2] 3 is omitted because it relates to a continuity boundary condition used previously.

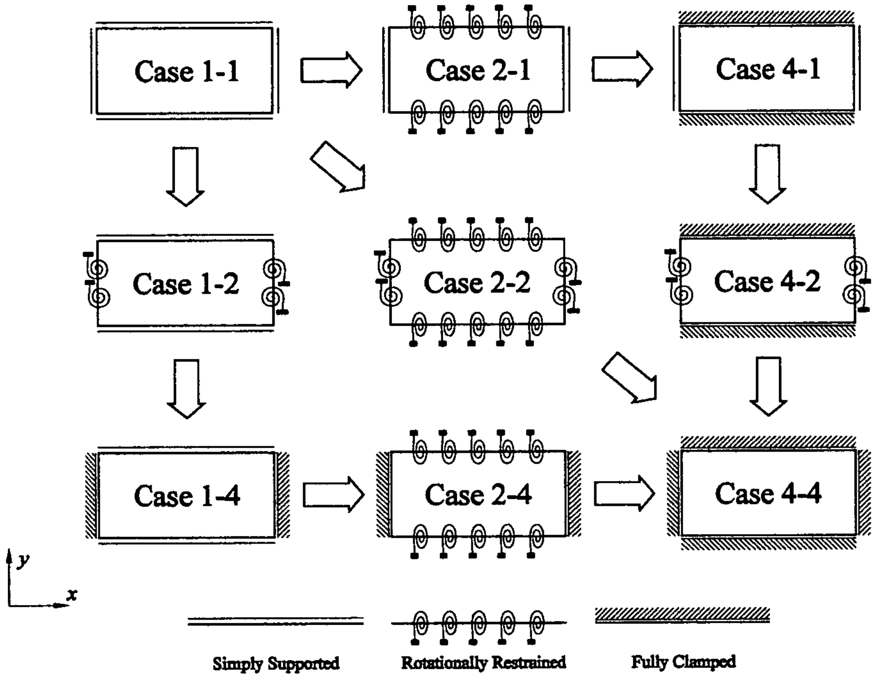

Figure 8.5: The figure shows all nine boundary conditions used in the study with their respective case names. The arrows show boundary conditions in which the application of increasing magnitudes of rotational restraint transforms a lower bound buckling prediction into an upper-bound prediction. For example, taking the top row; the lower-bound is that for a panel simply supported on all four edges, which using Case 2-1 and increasing κ to infinity gives the upper-bound for Case 2-1 - Case 4-1. These buckling predictions are shown in the buckling curves of figure 8.7 and 8.8 where each line on the curve represents one single row, column or in the case when rotational stiffness is applied to all four edges the leading diagonal.

Mesh (skin) Mesh (stiffeners)	20 x 20 20 x 2	40 x 40 40 x 4	60 x 60 60 x 4	120 x 120 120 x 4
Buckling factor	8.878	8.235	7.957	7.948
Difference (%)	—	7.8	3.49	0.11

(c) Panel 2 - Skew-tapered

Mesh (skin) Mesh (stiffeners)	20 x 20 20 x 2	40 x 40 40 x 4	60 x 60 60 x 4	120 x 120 120 x 4
Buckling factor	37.710	35.598	34.401	34.177
Difference (%)	—	9.62	3.47	0.65

(d) Panel 8 - Skew tapered

Table 8.6: Convergence study for panels 2 and 8 for the skew-tapered configuration with all four edges simply supported. The 'Difference (%)' row shows the percentage difference between adjacent mesh increments. All the meshes are uniform with the number of elements (ABAQUS type S8R5) in the longitudinal direction given first.

8.5 Modelling

8.5.1 General panels

Buckling predictions are carried out using ABAQUS [3].

A very fine mesh of type S8R5 element (see Appendix A) is used which gives buckling predictions within an accuracy of better than 1% based on a mesh convergence study of the panels. Rotational restraint is applied using type SPRING1 elements [3]. The S8R5 element satisfies classical thin plate theory, so no account is given to shear deformation of the plates making up the panel. The model does not account for the eccentricity of the panel stiffener with respect to the panel skin, which is consistent with the GARTEUR analysis of the panels and those panels analysed in chapter 6. A typical mesh for the rectangular approximation is shown in Figure 8.6. The mesh comprises 60 x 60 elements for the skin (3600 in total) and 60 x 4 elements for the stiffeners (240 elements per stiffener). The models have a total of 4320 elements.

A tabulated convergence study for the simply supported boundary conditons and the skew-tapered geometric configuration for each panel is shown in Table 8.6.

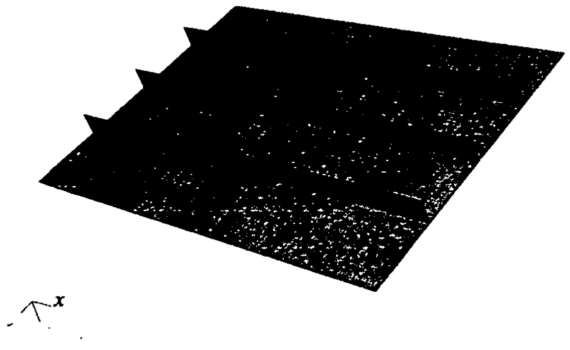

Figure 8.6: Typical mesh used for the analysis, in this case a rectangular configuration for Panel 8.

8.5.2 Spars

York *et al.* [117] performed optimisation on the wing panels with the spars included in the analysis. The results of the optimisation suggested that mass savings of 2.1% and 5.1% could be made for panels 2 and 8 respectively if the spars are included in the analysis. These results provide the impetus for including rotational restraint in the boundary condition cases and in order to make comparisons with this simplified rotational restraint model, the panels are modelled with the spars. The ply lay-up and spar thicknesses are taken from the optimised configuration reported in York *et al.* and are derived from a rectangular approximation of the spar geometry. Note that the mean depth of the spars is also different along the two longitudinal edges of the panels. The central spar has a mean depth larger than that of the spar running along the outer edge of the panel. The VICONOPT analysis ignores any load that may be distributed to the spars and therefore any weight savings are attributable only to the rotational stiffness provided by the spars.

The spars which run longitudinally along the edges of the panels of the wing structures are modelled discretely using the same element formulation used in the skin and stiffeners. The spars are initially modelled using the average depth of those in the wing. However in order to provide results with which valid comparisons can be made with the rotationally restrained cases (note this relates to boundary condition Case 2-1 in Figure 8.5), the boundary conditions and hence the spars should be the same on both longitudinal edges of the panel. The panels are therefore modelled using the rectangular approximations for the spar depth and two cases are considered. The first considers that the depth of the spars on the panel are the mean of the shallower spar (*i.e.* that of the spar running along the leading or trailing edge); and the second, that of the spar having the mean dimensions of the deeper central spar.

The properties of the spars are given in Tables 8.7

For the purposes of modelling, no load is applied to the spar. The spar has boundary conditions along the transverse edges synonymous with those of a diaphragm support (*i.e.* there is no out-of-plane deflection permitted at this edge). Because the base of the spar coincides with the longitudinal edge of the underside wing panel, transverse displacement is also prevented. The longitudinal stiffness of the spar also introduces some longitudinal restraint to the plate. This longitudinal stiffness proved to increase the buckling capacity over and above that of the fully clamped upper-bound solution. In order to determine the rotational stiffness that the spars give to the panel, neglecting this in-plane restraint, the spar is coupled to the panel using only rotational degrees of freedom according to the equations:

$$\begin{aligned} \theta_{x_{\mathrm{SPAR}}}^{y=0,b,} &- \theta_{x_{\mathrm{PANEL}}}^{y=0,b} = 0 \\ \theta_{y_{\mathrm{SPAR}}}^{y=0,b,} &- \theta_{y_{\mathrm{PANEL}}}^{y=0,b} = 0 \end{aligned}$$

where the superscript relates to the longitudinal panel edges and the subscript to the degree of freedom (θ_x, θ_y or θ_z). ‘SPAR’ relates to the top most edge of the spar at the junction between it and the panel edge and ‘PANEL’ relates to the degrees of freedom along the panel edges. Using these constraints, the maximum buckling load of the plate is synonymous with that of a clamped edge and the lower buckling load with that of a simply supported edge.

8.6 Results

Results of the analyses are presented as buckling curves relating the rotational stiffness applied along the panel edge with the critical buckling load of the panels. The buckling load is presented as a factor of the arbitrarily applied preloading (100kN/m). Hence the true buckling load of the panel is 100 times the presented buckling factor times the mean transverse panel width, b'. The buckling curves are shown in Figures 8.7 and 8.8 for panels 2 and 8 respectively.

Figures 8.7 and 8.8 showing the buckle curves comprise three graphs, each of which shows buckling curves for one of the three geometric configurations considered in the study. Each graph comprises 5 buckling curves, one for each set of boundary conditions described by the arrows in figure 8.5.

Each row and/or column in Figure 8.5 shows the boundary conditions relating to each curve. The first illustration in the row/column gives the lower-bound boundary conditon for the panel and comprises a set of simply supported edges. The second icon shows how this simply supported edge is transformed

Table 8.7: Membrane and bending stiffnesses for the panel spars for panel 2. See caption of Table 8.5 for explanation of Σ.

	Ply lay-up		Membrane Stiffness (MNm^{-1})				Bending Stiffness(Nm)			
Layer	Thickness (mm)	Orientation (Degrees)	A_{11}	A_{22}	A_{12}	A_{66}	D_{11}	D_{22}	D_{12}	D_{66}
1	0.623	45	25.290	25.290	18.686	20.053	120.434	120.434	88.988	95.493
2	0.623	-45	25.290	25.290	18.686	20.053	31.996	31.996	23.641	25.370
3	0.250	0	31.522	2.219	0.777	1.325	3.817	0.269	0.094	0.160
4	0.625	90	0.555	7.880	0.194	0.331	0.002	0.031	0.001	0.001
Total	3.117	Σ	165.314	121.360	76.688	83.524	104.166	101.820	75.148	80.683

(a) Panel 2 - Deep Spar

	Ply lay-up		Membrane Stiffness (MNm^{-1})				Bending Stiffness (Nm)			
Layer	Thickness (mm)	Orientation (Degrees)	A_{11}	A_{22}	A_{12}	A_{66}	D_{11}	D_{22}	D_{12}	D_{66}
1	0.250	45	10.149	10.149	7.499	8.047	14.549	14.549	10.750	11.536
2	0.250	-45	10.149	10.149	7.499	8.047	5.988	5.988	4.423	4.746
3	0.250	0	31.522	2.219	0.777	1.325	3.817	0.269	0.094	0.160
4	0.0625	90	0.555	7.880	0.194	0.331	0.002	0.031	0.001	0.001
Total	1.625	Σ	104.748	60.794	31.936	35.500	16.236	13.890	10.178	10.963

(b) Panel 2 - Shallow Spar

Table 8.8: Membrane and bending stiffnesses for the panel spars for panel 8. 8.1. See caption of Table 8.5 for explanation of Σ.

	Ply lay-up		Membrane Stiffness (MNm^{-1})				Bending Stiffness (Nm)			
Layer	Thickness (mm)	Orientation (Degrees)	A_{11}	A_{22}	A_{12}	A_{66}	D_{11}	D_{22}	D_{12}	D_{66}
1	1.625	45	65.966	65.966	48.741	52.305	1540.148	1540.148	1137.985	1221.195
2	1.625	-45	65.966	65.966	48.741	52.305	294.012	294.012	217.240	233.124
3	0.250	0	31.522	2.219	0.777	1.325	3.817	0.269	0.094	0.160
4	0.625	90	0.555	7.880	0.194	0.331	0.002	0.031	0.001	0.001
Total	7.125	Σ	328.017	284.063	196.905	212.532	1225.320	1222.973	903.546	969.654

(a) Panel 8 - Deep spar

	Ply lay-up		Membrane Stiffness (MNm^{-1})				Bending Stiffness (Nm)			
Layer	Thickness (mm)	Orientation (Degrees)	A_{11}	A_{22}	A_{12}	A_{66}	D_{11}	D_{22}	D_{12}	D_{66}
1	1.163	45	47.211	47.211	34.883	37.434	679.834	679.834	502.315	539.045
2	1.163	-45	47.211	47.211	34.883	37.434	158.165	158.615	116.885	125.410
3	0.358	0	45.139	3.178	1.112	1.897	9.344	0.658	0.230	0.393
4	0.0625	90	0.555	7.880	0.194	0.331	0.002	0.31	0.001	0.001
Total	5.493	Σ	280.233	210.962	142.147	154.194	584.897	559.125	412.941	443.233

(b) Panel 8 - Shallow spar

into the third illustration (showing the upper-bound boundary condition) by the application of increasing magnitudes of rotational restraint. For the case in which rotational restraint is applied along both the transverse and longitudinal edges, the leading diagonal of Figure 8.5 gives the relevant boundary condition icons.

In Figures 8.7 and 8.8, each of the buckling curves is identified by the appropriate lower- and upper- boundary condition case. For all cases, except when rotational restraint is applied along all four edges, the upper– or lower– boundary condition case for one curve gives either a lower- of upper- boundary condition case for another curve. This is readily seen by inspection of Figure 8.5 when the arrows describing the transition from a panel simply supported on all four edges to one that is clamped on all four edges change direction by 90°. For example: the top row of Figure 8.5 shows the transition of a panel with all four edges simply supported (Case 1-1) to Case 4-1 (longitudinal panel edges fully clamped and transverse edges simply supported) by the application of increasing magnitudes of rotational restraint applied along the longitudinal edge (Case 2-1). This buckling behaviour for a panel in this case is shown by the curves bounded by Case 1-1 and Case 4-1. This upper-bound, Case 4-1, provides a lower-bound buckling prediction for the curve represented by the right-hand column in Figure 8.5. This second curve shows the critical buckling load of the panel as the boundary conditions change from Case 4-1 (fully clamped along the longitudinal edges and simply supported transverse edges) to a panel fully clamped on all four edges (Case 4-4) by increasing the magnitude of rotational stiffness along the transverse plate edge (Case 4-2).

The effect on the buckling load of the panels by considering the panel geometry is quantified in Table 8.9 which shows the increases in buckle strength associated with considered changes in planform geometry.

8.6.1 Spars

Buckling loads for the panels with a supporting spar along the longitudinal edges are presented in Table 8.10 and by interpolation from the buckling curves, an equivalent rotational stiffness, κ is derived to model the spar.

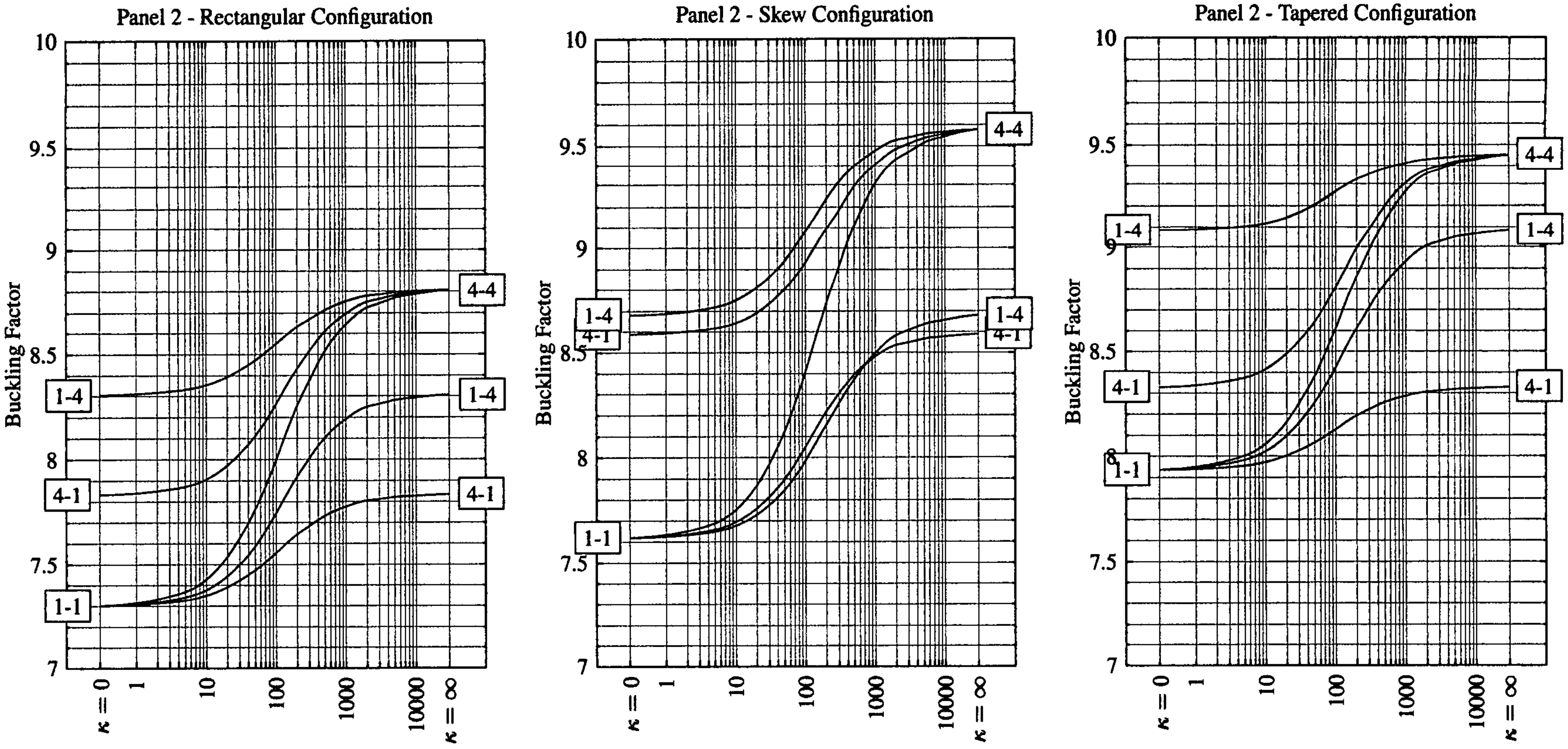

(a) (b) (c)

Figure 8.7: Buckling curves for Panel 2 showing buckling strength (ordinate) as a factor of the applied load of $100kN/m$ against rotational stiffness coefficient, κ (abscissa) defined in Eqn (8.1). The boxes at $\kappa = 0, \infty$, refer to the boundary condition giving lower- and upper-bound buckling loads for the panel which are combinations of simply supported and clamped supports. Each curve represents a separate boundary condition case, which can be identified by its lower- and upper-bound case. Case 1-2 is bounded by Case 1-1 and 1-4, Case 2-1 is bounded by Case 1-1 and Case 4-1, Case 2-2 is bounded by Case 1-1 and Case 4-4, Case 4-2 is bounded by Case 4-1 and 4-4 and Case 2-4 is bounded by Case 1-4 and 4-4.

Table 8.10: Buckling strengths of panels with spars attached to the longitudinal panel edges. The buckling predictions are used together with the buckling curves to derive, from a cubic spline interpolation, an equivalent rotation stiffness. Lower- and upper- bound results ($\kappa = 0, \infty$) are included for comparison. As a comparison for the analysis given in chapter 4, the arithmetic and geometric mean for the shallow and deep spar analysis are calculated to see how close an approximation these mean values are in predicting the buckling strength of the panel when it has the actual spars. Arithmetic and geometric mean are redefined in this section for completeness.

		Spar Depth				Mean	
	Case 1-1	1	2	3	Case 4-1	Arith.	Geom.
Rectangular	7.3014	7.3112	7.3826	7.3480	7.8330	7.3469	7.3468
Equiv. κ	0	1.2	3.9	5.9	∞		
%		1.84	15.27	8.77			
24 Skew	7.6193	7.6273	7.6787	7.6633	8.5883	7.6530	7.6453
Equiv. κ	0	0.9	7.7	5.6	∞		
%		0.83	6.13	4.54			
Tapered	7.9572	7.9734	8.0387	8.0095	8.3510	8.0061	8.0060
Equiv. κ	0	4.2	26.2	15.3	∞		
%		4.11	20.70	8.01			

(a) Panel 2

		Spar Depth				Mean	
	Case 1-1	1	2	3	Case 4-1	Arith.	Geom.
Rectangular	29.985	30.137	30.365	30.270	32.307	30.251	30.251
Equiv. κ	0	6.4	18.2	13.0	∞		
%		6.55	16.37	12.27			
Skew	31.862	32.081	32.377	32.224	34.214	32.153	32.152
Equiv. κ	0	9.46	24.6	15.9	∞		
%		9.31	21.90	15.39			
Tapered	34.401	34.51	34.743	34.656	36.121	34.627	34.626
Equiv. κ	0	3.7	12.5	9.0	∞		
%		6.34	19.88	14.83			

(b) Panel 8

to the longitudinal panel edges. The panel has a bending stiffness many times smaller in this direction that in the other.

8.8 Conclusions

A study has been presented in which panels from a practical wing have been evaluated as if they were: rectangular; skew and; skew and tapered in planform. The skew and tapered planform geometry is the actual geometry of the panel.

Buckling curves for the panels are produced and relate the buckling strength of the panels as the panel edges are rotationally restrained by applying increasing magnitudes of rotational stiffness along opposite edge of the panels. The results of the study show that buckling strength increases occur as the planform geometry of the plate approaches that of the actual planform geometry of the plate used in the aircraft wing.

The study shows that making simplifying assumptions about the geometry of the wing panels leads to uneconomic design. In the most extreme cases, a skew tapered panel has a buckling strength greater than its rectangular equivalent. By taking the more complex planform geometry into account at the design stage, these buckling strength increases potentially lead to weight savings, by permitting a reduction in skin and stiffener thicknesses.

The study also highlights the importance of using the true panel planform geometry because the simplifying assumption of using skew panels as opposed to skew and tapered assumptions in the case of panel 2 analysis lead to buckling predictions that were not foreseeable – the upper-bound (*i.e.* panels with clamped edges) results for panel 2 for the skew panel gave higher buckling predictions that the analysis of the true wing geometry. It can be concluded that improving on the rectangular approximation of a panel and designing it as being skew will lead to 'unsafe' design for this boundary condition.

The effect of the spar using the physical properties given in York [117] on the buckling load of the panels was found to impart some buckling resistance to the panel. In the most extreme cases, the deepest spars increased the buckling strength of the panel to 20% of the difference between the simply supported and fully clamped cases.

close these mean values approximate the actual spars on the panels (Case 3 above). The geometric mean is given as:

$$k = \frac{k_1 + k_2}{2} \tag{8.2}$$

and the geometric mean is given as:

$$k = \sqrt{k_1 k_2} \tag{8.3}$$

where k_1 and k_2 are the critical buckling factor for the panel with shallow and/or deep spars on both longitudinal edges. The mean approximations in the table can be seen to be in good agreement with the panel buckling having the actual spars. This is partially to be expected because the buckling predictions for both set of spars (shallow and deep) are quite close.

The buckling predictions for the panels with either case of spars along the longitudinal edges have low rotational edge stiffness and the buckling loads of the panels are close to the simply supported buckling load of the panels. This is especially true for the shallow and unequal spar cases for panel 2 where the buckling strength of the panels is increased by less than 10% of the difference between the simply supported and clamped panels. The effect of a deep spar is more significant, particularly for the tapered panel, where the buckling strength increases are 20% of the difference between the simply supported and fully clamped case. The effect of the different sized spars is intuitive and can be explained by the rotational stiffness parameter, GJ/bD. Where: G is the shear modulus of the spar; J is the polar second moment of area; b is the average width of the plate and; D is the bending stiffness of the panel skin. For the panel 2 shallow spar, $GJ/bD = 0.03$ and for the deep spar, $GJ/bD = 0.37$.

For panel 8, the effect of adding spars to the longitudinal edges of the panels is more significant with the percentage of buckling strength attributed to the rotational stiffness of the spars being higher than for panel 2. This can be attributed to a larger rotational stiffness parameter for the spars. For the deep spar, $GJ/bD = 0.74$ and for the shallow spar, $GJ/bD = 0.21$.

The tables giving equivalent rotational stiffness show that no real conclusions can be drawn as to which geometry is most affected by the addition of spars in the model. Higher equivalent buckling strengths are obtained for the tapered case in panel 2, but for the skew case in panel 8. The spars typically result in buckling strength increases in the order of 1% and this is attributed to the spars applying rotational stiffness

- the tapered panel geometry over that of the skew panel.

With the exception of the boundary conditon cases with clamped longitudinal edges for panel 2, changing the geometric planform area from being rectangular manifests a buckling strength increase as does changing the skew planform to the actual, skew–tapered planform.

The exception to this is for the skew geometry of Panel 2, which has a higher buckling strength than the tapered configuration when the panel edges are clamped. The buckling strength increases attributed to the skew geometry over the tapered case is 1% (Case 4-4) or 3% (Case 1-4). These buckling strength increases are much smaller than the increases calculated when comparing rectangular and tapered or skew geometry. For case 4-1 the buckling strength increase of the tapered panel over the rectangular panel is over three times that of the skew panel over the tapered panel. For case 4-4 the buckling strength increase of the skew panel over the tapered panel is over eight times that of the tapered panel over the rectangular one.

8.7.4 Spars

The results of modelling the spars on the panel are presented and discussed in this section.

Table 8.10 shows the bucking predictions with: (1) a rectangular approximation of the shallow spar on both longitudinal panel edges; (2) a rectangular approximation of the deepest spar on both panel edges; and (c) rectangular approximations of the actual spars *i.e.* a deep central spar and shallow spar on the leading edge of the panel. The table shows an equivalent rotational restraint obtained from a cubic spline interpolation through the data presented in the bucking curves for boundary condition Case 2-1 (see Figures 8.7 and 8.8). In addition, the buckling stress increase of the panel because of rotational stiffness of the spar is shown as a proportion of the difference of the simply supported and fully clamped buckling load. This value more meaningfully represents the effect of the rotational stiffness of the spars on the buckling load of the panel. The buckling predictions are made by coupling only the rotational degrees of freedom at the spar/panel skin intersection so that the spars do not apply any in-plane restraint. Equations (8.5.2) show the rotational coupling which preserves an angle of 90° between the junction of the plate and spar. Initial tests confirmed that the in-plane restraint provided to the panel by the spars was considerable (if comparisons are made between the results presented in Table 8.10) and buckling predictions for the deepest spars were higher than those for the upper–bound buckling case (Case 4-1).

As a comparison with the work on unequal rotational edge restraint presented in Chapter 2, the arithmetic and the geometric mean of the buckling predictions for deep and shallow cases are calculated to see how

Table 8.9: Buckling load for upper– and lower– bound buckling predictions for Panels 2 and 8 with the three geometric configurations considered. Buckling strength differences are shown for skew and tapered geometries as a proportion of that over the rectangular buckling prediction

	Case			
	1-1	1-4	4-1	4-4
Rectangular (Datum)	7.301	8.305	7.833	8.805
Skew	7.619	8.681	8.588	9.577
Difference (%) (Skew/Rectangular)	*4.35*	*4.53*	*9.64*	*8.77*
Tapered	7.957	9.108	8.351	9.479
Difference (%) (Tapered/Rectangular)	*8.98*	*9.67*	*6.61*	*7.65*
Difference (%) (Tapered/Skew)	*4.43*	*4.91*	*-2.76*	*-1.03*

(a) Panel 2

	Case			
	1-1	1-4	4-1	4-4
Rectangular (Datum)	29.985	33.018	32.307	35.227
Skew	31.862	37.816	34.214	39.542
Difference (%) (Skew/Rectangular)	*6.26*	*14.53*	*9.64*	*8.77*
Tapered	34.401	40.571	36.121	42.741
Difference (%) (Tapered/Rectangular)	*14.73*	*22.88*	*11.81*	*21.33*
Difference (%) (Tapered/Skew)	*7.97*	*7.29*	*5.57*	*8.09*

(b) Panel 8

buckling load curves will be in the classic garland form. Hence, the Case 2-1 buckling curve must be located on the upward arc of a garland, whilst the Case 1-2 buckling curve must cut through this cusp if $\kappa < 600$ with the result that the Case 2-1 panel has a higher buckling load than the Case 1-2 panel in this region.

In addition to the unexpected trend in the buckling curves for the skew case of panel 2, the upper–bound (Case 4-4) buckling load of the skew panel is higher than of the tapered configuration. In both cases, the final buckling mode of the panels is the same. This results implies that the skew panel is stronger than the tapered panel when it has clamped edges. It is likely that this result is also a consequence of the aspect ratio of the skew panel being in the region of a cusp.

8.7.2 Panel 8

The buckling curves for Panel 8 in Figure 8.8 are more uniform and predicatable than those for panel 2. The curves for Panel 8 consistently show that there are buckling strength increases as the true geometry of the panels is more accurately modelled.

Similar observations about the general form of the curves can be made for panel 8. The lower-bound curve is that for the boundary condition in which rotational stiffness is increased along the longitudinal panel edge and the upper-bound curve is given for the boundary condition case in which rotational restraint is increased in magnitude along the transverse edges.

The spread of the curves is more variable in the panel 8 buckling curves compared with panel 2. This spread is due to the aspect ratio of the panels. Bucking strength versus aspect ratio curves given in chapter 4 clearly show that the difference between the buckling loads of simply supported and clamped plates varies with aspect ratio due to asynchronous change in the buckling modes.

8.7.3 Bucking strength increases

Table 8.9 quantifies the changes in buckling load for the upper– and lower– boundary conditions shown in the buckling curves.

The table shows the change in buckling strength of:

- the skew panel geometry over that of the rectangular panel;
- the tapered panel geometry over that of the rectangular panel and;

8.7 Discussion

8.7.1 Panel 2

Figure 8.7 shows the buckling curves for Panel 2. All three sets of curves have an ordinate with the same range and lower and upper values. For the simply supported boundary condition case it is immediately obvious that changing the panel geometry from being rectangular to the actual skew-tapered geometry via a skew geometry results in an increase in the buckling load of the panel. The buckling strength increases for this case are given in Table 8.9.

The buckling curves for the tapered and the rectangular curves are predictably bounded by curves for Case 2-1 (lower bound, bounded by Case 1-1 and 4-1) and Case 2-4 (upper-bound, bounded by Case 1-4 and Case 4-4). This implies that the boundary condition that has the greatest influence on the buckling load of the panels involves the transverse edge of the panel, and that the panel buckling load is least influenced by the boundary condition applied along the longitudinal panel edge. This is predicable because the panel has a much higher bending stiffness parallel to the longitudinal edge compared with that normal to it. For these geometric configurations, the buckling curves remain distinct and there is no crossing over. For the skew only case (Figure 8.7 part (b)), the curves are not so predicable. The buckling curves for boundary condition cases 1-2 and 2-1 cross over between $\kappa = 600 - 900$, with the lower–bound curve before $\kappa = 600$, being that for case 1-2 and after $\kappa = 900$ that for Case 1-2. The result of the cross-over is that for $\kappa \leq 600$, the lower-bound buckling curve is different from that for either the tapered or rectangular case. For $\kappa \geq 900$, the lower-bound curve is the same for the tapered and rectangular case. For the skew case, the buckling load for the skew plate case 4-1 (lower-bound) is higher than the same case for the tapered geometry, which, in turn is higher than for the rectangular geometry. In contrast, the Case 1-4 boundary condition is higher in the skew case than for the rectangular case, but lower than the tapered case. Boundary conditions Case 2-1 and 1-2 and Case 4-2 and 2-4 show markedly less difference than in the other geometric configurations.

The initial hypothesis for the crossing of the buckle curves in the skew configuration case is a change in bucking mode in the region $\kappa = 600 - 900$, however inspection of the buckling modes for the panels reveals that the buckling modes for all the analyses, not just the skew panels, are the same: an overall buckle, with one half-wavelength approximately the length of the panel. The crossing of the buckling curves and the relatively small difference in magnitude between boundary condition cases 2-4 and 4-2 and Cases 1-2 and 2-1 must relate to the aspect ratio of the panel. The panel must have an aspect ratio in the region where a buckling mode change takes place. Because the panels are orthotropic and skew, the aspect ratio versus

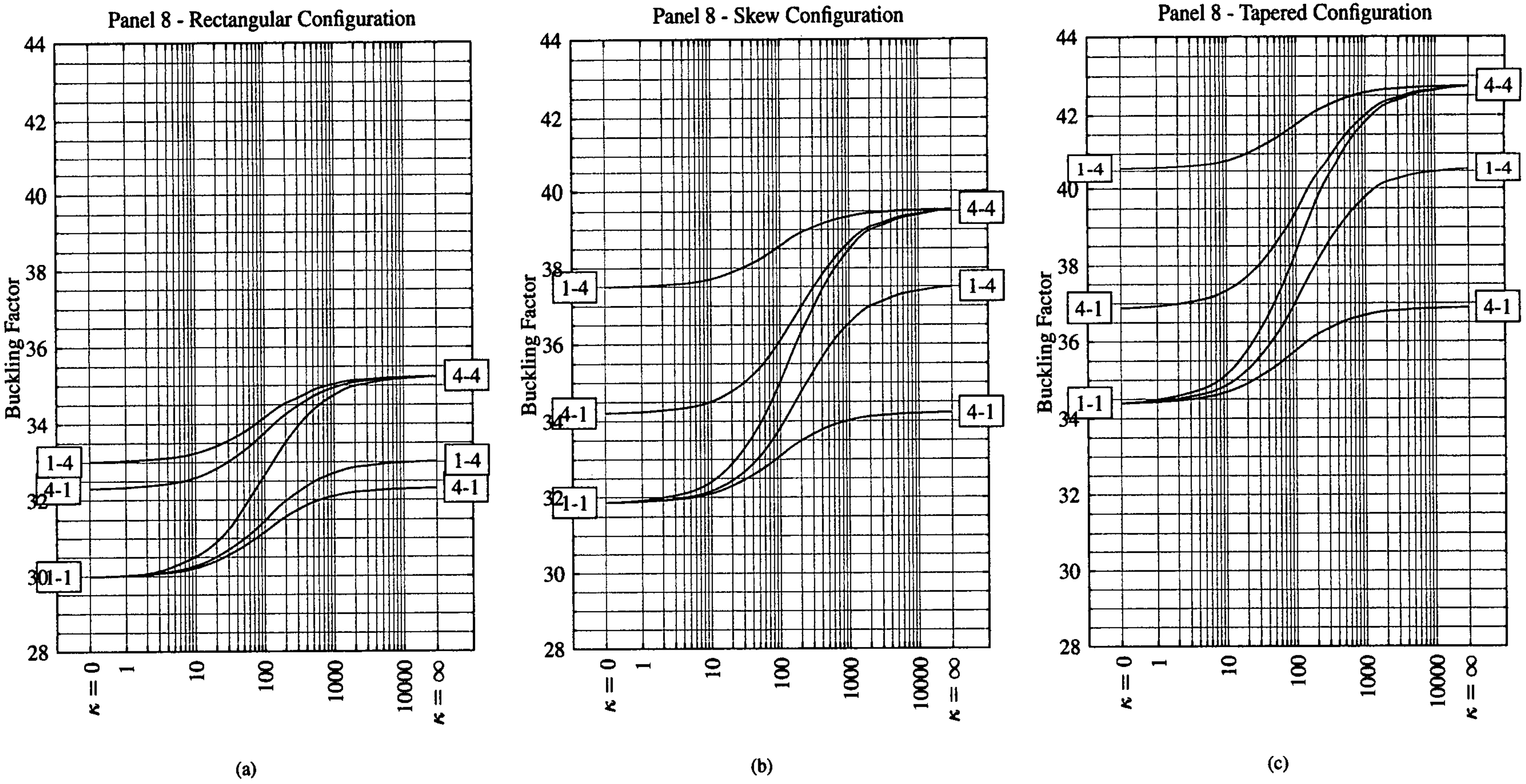

Figure 8.8: Buckling curves for Panel 8 showing buckling strength (ordinate) as a factor of the applied load of $100kN/m$ against rotational stiffness coefficient, κ (abscissa) defined in Eqn (8.1). The boxes at $\kappa = 0, \infty$, refer to the boundary condition giving lower- and upper-bound buckling loads for the panel which are combinations of simply supported and clamped supports. Each curve represents a separate boundary condition case, which can be identified by its lower- and upper-bound case. Case 1-2 is bounded by Case 1-1 and 1-4, Case 2-1 is bounded by Case 1-1 and Case 4-1, Case 2-2 is bounded by Case 1-1 and Case 4-4, Case 4-2 is bounded by Case 4-1 and 4-4 and Case 2-4 is bounded by Case 1-4 and 4-4.

Chapter 9

Conclusions

This chapter presents the conclusions of the presented work and gives recommendations for further investigations to complement it. A set of overall conclusions are presented which are taken from detailed conclusions of each chapter that follow.

9.1 Overall Concluding Remarks

The thesis has presented a large body of work dealing with the stability of quadrilateral plates and panels with geometries that have, until now, largely been ignored in the open literature even though they are frequently encountered in modern aerospace design.

The results show that making rectangular approximations of plates and panels leads to over–design for buckling failure and that by considering the actual planform geometry of plates, weight savings can potentially be made by considering thinner plates and panel stiffeners.

The thesis investigates the buckling strength of skew plates and panels following a logical progression from the effect of skew angle on the buckling load of a plate through to the effect of skew angle and planform taper on the buckling load on actual wing panels taken from an example aircraft wing.

The buckling load of skew plates is first considered. Because of the skew transverse edge of the panel, when a number of plates are continuous over a simple support, a rotational restraint arises along the skew edge and there is a corresponding increase in buckling load. The effect of this buckling strength increase for a plate infinite in length and/or width and split into equal skew bays has been compared with the increases in buckling load associated with isolated plates having discrete magnitudes of rotational restraint along their edges. The results show that continuity does not provide a single magnitude of rotational restraint along the plate edges, but that the magnitude of rotational restraint provided by a continuous support varies with aspect ratio. The variation in rotational restraint provided by continuity increases as the skew angle of the plate increases. Buckling predictions for continuous skew plates are obtained from a finite strip analysis (VICONOPT) from the open literature and buckling predictions for isolated plates with varying degrees of rotational restraint along the edges from a finite element analysis.

Plate buckling results are presented in terms of a constant planform area to compare the buckling strength changes as a direct consequence of a change in skew angle. The buckling strength of skew plates is not often presented in these terms and as a consequence buckling strength changes as a result of skew angle appear higher than they actually are. The buckling curves show that for varying magnitudes of rotational restraint applied along the plates edges, there are instances where an increase in skew angle doesn't manifest a buckling strength increase. These instances occur when a peak on one buckling curve coincides with a trough on the buckling curve for a plate with a higher skew angle. The results show the importance of correctly assessing rotational stiffness applied to a plate and using the correct plate geometry in predicting its buckling load.

The continuous analysis is verified using a finite element analysis, but is restricted in accuracy because a limitation is placed on the number of identical bays over which a buckling mode can repeat. The maximum number of identical bays over which this mode may repeat is restricted to five. The finite strip (VICONOPT) method solution accounts for continuity over an infinite number of bays and so the finite element buckling predictions are upper–bound solutions to the continuous analysis except when the number of bays modelled coincides with the number of bays over which the buckling mode repeats. In this latter case, the finite element buckling prediction is exact in the sense that the solution to the problem is modelled exactly. The results from the finite element analysis closely match those obtained from the finite strip method with greater errors bing observed for plates with higher skew angles. The finite element analysis suggested that when a plate was considered to be infinite in breadth as well as length (bi-axial continiuty) the applied assumption that the transverse buckling mode has a half-wavelength equal to the plate breadth and therefore repeats over two transverse bays is not correct for skew plates. This finding was verified by repeating the published VICONOPT analysis.

Making the incorrect assumption that the plate buckling mode repeats over no more than 2 transverse bays leads, in the most extreme case (that for $\alpha = 30°$, $a/b = 2.0$), the buckling strength is over estimated by 9%. This will result in 'unsafe' design. The study highlights the importance of rechecking buckling assumptions made and verified using rectangular plates and/or panels and adopting them for skew plates.

The effect of skew angle on the buckling strength of plates is extended to consider the effect of skew on stiffened plates. Panels made from an isotropic material are considered and are therefore generally orthotropic. The orthotropy of the plate is a direct consequence of the geometry of its cross–section. Buckling strength curves relating the effect of increasing orthotropy, aspect ratio and skew angle of the plate are presented. A smeared stiffener model of the panel is derived and accurately predicts the buckling load of the panel when the buckling modes are the same *i.e.* of an overall type.

The planform taper on skew and rectangular plates is considered next. Many skew aircraft wing panels taper from root to tip and this is an especially common geometry found on modern aircraft. A set of comprehensive buckling curves is presented showing critical buckling load for a given aspect ratio for different magnitudes of taper. The effect of taper on the buckling load of the plates is seen to have a greater effect when the aspect ratio of the plates is greater than one. This is attributed to the diminishing effect of the transverse edge boundary conditon or geometry and increased influence of the longitudinal edge. The effect of taper is seen to increase the buckling strength of plates that have high aspect ratios (a/b=20). For plates with parallel longitudinal edges and skew transverse edges, the buckling load of the plates has converged onto that for a rectangular plate. The results suggest that by taking into account taper at the design stage, greater economy can be had than by considering an isolated an isolated skew plate if it has a large enough aspect ratio. Using a skew or tapered planform geometry to gain maximum economy is dependant on the aspect ratio of the panel.

The findings of the previous work are combined in the chapter eight. This chapter considers the effect of the planform geometry on the buckling load of a number of optimised panels taken from the open literature. Buckling predictions are calculated for the panels assuming simply supported boundary conditions for rectangular and skew approximations and compared with the buckling strength of the actual wing panel which is skew and tapered. The results show that for the simply supported cases, the buckling predictions follow the findings in the thesis that the buckling strength of the panels increases as the actual planform geometry of the panels are calculated from rectangular to skew to skew tapered. The panels show similar increases in buckling strength moving from the rectangular to the skew and the skew to skew–tapered planform areas.

Rotational stiffness applied along the panel edges to approximate the effect of a supporting spar, rib or stiffener, highlights the importance of using the correct planform geometry for panel design. In the case of the panel with the highest aspect ratio, a skew clamped panel was found to have a higher buckling strength than the skew–tapered panel.

More specific conclusions from each chapter are presented in the remainder of the chapter.

9.2 Chapter 4 – The buckling strength of uni-axial compression loaded skew plates with elastic rotational restraint

A comprehensive set of buckling curves has been presented for the buckling assessment of isotropic skew plates under uniform, uni-axial, compression load. The new curves illustrate the changes in buckling strength arising from the addition of symmetric combinations of elastic edge restraints against rotation for a wide range of aspect ratios and skew angles.

The new curves provide a greater insight into the buckling behaviour of skew plates and continuous structures. They permit a more appropriate choice of aspect ratio to exploit strength gains when elastic restraint against rotation or continuity exists in a structure, which could otherwise not be used to advantage, because the information is unavailable in the open literature.

The buckling curves have also, as is rarely the case, been presented in terms of maintaining a constant planform area independent of the skew angle of the plate. The results allow the comparison of buckling strength between plates as a result of skew angle. The results show that buckling strength gains are not as great as the often used presentation of analyses suggests.

Finally, the buckling predictions obtained for skew plates with equal magnitudes of elastic rotational restraint applied along the longitudinal plate edges are used to assess the accuracy of predicting buckling loads of plates having unequal values of elastic restraint applied along the longitudinal edges. The results suggest that good buckling predictions can be made using the approximations.

9.3 Chapter 5 – Elastic buckling of continuous skew plates

This chapter presents analysis of continuous skew plates and compares the finite element solution with that of VICON.

The finite element solution and continuous VICONOPT solution agree well over the range of aspect ratios and skew angles considered in the study. There is a larger margin of difference as the skew angle increases and when bi-axial continuity is considered, as these boundary conditions give rise to complex buckle modes which may repeat over many bays more than was used in the finite element analysis. The VICON predictions consider buckling repetition over an infinite number of bays compared with the finite element which considers plate arrays of up to five bays.

The buckling predictions for bi-axial continuity for $\alpha = 30°$ show that the assumption that buckle modes repeat over no more than two transverse bays used in the published VICONOPT solutions is not correct. Transverse repetition over more than 2 bays needs to be considered. This was proved using the finite element buckling predictions in which plate arrays with more than two transverse bays produced buckling loads upto 9% lower than predicted using VICONOPT. The finite element solutions were verified by rerunning the VICONOPT analysis with a greater range of transverse half-wavelengths.

9.4 Chapter 6 – Orthotropic stiffened skew plates and panels

This chapter presents a comprehensive study on the critical buckling load of skew, stiffened panels. The study considers the effect of aspect ratio, stiffener depth and edge boundary conditon on benchmark panels, originally presented by Stroud *et al.* [85], that are made skew.

The benchmark panels are square and these panels are analysed using ABAQUS finite element code and compared against other results in the open literature as a verification exercise. The results also provide a further set of buckling predictions.

Two of the aluminium, blade stiffened benchmark panels are investigated further and buckling curves are drawn showing the relationship between panel buckling and aspect ratio as the depth of the stiffeners on the benchmark panel increase. The buckling curves identify the critical aspect ratios at which local buckling mode failure is superceded by an 'overall' mode. Both boundary conditons of all edges simply supported and all edges fully clamped are considered in the study to give upper– and lower– buckling loads for the panels.

An equivalent 'smeared stiffener' model of the benchmark panels is presented. The smeared stiffener model gives very accurate buckling predictions for a panel that is simply supported along all edges when the mode of failure of the panel and 'smeared stiffener' plate are the same (*i.e.* of the overall type). The smeared stiffener model does not produce good buckling predictions for the panel when its edges are fully clamped. In this case, the plate model overestimates the buckling load of the plate. This overestimation is explained by a difference in edge boundary conditon between the two structures.

The buckling strength increase of a skew panel over an equivalent rectangular panel is calculated using the 'smeared stiffener' models for the simply supported boundary conditon. The comparisons show that when $\alpha = 45°$, the buckling strength advantages of considering skew planform geometry can be as high as 10%. The comparison shows that there are potentially economic savings to be made by considering the skew planform geometry of a panel at the design stage rather than making a crude rectangular approximation.

At low aspect ratios, when the buckling strength of the panel skin governs the critical buckling load of the panels (*i.e.* a local buckling mode), skew edges do not result in significant buckling strength increases. Instead, the buckling strength of the panel skin is governed by the torsional stiffness of the stiffener which is effectively applying a rotational restraint along the longitudinal edges of the plate running between the stiffeners.

The effect that skew has on the buckling loads of skew panels is extended in chapter 8 to include the effects of a planform taper.

9.5 Chapter 7 – Buckling of isotropic skew plates tapered in planform

The chapter presents a detailed study on the linear-elastic buckling strength of thin plates tapered in planform and extends the currently limited knowledge of their behaviour. The results are presented as a series of buckling curves showing the relationship between plate buckling strength and plate aspect ratio.

The study shows that the buckling strength of plates that are tapered in planform are significantly stronger than a rectangular plate with the same aspect ratio. These strength gains are prominent not only over a small range of aspect ratios as is the case of skew plates, but also over much higher aspect ratios because the geometry of the longitudinal plate edge is changed. At the highest aspect ratios ($a/b_1 = 20$) in the study, there are significant strength gains over an equivalent rectangular or skew plate. These gains are as high as 15% when $\beta = 0.4$.

The buckling strength increase curves have shown that when the aspect ratio of a plate is small (less than one), buckling strength increases are largely the result of a skew tranverse edge. For aspect ratios higher than one, buckling strength increases are attributed to the tapered longitudinal edges. This is a significant observation because in practice wing panels and plates will typically have aspect ratio higher than one.

The buckling curves for the tapered plates are very different in appearance than for a skew or rectangular plate with equivalent aspect ratio. The study proves that the existence of cusps arising from clear and distinct buckle mode changes do not occur in the case of plates that are tapered. The narrowed edge of the plate restricts buckling deflection, with the result that the mode change is forced to occur gradually as the plate aspect ratio increases and that where cusps would be expected to form in the case of rectangular and skew plates, now smoothly defined peak occurs. These peaks decrease in magnitude both with an increase in aspect ratio and also as the taper of the plate increases. This latter observation leads to very smooth buckle curves for plates at very high taper.

Making simplifying assumptions as to the geometry of plates when designing them, for example by assuming that they are rectangular when they are in fact tapered, can lead to large strength advantages being disregarded. For the tapered plates considered in the chapter a 60% increase in buckling strength is attributed to taper for a plate with $\alpha = 45°$ and aspect ratio, $a/b_1 = 2.5$ (Figure 7.17 (d)).

The results of making simplifying assumptions is discussed in the following chapter where the work contained in this chapter is extended to cover composite laminated panels and an example is used to quantify possible strength advantages of using the correct geometry to design wing panels.

9.6 Chapter 8 – Skew-tapered panels in a swept aircraft

A study has been presented in which panels from a practical wing have been evaluated as if they were: rectangular; skew and; skew and tapered in planform. The skew and tapered planform geometry is the actual geometry of the panel.

Buckling curves for the panels are produced and relate the buckling strength of the panels as the panel edges are rotationally restrained by applying increasing magnitudes of rotational stiffness along opposite edge of the panels. The results of the study show that buckling strength increases occur as the planform geometry of the plate approaches that of the actual planform geometry of the plate used in the aircraft wing.

The study shows that making simplifying assumptions about the geometry of the wing panels leads to uneconomic design. In the most extreme cases, a skew tapered panel has a buckling strength greater than its rectangular equivalent. By taking the more complex planform geometry into account at the design stage, these buckling strength increases potentially lead to weight savings, by permitting a reduction in skin and stiffener thicknesses.

The study also highlights the importance of using the true panel planform geometry because the simplifying assumption of using skew panels as opposed to skew and tapered assumptions in the case of panel 2 analysis lead to buckling predictions that were not foreseeable – the upper-bound (*i.e.* panels with clamped edges) results for panel 2 for the skew panel gave higher buckling predictions that the analysis of the true wing geometry. It can be concluded that improving on the rectangular approximation of a panel and designing it as being skew will lead to 'unsafe' design for this boundary condition.

The effect of the spar using the physical properties given in York [117] on the buckling load of the panels was found to impart some buckling resistance to the panel. In the most extreme cases, the deepest spars increased the buckling strength of the panel to 20% of the difference between the simply supported and fully clamped cases.

9.7 Discussion of the current eigenvalue buckling predictions in the context of post-buckling anaylsis of plates

It is well known that plates and panels can carry loads higher than the elastic buckling stresses predicted using an eigenvalue analysis. The buckling load predicted using an eigenvalue analysis represents the point on a load-deflection curve at which the initially flat plate deflects into its undevelopable buckled shape to maintain equilibrium. This is accompanied by an effective loss of stiffness of the plate and change in stress state. On the load-deflection curve, this bifurcation point appears as a sharp 'knee' (see Figure 2.12 and 9.1) at a stress equivalent to that calculated using the eigenvalue analysis *i.e.* $\sigma_{cr} = (k\pi^2 D)/(b^2 t)$ and a strain of $\epsilon_{cr} = (k\pi^2 t^2)/(12(1-\nu^2)b^2)$ where the k is the critical buckling coefficient of the plate used to present buckling results throughout the thesis. The results presented in this thesis therefore represent the critical loading when plate equilibrium is no longer satisfied when it is flat but deflected (*i.e.* in its buckled form). Loading past this (bifurcation) point causes tensile membrane stresses to develop [61] which stabilise the plate and give the plate its post-buckling strength. In addition, when plates have high aspect ratios, it is commonly found [81, 82] that they undergo buckling mode changes in the post buckling regime resulting in 'snap-through' phenomenon. The ultimate limit load of the plate is reached when the plate looses its stiffness as a result of instability and material yielding.

Section 2.7.2, which gives an example of the initial post-buckling reserve strength of a square plate together with a brief description of the relevant theory, and shows that the initial post-buckling response of thin-plates, unlike shells is generally stable.

9.7.1 Geometric imperfections

Manufacturing techniques often introduce geometric imperfections in plates that mean they are not perfectly flat. Under a uni-axial in-plane loading, this will cause the plate to behave in a less stiff manner than if it was perfectly flat. The imperfections will cause bending stresses to develop from the onset of loading. For small deflections (those having a magnitude less then the plate thickness), load-displacement curve for the imperfect plate will differ from the perfectly plate by describing a far more rounded knee inside the curve for the perfect plate. As the magnitude of an imperfection becomes larger the knee of the curve becomes increasingly rounded until it is indistinguishable. The imperfection causes larger bending and membrane stresses to form at lower loads than for the perfect plate and consequently the ultimate failure load for a perfect plate is higher than for an imperfect one [62, 61].

Because of the lack of reliable data on manufacturing imperfection data, they are often described as magnitudes of the first eigenmodes for the structure [31].

Figure 9.1 shows sketches of load/deflection curves and the post-buckling regimes for four representative cases: perfectly flat plate made from an elastic material; a perfectly flat plate in which the material is yielding; a plate with a small imperfection (of a magnitude less than that of the plate thickness; and a plate with a larger imperfection (of magnitude in the order of that of the plate thickness). The curve for the perfectly flat plate clearly shows the buckling load predicted by the eigenvalue analysis (EV) as the sharp knee when the longitudinal strain $\epsilon/\epsilon_{cr} = 1$ and the applied load $\sigma/\sigma_{cr} = 1$.

9.8 Recommendations for further work

The studies have amassed a large body of work dealing with elastic buckling of skew plates and panels and has only considered orthogonal uni-axial compression loading on the basis that this loading is generally that used for design purposes. The effect of shearing loads on the critical buckling loads of skew plates, has been considered in the literature, but there is little information on the interaction between in-plane compression loads and shear, nor does there seem much agreement on which is the correct buckle load for these shear loaded cases because a large range of buckling values are presented. It is also of interest to see how loads will be redistributed throughout a swept-back wing structure, once a panel or plate has buckled; a structure may well be able to carry more loading than the individual buckling load of the weakest panel because of load redistribution.

Very little work on the stability of skew plates outwith the elastic buckling range has been undertaken and

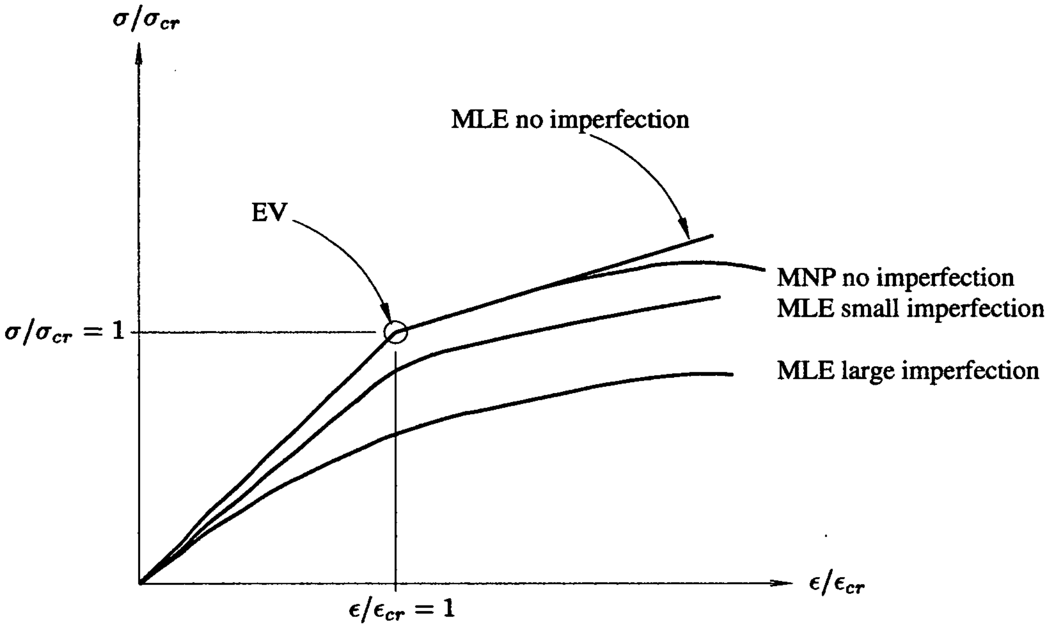

Figure 9.1: Sketches of load/end-shortening curves for a plate for four cases: "MLE no imperfection" a perfectly flat plate made from a linear elastic material with no yield point (MLE = linear elastic material); "MNP no imperfection" a perfectly flat plate made from a material with a definite yield point (MNP = nonlinear plastic material); "MLE small imperfection" a plate with a small imperfection of magnitude less than the thickness of the plate made from an elastic material with no yield point; and "MLE large imperfection" a plate with an imperfection of magnitude in the order of the plate thickness made from a linear elastic material with no yield point. The abscissa of the graph shows the end–shortening of the plate normalised to that of the linear elastic (eigenvalue) buckling prediction and the ordinate, the applied loading normalised with respect to the critical linear elastic (eigenvalue) buckling load of the plate. The eigenvalue buckling prediction (EV) lies at $\epsilon/\epsilon_{cr} = 1$ and $\sigma/\sigma_{cr} = 1$.

that that has, has considered only large deflection analysis of plates *i.e.* analysis only valid initially after the elastic buckling limit has been reached. Preliminary explorations in this area, to determine the ultimate load carrying capacity of thin plates by the author have suggested that the behaviour of skew plates past the initial buckling load is significantly different to that of square and rectangular plates. Additionally, although the effect on initial imperfections caused by manufacturing tolerances is at least partially understood and accounted for in structural engineering codes for rectangular plates, it is not known how these will affect the buckling capacity of skew plates.

Investigations into the post buckling behaviour of plates to determine the ultimate carrying load of skew plates should also be accompanied by experimental work with which to validate it. In fact there has, to the author's knowledge, been no experimental work on the behaviour of skew plates, although Young and Hyer [119] conducted an experimental investigation into a composite plate with a skew stiffener. In addition, the entire range of buckling solutions for skew plates and panels need to be verified experimentally.

Appendix A

ABAQUS elements

This appendix briefly describes the elements used in the studies presented in the thesis. A more in depth account of the element derivation is given in reference [3]. Two types of shell elements are used, ABAQUS type S8R5 (Chapters 4, 5, 7 and 8) and ABAQUS type S4R (chapter 6). The latter element was used for the stiffened panel analysis because the execution time was less than that of the S8R5, the use of which became prohibitive when dealing with the large meshes and obtaining a large number of results.

A.1 ABAQUS type S8R5 element

ABAQUS type S8R5 element is an eight-noded, quadrilateral, small strain, thin-shell element with five degrees-of-freedom at each node. Reduced integration is used. The element is shown in Figure A.1. Not being shear deformable, the element is only suitable for thin-shell and/or plate analysis.

Second-order, quadratic serendipty type shape functions are used and define a nodal quantity, N_i, at an element node, i shown in Figure A.1 by [120]:

for corner nodes ($i = 1, 2, 3$ or 4)

$$N_i = [(1 + \xi\xi_i)(1 + \eta\eta_i)(\eta\eta_i + \xi\xi_i - 1)]/4$$

for mid-side nodes when $\xi_i = 0$ *i.e.* when $i = 5$ or 7

$$N_i = [(1 + \eta\eta_i)(1 - \xi^2)]/2$$

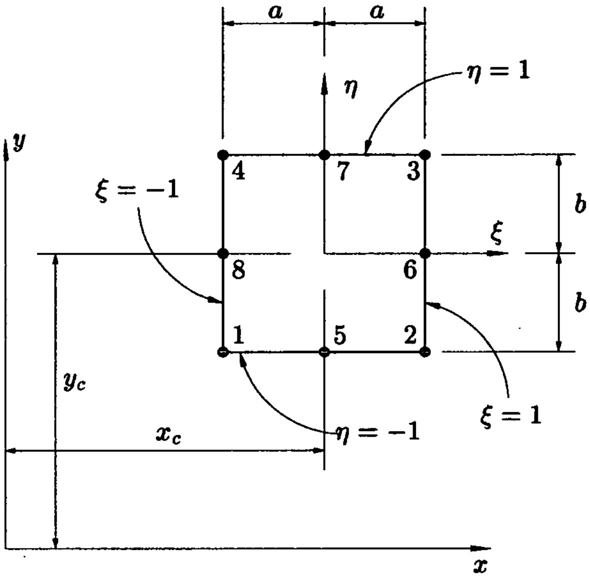

Figure A.1: ABAQUS type S8R5 element.

and for mid-side nodes when $\eta_i = 0$ *i.e.* when $i = 6$ or 8

$$N_i = [(1 - \eta^2)(1 + \xi\xi_i)]/2$$

where η_i and ξ_i are the local coordinates of node i.

A.2 ABAQUS type S4R

The ABAQUS type S4R element is a four–noded element described as a 'general purpose' element [3]. The elements provide robust and accurate solutions for 'thick' and 'thin' plate problems, hence the element numerically satisfies the Kirchoff–Love hypothesis as the thickness of the plate decreases. The elements use a through-thickness interpolation scheme that is not susceptable to 'shear–locking'. In the context of the thesis, the panels analysed are sufficiently thin that a 'thin-plate' solution is obtained. The S4R element uses bi-linear shape functions and reduced integration.

The element is sketched in Figure A.2 and bi-linear shape functions presented below for completeness.

A nodal quantity, N_i, using bi-linear shape functions is given by [120]:

$$N_i = [(1 + \eta\eta_i)(1 + \xi\xi_i)]/4$$

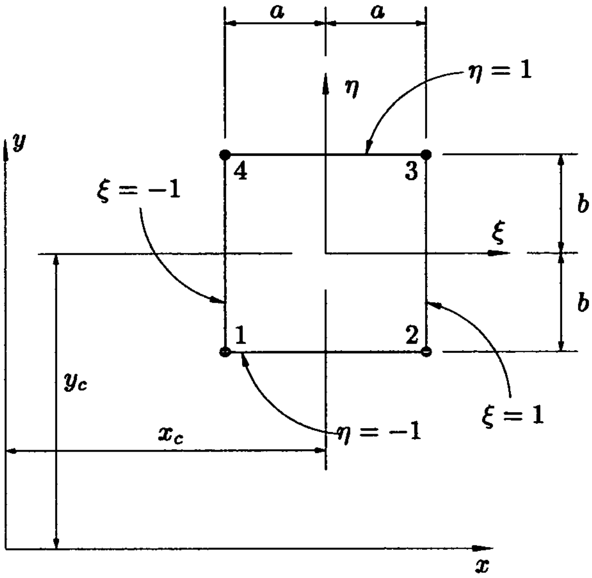

Figure A.2: ABAQUS type S4R element.

where η_i and ξ_i are the local coordinates of node i.

Appendix B

Tabulated values for plates with unsymmetrical boundary conditons

κ	0	0.4	1	2	4	10	20	100	1000	10000	∞
0	4.0000	4.0139	4.0358	4.0707	4.1364	4.3061	4.5217	5.1884	5.6617	5.7304	5.7384
0.4	4.0154 *0.03*	4.0307	4.0537	4.0894	4.1558	4.3263	4.5425	5.2110	5.6858	5.7547	5.7627
1	4.0390 *0.08*	4.0544 *0.02*	4.0780	4.1152	4.1830	4.3551	4.5725	5.2439	5.7210	5.7903	5.7983
2	4.0772 *0.16*	4.0926 *0.08*	4.1162 *0.02*	4.1544	4.2247	4.4001	4.6199	5.2966	5.7775	5.8473	5.8555
4	4.1496 *0.32*	4.1649 *0.22*	4.1886 *0.13*	4.2268 *0.05*	4.2991	4.4811	4.7061	5.3943	5.8830	5.9540	5.9623
10	4.3391 *0.77*	4.3545 *0.65*	4.3781 *0.53*	4.4163 *0.37*	4.4887 *0.17*	4.6782	4.9176	5.6399	6.1517	6.2262	6.2349
20	4.5872 *1.45*	4.6025 *1.32*	4.6262 *1.17*	4.6644 *0.96*	4.7367 *0.65*	4.9263 *0.18*	5.1743	5.9440	6.4895	6.5691	6.5783
100	5.4367 *4.79*	5.4521 *4.63*	5.4757 *4.42*	5.5139 *4.1*	5.5863 *3.56*	5.7758 *2.41*	6.0239 *1.34*	6.8734	7.3132	7.3537	7.3586
1000	5.7925 *2.31*	5.8079 *2.15*	5.8315 *1.93*	5.8697 *1.6*	5.9421 *1.*	6.1316 *-0.33*	6.3797 *-1.69*	7.2292 *-1.15*	7.5850	7.6308	7.636
10000	5.8387 *1.89*	5.8541 *1.73*	5.8777 *1.51*	5.9159 *1.17*	5.9883 *0.58*	6.1778 *-0.78*	6.4259 *-2.18*	7.2754 *-1.07*	7.6312 *0.01*	7.6775	7.683
∞	5.8443 *1.85*	5.8597 *1.68*	5.8833 *1.47*	5.9215 *1.13*	5.9939 *0.53*	6.1834 *-0.83*	6.4315 *-2.23*	7.2810 *-1.05*	7.6368 *0.01*	7.6830 *0.00*	7.6886

Table B.1: Buckling factor for 0° Arithmetic Mean Approximation, $a/b = 1.0$. The difference between the actual and approximate solution is given in italics. A negative difference infers that the approximate solution underestimates the correct solution

κ	0	0.4	1	2	4	10	20	100	1000	10000	∞
0	4.1019	4.1166	4.1376	4.1711	4.2342	4.3968	4.6029	5.2384	5.6929	5.7596	5.7674
0.4	4.1173 *0.02*	4.1326	4.1546	4.1890	4.2527	4.4160	4.6227	5.2599	5.7159	5.7829	5.7907
1	4.1399 *0.06*	4.1553 *0.02*	4.1779	4.2135	4.2786	4.4435	4.6513	5.2914	5.7496	5.8168	5.8247
2	4.1765 *0.13*	4.1918 *0.07*	4.2145 *0.02*	4.2510	4.3184	4.4864	4.6965	5.3417	5.8035	5.8714	5.8793
4	4.2457 *0.27*	4.2611 *0.20*	4.2837 *0.12*	4.3203 *0.04*	4.3895	4.5638	4.7789	5.4351	5.9044	5.9734	5.9814
10	4.4271 *0.69*	4.4424 *0.60*	4.4651 *0.48*	4.5016 *0.34*	4.5709 *0.15*	4.7522	4.9810	5.6699	6.1613	6.2336	6.2420
20	4.6641 *1.33*	4.6794 *1.23*	4.7021 *1.09*	4.7386 *0.9*	4.8079 *0.61*	4.9892 *0.16*	5.2262	5.9604	6.4839	6.5610	6.5700
100	5.4744 *4.51*	5.4898 *4.37*	5.5124 *4.18*	5.5490 *3.88*	5.6182 *3.37*	5.7996 *2.29*	6.0366 *1.28*	6.8469	7.4909	7.5826	7.5925
1000	5.9715 *4.89*	5.9868 *4.74*	6.0095 *4.52*	6.0460 *4.18*	6.1153 *3.57*	6.2966 *2.2*	6.5336 *0.77*	7.3440 *-1.96*	7.8411	7.8853	7.8906
10000	6.0162 *4.45*	6.0315 *4.30*	6.0542 *4.08*	6.0907 *3.74*	6.1600 *3.12*	6.3413 *1.73*	6.5783 *0.26*	7.3887 *-2.56*	7.8857 *0.01*	7.9304	7.9358
∞	6.0216 *4.41*	6.0369 *4.25*	6.0596 *4.03*	6.0961 *3.69*	6.1654 *3.07*	6.3467 *1.68*	6.5837 *0.21*	7.3941 *-2.61*	7.8911 *0.01*	7.9358 *0.00*	7.9412

Table B.2: Buckling factor for 15° Arithmetic Mean Approximation, $a/b = 1.0$. The difference between the actual and approximate solution is given in italics. A negative difference infers that the approximate solution underestimates the correct solution

κ	0	0.4	1	2	4	10	20	100	1000	10000	∞
0	4.5134	4.5259	4.5437	4.5723	4.6259	4.7631	4.9356	5.4645	5.8533	5.9126	5.9196
0.4	4.5264 *0.01*	4.5393	4.5578	4.5870	4.6410	4.7789	4.9519	5.4823	5.8724	5.9319	5.9389
1	4.5454 *0.04*	4.5583 *0.01*	4.5773	4.6074	4.6624	4.8015	4.9755	5.5084	5.9004	5.9602	5.9673
2	4.5761 *0.08*	4.5890 *0.04*	4.6080 *0.01*	4.6387	4.6954	4.8369	5.0127	5.5500	5.9453	6.0057	6.0128
4	4.6342 *0.18*	4.6471 *0.13*	4.6661 *0.08*	4.6968 *0.03*	4.7549	4.9012	5.0810	5.6273	6.0292	6.0906	6.0978
10	4.7859 *0.48*	4.7988 *0.42*	4.8178 *0.34*	4.8485 *0.24*	4.9066 *0.11*	5.0583	5.2490	5.8219	6.2425	6.3070	6.3146
20	4.9831 *0.96*	4.9960 *0.89*	5.0150 *0.79*	5.0457 *0.66*	5.1038 *0.45*	5.2555 *0.12*	5.4527	6.0620	6.5094	6.5781	6.5861
100	5.6527 *3.44*	5.6656 *3.34*	5.6846 *3.20*	5.7153 *2.98*	5.7734 *2.60*	5.9251 *1.77*	6.1223 *0.99*	6.7919	7.3376	7.4221	7.4321
1000	6.2420 *6.64*	6.2550 *6.52*	6.2740 *6.33*	6.3047 *6.05*	6.3628 *5.53*	6.5145 *4.36*	6.7117 *3.11*	7.3813 *0.60*	7.9706	8.0696	8.0812
10000	6.3421 *7.27*	6.3551 *7.13*	6.3741 *6.94*	6.4048 *6.65*	6.4629 *6.11*	6.6146 *4.88*	6.8118 *3.55*	7.4814 *0.80*	8.0708 *0.01*	8.1709	8.1828
∞	6.3541 *7.34*	6.3671 *7.21*	6.3861 *7.02*	6.4168 *6.72*	6.4749 *6.18*	6.6266 *4.94*	6.8238 *3.61*	7.4934 *0.82*	8.0827 *0.02*	8.1828 *0.00*	8.1948

Table B.3: Buckling factor for 30° Arithmetic Mean Approximation, $a/b = 1.0$. The difference between the actual and approximate solution is given in italics. A negative difference infers that the approximate solution underestimates the correct solution

κ	0	0.4	1	2	4	10	20	100	1000	10000	∞
0	5.9451	5.9528	5.9639	5.9817	6.0148	6.0985	6.2019	6.5144	6.8005	6.7957	6.8005
0.4	5.9530 *0.00*	5.9608	5.9721	5.9901	6.0234	6.1075	6.2112	6.5247	6.7668	6.8071	6.8120
1	5.9645 *0.01*	5.9723 *0.00*	5.9838	6.0021	6.0358	6.1205	6.2248	6.5399	6.7833	6.8239	6.8288
2	5.9830 *0.02*	5.9909 *0.01*	6.0024 *0.00*	6.0209	6.0553	6.1411	6.2463	6.5641	6.8098	6.8507	6.8557
4	6.0180 *0.05*	6.0258 *0.04*	6.0373 *0.02*	6.0559 *0.01*	6.0908	6.1787	6.2860	6.6090	6.8591	6.9008	6.9059
10	6.1084 *0.16*	6.1162 *0.14*	6.1277 *0.12*	6.1463 *0.08*	6.1812 *0.04*	6.2716	6.3843	6.7220	6.9839	7.0277	7.0330
20	6.2244 *0.36*	6.2323 *0.34*	6.2438 *0.30*	6.2623 *0.26*	6.2973 *0.18*	6.3877 *0.05*	6.5037	6.8608	7.1385	7.1851	7.1907
100	6.6135 *1.52*	6.6213 *1.48*	6.6328 *1.42*	6.6514 *1.33*	6.6863 *1.17*	6.7767 *0.81*	6.8928 *0.47*	7.2818	7.6141	7.6702	7.6770
1000	6.9700 *2.49*	6.9779 *3.12*	6.9894 *3.04*	7.0079 *2.91*	7.0429 *2.68*	7.1333 *2.14*	7.2493 *1.55*	7.6384 *0.32*	7.9949	8.0594	8.0672
10000	7.0352 *3.52*	7.0431 *3.47*	7.0546 *3.38*	7.0731 *3.25*	7.1081 *3.00*	7.1985 *2.43*	7.3145 *1.80*	7.7036 *0.43*	8.0601 *0.01*	8.1253	8.1333
∞	7.0432 *3.57*	7.0511 *3.51*	7.0626 *3.42*	7.0811 *3.29*	7.1161 *3.04*	7.2065 *2.47*	7.3225 *1.83*	7.7116 *0.45*	8.0681 *0.01*	8.1333 *0.00*	8.1413

Table B.4: Buckling factor for 45° Arithmetic Mean Approximation, $a/b = 1.0$. The difference between the actual and approximate solution is given in italics. A negative difference infers that the approximate solution underestimates the correct solution

κ	0	0.4	1	2	4	10	20	100	1000	10000	∞
0	4.0000	4.0139	4.0358	4.0707	4.1364	4.3061	4.5217	5.1884	5.6617	5.7304	5.7384
0.4	4.0153 *0.03*	4.0307	4.0537	4.0894	4.1558	4.3263	4.5425	5.2110	5.6858	5.7547	5.7627
1	4.0388 *0.08*	4.0543 *0.02*	4.0780	4.1152	4.1830	4.3551	4.5725	5.2439	5.7210	5.7903	5.7983
2	4.0765 *0.14*	4.0921 *0.06*	4.1160 *0.02*	4.1544	4.2247	4.4001	4.6199	5.2966	5.7775	5.8473	5.8555
4	4.1469 *0.25*	4.1627 *0.17*	4.1871 *0.10*	4.2261 *0.03*	4.2991	4.4811	4.7061	5.3943	5.8830	5.9540	5.9623
10	4.3258 *0.46*	4.3424 *0.37*	4.3678 *0.29*	4.4085 *0.19*	4.4846 *0.08*	4.6782	4.9176	5.6399	6.1517	6.2262	6.2349
20	4.5494 *0.61*	4.5668 *0.54*	4.5936 *0.46*	4.6364 *0.36*	4.7164 *0.22*	4.9200 *0.05*	5.1743	5.9440	6.4895	6.5691	6.5783
100	5.2434 *1.06*	5.2635 *1.01*	5.2943 *0.96*	5.3437 *0.89*	5.4359 *0.77*	5.6706 *0.54*	5.9636 *0.33*	6.8734	7.3132	7.3537	7.3586
1000	5.5082 *-2.71*	5.5293 *-2.75*	5.5616 *-2.79*	5.6135 *-2.84*	5.7104 *-2.93*	5.9569 *-3.17*	6.2648 *-3.46*	7.2204 *-1.27*	7.5850	7.6308	7.6362
10000	5.5416 *-3.29*	5.5629 *-3.33*	5.5954 *-3.37*	5.6476 *-3.42*	5.7451 *-3.51*	5.9931 *-3.75*	6.3028 *-4.05*	7.2643 *-1.22*	7.6311 *0.00*	7.6775	7.6830
∞	5.5457 *-3.36*	5.5669 *-3.40*	5.5995 *-3.43*	5.6517 *-3.48*	5.7493 *-3.57*	5.9974 *-3.81*	6.3074 *-4.12*	7.2696 *-1.21*	7.6366 *0.01*	7.6830 *0.00*	7.6886

Table B.5: Buckling factor for 0° Geometric Mean Approximation, $a/b = 1.0$. The difference between the actual and approximate solution is given in italics. A negative difference infers that the approximate solution underestimates the correct solution

κ	0	0.4	1	2	4	10	20	100	1000	10000	∞
0	4.1019	4.1166	4.1376	4.1711	4.2342	4.3968	4.6029	5.2384	5.6929	5.7596	5.7674
0.4	4.1172 *0.02*	4.1326	4.1546	4.1890	4.2527	4.4160	4.6227	5.2599	5.7159	5.7829	5.7907
1	4.1397 *0.05*	4.1552 *0.01*	4.1779	4.2135	4.2786	4.4435	4.6513	5.2914	5.7496	5.8168	5.8247
2	4.1758 *0.11*	4.1914 *0.06*	4.2143 *0.02*	4.2510	4.3184	4.4864	4.6965	5.3417	5.8035	5.8714	5.8793
4	4.2433 *0.21*	4.2591 *0.15*	4.2824 *0.09*	4.3197 *0.03*	4.3895	4.5638	4.7789	5.4351	5.9044	5.9734	5.9814
10	4.4151 *0.42*	4.4316 *0.35*	4.4558 *0.28*	4.4946 *0.18*	4.5673 *0.08*	4.7522	4.9810	5.6699	6.1613	6.2336	6.2420
20	4.6300 *0.59*	4.6473 *0.53*	4.6727 *0.46*	4.7134 *0.36*	4.7896 *0.23*	4.9836 *0.05*	5.2262	5.9604	6.4839	6.5610	6.5700
100	5.2996 *1.17*	5.3194 *1.13*	5.3484 *1.08*	5.3950 *1.00*	5.4822 *0.87*	5.7042 *0.61*	5.9819 *0.36*	6.8469	7.4909	7.5826	7.5925
1000	5.6713 *-0.38*	5.6925 *-0.41*	5.7236 *-0.45*	5.7734 *-0.52*	5.8667 *-0.64*	6.1043 *-0.92*	6.4015 *-1.27*	7.3271 *-2.19*	7.8411	7.8853	7.8906
10000	5.7035 *-0.97*	5.7248 *-1.00*	5.7561 *-1.04*	5.8062 *-1.11*	5.9000 *-1.23*	6.1390 *-1.52*	6.4379 *-1.88*	7.3688 *-2.82*	7.8856 *0.00*	7.9304	7.9358
∞	5.7074 *-1.04*	5.7287 *-1.07*	5.7600 *-1.11*	5.8102 *-1.18*	5.9041 *-1.29*	6.1431 *-1.58*	6.4422 *-1.95*	7.3738 *-2.88*	7.8910 *0.01*	7.9358 *0.00*	7.9412

Table B.6: Buckling factor for 15° Geometric Mean Approximation, $a/b = 1.0$. The difference between the actual and approximate solution is given in italics. A negative difference infers that the approximate solution underestimates the correct solution

κ	0	0.4	1	2	4	10	20	100	1000	10000	∞
0	4.5134	4.5259	4.5437	4.5723	4.6259	4.7631	4.9356	5.4645	5.8533	5.9126	5.92
0.4	4.5263 *0.01*	4.5393	4.5578	4.5870	4.6410	4.7789	4.9519	5.4823	5.8724	5.9319	5.94
1	4.5452 *0.03*	4.5583 *0.01*	4.5773	4.6074	4.6624	4.8015	4.9755	5.5084	5.9004	5.9602	5.97
2	4.5756 *0.07*	4.5887 *0.04*	4.6079 *0.01*	4.6387	4.6954	4.8369	5.0127	5.5500	5.9453	6.0057	6.01
4	4.6326 *0.14*	4.6458 *0.10*	4.6653 *0.06*	4.6964 *0.02*	4.7549	4.9012	5.0810	5.6273	6.0292	6.0906	6.1
10	4.7781 *0.31*	4.7918 *0.27*	4.8118 *0.21*	4.8440 *0.15*	4.9043 *0.06*	5.0583	5.2490	5.8219	6.2425	6.3070	6.31
20	4.9609 *0.51*	4.9751 *0.47*	4.9959 *0.41*	5.0293 *0.33*	5.0919 *0.21*	5.2518 *0.05*	5.4527	6.0620	6.5094	6.5781	6.59
100	5.5367 *1.32*	5.5525 *1.28*	5.5757 *1.22*	5.6130 *1.14*	5.6829 *0.99*	5.8614 *0.68*	6.0856 *0.39*	6.7919	7.3376	7.4221	7.43
1000	5.9979 *2.47*	6.0151 *2.43*	6.0402 *2.37*	6.0806 *2.28*	6.1563 *2.11*	6.3496 *1.72*	6.5925 *1.28*	7.3577 *0.27*	7.9706	8.0696	8.08
10000	6.0728 *2.71*	6.0902 *2.67*	6.1156 *2.61*	6.1565 *2.51*	6.2331 *2.34*	6.4289 *1.93*	6.6748 *1.47*	7.4496 *0.37*	8.0701 *0.01*	8.1709	8.18
∞	6.0816 *2.74*	6.0991 *2.70*	6.1245 *2.64*	6.1655 *2.54*	6.2422 *2.37*	6.4383 *1.96*	6.6846 *1.49*	7.4604 *0.38*	8.0819 *0.01*	8.1828 *0.00*	8.19

Table B.7: Buckling factor for 30° Geometric Mean Approximation, $a/b = 1.0$. The difference between the actual and approximate solution is given in italics. A negative difference infers that the approximate solution underestimates the correct solution

κ	0	0.4	1	2	4	10	20	100	1000	10000	∞
0	5.9451	5.9528	5.9639	5.9817	6.0148	6.0985	6.2019	6.5144	6.8005	6.7957	6.8005
0.4	5.9529 *0.00*	5.9608	5.9721	5.9901	6.0234	6.1075	6.2112	6.5247	6.7668	6.8071	6.8120
1	5.9644 *0.01*	5.9723 *0.00*	5.9838	6.0021	6.0358	6.1205	6.2248	6.5399	6.7833	6.8239	6.8288
2	5.9829 *0.02*	5.9908 *0.01*	6.0023 *0.00*	6.0209	6.0553	6.1411	6.2463	6.5641	6.8098	6.8507	6.8557
4	6.0175 *0.05*	6.0254 *0.03*	6.0371 *0.02*	6.0557 *0.01*	6.0908	6.1787	6.2860	6.6090	6.8591	6.9008	6.9059
10	6.1062 *0.13*	6.1142 *0.11*	6.1260 *0.09*	6.1450 *0.06*	6.1805 *0.03*	6.2716	6.3843	6.7220	6.9839	7.0277	7.0330
20	6.2181 *0.26*	6.2263 *0.24*	6.2383 *0.22*	6.2576 *0.18*	6.2939 *0.13*	6.3866 *0.04*	6.5037	6.8608	7.1385	7.1851	7.1907
100	6.5796 *1.00*	6.5883 *0.97*	6.6010 *0.93*	6.6214 *0.87*	6.6597 *0.77*	6.7579 *0.53*	6.8818 *0.31*	7.2818	7.6141	7.6702	7.6770
1000	6.8942 *1.36*	6.9033 *2.02*	6.9166 *1.97*	6.9381 *1.88*	6.9782 *1.74*	7.0810 *1.39*	7.2109 *1.01*	7.6300 *0.21*	7.9949	8.0594	8.0672
10000	6.9502 *2.27*	6.9594 *2.24*	6.9728 *2.18*	6.9944 *2.10*	7.0349 *1.94*	7.1385 *1.58*	7.2694 *1.17*	7.6920 *0.28*	8.0599 *0.01*	8.1253	8.1333
∞	6.9571 *2.30*	6.9663 *2.26*	6.9797 *2.21*	7.0013 *2.12*	7.0418 *1.97*	7.1456 *1.60*	7.2766 *1.19*	7.6996 *0.29*	8.0678 *0.01*	8.1333 *0.00*	8.1413

Table B.8: Buckling factor for 45° Geometric Mean Approximation, $a/b = 1.0$. The difference between the actual and approximate solution is given in italics. A negative difference infers that the approximate solution underestimates the correct solution

κ	0	0.4	1	2	4	10	20	100	1000	10000	∞
0	4.0000	4.0152	4.0386	4.0760	4.1454	4.3206	4.5375	5.1941	5.5571	5.5994	5.6043
0.4	4.0157 *0.01*	4.0313	4.0548	4.0924	4.1624	4.3386	4.5566	5.2162	5.5671	5.6095	5.6145
1	4.0393 *0.02*	4.0549 *0*	4.0786	4.1165	4.1871	4.3648	4.5845	5.2486	5.5818	5.6244	5.6294
2	4.0775 *0.04*	4.0932 *0.02*	4.1168 *0.01*	4.1551	4.2266	4.4067	4.6291	5.3004	5.6055	5.6484	5.6534
4	4.1500 *0.11*	4.1656 *0.08*	4.1893 *0.05*	4.2275 *0.02*	4.2999	4.4845	4.7120	5.3721	5.6503	5.6938	5.6989
10	4.3400 *0.45*	4.3556 *0.39*	4.3792 *0.33*	4.4175 *0.25*	4.4899 *0.12*	4.6799	4.9205	5.4778	5.7668	5.8120	5.8173
20	4.5886 *1.13*	4.6043 *1.05*	4.6279 *0.95*	4.6661 *0.8*	4.7386 *0.56*	4.9286 *0.16*	5.1772	5.6138	5.9174	5.9649	5.9705
100	5.0295 *-3.17*	5.0451 *-3.28*	5.0687 *-3.43*	5.1070 *-3.65*	5.1794 *-3.59*	5.3694 *-1.98*	5.6181 *0.08*	6.0589	6.4164	6.4727	6.4794
1000	5.4118 *-2.62*	5.4274 *-2.51*	5.4511 *-2.34*	5.4893 *-2.07*	5.5618 *-1.57*	5.7517 *-0.26*	6.0004 *1.4*	6.4412 *0.39*	6.8236	6.8882	6.8958
10000	5.4771 *-2.18*	5.4928 *-2.08*	5.5164 *-1.92*	5.5547 *-1.66*	5.6271 *-1.17*	5.8171 *0.09*	6.0657 *1.69*	6.5066 *0.52*	6.8889 *0.01*	6.9543	6.9621
∞	5.4849 *-2.13*	5.5006 *-2.03*	5.5242 *-1.87*	5.5625 *-1.61*	5.6349 *-1.12*	5.8249 *0.13*	6.0735 *1.73*	6.5144 *0.54*	6.8967 *0.01*	6.9621 *0.0*	6.9699

Table B.9: Buckling factor for 0° Arithmetic Mean Approximation, $a/b = 2.0$. The difference between the actual and approximate solution is given in italics. A negative difference infers that the approximate solution underestimates the correct solution

κ	0	0.4	1	2	4	10	20	100	1000	10000	∞
0.0	4.0488	4.0644	4.0872	4.1238	4.1916	4.3626	4.5737	5.2034	5.5982	5.6469	5.6525
0.4	4.0645 *0.00*	4.0801	4.1031	4.1399	4.2082	4.3801	4.5923	5.2244	5.6129	5.6607	5.6662
1	4.0875 *0.01*	4.1032 *0.00*	4.1263	4.1634	4.2323	4.4057	4.6196	5.2550	5.6333	5.6798	5.6852
2	4.1249 *0.03*	4.1406 *0.02*	4.1637 *0.01*	4.2010	4.2709	4.4467	4.6632	5.3034	5.6636	5.7089	5.7142
4	4.1957 *0.10*	4.2114 *0.08*	4.2345 *0.05*	4.2718 *0.02*	4.3426	4.5227	4.7443	5.3901	5.7154	5.7598	5.7650
10	4.3812 *0.43*	4.3969 *0.38*	4.4200 *0.32*	4.4573 *0.24*	4.5281 *0.12*	4.7137	4.9482	5.5497	5.8375	5.8824	5.8877
20	4.6239 *1.10*	4.6396 *1.03*	4.6627 *0.93*	4.7000 *0.79*	4.7708 *0.56*	4.9563 *0.16*	5.1990	5.6905	5.9880	6.0349	6.0404
100	5.0880 *-2.22*	5.1037 *-2.31*	5.1267 *-2.44*	5.1641 *-2.63*	5.2349 *-2.88*	5.4204 *-2.33*	5.6631 *-0.48*	6.1272	6.4770	6.5325	6.5390
1000	5.4621 *-2.43*	5.4778 *-2.41*	5.5009 *-2.35*	5.5383 *-2.21*	5.6091 *-1.86*	5.7946 *-0.74*	6.0373 *0.82*	6.5013 *0.38*	6.8755	6.9391	6.9466
10000	5.5265 *-2.13*	5.5421 *-2.09*	5.5652 *-2.02*	5.6026 *-1.86*	5.6734 *-1.50*	5.8589 *-0.40*	6.1016 *1.10*	6.5656 *0.51*	6.9398 *0.01*	7.0041	7.0118
∞	5.5341 *-2.09*	5.5498 *-2.05*	5.5729 *-1.98*	5.6103 *-1.82*	5.6810 *-1.46*	5.8666 *-0.36*	6.1093 *1.14*	6.5733 *0.52*	6.9475 *0.01*	7.0118 *0.00*	7.0195

Table B.10: Buckling factor for 15° Arithmetic Mean Approximation, $a/b = 2.0$. The difference between the actual and approximate solution is given in italics. A negative difference infers that the approximate solution underestimates the correct solution

κ	0	0.4	1	2	4	10	20	100	1000	10000	∞
0	4.2102	4.2244	4.2451	4.2783	4.3399	4.4948	4.6853	5.2517	5.6512	5.7103	5.7172
0.4	4.2244 *0.00*	4.2387	4.2596	4.2929	4.3549	4.5107	4.7021	5.2710	5.6715	5.7305	5.7374
1	4.2454 *0.01*	4.2596 *0.00*	4.2806	4.3143	4.3768	4.5339	4.7267	5.2993	5.7010	5.7601	5.7670
2	4.2793 *0.02*	4.2935 *0.01*	4.3145 *0.01*	4.3484	4.4118	4.5709	4.7661	5.3446	5.7480	5.8069	5.8138
4	4.3434 *0.08*	4.3577 *0.06*	4.3786 *0.04*	4.4125 *0.02*	4.4767	4.6396	4.8393	5.4290	5.8342	5.8923	5.8990
10	4.5111 *0.36*	4.5253 *0.32*	4.5463 *0.27*	4.5802 *0.20*	4.6443 *0.10*	4.8120	5.0232	5.6415	6.0319	6.0833	6.0892
20	4.7294 *0.94*	4.7437 *0.88*	4.7646 *0.80*	4.7985 *0.68*	4.8627 *0.48*	5.0303 *0.14*	5.2486	5.8945	6.2137	6.2596	6.2650
100	5.2809 *0.56*	5.2952 *0.46*	5.3161 *0.32*	5.3500 *0.10*	5.4142 *-0.27*	5.5818 *-1.06*	5.8002 *-1.60*	6.3517	6.6750	6.7272	6.7333
1000	5.6260 *-0.45*	5.6402 *-0.55*	5.6612 *-0.70*	5.6951 *-0.92*	5.7592 *-1.28*	5.9269 *-1.74*	6.1452 *-1.10*	6.6967 *0.33*	7.0418	7.1013	7.1084
10000	5.6861 *-0.42*	5.7004 *-0.53*	5.7213 *-0.67*	5.7552 *-0.89*	5.8194 *-1.24*	5.9870 *-1.58*	6.2054 *-0.87*	6.7569 *0.44*	7.1019 *0.01*	7.1621	7.1693
∞	5.6933 *-0.42*	5.7076 *-0.52*	5.7286 *-0.67*	5.7625 *-0.88*	5.8266 *-1.23*	5.9942 *-1.56*	6.2126 *-0.84*	6.7641 *0.46*	7.1092 *0.01*	7.1693 *0.00*	7.1765

Table B.11: Buckling factor for 30° Arithmetic Mean Approximation, $a/b = 2.0$. The difference between the actual and approximate solution is given in italics. A negative difference infers that the approximate solution underestimates the correct solution

κ	0	0.4	1	2	4	10	20	100	1000	10000	∞
0	4.5986	4.6097	4.6258	4.6516	4.6993	4.8188	4.9648	5.4012	5.7272	5.7787	5.7848
0.4	4.6097 *0.00*	4.6208	4.6370	4.6629	4.7108	4.8309	4.9776	5.4160	5.7436	5.7953	5.8015
1	4.6260 *0.00*	4.6371 *0.00*	4.6533	4.6794	4.7277	4.8485	4.9962	5.4376	5.7676	5.8197	5.8259
2	4.6522 *0.01*	4.6633 *0.01*	4.6795 *0.00*	4.7057	4.7545	4.8767	5.0260	5.4723	5.8061	5.8588	5.8651
4	4.7015 *0.05*	4.7126 *0.04*	4.7288 *0.02*	4.7550 *0.01*	4.8043	4.9289	5.0813	5.5367	5.8779	5.9319	5.9383
10	4.8292 *0.22*	4.8403 *0.19*	4.8565 *0.16*	4.8827 *0.12*	4.9320 *0.06*	5.0597	5.2197	5.6993	6.0599	6.1169	6.1237
20	4.9940 *0.59*	5.0051 *0.55*	5.0214 *0.50*	5.0475 *0.43*	5.0969 *0.31*	5.2245 *0.09*	5.3894	5.9001	6.2858	6.3469	6.3542
100	5.5553 *2.85*	5.5664 *2.78*	5.5827 *2.67*	5.6089 *2.50*	5.6582 *2.19*	5.7859 *1.52*	5.9507 *0.86*	6.5121	6.9790	7.0528	7.0616
1000	6.0385 *5.43*	6.0496 *5.33*	6.0658 *5.17*	6.0920 *4.92*	6.1413 *4.48*	6.2690 *3.45*	6.4339 *2.36*	6.9952 *0.23*	7.4784	7.5282	7.5342
10000	6.0887 *5.37*	6.0999 *5.25*	6.1161 *5.09*	6.1423 *4.84*	6.1916 *4.38*	6.3193 *3.31*	6.4841 *2.16*	7.0455 *-0.10*	7.5286 *0.01*	7.5789	7.5849
∞	6.0948 *5.36*	6.1059 *5.25*	6.1222 *5.09*	6.1484 *4.83*	6.1977 *4.37*	6.3254 *3.29*	6.4902 *2.14*	7.0515 *-0.14*	7.5347 *0.01*	7.5849 *0.00*	7.5910

Table B.12: Buckling factor for 45° Arithmetic Mean Approximation, $a/b = 2.0$. The difference between the actual and approximate solution is given in italics. A negative difference infers that the approximate solution underestimates the correct solution

κ	0		0.4		1		2		4		10		20		100		1000		10000		∞
0	4.0000		4.0152		4.0386		4.0760		4.1454		4.3206		4.5375		5.1941		5.5571		5.5994		5.6043
0.4	4.0156	*0.01*	4.0313		4.0548		4.0924		4.1624		4.3386		4.5566		5.2162		5.5671		5.6095		5.6145
1	4.0391	*0.01*	4.0549	*0.00*	4.0786		4.1165		4.1871		4.3648		4.5845		5.2486		5.5818		5.6244		5.6294
2	4.0768	*0.02*	4.0927	*0.01*	4.1166	*0.00*	4.1551		4.2266		4.4067		4.6291		5.3004		5.6055		5.6484		5.6534
4	4.1473	*0.04*	4.1635	*0.03*	4.1878	*0.02*	4.2269	*0.01*	4.2999		4.4845		4.7120		5.3721		5.6503		5.6938		5.6989
10	4.3266	*0.14*	4.3435	*0.11*	4.3689	*0.09*	4.4097	*0.07*	4.4859	*0.03*	4.6799		4.9205		5.4778		5.7668		5.8120		5.8173
20	4.5507	*0.29*	4.5685	*0.26*	4.5952	*0.23*	4.6381	*0.19*	4.7182	*0.13*	4.9223	*0.04*	5.1772		5.6138		5.9174		5.9649		5.9705
100	4.9230	*-5.22*	4.9422	*-5.25*	4.9711	*-5.29*	5.0175	*-5.34*	5.1042	*-4.99*	5.3250	*-2.79*	5.6007	*-0.23*	6.0589		6.4164		6.4727		6.4794
1000	5.2244	*-5.99*	5.2448	*-5.79*	5.2755	*-5.49*	5.3247	*-5.01*	5.4167	*-4.13*	5.6510	*-2.01*	5.9437	*0.44*	6.4299	*0.21*	6.8236		6.8882		6.8958
10000	5.2742	*-5.81*	5.2948	*-5.61*	5.3257	*-5.31*	5.3754	*-4.83*	5.4684	*-3.96*	5.7049	*-1.84*	6.0003	*0.59*	6.4912	*0.28*	6.8886	*0.01*	6.9543		6.9621
∞	5.2801	*-5.79*	5.3007	*-5.59*	5.3317	*-5.29*	5.3815	*-4.81*	5.4745	*-3.94*	5.7112	*-1.82*	6.0070	*0.61*	6.4984	*0.29*	6.8963	*0.01*	6.9621	*0.00*	6.9699

Table B.13: Buckling factor for 0° Geometric Mean Approximation, $a/b = 2.0$. The difference between the actual and approximate solution is given in italics. A negative difference infers that the approximate solution underestimates the correct solution

κ	0		0.4		1		2		4		10		20		100		1000		10000		∞
0	4.0488		4.0644		4.0872		4.1238		4.1916		4.3626		4.5737		5.2034		5.6929		5.7596		5.6525
0.4	4.0644	*0.00*	4.0801		4.1031		4.1399		4.2082		4.3801		4.5923		5.2244		5.7159		5.7829		5.6662
1	4.0874	*0.00*	4.1032	*0.00*	4.1263		4.1634		4.2323		4.4057		4.6196		5.2550		5.7496		5.8168		5.6852
2	4.1242	*0.01*	4.1401	*0.01*	4.1635	*0.00*	4.2010		4.2709		4.4467		4.6632		5.3034		5.8035		5.8714		5.7142
4	4.1931	*0.04*	4.2093	*0.03*	4.2331	*0.02*	4.2712	*0.01*	4.3426		4.5227		4.7443		5.3901		5.9044		5.9734		5.7650
10	4.3686	*0.14*	4.3855	*0.12*	4.4102	*0.10*	4.4500	*0.07*	4.5243	*0.04*	4.7137		4.9482		5.5497		6.1613		6.2336		5.8877
20	4.5880	*0.31*	4.6057	*0.29*	4.6317	*0.26*	4.6735	*0.22*	4.7515	*0.15*	4.9504	*0.04*	5.1990		5.6905		6.4839		6.5610		6.0404
100	4.9807	*-4.28*	5.0000	*-4.30*	5.0282	*-4.32*	5.0735	*-4.34*	5.1583	*-4.30*	5.3741	*-3.16*	5.6440	*-0.82*	6.1272		7.4909		7.5826		6.5390
1000	5.6344	*-1.03*	5.6562	*-1.04*	5.6881	*-1.07*	5.7394	*-1.11*	5.8353	*-1.17*	6.0795	*-1.33*	6.3848	*-1.53*	6.9313	*-7.47*	7.8411		7.8853		7.8906
10000	5.6664	*-1.62*	5.6883	*-1.63*	5.7204	*-1.66*	5.7720	*-1.69*	5.8684	*-1.76*	6.1140	*-1.92*	6.4211	*-2.13*	6.9707	*-8.07*	7.8856	*0.00*	7.9304		7.9358
'inf	5.3311	*-5.69*	5.3517	*-5.55*	5.3819	*-5.34*	5.4304	*-4.97*	5.5211	*-4.23*	5.7522	*-2.30*	6.0411	*0.01*	6.5582	*0.29*	7.4189	*-5.98*	7.4611	*-5.98*	7.0195

Table B.14: Buckling factor for 15° Geometric Mean Approximation, $a/b = 2.0$. The difference between the actual and approximate solution is given in italics. A negative difference infers that the approximate solution underestimates the correct solution

κ	0	0.4	1	2	4	10	20	100	1000	10000	∞
0	4.2102	4.2244	4.2451	4.2783	4.3399	4.4948	4.6853	5.2517	5.6512	5.7103	5.72
0.4	4.2244 *0.00*	4.2387	4.2596	4.2929	4.3549	4.5107	4.7021	5.2710	5.6715	5.7305	5.74
1	4.2452 *0.00*	4.2596 *0.00*	4.2806	4.3143	4.3768	4.5339	4.7267	5.2993	5.7010	5.7601	5.77
2	4.2787 *0.01*	4.2932 *0.01*	4.3144 *0.00*	4.3484	4.4118	4.5709	4.7661	5.3446	5.7480	5.8069	5.81
4	4.3414 *0.03*	4.3560 *0.03*	4.3775 *0.02*	4.4121 *0.01*	4.4767	4.6396	4.8393	5.4290	5.8342	5.8923	5.9
10	4.5010 *0.14*	4.5162 *0.12*	4.5385 *0.10*	4.5743 *0.08*	4.6413 *0.04*	4.8120	5.0232	5.6415	6.0319	6.0833	6.09
20	4.7008 *0.33*	4.7167 *0.31*	4.7400 *0.28*	4.7774 *0.24*	4.8473 *0.17*	5.0256 *0.05*	5.2486	5.8945	6.2137	6.2596	6.27
100	5.1712 *-1.53*	5.1887 *-1.56*	5.2143 *-1.60*	5.2554 *-1.67*	5.3324 *-1.78*	5.5285 *-2.00*	5.7739 *-2.05*	6.3517	6.6750	6.7272	6.73
1000	5.4449 *-3.65*	5.4633 *-3.67*	5.4903 *-3.70*	5.5336 *-3.73*	5.6146 *-3.76*	5.8211 *-3.50*	6.0795 *-2.16*	6.6878 *0.19*	7.0418	7.1013	7.11
10000	5.4912 *-3.84*	5.5098 *-3.85*	5.5370 *-3.87*	5.5806 *-3.90*	5.6623 *-3.90*	5.8706 *-3.50*	6.1312 *-2.05*	6.7447 *0.26*	7.1017 *0.01*	7.1621	7.17
'inf	5.4968 *-3.86*	5.5153 *-3.87*	5.5425 *-3.89*	5.5863 *-3.91*	5.6680 *-3.92*	5.8765 *-3.49*	6.1373 *-2.04*	6.7515 *0.27*	7.1088 *0.01*	7.1693 *0.00*	7.18

Table B.15: Buckling factor for 30° Geometric Mean Approximation, $a/b = 2.0$. The difference between the actual and approximate solution is given in italics. A negative difference infers that the approximate solution underestimates the correct solution

κ	0	0.4	1	2	4	10	20	100	1000	10000	∞
0	4.5986	4.6097	4.6258	4.6516	4.6993	4.8188	4.9648	5.4012	5.7272	6.7957	5.7848
0.4	4.6097 *0.00*	4.6208	4.6370	4.6629	4.7108	4.8309	4.9776	5.4160	6.7668	6.8071	5.8015
1	4.6259 *0.00*	4.6370 *0.00*	4.6533	4.6794	4.7277	4.8485	4.9962	5.4376	6.7833	6.8239	5.8259
2	4.6518 *0.01*	4.6631 *0.00*	4.6794 *0.00*	4.7057	4.7545	4.8767	5.0260	5.4723	6.8098	6.8507	5.8651
4	4.7003 *0.02*	4.7117 *0.02*	4.7282 *0.01*	4.7548 *0.00*	4.8043	4.9289	5.0813	5.5367	6.8591	6.9008	5.9383
10	4.8236 *0.10*	4.8353 *0.09*	4.8523 *0.08*	4.8795 *0.06*	4.9304 *0.03*	5.0597	5.2197	5.6993	6.9839	7.0277	6.1237
20	4.9783 *0.27*	4.9903 *0.26*	5.0078 *0.23*	5.0360 *0.20*	5.0885 *0.14*	5.2219 *0.04*	5.3894	5.9001	7.1385	7.1851	6.3542
100	5.4723 *1.32*	5.4855 *1.28*	5.5048 *1.24*	5.5357 *1.16*	5.5934 *1.02*	5.7401 *0.72*	5.9242 *0.41*	6.5121	7.6141	7.6702	7.0616
1000	6.0634 *5.87*	6.0781 *-10.18*	6.0994 *-10.08*	6.1337 *-9.93*	6.1976 *-9.64*	6.3602 *-8.93*	6.5641 *-8.05*	7.2155 *-5.24*	7.9949	8.0594	8.0672
10000	6.1127 *-10.05*	6.1274 *-9.98*	6.1490 *-9.89*	6.1835 *-9.74*	6.2479 *-9.46*	6.4118 *-8.76*	6.6174 *-7.90*	7.2741 *-5.16*	8.0599 *0.01*	8.1253	8.1333
∞	5.9083 *2.14*	5.9225 *2.09*	5.9433 *2.02*	5.9767 *1.90*	6.0390 *1.70*	6.1974 *1.20*	6.3962 *0.66*	7.0309 *-0.44*	7.7903 *-3.43*	7.8536 *-3.44*	7.5910

Table B.16: Buckling factor for 45° Geometric Mean Approximation, $a/b = 2.0$. The difference between the actual and approximate solution is given in italics. A negative difference infers that the approximate solution underestimates the correct solution

Appendix C

Uniform axial strain loading for stiffened panels

This appendix descibes the loading distributions used to obtain a uni-axial strain for the stiffened panel analysis. The loading distribution is described in further detail in the PASCO User Manual [84].

C.1 In-plane Compression Loading

The stiffness of the model is assumed to be adequately modelled using plane-strain assumptions *i.e.* that stresses σ_z, τ_{yz} and τ_{xz} are much smaller than σ_x, σ_y and $\tau_x y$ and can be neglected from the stiffness matrix leaving the following elastic relations,

$$\left\{ \begin{array}{c} N_x \\ N_y \\ N_{xy} \end{array} \right\}_i = \left[\begin{array}{ccc} A_{11} & A_{12} & 0 \\ A_{12} & A_{22} & 0 \\ 0 & 0 & A_{66} \end{array} \right]_i \left\{ \begin{array}{c} \epsilon_x \\ \epsilon_y \\ \tau_{xy} \end{array} \right\}_i \tag{C.1}$$

where,

$$\mathbf{A}_i = \frac{E_i A_i}{1-\nu_i^2} \left[\begin{array}{ccc} 1 & \nu & 0 \\ \nu & 1 & 0 \\ 0 & 0 & \frac{1-\nu}{2} \end{array} \right] \tag{C.2}$$

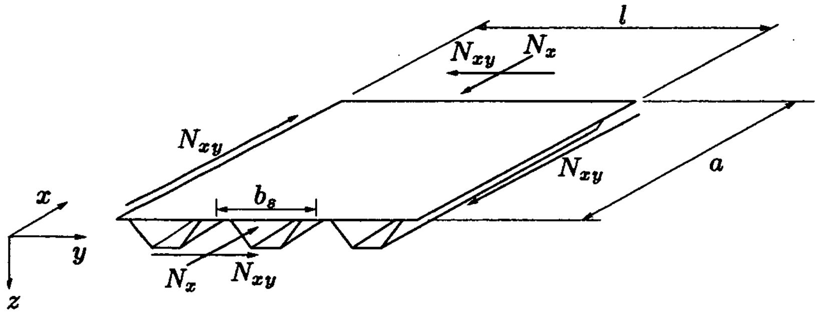

(a) Typical section of stiffened panel showing loading considered in the analysis

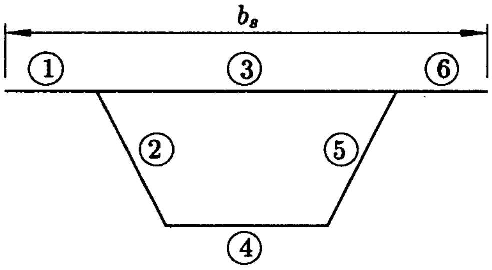

(b) Typical repeating section of width b_s of hat-stiffened panel showing elements 1-6 making up the section

Figure C.1: Typical section of stiffened panel showing loading considered in the analysis

The total longitudinal strain is given by,

$$\epsilon_x = \frac{N_x . b_s}{\sum_{i=1}^{i=n} \overline{A_i} . b_i} \tag{C.3}$$

where the i corresponds to each element making up a repeating section of the stiffened panel, having length b_s. These quantities are shown in figures C.1(a) and C.1(b). Figure C.1(a) shows a typical hat-stiffened panel with the in-plane uni-axial compression and shear loading and figure C.1(b) a repeating section of the panel made up of its six constitutive elements, numbered 1-6, each having length b_i. The N_x in equation (C.3) is the preloading required to be applied. In the case of all the models in this chapter, a load of $175.13kN/m(1000lb/in)$ is used as in the Stroud *et al.* models. The $\overline{A_i}$ term is given by $A_{11} - (A_{12}^2/A_{22})$ where the A_{xy} correspond to the relevant elements in $\mathbf{A}$ of equation (C.2).

The in-plane load to be applied to each panel element is therefore given by,

$$N_{x_i} = \epsilon_x \overline{A_i} \tag{C.4}$$

Note that in all cases, the loading is given in terms of a load per unit length of element.

C.2 In-plane shear loading

For shear loading, the shear stress is calculated by distributing shear loads in proportion to their shear flexibility defined as, S_i for a plate of length b_i defined as,

$$S_i = \frac{b_i}{A_{66}} \tag{C.5}$$

The total shear flexibility depends on whether the plates are connected in series or parallel (as in the case of the hat stiffened panel). For series connection,

$$S_p = \sum_{i=1}^{i=n} S_i \tag{C.6}$$

and for parallel connection,

$$\frac{1}{S_p} = \sum_{i=1}^{i=n} \frac{1}{S_i} \tag{C.7}$$

Hence the shear force per length of plate element, N_{xy_i} is given by

$$N_{xy_i} = \frac{S_p . N_{xy_i}}{S_i} \tag{C.8}$$

Appendix D

Closed form solutions for orthotropic rectangular plates by method of affine transformations

Brunelle and Oyibo [17] presented a general solution to predict the buckling solution of an orthotropic plate using avaliable closed-form and approximate solutions using an affine transformation. The transformation maps the critical parameters governing plate buckling into an affine plane through a transformation dependant upon the plate bending stiffnesses. Such orthotopic rescaling is given a thorough account by Whitney [99] and has since been considered by Bao, Jiang and Roberts [10].

A brief account of the method is given here in order that the minimum buckling coefficient for restangular plates having the same orthotropic ratio as the skew panels can be obtained to give a theoretical minumum buckling load for the skew panels considered.

Given the general governing partial differential equation for plate equilibrium with orthotropy.

$$D_{11}\frac{\partial^4 w}{\partial x^4} + 2(D_{12} + 2D_{66})\frac{\partial^4 w}{\partial x^2 \partial y^2} + D_{22}\frac{\partial^4 w}{\partial y^4} = N_x\frac{\partial^2 w}{\partial x^2} \tag{D.1}$$

The x and y are transformed into the affine space using:

$$x = \sqrt[4]{D_{11}} \quad x_o \tag{D.2}$$

$$y = \sqrt[4]{D_{22}} \quad y_o \tag{D.3}$$

so that

$$\frac{a}{b} = \frac{a_o}{b_o}\sqrt[4]{\frac{D_{11}}{D_{22}}} \tag{D.4}$$

where x, y, a, b are the plate dimensions as previously defined and parameters with subscript 'o' are these parameters transformed in the affine space.

The material orthotropy is characterised by one independant, nondimensional material parameter, η, and for simplicty, a second nondimensional parameter, λ. It is noted that a second independant parameter; a transformed Poisson's ratio is required if a boundary condition which imposes a general force is included in the analysis. This boundary conditon is outwith the scope of this discussion and therefore this second parameter is not considered here. η and λ are given by:

$$\eta = \frac{D_{12} + 2D_{66}}{\sqrt{D_{11}D_{22}}} \tag{D.5}$$

$$\lambda = \frac{D_{22}}{D_{11}} \tag{D.6}$$

Use of the material parameters defined above, transforms the governing plate equation to:

$$\frac{\partial^4 w}{\partial x^4} + 2\eta\sqrt{\lambda}\frac{\partial^4 w}{\partial x^2 \partial y^4} + \lambda\frac{\partial^4 w}{\partial y^4} = N_x\frac{\partial^2 w}{\partial x^2} \tag{D.7}$$

and the use of the transformations on the x and y coordinates to:

$$\frac{\partial^4 w}{\partial x_o^4} + 2\eta\frac{\partial^4 w}{\partial x_o^2 \partial y_o^4} + \frac{\partial^4 w}{\partial y_o^4} = \frac{N_x}{D_{11}}\frac{\partial^2 w}{\partial x_o^2} \tag{D.8}$$

Hence, this equation is synonymous with the equation of equilibrium for a rectangular, isotropic plate because when $D_{11} = D_{22}$ and $\nu_{12} = \nu_{21}$, $\eta = 1$. The implication of this is that a buckling solution for any rectangular isotropic plate can be readily converted to a buckling solution for any orthotropic plate. The following discussion gives the formulation for such a conversion and makes comparison with the isotropic and orthotropic solutions.

For a simply supported plate, the general closed-form solution to the critical buckling load is given by,

$$N_x = \frac{\pi^2 D}{b^2}\left(\frac{mb}{a} + \frac{a}{mb}\right)^2 \tag{D.9}$$

whereas solution of the previous partial differential equation leads, by similar means, to:

$$N_x = \frac{\pi^2\sqrt{D_{11}D_{22}}}{b^2}\left(\frac{m^2b_o^2}{a_o^2} + \frac{a_o^2}{m^2b_o^2} + 2\eta\right) \tag{D.10}$$

where, m is the number of half-wavelengths in the longitudinal direction making up the buckle mode. The minumum buckling load for the orthotropic plate is therefore determined when (by inspection) $a_o/b_o = 1$ and $m = 1$.

Hence the minimum buckling load for any specially orthotropic rectangular plate is given by:

$$N_x = (2 + 2\eta)\,\frac{\pi^2\sqrt{D_{11}D_{22}}}{b^2} \tag{D.11}$$

which can be given in terms of the buckling coefficient used throughtout, $k = (N_xb^2)/(\pi^2D_{22})$, hence

$$k = \frac{\left(\frac{a_o^2}{m^2b_o^2} + \frac{m^2b_o^2}{a_o^2} + 2\eta\right)\sqrt{D_{11}}}{\sqrt{D_{22}}} \Rightarrow k_{min} = (2 + 2\eta)\sqrt{\frac{D_{11}}{D_{22}}} \tag{D.12}$$

Bibliography

[1] ESDU 02.01.48. Buckling stress coefficients for flat plates tapered in plan under compression. Technical report, Engineering Sciences Data Unit, 1971. Reprinted Jan. 1971.

[2] A. Aalberg, M. Langseth, and P.K. Larsen. Stiffened aluminium panels subject to axial compression. *Thin-walled Structures*, 39:861–885, 2001.

[3] *ABAQUS Users' manual, Version 5.8.* Habbit, Karlsson and Sorensen Inc., Warrington, Cheshire, U.K., 1998.

[4] M.S. Anderson and F.W. Williams. Buckling and vibration of any prismatic assembly of shear and compression loaded anisotropic plates with an arbitary supporting structure. *International Journal of Mechanical Science*, 25(8):585–596, 1983.

[5] R.A. Anderson. Charts giving critical compressive stress of continuous flat sheet divided into parallelogram-shaped panels. Technical Report TN 2392, NACA, July 1951.

[6] R.A. Anderson and J.W. Semonian. Charts relating the compressive buckling stress of longitudinally supported plates to the effect deflectional and rotational stiffness at the supports. Technical Report NACA TN 1202, National Advisory Committee for Aeronautics, Washington, District of Columbia, USA., 1954.

[7] J.H. Argyris. Continua and discontinua (an apercu of recent developments of the matrix displacement method). In *Proceedings of Matrix Methods in Structral Engineering*, pages 11–190, Wright-Patterson Air Force Base, Ohio, October 1966.

[8] J.E. Ashton. Stability of clamped skew plates under combined loads. *Journal of Applied Mechanics*, 36(1):139–140, March 1969.

[9] L.C. Bank and Jiansheng Jin. Buckling of orthotropic plates with free and rotationally restrained unloaded edges. *Thin-walled Structures*, 24:83–96, 1996.

[10] G. Bao, J. Jiang, and J.C. Roberts. Analytic and finite element solutions for bending and buckling of orthotropic rectangular plates. *International Journal of Solids and Structures*, 34(14):1797–1822, 1997.

[11] S. B. Batdorf, M. Stein, and C. Libove. Critical combinations of longitudinal and transverse direct stress for an infinitely long, flat plate with edges elastically restrained against rotation. Technical Report ARR l6A05a, NACA, 1946.

[12] O. K. Bedair. Analysis of stiffened plates under lateral loading using sequential quadratic programming (SQP). *Computers and Structures*, 62(1):63–80, 1997.

[13] O. K. Bedair and A. N. Sherbourne. Plate-stiffener assemblies in uniform compression. Part 1:Buckling. *Journal of Engineering Mechanics*, 119(10):1937–1955, Oct. 1993.

[14] K. Bedair Osama. A contribution to the stability of stiffened plates under uniform compression. *Computers and Structures*, 66(5):535–570, 1998.

[15] E.A. Brades and G.B. Brook, editors. *Smithell's Metals Reference Book.* Butterworth and Heinemann, VII edition, 1989.

[16] F.A. Brogan, C. Rankin, and H.D. Cabiness. *STAGS User manual, Version 2.* Number LMSC P032594. Lockheed Palo Alto Research Laboratory, June 1994.

[17] E.J. Brunelle and G.A. Oyibo. Generic buckling curves for specially orthotopic rectangular plates. *AIAA Journal*, 21(8):1150–1156, 1983.

[18] B. Budiansky and P. C. Hu. The Lagrangian multiplier method of finding upper and lower limits to critical stresses of clamped plates. Technical Report Rep 848, NACA, 1946.

[19] H.V. Budiansky and Connor. Notes on the Lagrangian multiplier method in elastic-stability analysis. Technical Report NACA-TN-1558, NACA, 1948.

[20] P.S. Bulson. *The Stability of Flat plates.* Chatto and Windus, London, 1970.

[21] Y.K. Chan and A.P. Kabaila. A compatible element for buckling analysis of skew plates with parallel edges. *Theory and practice in finite element structural analysis*, pages 479–497, 1973.

[22] C-Y Chia. *Non-linear analysis of plates.* McGraw Hill, 1980.

[23] R.C. Coates, M.G. Coutie, and F.K. Kong. *Structural Analysis.* Chapman and Hall, 3rd edition, 1988.

[24] M.A. Crisfield. A fast incremental/iterative solution procedure than handles "snap–through". *Computers and Structures*, 13:55–62, 1981.

[25] D.J. Dawe and V. Peshkam. Buckling and vibration of finite–length composite plate structures with diaphragm ends, Part I: finite strip formulation. *Computer Methods in Applied Mechanics and Engineering*, 77:1–30, 1989.

[26] D.J. Dawe and V. Peshkam. A note on finite strip buckling analysis of composite plate structures. *Composite Structures*, 34:163–168, 1996.

[27] S. Durvasula. Buckling of clamped skew plates. *AIAA Journal*, 8(1):178–181, 1970.

[28] S. Durvasula. Buckling of simply supported skew plates. *Proceedings of the ASCE, Journal of the Engineering Mechanics Division*, 97(3):967–979, 1971.

[29] S. Durvasula, P.S. Nair, and M.S.S. Prabhu. Vibration and buckling of orthotropic skew plates. *J. Indian Inst. Sci.*, 53:209–231, 1971.

[30] ESDU 02.01.47. ESDU 02.01.47: Buckling stress coefficients for parallelogram shaped panels in continuous flat sheet under uniform compression. Technical report, Engineering Sciences Data Unit, 1957. Reprinted with Amendment A, April 1984.

[31] C.A. Featherston. Imperfection sensitivity of flat plates under combined compression and shear. *Non-Linear Mechanics*, 36:249–259, 2001.

[32] I. Fried and K. Schmitt. Numerical results from the application of gradient iterative techniques to the finite element vibration and stability analysis of skew plates. *Aeronautical Journal*, 76:166–169, March 1972.

[33] Williams. F.W and M.S. Anderson. Buckling and vibration of shear-loaded prismatic plate assmblies with supporting structures utilising symmetric or repetative cross-sections. In D.J. Dawe, R.W. Horsington, A.G. Kamtekar, and G.H. Little, editors, *Aspects of the analysis of plate structures – A volume in honour of W.H. Wittrick*, chapter 4, pages 51–71. Oxfor Science Publications, 1985.

[34] G. Gerard and H. Becker. *NACA TN 3781 - Handbook of structural stability, Part 1: Buckling of flat plates.* NACA, Washington, July 1957.

[35] K. Ghavami. Experimental study of stiffened plates in compression up to collapse. *Constr. Steel Research*, 28:197–221, 1994.

[36] G.Y. Grondin, A.E. Elwi, and J.J.R. Cheng. Buckling of stiffened steel plates - a parametric study. *Journal of Constructional Steel Research*, 50:151–175, 1999.

[37] J. Guest. The buckling of uniformly compressed parallelogram plates having all edges clamped. Technical Report ARL-SM-172, Aeronautical Research Laboratories, Australia, 1951.

[38] J. Guest. A lower-bound solution to the buckling stress of uniformly clamped parallelogram plates. *Australian Journal of Applied Science*, 7:336–345, Dec. 1956.

[39] M. Hamada. Compressive or shearing buckling load and fundamental frequency of a rhomboidal plate with all edges clamped. *Bulletin of JSME*, 2(8):520–526, 1959.

[40] Hasegawa. On buckling of clamped rhombic thin plates in shear. *Journal of the Aeronautical Sciences*, 21:720, October 1954.

[41] M. Herdi and N. Tutuncu. A parametric stability analysis of composite plates tapered in planform. *Journal of Strain Analysis*, 35(1):59–64, January 2000. Technical Note.

[42] K. H. Hoon, J. Rhodes, and L. K. Seah. Tests on intermediately stiffened plate elements and beam compression elements. *Thin-walled Structures*, 16:111–143, 1993.

[43] L.G. Jaeger. *Elementary theory of elastic plates*. Pergammon Press, 1984.

[44] N Jaunky, N.F. Knight, Jnr, and D.R. Ambur. Buckling of arbitrary quadrilateral anisotropic plates. *AIAA Journal*, 33(5):938–944, May 1995.

[45] J. B. Kennedy, K. Madanaphalii, and M. K. Prabhakara. Combined buckling of orthotropic skew plates. *Proceedings of the ASCE, Journal of the Engineering Mechanics Division*, pages 71–79, Feb 1979.

[46] J. B. Kennedy and M. K. Prabhakara. Buckling of simply supported orthotropic skew plates. *The Aeronautical Quarterly*, 29:161–172, 1978.

[47] P.W. Khong and J.H. Ong. Post-buckling of a plate with elastic restraints at two unloaded edges. *Computers and Structures*, 56(6):933–938, 1995.

[48] S. Kitipornchai, Y. Xiang, C.M. Wang, and K.M. Liew. Buckling of thick skew plates. *International Journal for Numerical Methods in Engineering*, 36:1299–1310, 1993.

[49] B. Klein. Buckling of simply supported plates tapered in planform. *Journal of Applied Mechanics*, pages 207–213, June 1956.

[50] B. Klein. The buckling of tapered plates in compression. *Aircraft Engineering*, 58(4):427–430, December 1956.

[51] B. Klein. Buckling of simply-supported rhombic plates under externally applied shear. *Journal of the Royal Aeronautical Society*, 61:357–358, May 1957.

[52] B. Klein. Shear buckling of simply supported plates tapered in planform. *Journal of the Franklin Institute*, pages 43–48, July 1957.

[53] A.R. Krishta-Reddy and R. Palaninathan. Buckling of laminated skew plates. *Thin-walled Structures*, 22:241–259, 1995.

[54] S.G. Lekhnitskii. *Theory of Elasticity of and Anisotropic Body*. Holden–Day, 1963.

[55] Li Long-yuan and P. Bettes. Buckling of stiffened plates and design of stiffeners. *International Journal for Pressure Vessels and Piping*, 74:177–187, 1997.

[56] E. E. Lundquist and E. Z. Stowell. Critical compressive stress for flat rectangular plates supported along all edges and elastically restrained against rotation along the unloaded edges. Technical Report TR 733, NACA, 1942.

[57] E.E. Lundquist and E.Z. Stowell. Critical compressive stress for outstanding flanges. Technical Report NACA 734, National Advisory Committee on Aeronautics, Langley Field, Vancouver, 1941.

[58] E.E. Lunquist, E.Z. Stowell, and E.H. Schuette. Principles of moment distribution applied to stability of structures composed of plates and bars. Technical Report NACA AR 3K06, National Advisory Committee on Aeronautics, Washington, District of Colombia, USA, 1943.

[59] Mahabaliraja and S. Durvasula. Stability of simply supported skew plates under combined loading. *Journal of Applied Mechanics*, 39:310–311, March 1972.

[60] E.H. Mansfield. Elastic instability of a swept panel. *Aircraft Engineering*, 24:48–49, February 1952.

[61] R. Maquoi and M. Skaloud. Stability of plates and plated structures: General report. *Journal of Construction Steel Research*, 55:45–68, 2000.

[62] A.F. Mateus and J.A. Witz. A parametric study of the post-buckling behaviour of steel plates. *Engineering Structures*, (23), 172-185 2000.

[63] R.D. Mindlin. Influence of rotary inertia and shear on flexural motions of isotropic, elastic plates. *Journal of Applied Mechanics*, March 1951.

[64] T. Mizusawa and T. Kajita. Vibration and buckling of skew plates with edges elastically restrained against rotation. *Computers and Structures*, 22(6):987–994, 1986.

[65] T. Mizusawa, T. Kajita, and M. Naruoka. Analysis of skew plate problems with various constraints. *Journal of Sound and Vibration*, 73(4):575–584, 1980.

[66] T. Mizusawa, T. Kajita, and M. Naruoka. Buckling of skew plate structures using B–spline functions. *International Journal for Numerical Methods in Engineering*, 15:87–96, 1980.

[67] T. Mizusawa and J. W. Leonard. Vibration and buckling of plates with mixed boundary conditions. *Engineering Structures*, 12:285–290, Oct 1990.

[68] L. S. D. Morley. *Skew Plates and Structures*. Pergamon Press, Oxford, 1963.

[69] M. Mukhopadhyay and Mukherjee. Finite element buckling analysis of stiffened plates. *Computers and Structures*, 34(6):795–803, 1990.

[70] Column Research Committee of Japan, editor. *Handbook of Structural Stability*. Corona, Tokyo, 1971.

[71] J.K. Paik and A.K. Thayamballi. Buckling strength of steel plating with elastically restrained edges. *Thin-walled Structures*, 37:27–55, 2000.

[72] V. Peshkam and D. J. Dawe. Buckling and vibration of finite-length composite prismatic plate structures with diaphragm ends, part II: Computer programs and buckling applications. *Computer Methods in Applied Mechanics in Engineering*, 77:227–252, 1989.

[73] G.G. Pope. The buckling of plates tapered in plan. Technical Report ARC R and M 3324, ARC, 1963.

[74] H.D. Radloff, M.W. Hyer, and M.P. Nemeth. The buckling response of symmetrically laminated composite plates having a trapezoidal area. Technical Report NASA-CR-196975, NASA, 1994.

[75] E Reissner. The effect of transverse shear deformation on the bending of elastic plates. *Journal of Applied Mechanics*, 12:69–77, June 1945.

[76] J. Rhodes and J.M. Harvey. The post-buckling behaviour of thin, flat plates in compression with the unloaded edges elastically restrained against rotation. *Journal of Mechanical Engineering*, 13(2):82–91, 1971.

[77] E. Riks. An incremental approach to the solution of snapping and buckling problems. *International Journal of Solids and Structures*, 15(7):529–551, 1979.

[78] R.J. Roark. *Formulas for Stress and Strain.* McGraw-Hill, IV edition, 1965.

[79] C. Sarath Babu and T. Kant. Two shear deformable finite element models for buckling analysis of skew fibre-reinforced composite and sandwich panels. *Composite Structures*, 49:115–124, 1999.

[80] R.S. Srinivasan and S.V. Ramachandran. Stability of generally orthotropic skew plate. *Journal of the Engineering Mechanics Division*, (102):569–572, 1976.

[81] M. Stein. Loads and deformations of buckled rectagular plates. Technical Report TR R-40, NASA, 1959.

[82] F. Stoll. Analysis of the snap phenomenon in buckled plates. *International Journal of Non-Linear Mechanics*, 29(2):123–138, 1994.

[83] Stowell and Schwartz. Critical stress for an infinitely long flat plate with elastically restrained edges under shear and direct stress. Technical Report NACA-ARR-3K13 / WR-L-340, NACA, 1943.

[84] Jefferson W. Stroud and M. S. Anderson. PASCO: Structural panel analysis and sizing code, capability and analytical foundations. Technical Report TM–80181, NASA, Langley Research Centre, Hampton, Virginia 23665, November 1981.

[85] Jefferson W. Stroud, William H. Greene, and Melvin S. Anderson. Buckling loads of stiffened panels subjected to combined longitudinal compression and shear: Results obtained with PASCO, EAL and STAGS computer programs. Technical Report TP 2215, NASA, Langley Research Centre, Hampton, Virginia, U.S., 1984.

[86] L.G. Tham and H.Y. Szeto. Buckling analysis of arbitrarily shaped plates by finite strip method. *Computers and Structures*, 36(4):729–735, 1990.

[87] P.V. Thangam Babu and D.V. Reddy. Stability analysis of skew orthotropic plates by the finite strip method. *Computers and Structures*, 8:599–607, 1978.

[88] S. Timoshenko. *Theory of Elastic Stability.* Engineering Science Monograph, McGraw Hill, 2 edition, 1961.

[89] S Timoshenko and S Woinowsky-Kreieger. *Theory of plates and shells.* McGraw Hill Book Company Inc., second edition, 1959.

[90] A.C. Ugural. *Stresses in Plates and Shells.* McGraw-Hill, ii edition, 1999.

[91] G. Venkateswara Rao, J Venkataramana, and K. Kanaka Raju. Stability of moderately thick rectangular plates using a high precision triangular finite element. *Computers and Structures*, 5:257–259, 1975.

[92] J. R. Vinson and R. L. Sierakowski. *The Behaviour of Structures Composed of Composite Materials.* Martinus Nijhoff, 1986.

[93] C.M. Wang, S. Kitipornchai, and Y. Xiang. *Shear effect for Mindlin plate buckling.* Number ISBN 0 86776 5615. Dept. of Civil Engineering, University of Queensland Publication, 1994.

[94] C.M. Wang, K.M. Liew, and W.A.M. Alwis. Buckling of skew plates and corner conditions for simply supported edges. *Journal for Engineering Mechanics*, 118(4):162–173, 1992.

[95] C.M. Wang, J.N. Reddy, and K.H. Lee. *Shear Deformable Beams and Plates - Relationships with Classical Solutions.* Elsevier, 2000.

[96] S. Wang. Buckling analysis of skew fibre–reinforced composite laminates based on first–order shear deformation plate theory. *Computers and Structures,* 37:5–19, 1997.

[97] S. Wang. Buckling of thin skew fibre–reinforced composite laminates. *Thin-Walled Structures,* 28(1):21–41, 1997.

[98] X. Wang, A.G. Striz, and C.W. Bert. Buckling and vibration analysis of skew plates by the differential quadrature method. *AIAA Journal,* 32(4):886–889, 1994.

[99] J.M. Whitney. *Structural analysis of laminated anisotropic plates.* Technomic publishing, Lancaster, 1987.

[100] D.G. Williams and B. Aalami. *Thin Plate Design for In-Plane Loading.* Granada Publishing, 1979.

[101] F.W. Williams and M.S. Anderson. Incorportation of Lagrangian multipliers into an algorithm for finding exact natural frequencies or critical buckling loads. *International Journal of Mechanical Sciences,* 25(8):579–584, 1983.

[102] F.W. Williams, M.S. Anderson, D. Kennedy, R. Butler, and G. Aston. *User Manual for VICONOPT: An exact analysis and optimum design program covering the buckling and vibration of prismatic assemblies of flat, in-plane loaded, anisotropic plates with approximations for discrete supports and transverse stiffeners.* NASA, 1990. NASA CR 181966.

[103] F.W. Williams, D. Kennedy, R. Butler, and M.S. Anderson. VICONOPT: Program for exact vibration and buckling analysis or design of prismatic plate assemblies. *AIAA Journal,* 29(11):1927–1928, 1991.

[104] F.W. Williams and W.H. Wittrick. Exact buckling and frequency calculations surveyed. *Journal of Structural Engineering,* 109(1):169–187, January 1983.

[105] W. H. Wittrick. Buckling of oblique plates with clamped edges under uniform compression. *The Aeronautical Quarterly,* 4:151–163, February 1953.

[106] W. H. Wittrick. Buckling of oblique plates with clamped edges under uniform shear. *The Aeronautical Quarterly,* 5:39–51, May 1954.

[107] W. H. Wittrick and R. W. Horsington. Buckling and vibration of composite folded–plate structures of finite length in combined shear and compression. *Proceedings of the Royal Society of London,* 392:107–144, 1984.

[108] W.H. Wittrick and F.W. Williams. A general algorithm for computing natural frequencies of elastic structures. *Quarterly Journal of Mechanics and Applied Mathematics,* 24(3):263–284, 1971.

[109] W.H. Wittrick and F.W. Williams. An algorithm for computing critical buckling loads of elastic structures. *Journal of Structural Mechanics,* 1(4):497–518, 1973.

[110] Y. Xiang, C. M. Wang, and S. Kitipornchai. Shear buckling of simply supported skew Mindlin plates. *AIAA Journal,* 33(2):377–378, 1994.

[111] N. Yamaki. Post-buckling behaviour of rectangular plates with small initial curvature loaded in edge compression. *Journal of Applied Mechanics,* sept 1959.

[112] C. B. York. Influence of continuity and aspect ratio on buckling of skew plates and plate assemblies. *International Journal of Solids and Structures,* 33(15):2133–2159, 1996.

[113] C. B. York. Buckling design curves for isotropic rectangular plates with continuity or elastic edge restraints against rotation. *Aeronautical Journal,* 2000. In Press.

[114] C. B. York and F. W. Williams. Theory and buckling results for infinitely wide stiffened skew plate assemblies. *Computers and Structures*, 28:189–200, 1994.

[115] C. B. York and F. W. Williams. Buckling analysis of skew plate assemblies: Classical theories incorporating lagrangian multipliers. *Computers and Structures*, 56(4):625–635, 1995.

[116] C. B. York and F. W. Williams. Aircraft wing panel buckling analysis: efficiency by approximations. *Computers and Structures*, 68:665–676, 1998.

[117] C. B. York, F. W. Williams, D. Kennedy, and R. Butler. A parametric study of optimum designs for benchmark stiffened wing panels. *Composite Engineering*, 3(7–8):619–632, August 1993.

[118] Y. Yoshimura and K. Iwata. Buckling of simply supported oblique plates. *Journal of Applied Mechanics*, 30(2):363–366, September 1963.

[119] R.D. Young and M.W. Hyer. Accurate modeling of the postbuckling response of composite panels with skewed stiffeners. In N.F. Knight, Jnr and M.P. Nemeth, editors, *Stability Analysis of Plates and Shells – A Volume in Honor of Dr. Manuel Stein*, pages 425–434. NASA, NASA, January 1998. NASA/CP-1998-206280.

[120] O.C. Zienkienwicz. *The Finite Element Method in Engineering Science*. McGraw Hill, 1971.